Evaluation of the Thermal Impact from Battery Packs from Electrical Vehicles in Underground Mining Environment

by

Daniel Marques De Almeida

A thesis submitted in partial fulfillment

of the requirements for the degree of

Master of Applied Science (M.A.Sc.) in Natural Resource Engineering

Faculty of Graduate Studies

Laurentian University

Sudbury, Ontario

THESIS DEFENCE COMMITTEE/COMITÉ DE SOUTENANCE DE THÈSE
Laurentian Université/Université Laurentienne
Faculty of Graduate Studies/Faculté des études supérieures

Title of Thesis
Titre de la thèse: EVALUATION OF THE THERMAL IMPACT FROM BATTERY PACKS FROM ELECTRICAL VEHICLES IN UNDERGROUND MINING ENVIRONMENT

Name of Candidate
Nom du candidat: De Almeida, Daniel

Degree
Diplôme: Master of Science

Department/Program
Département/Programme: Engineering

Date of Defence
Date de la soutenance January 10, 2019

APPROVED/APPROUVÉ

Thesis Examiners/Examinateurs de thèse:

Dr. Markus TImusk
(Supervisor/Directeur(trice) de thèse)

Dr. Krishna Challagulla
(Committee member/Membre du comité)

Dr. JA Scott
(Committee member/Membre du comité)

Dr. Jie Liu
(External Examiner/Examinateur externe)

Approved for the Faculty of Graduate Studies
Approuvé pour la Faculté des études supérieures
Dr. David Lesbarrères
Monsieur David Lesbarrères
Dean, Faculty of Graduate Studies
Doyen, Faculté des études supérieures

ACCESSIBILITY CLAUSE AND PERMISSION TO USE

I, **Daniel De Almeida**, hereby grant to Laurentian University and/or its agents the non-exclusive license to archive and make accessible my thesis, dissertation, or project report in whole or in part in all forms of media, now or for the duration of my copyright ownership. I retain all other ownership rights to the copyright of the thesis, dissertation or project report. I also reserve the right to use in future works (such as articles or books) all or part of this thesis, dissertation, or project report. I further agree that permission for copying of this thesis in any manner, in whole or in part, for scholarly purposes may be granted by the professor or professors who supervised my thesis work or, in their absence, by the Head of the Department in which my thesis work was done. It is understood that any copying or publication or use of this thesis or parts thereof for financial gain shall not be allowed without my written permission. It is also understood that this copy is being made available in this form by the authority of the copyright owner solely for the purpose of private study and research and may not be copied or reproduced except as permitted by the copyright laws without written authority from the copyright owner.

Library and Archives Canada

Published Heritage Branch

395 Wellington Street
Ottawa ON K1A 0N4
Canada

Bibliotheque et Archives Canada

Direction du Patrimoine de l'edition

395, rue Wellington
OttawaONK1A0N4
Canada

Your file Votre reference
ISBN: 978-0-494-57664-9
Our file Notre reference
ISBN: 978-0-494-57664-9

Abstract

One of the main aspects which governs the size of ventilation facilities in underground mines is the amount of heat load generated in the underground environment. This heat load comes from many different sources, one of which is the heat contributed by underground diesel machinery operation. One strategy to mitigate the heat and other emissions from such equipment is to substitute these units to similar performance, but more thermally efficient, electric machinery.

This study presents a heat load evaluation of the Lithium-iron Phosphate battery system used in a prototype electric mining vehicle. The set of equations which governs the heat generation from these devices have been developed by previous researchers and is used in this thesis to calculate the heat generation and loss. However, in the mining industry, the current methodology for heat load calculation from electric vehicles (EVs) is usually based on the rated power or on a simple power loss equation. This strategy might lead to incorrect estimations of the heat load from this type of machinery.

Experimental and simulation work has been conducted as a means to evaluate the heat flux from the Lithium-iron Phosphate battery system. The battery was tested through charging and discharging it under different levels of current within the 10% to 90% range of its maximum capacity. The test was performed firstly with a single cell and then with a module. Furthermore, the battery system was set in operation under different environment temperature settings. These current and temperature levels represent the range of possible conditions in which the prototype will face in service. Through the estimation of the heat released from the other main electrical components in the vehicle, it was possible to calculate the heat impact of these units in the surrounding environment.

Acknowledgements

I would like to express my deep gratitude towards my thesis supervisor, Dr. Markus Timusk of the Bharti School of Engineering at Laurentian University, who provided me with assistance, encouragement, and inspiration to pursue the required knowledge to develop this thesis. This was a great opportunity to develop myself intellectually and professionally under his guidance. Without his support, this work would not be possible.

I would also like to thank John Le, from Tracks and Wheels, who opened the doors of his company to me, and Dr. Seyed Mahdi Mousavi, who helped me with each step of my research. Both individuals provided me with invaluable assistance, which was essential for the development of this research project. Their contribution is highly appreciated.

Finally, I would also like to acknowledge the Laurentian University staff, especially Dr. Ramesh Subramanian, to Damien Duff from Centre for Excellence in Mining Innovation – CEMI, and again, to Dr. Markus Timusk, for their financial and academic support.

Table of Contents

Figures and Tables

1 Introduction

The levels of safety and comfort for personnel are of significant concern in underground mines. Internal combustion (IC) engines, such as those used in mobile mining equipment, emit a considerable amount of waste heat, hazardous gases, and particulate matter into the environment. Once they have been released into the working environment, mitigation of these emissions is mainly achieved through costly operations, such as ventilation and refrigeration. As these costs continue to increase, the industry is being forced to seek alternatives to IC engines for underground environments.

This thesis is related to a larger project undertaken by a manufacturer of mining equipment (Tracks and Wheels of Sudbury, Ontario) which involves the design and production of an Electric Vehicle (EV), referred to as the Commander 5EV, presented in Figure 1-1. This general-purpose utility vehicle is designed to transport five passengers, including the driver, and has a cargo bed suitable for a maximum payload of 6350kg (14000 lbs). The machine is powered by two electric motors (one per axle), has a battery pack rated at 100kWh, and can provide a range and performance that is intended to be acceptable to mining operators. One of the principal motivations for the development of the Commander 5EV is to replace diesel-powered vehicles and thereby reduce emissions of contaminants and heat in the underground environment, thereby providing a more economical and safer alternative.

Figure 1-1: Electric mine truck manufactured by Tracks and Wheels, Commander 5EV (Tollinsky, 2017).

In addition, the primary focus of this thesis is on the heat generation from EV's, specifically from battery systems. The study also estimates the heat generated from other components in EV's (electric motors, motor controllers, DC/DC converters, etc). Combining all sources of heat generation from EV's will then help in providing an overall estimate of heat load on the underground environment.

1.1 Mobile Machinery in Underground Mining

Since the 1960's, diesel engines have been widely used for mobile equipment in underground mining (McGinn, 2007). However, despite this historic presence, the mining industry is currently looking for alternatives due to three main issues. The first issue is emissions of toxic gasses and particulate matter which must be removed from the local environment. The second issue is related to increased risk of overheating IC engines, which are approaching their operational limits in some of the hottest operating environments currently experienced. The third concern is the heat load on mine cooling systems from relatively inefficient IC engines. It is estimated that approximately two-thirds of the energy input into an internal combustion engine is expected to be lost to the environment in the form of waste heat (McPherson, 1993). A breakdown of the energy flow can be seen in Figure 1-2. In comparison, the heat generated from electric vehicles is approximately three times lower when compared to a regular internal combustion engine (McPherson, 1993). This is principally due to the higher efficiency of electric power trains in comparison to their diesel counterparts.

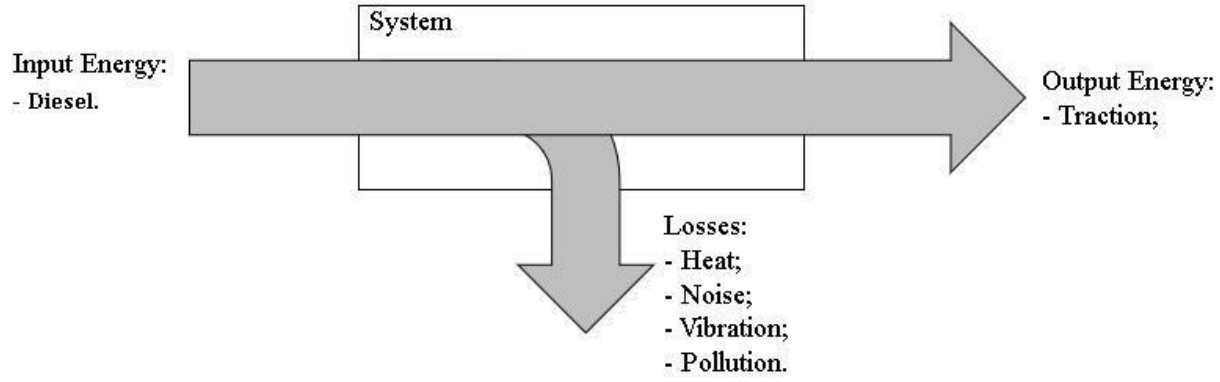

Figure 1-2: Energy Flow Diagram for Diesel Mobile Equipment.

Currently, diesel engines still have a solid presence in the mines underground, however with the enforcement of strict safety regulations, increasing commercial advantages of electric machinery, and developing alternative mobile technologies, their replacement is underway.

1.2 Scope

This study focuses on the heat load of battery electric vehicles in underground mines, with special attention on battery packs in electric vehicles. In relation to the other components, such as electric motors, motor controllers, DC/DC converter, hydraulic pumps, air conditioner, and heater, the heat load is calculated based on predictions and estimations. This means that predictions, and estimations were made for different expected driven conditions, following information provided by the manufacturer's brochure for each device.

In relation to the battery pack, the heat generation and loss are based on a well-known set of equation. As for the heat generation, these calculations are specifically related to the chemistry used, which in this case is Lithium-iron Phosphate. This chemistry is becoming the standard in mining electric vehicle applications, due to its good balance between cost, reliability, safety, energy capacity, and energy density. The heat loss is calculated differently, and it is based on the traditional method of heat loss through radiation and convection.

The set of tests conducted examines the heat magnitude and distribution over the exterior surface of the battery for a single cell and for module with 8 multiple cells. The battery is tested under different regimes of currents for discharging and charging, that simulates the demands that these units are expected to face when in service in the underground mining environment. The results obtained through the experimental phase are then compared to a simulation built in a finite-numerical software, to confirm or dismiss the earlier predictions.

1.3 Objectives and Thesis Structure

The overall objective of this work is to gain an understanding of the heat generated from electric vehicle operations in the context of underground mines. The specific focus being on the battery systems in terms of heat loads. This objective was achieved through a review of the literature, experimental and simulation work.

The literature review examines existing studies relating to the generation of heat from electric vehicles in underground mines, focusing on battery systems. The section begins with the economic aspects of mine ventilation, and their impact on the entire mining operation. Then, studies related to underground heat sources are presented for different mine sites, with a focus on contribution of diesel machinery. Additional studies related to alternative methods of underground propulsion are then discussed. This section concludes with a review of relevant studies related to the emission of heat from electrical units, with a focus on Lithium-ion battery cells.

The experimental objective of this work is to estimate the heat generated by the battery system of an electric mining vehicle under a range of different driving, charging conditions and ambient temperatures. The experiments were followed by a series of simulations in order to replicate the experimental results and validate assumptions of the equations and parameters that govern the heat flux and heat generation process in battery systems. Two overall cases were modeled using a finite element analysis tools, the single cell case and the multi-cell module. Both cases were simulated under the same conditions presented during the experimental phase. Lithium-iron Phosphate for single cell case, the 3D model was generated reflecting the internal geometric features of the real battery. For the multi-cell module case, a 2D model was generated.

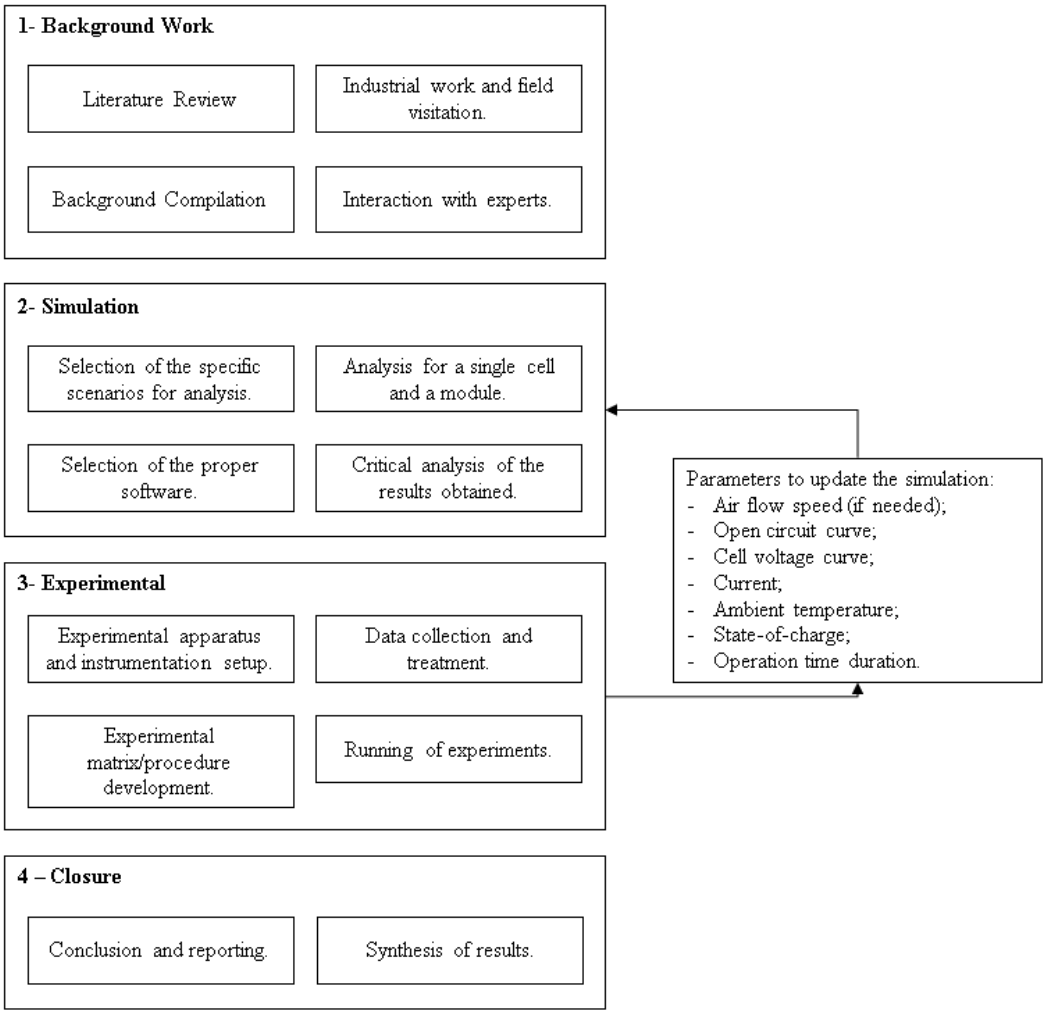

Figure 1-3: Thesis methodology block diagram.

2 Background Work

2.1 Overview

This section begins by exploring the main topic of mine ventilation and cooling. It then progressively narrows down to the various contributors to the heat load in mines, sources of this heat and in particular the contribution of mobile equipment propulsion methods for mining machinery. A

review of current studies about the heat impact on machinery in underground mines is presented in this chapter. A brief review of academic work about the heat and emissions effects of diesel engines to their surroundings, the alternative technologies for propulsion of mining machinery, methods for predicting the heat loss from electric machines and battery systems is also presented.

2.2 Mine Ventilation and Mining Mobility

The main task of mining ventilation is to dissipate air contaminants, provide fresh-air to the miners, and lower the mine temperature. Needed to keep the work environment safe and comfortable for underground miners, mine ventilation can often represent the highest operating expenses among the mine operations, see Figure 2-1. This is especially true in the case of mines in tropical areas, deep (hot) mines and in some sites in temperate climates (Vergne, 2008). Thus, any measure toward the mitigation of air contaminants and the heat load in underground environments can result in considerable savings for the mining operation.

In a recent study conducted by the Canadian Federal Government (CIPEC, 2005), ten different underground mining sites were surveyed in order to evaluate the cost contribution of their internal operations. Figure 2-1 shows that mining ventilation represents, on average, to 37% of the total cost per mass of ore hoisted. This result confirms the statement from Euler de Souza, a specialist in mine ventilation, in which it is affirmed that the cost for ventilation can range from 25% to 40% of the total energy cost, and it can represent from 40% to 50% of the total power consumption in a typical underground mine (De Souza, 2015). It should be noted that these numbers are affected by a broad range of factors.

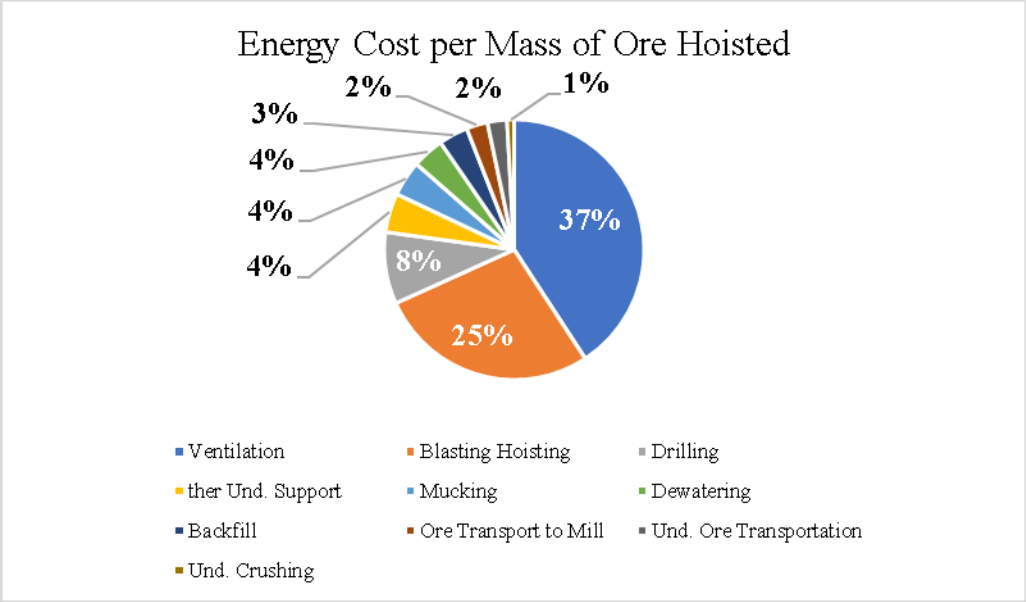

Figure 2-1: Energy Cost Comparison between the Total Mine Operation and the Mine Ventilation (adapted from CIPEC, 2005).

Mine ventilation is a vital component of and has considerable impact on mining operations. Together with removal of heat, the main task of main ventilation is to dissipate air harmful contaminants, such as the ones from diesel engines. In some cases, the removal of diesel emissions is estimated to represent as much as 70% of the total air demand (Hartman *et al*., 1997). By replacing diesel units by equivalent electrical versions (which do not have any gaseous or particulate emissions), 40% to 60% of ventilation demand was reduced (Varaschin J., 2016). This result is possible because compared to IC units, electrical vehicles generate less heat (estimated in 40% of IC units), and do not emit no harmful gases. Consequently, the total energy consumed by the fans was also decreased in 70% (Varaschin J., 2016). According to the same study, the implementation of electric units can lead to savings as high as 20%, despite the fact that these units are, on average, 25% more expensive than their diesel counterparts. Even though the introduction of electric units in underground environments can represent a new paradigm in underground mines, mining ventilation is still needed to dissipate dust, and to control the environmental temperature.

2.3 Heat Sources Underground

The most significant sources of heat in underground mining environments include geothermal, air flow losses, waste heat from machinery, and air auto-compression. The heat distribution and magnitude vary from mine to mine. Some aspects to determine the impact of each heat source include site location, depth, productivity, geothermal gradient, machine efficiency, type of material excavated and size of excavated material. Figure 2-2 presents a typical distribution of heat loads in an underground mine. This is a general assumption and does not represent a specific mining site. However, it illustrates the general distribution of the heat. The heat sources are distributed among several categories, in which "Others" is referred to Explosives, Ground Water, Backfill, Lighting, and Personnel combined.

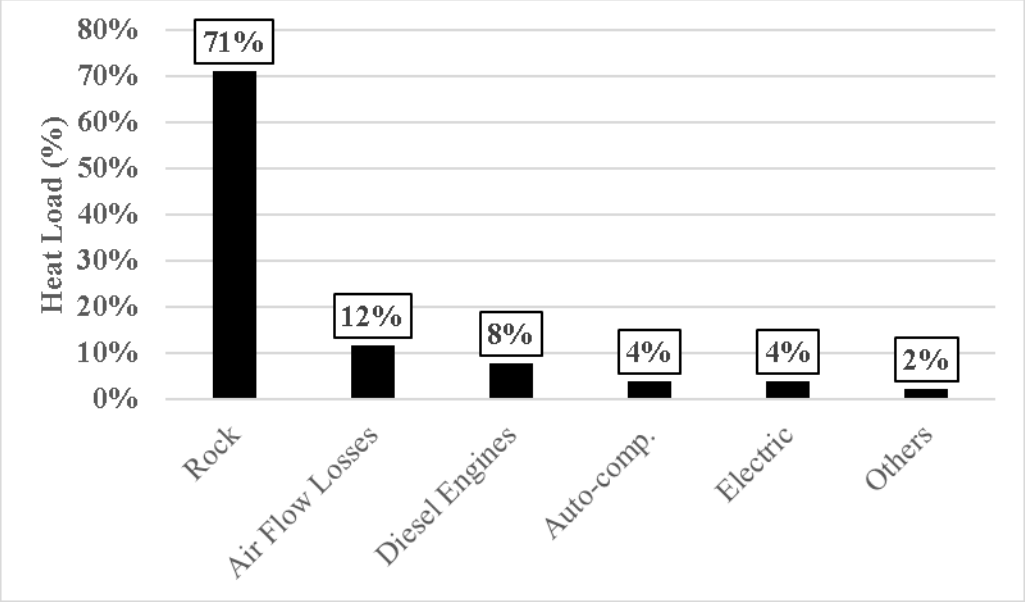

Figure 2-2: Typical heat load underground mines depending on each source (adapted from Vergne, 2008).

In a specific heat balance study (Enderlin, 1973) conducted in seven hot underground mines, the average heat proportion obtained was 48% - geothermal, 20% - equipment, 19% - water, 11% - auto-compression, and 2% - blasting and personnel. As a side note, in this study several devices are included under the label of "Equipment", such as: pumps, haulage motors, transform stations, fans,

underground hoists, electrical load centers, mechanical refrigeration units, and slushers. The exception is the results expressed for Creighton in Sudbury, Ontario. In this mine, heat from diesel equipment is expressed separately. The result for the contribution shares from each class of equipment among the electrical/mechanical devices are 46% (diesel equipment), 36% (electrical fans), 11% (stationary electrical load centers), and 7% (pumps). The impact of electro-mechanical equipment, pumps, fans, electrical load centers and diesel equipment, on the total heat load generated from all sorts of heat source approaches 14%, as can be seen in Figure 2-3 (Enderlin, 1973).

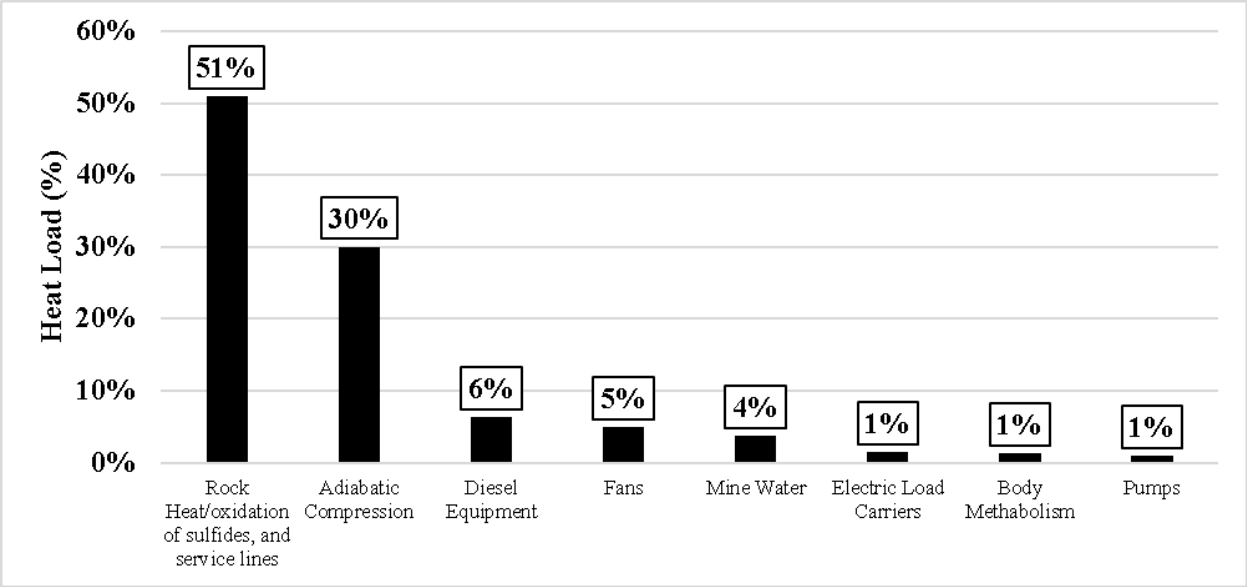

Figure 2-3: Heat sources founded in Craighton underground mine (adapted from Enderlin, 1973).

In another study of heat balance in underground mine at Blyvooruitzicht Gold Mining Company Limited, the average result for the heat distribution between August – 1977 and March 1978 can be seen in Figure 2-4. The results were obtained from measurements at the shaft longwall stope, within an error margin between -6% and 22%. In this study, five major sources of heat were identified, namely Rock, Electrical Power, Workers, Diesel equipment, and Explosives. The Electrical Power category includes winches, fans, lighting, hoist, level pumps and the level cooling plant. It is important to emphasize that each mining site is unique, and Blyvooruitzicht is no different. This because the heat contribution of all electrical components surpasses in more than 13 times the heat released from diesel

units. The reason for this result is that this mine site employs in a large number high power electrical machinery, especially in relation to the hoist, winches, and the fans, in detriment of diesel locomotives.

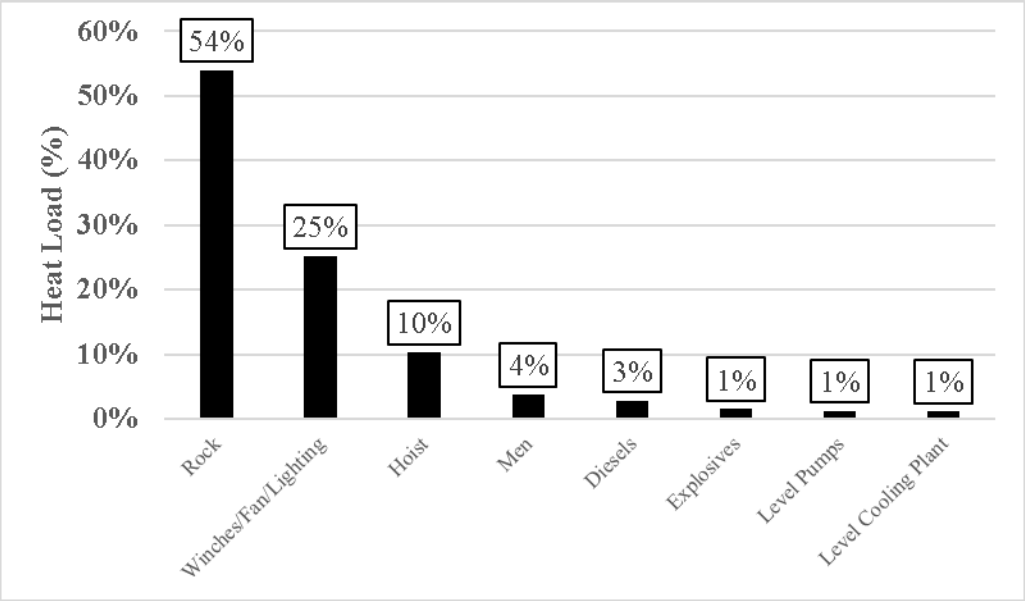

Figure 2-4: Average heat sources from August – 1977 to March - 1978 founded in Blyvooruitizicht underground mine (adapted from Deglon P. and Hemp R., 1980).

In conclusion, the current section had provided information about the main sources of underground heat. It was confirmed that, typically, geothermal, auto-compression and diesel machines are the main sources of heat in this environment. However, the proportional contributions of each source can vary significantly from site to site. Furthermore, it was shown that the mitigation of these heat loads is beneficial to the mine operation since the cost with mine ventilation and cooling is considerable. This cost is intrinsically correlated to the depth and productivity of the mine (Vergne, 2008). Hence, any mitigation of the heat sources is valid and needed to keep the operation profitable. One of the current possibilities available to the industry is the replacement of thermally inefficient IC Diesel vehicles with more efficient EV vehicle technology.

2.4 Propulsion of Machinery in Underground Mines

In underground mining, there are many different types of mobile equipment, of which some of the most commonly employed are load-haul-dump (LHD) vehicles, personnel carriers, locomotives, and haul-trucks. Listed below are the power-trains currently available for these units for mining applications:

- Diesel Internal Combustion (IC) Propulsion;
- Hybrid diesel-electric propulsion;
- Hydrogen fuel cell propulsion;
- Full electrical propulsion.

Diesel Internal Combustion (IC) Propulsion

Diesel Internal Combustion (IC) powertrains are the most common type of propulsion for mining vehicles. Diesel IC units usually have longer range than the alternatives. This because, as a fuel, diesel has a relatively high energy capacity when compared to other sources. Other advantages of this technology include competitive cost of acquisition and operation, and compared to gasoline, diesel is safer to store, making it the preferred alternative to gasoline as a fuel for mining vehicles. Furthermore, refueling these vehicles is a quick and simple task. Nowadays, in order to be used in underground mining applications, diesel engines must to comply to Tier 4 regulation for emissions. These emissions can include carbon monoxide and dioxide, nitrogen and sulfur oxides, hydrocarbons, and diesel particulate matter, in which the last one, is considered to be a carcinogenic substance (Burke J., 2017). As a result, the emission of hazardous gases over time has been greatly reduced, however, they cannot be eliminated. In addition, diesel engines not only emit toxic gases, but also considerable amounts of heat to the environment, they generate excessive noise and vibration, and they have high maintenance cost (these are complex machines, which require specialized mechanics). These negative

aspects are, to a certain degree, consequences of the low powertrain efficiency (30% to 35% for diesel units). Lastly, the operation of diesel machines in underground environments represents a challenging task in financial terms, since the oil prices tend to be considerably volatile (Paraszczak *et al*., a, 2014; "Diesel to Electric: What is the Future of Mining?", 2016; Wood A., n.d.).

Currently, several methods capable of decreasing diesel emissions are commercially available. However, these technologies have limited impact on the pollution control, some are expensive to implement, others reduce the machinery`s performance, and in some cases, they can even increase the machinery heat load. For this reason, the mining industry is seeking for alternatives.

Hybrid Diesel-Electric Propulsion

One of the alternatives to conventional Diesel IC powertrains are hybrid vehicles. By combining the diesel engine with an electric power-train, better mileage can be achieved, mostly because the electric motor allows for the use of regenerative braking, and they have higher efficiency then IC engines. Usually in hybrid technology, the IC engine can be used to charge the battery pack, or to directly power the electric motor. This strategy allows the IC engine to run on the nominal capacity, reducing the possibility of internal components wearing (Fleet M., 2012), maximizing its performance and reducing the fuel consumption. Consequently, the machine durability and robustness are improved, and the consumption of lubricants and fuel is reduced. As a result, even though these machines have higher capital cost than regular diesel machines, their cost of operation is reduced (Anon., 2014). It is estimated that the fuel savings are between 45% to 60% in comparison to regular diesel mining machines (Norris J., 2013). Other sources claim that the fuel consumption reduction is less dramatic, 20% reduction for hybrid vehicles using AC motor, and 60% for SR (Switched-Reluctance) motors (Wood A., 2014), or even low as 15% (Demers *et al*, 2010). Conversely, the fuel savings are strictly correlated to the type of machine, duty cycle, and production rate analyzed. The

reduce consumption of lubricants is also a result of less movable parts. The explanation for this is, since electric motors have high torque at lower RPMs, there is no need for gear box and transmission. Less movable parts results in a higher reliability overall, which in turn leads to higher productivity because less time is spent during maintenance (Ozdogan, M., 2015). Due to the higher machine efficiency overall, a small fraction of the energy input is wasted in the form of heat loss. Consequently, less power is required to propel the vehicle, which allows for the diesel engine to be downsized (Paraszczak *et al*., a, 2014).

Hydrogen Fuel Cell Propulsion

Fuel cell propulsion has been investigated as a viable alternative to diesel mining vehicles since the early 2000`s. The initial studies started with the proposal of a locomotive, and later with the development of the Caterpillar R1300 LHD (Barnes D. and Miller A., 2005). In the fuel cell application, hydrogen is absorbed and safely stored in the proton-exchange membrane (PEM) fuel cell, which is combined with the metal-hydride bed. This process requires low temperature and pressure. When the PEM is heated, the hydrogen is oxidized by the oxygen in the air, generating electricity and water in the process (Barnes D. and Miller A., 2005). The electrochemical reaction can be sustained as long as hydrogen and oxygen are continuously provided. Also, a small battery pack might be needed in order to store energy provided by the regenerative breaking if is available. See Figure 2-5 for a general comprehension of the main components in a fuel-cell vehicle.

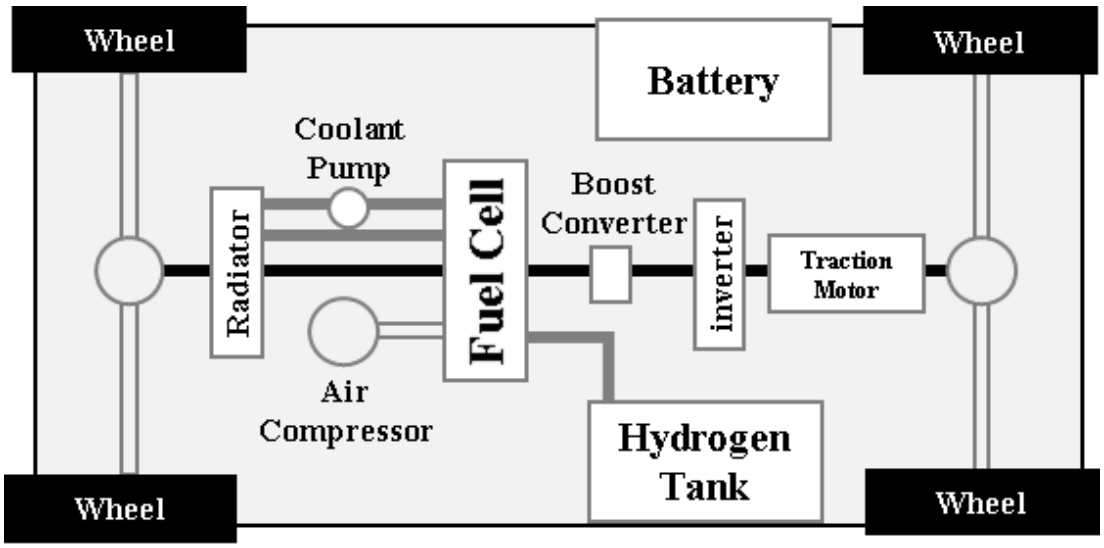

Figure 2-5: Major components in a fuel-cell vehicle (adapted from Fuel Cell Research Lab, nd).

Compared to diesel IC machines, fuel cell vehicles do not emit pollutants and do not release considerable amounts of heat to the environment. In comparison to electric vehicles, they are flexible, capable of extended use, and possess a considerably fast refueling process. (Miller A. *et al*, 2012). In mining applications relating to locomotives and LHDs, the heavy weight of the metal-hydride bed is beneficial as a mean to provide more traction to the unit, whereas a negative aspect of fuel cells is the high cost due to the use of platinum in its structure.

The development of fuel cell technology faces numerous challenges in underground mining applications. The process of absorption and release of hydrogen from the metal-hydride bed requires close temperature control to minimize the volume of hydrogen leaked to the environment, which in the underground mining ambient can be a safety and financial issue as hydrogen is a flammable and expensive fuel. Usually, wasted heat from the battery and fuel cells are used during the warm up phase in order to generate electricity. The thermodynamic efficiency of this process is around 50% (Valicek P. and Fourie F., 2014). Furthermore, fuel cells need to be used under the proper temperature range, since irreversible damaging can occur if they are freeze ("Fuel Cell Technology", 2001). These characteristics add complexity in the operation of fuel cell vehicles. One of the biggest disadvantages

of this technology is how to provide hydrogen fuel underground since it is flammable, volatile, difficult to contain and store, and susceptible to leakage when refueling the unit.

In the end, hydrogen can't be considered as a very efficient energy source when in a stored medium. With electricity being easily available underground, the development of fast charging centers, and higher energy power capacity batteries, hydride storage devices are becoming less common compared to EVs.

Full Electrical Propulsion

Electric propulsion is continuing to develop as a very reliable alternative to diesel machines. In the next paragraphs, the three subcategories of underground EV's commonly available at the present time are examined. Herein, this class of vehicle includes battery electric vehicles (BEVs), power cables, and overhead trolley lines. It has been estimated that the implementation of electric mining vehicles can bring savings in the ventilation system of around 70% or more (Varaschin, 2016; Paraszczak *et al*., b, 2014). This is mainly due to the absence of emissions, the use of regenerative breaking (which also can be used in hybrid and fuel cell vehicles), and the higher efficiency of these units in comparison to diesel propulsion. Hence, the efficiency of EVs is assumed to be three times higher than diesel machines, which for the same application, can correspond to three times less heat released by EVs (MacPherson, 2009; Paraszczak *et al*., b, 2014). In one study by (Varaschin, 2016), it was assumed that the energy efficiency for a diesel IC unit was 37%, and for the EV, 92%. Being more efficient also translates in a reduced power consumption, adding to the fact that electricity is cheaper than diesel fuel (evaluated for the US market in the period between 1999 and 2014) (Varaschin, 2016), which presents a supportive financial case for EVs. In comparison to diesel vehicles, mining EVs consume 70% less energy, and there is an estimation that 30% of the total energy spent can be recovered through the regenerative breaking ("Diesel to Electric: What is the Future of Mining?", 2016;

Jensen, S., 2013). These are not the only benefit for EVs in general. They usually tolerate better overloads and can achieve higher speeds of operation in relation to IC units, two parameters that have a positive impact on productivity (Paraszczak *et al*., b, 2014).

BEVs offer the advantages such as these: no emissions of noxious gases and particulate matter, good mobility, higher speeds when hauling, low maintenance, high torque available at a low RPM. Unlike diesel engines and fuel cell technologies, BEVs don't compete with the underground personnel for the oxygen consumption. As a matter of fact, the use of regenerative breaking reduces the heat load to the environment by redirecting the kinetic energy back to the battery pack (Paraszczak *et al*., b, 2014). However, their batteries have low energy capacity compared to diesel fuel. Lead acid batteries usually have 40 W/kg of power, Lithium-iron phosphate batteries possess around 90 to 110 Wh/kg, whereas some experimental batteries can reach up to 250 W/kg. In contrast, diesel fuel specific energy is 13 000 W/kg (Paraszczak *et al*., a, 2014). The low energy capacity of batteries impacts on BEVs having a considerable battery size in order to provide reasonable vehicle`s range. In a one reported case, BEV Load Haul Dump (LHD) vehicles having 1.5-2 tons of batteries were able to be operated between 2 to 2.5 hours, requiring 2 hours of charging time (Greenhill & Knights, 2013). In another application, it was possible to identify that the BEV Haulmaster 800-20EB using LFP batteries was capable of operating continuously for 4 hours, requiring a lower charging time of 1 to 2 hours (Paraszczak *et al*., b, 2014). Nonetheless, the technology is improving over time. For instance, it is feasible in economical and productive terms to convert the Caterpillar CL115 LHD from having a diesel motor to being powered by an electrical battery. In the space available in the engine bay, it is possible to place a battery pack that can last half a shift (in the case of lead acid technology), a single shift (in the case of NaMx chemisty), and two shifts (for Li-ion batteries) without the need of recharging (Schatz R. *et al*, 2015). Due to the fact that long charging times is one of the downsides of battery electric vehicles, an alternative strategy would be to swap batteries after their usage, which is

a practice that takes about 15 minutes (Paraszczak *et al*., b, 2014). Even though the practice of battery replacement can improve the productivity of BEVs, this strategy imposes an issue that extra batteries need to be purchased, thus decreasing the financial advantages of purchasing these machines. As for the battery chemistry, the decision lies on the total weight, energy capacity, and cost related to each technology, especially for Li-ion technology, which can be considerably high. It is estimated that switching from 4 to 8 hours battery capacity doubles its size, weight and price (Leonida, C., 2017). In economic terms, it is expected that lead-acid BEVs are 25% more expensive their diesel counterparts, and operational savings can range from marginal to 20% (Varaschin, 2016). The use of BEVs impose some limitations. For instance, a dedicated charging station is required to charge batteries, and in case of fast-charging stations, a significant investment might be needed. In addition to this, the battery pack has a limited life expectancy of approximately 12 000 hours, which usually coincides with the life cycle of the machine as a whole (Leonida, C., 2017).

Beside BEVs, underground electric vehicles used in mining can also be cable-powered (or tethered) or trolley-powered, where the latter has a historical presence in underground mines, dating back 30 years. Today, even though tethered electric LHDs account for 5% to 10% of the total underground LHDs (Leonida C., n.d.), BEVs are the most common type of EVs (Jacobs, 2013). Comparing a diesel with a tethered electric LHD (Sandvik LH514 and Sandvik LH514E) shows that the electric version is 20% more expensive to purchase and 17% more expensive to maintain (Moore, 2010; Jacobs, 2013). The higher maintenance cost in this case is due to the frequently required cable repairs, as seen in Table 2-1. Nevertheless, when the mine ventilation savings of using BEVs are included to the financial calculation, the use of these units result in 30% cheaper operations (Jacobs, 2013). Both trolley and cable-powered units present limited mobility and flexibility and are usually recommended for cases in which the machine operates for the most part in confined locations (such as with the LHD cable-powered vehicle), or when a specific path is constantly used (as when a truck

trolley is used). In the case of the trolley technology, large investments in infrastructure are required, which in turn reduces its applicability in underground mines. Usually these machines have small diesel engines, which are used when the machines need to be relocated to different sections of the mine, where the electrical power infrastructure is non-existent. In conclusion, it is expected that with the current advancements in battery technologies, these technologies will soon be phased out (Paraszczak *et al*., a, 2014; Burke J., 2017; Leonida C., n.d.).

Table 2-1: Maintained cost comparison between a diesel LHD and a tethered electric LHD (Jacobs, 2013)

Maintenance parameters	Diesel (Sandvik LH514)	Electric (Sandvik LH514)
Parts - Machine	70 $/hr/unit	50 $/hr/unit
Parts – Trailing cable	-	30 $/hr/unit
Labour	20 $/hr/unit	25 $/hr/unit
Total	90 $/hr/unit	105 $/hr/unit

Table 2-2 presents a summary of the main characteristics of each propulsion technology available for mining vehicles. EVs embody the best balance of efficiency, cost of operation, reliability, and performance among the options available. In addition, they represent a solution for the elimination of hazard emissions altogether, and to reduce the heat impact of mining vehicles in the given environment. It is important to note, that for battery-electric vehicles, the heat load is highly dependent on the duty cycle (loaded, regeneration, charging, etc). This research aims to aim to determine the magnitude of the heat loads for a range of different duty cycles for these vehicles.

Table 2-2: Summary of the main characteristics of mining vehicles propulsion alternatives.

Methods of Propulsion	***Significant Advantages***	***Significant Disadvantages***	***Relative Heat Load***
Diesel IC	Long range; Low cost of acquisition and operation; Safe fuel storage; High specific energy; Short refueling time.	Pollutant emissions; Considerable noise and vibration; High maintenance cost; Cost of operation fluctuates with oil prices; Considerably inefficient.	Very High.
Hybrid (Battery / IC)	Very long range; Allows regenerative breaking; Considerable machine durability; Better overall efficiency than conventional diesel units; Engine can be downsized; Reduced pollutant emissions.	Same drawbacks as for the diesel units.	Considerable high.
Fuel Cell	Flexibility; Considerable range; High energy capacity; Low operational temperature and pressure; High power density; No pollutant emissions; Heavy weight (ideal for LHD and locomotive applications); Low noise; Quick refueling time.	Hard control temperature parameters; More costly then rechargeable batteries; Infrastructure for fuel supply; Safety concerns; Complex technology; Emission of water vapor (additional latent heat); Relatively inefficient.	Average
Battery Electric	No emissions; Flexibility; Good mobility; Low maintenance; High efficiency; Reduced noise and vibration;High torque since low RPM.	Low energy capacity; Limited range; Limited cargo capacity; Long charging time.	See Chapter 4
Cable Electric	Ideal for confined areas; No need for charging; High productivity; High efficiency; Reduced noise and vibration.	Frequent cases of cable disrupting; Requires proper infrastructure; Diesel generator is required; Reduce mobility.	Minimal (when fully electric) High (when on diesel)
Trolley Electric	High load capacity; High performance; Reduced energy consumption; High efficiency; Reduced noise and vibration; High productivity.	Requires diesel generator; Expensive infrastructure is required; Reduce mobility; Large tunneling sections is needed.	Minimal (when fully electric) High (when on diesel)

2.5 Previous Evaluations of Heat Load applied to Diesel and Electric Vehicles

There are several possible approaches in evaluating the heat load from machinery in the underground mining environment. These approaches include using an overall efficiency calculation, estimations of power consumption, direct measurement using infra-red imaging, and summation of estimates and models from individual heat producing components of the vehicle. The following sections provide a brief review of each method.

2.5.1 Machinery Heat Load Estimation based on Efficiency Calculations

One method for determining the heat load for mobile equipment is by efficiency calculation of the machinery (or constituent components). This method has been applied in studies to both diesel and electric vehicles (McPherson, 1986; Vergne, 2008; Marks, 2012).

In the case of diesel machinery, the efficiency calculation approach to heat load estimation is based on using the engine fuel consumption under a rated driving cycle in one shift for diesel machinery. The total heat load is approximately distributed into three different areas: the radiator, the engine, and the exhaust gases. Water vapour is emitted from the exhaust pipe through combustion. This means that heat is lost in sensible and latent forms. Because water vapour is converted into liquid, heat impact will be felt in underground environments over an extended period of time. This approach has been described in several different text books (McPherson, 1986; Vergne, 2008; Marks, 2012).

The heat emitted (HE) can be calculated using fuel consumption (Fc) given in a specific time frame (t), the combustion efficiency (Ce), and the calorific power of diesel fuel (Cpw), as demonstrated in the following equation.

$$HE = \frac{(F_c\ C_e\ C_{pw})}{t} \quad (2\text{-}1)$$

In this equation, combustion efficiency is assumed to be at 95%, calorific power of diesel to be 34000 kJ/l, and the ratio between the heat emitted and the mechanical work to be 2.83 kJ/s (McPherson, 1986). The rated power for the machine is the sum of the heat emitted plus the mechanical work. Therefore, the calculated ratio shows that diesel engines have a rated power of 26.1% efficiency. This result is expected since diesel engines are summed to normally have efficiencies ranging from 20% to 25% (Smil, 2010).

When applied to electric vehicles, the efficiency calculation approach to heat load determination involves estimating of the mechanical work. In this methodology, heat loss is calculated based on both electric power-train efficiency and useful energy. Part of the useful energy is used as mechanical work, while the remaining energy is converted into heat through frictional losses (McPherson, 1986). Figure 2-6 summarises this concept.

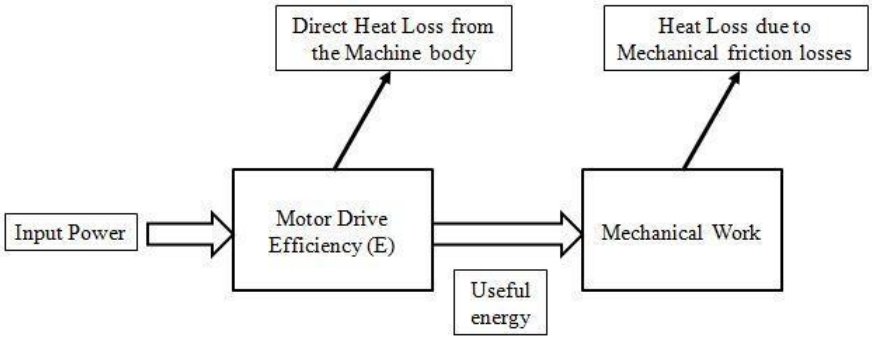

Figure 2-6: Heat generation impact from electric machinery (adapted from McPherson, 1986).

The heat load approach from efficiency calculation approach was applied by Marks (2012), which found that electric motors emit 2.6 times less heat into the environment than diesel motors, while other studies demonstrate an emission of 3 times less (McPherson, 1986; Vergne, 2008; Paraszczak, 2014; and Halim and Kerai, 2013). Based on these two ratios and knowing the efficiency rate of the

diesel engine (i.e. 26.1%), we can estimate the efficiency of electric units to be between 75.3% and 71.5%. However, knowing that electrical units that have 70% (Halim and Kerai, 2013) of the rated power of diesel engines can accomplish the same mechanical work, the final efficiency for the electrical unit will be between 59.4% and 64. 8% according to these estimations.

This method is based on general assumptions that might not be applicable to all machines under all operations in underground mines. These assumptions include the combustion efficiency and the ratio between the mechanical work and the heat emitted. However, it is a practicable method that allows a general estimation of the heat generated by a fleet of diesel machineries underground.

2.5.2 Machinery Heat Loss based on Power Consumption and Psychometric Conditions

The evaluation of the heat load is based on experimental data. For a specific study evaluating the heat load of a mining BEV (Halim and Kerai, 2013), five different points in front of and behind the vehicle in a tunnelling section were studied measuring the dry bulb temperature (DB), wet bulb temperature (WB), and barometric pressure. Psychometric equations calculated heat loss from the machinery. The study additionally considered whether the heat emitted is equal to the rated power. The calculation for power consumption was based on the voltage (V=1000 volts), current (I=100 amperes), and power factor (cosϴ=0.85), in accordance with the three-phase power consumption equation (2-2):

$$E = \frac{(\sqrt{3}\, V\, I\, \cos\theta)}{1000} \qquad (2\text{-}2)$$

In this case, the electric vehicle was measured while it was parked. This measurement did not impact the results since the motor drive-shaft is disengaged, allowing for continuous motion of the engine, even when the vehicle is not moving.

The study concluded that the average heat emitted, and the power consumed in the electric vehicle, are 145 kW and 147 kW respectively. It is important to note that due to the absence of moisture, electric vehicles emit only sensible heat. These numbers slightly differ due to the precision measurement technique. The study results supported the prior belief that heat emitted is equal to the power consumed when the machines do not undergo work against gravity. This contradicts the manufacturer of the LHD514E which asserted the heat emission to be approximately 107 kW (Rakochy, 2012). The sources of this heat emission were determined to be the drive-train (97,2 kW of heat loss) and the thermal efficiency (9 kW of heat loss). The manufacturer did indeed use the efficiency calculation method but did not provide an adequate rationale for the values used in the calculation of the thermal efficiency and drive-train losses. The manufacturer estimated the value of the heat loss be 1.36 lower than that value estimated in the study by Halim and Kerai (2013). If manufacturer estimated the efficiency for the electric machine to be approximately 73%, matching the previously theorised efficiency range of 71.5% to 75.3%, then both studies would produce the same result.

Calculating power consumption to determine heat loss is also used for other devices, such as electrical equipment (Hartman, Mutmanky, and Wang, 1982). This method is used by ASHRAE to measure heat loss from electrical equipment that operates inside buildings (Hosni, Jones, Xu, 1999), as well as by The Engineering Tool Box (Electrical Motors and Heat Loss, n.d.)), which states that if the electric motor is used in a closed environment, all power input is eventually converted into heat.

It is important to point out that, if no work against gravity is conducted, all the energy consumed by any machine in a close environment will inevitably be converted into heat. This means that, if the machine is driven to a location with a different depth within the underground mining environment, the power consumption will not be equal to the heat load. Also, this method does not

take into consideration the time for the heat generated to dissipate to the environment, hence the difference between the heat generation and the heat loss.

In conclusion, the psychometric measurement strategy is not practicable, it is time consuming, and the measurement points need to be well defined in order to encompass the region affected by the heat load behind the vehicle.

2.5.3 Machinery Heat Loss based on Infrared Thermo Images

Infra-red thermal imaging can be used indirectly to determine heat emission, through the use of heat transfer equations in combination with the temperature readings. This method is an alternative to conventional, localised, and invasive methods of temperature measurement which employ thermocouples. Infra-red cameras can be used to determine the degree of general temperature homogeneity by identifying hot and cold spots, thus enabling comparison between simulations and experimental results. Infra-red cameras also allow for evaluation of the heat generated from the machine as a whole as opposed to evaluating the heat sources locally.

In previous studies, both radiators from IC vehicles (Menéndez-Díaz *et al*., 2014), (Calisir *et al*., 2015) and batteries have been evaluated using thermal cameras (Niculuta, 2012). The disadvantage of this methodology is that thermal images are not adequate to calculate heat emission parameters such as the airflow magnitude and the emissivity, which is an estimated value. Acquiring these values may nonetheless be challenging depending on the scope of the analysis. The magnitude of the airflow however is required to determine whether natural or forced convections equations will be used to calculate heat transfer. The value of the emissivity of most materials is already known and tabulated. However, past studies have calculated heat radiation by painting the studied objects with a colour whose emissivity is well-known, such as black (Forgez *et al.*, 2010). This procedure is invasive and

affects the measurement, especially if radiated heat is the main contributor to the overall heat transfer. Furthermore, the process of painting is time consuming and, depending on the situation, can make the object of study useless after the experiment. The other issue is that, for complex geometries, heat transfer from the faces will interfere with each other, complexifying the analysis and the acquisition of the thermal-images. All this considered, the use of infra-red thermal cameras is an alternative to the use of thermocouples if the intention is to calculate the heat loss using heat transfer equations. This method may be used not only to discover the temperature distribution but also the heat load contribution from each machine`s component. However, it is ideal to use this measuring technology in cases in which the emissivity of the surfaces is well known, and the geometry of the object is not complex.

2.5.4 Estimation of the Heat Generation from Components in a BEVs

Although this thesis focusses on calculating the heat generated from the battery pack, it is also beneficial to calculate the heat produced by the other main components in a BEV in order to put the battery heat contribution into context. To obtain the values required for the heat transfer calculation, data from the manufacturer of the component used in the Commander 5EV must be used. This section presents the parameters and curves obtained from the manufacturers of each component[1].

Figure 2-8 presents the energy contribution of a combined cycle of city and highway duty cycles. In comparison, Figure 2-7 presents combustion vehicles.

[1] The specific names and model numbers of specific electrical components have not been reported for the purposes of commercial confidentiality.

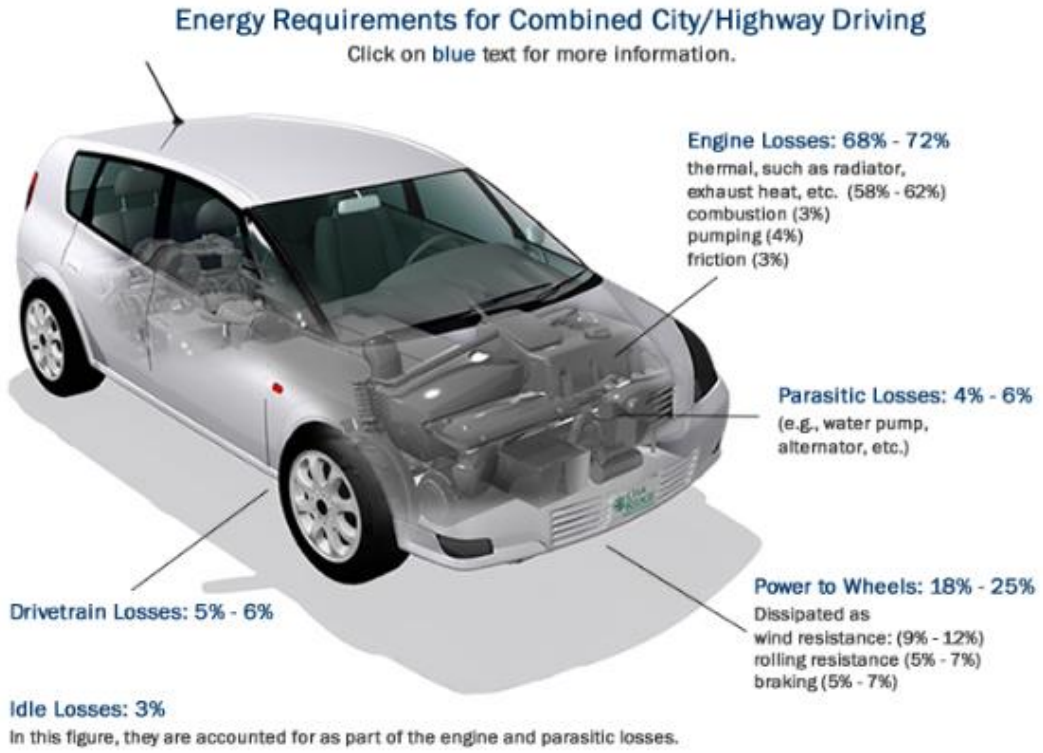

Figure 2-7: Energy input destination for a combined cycle in combustion vehicles (US Department of Energy, n.d.).

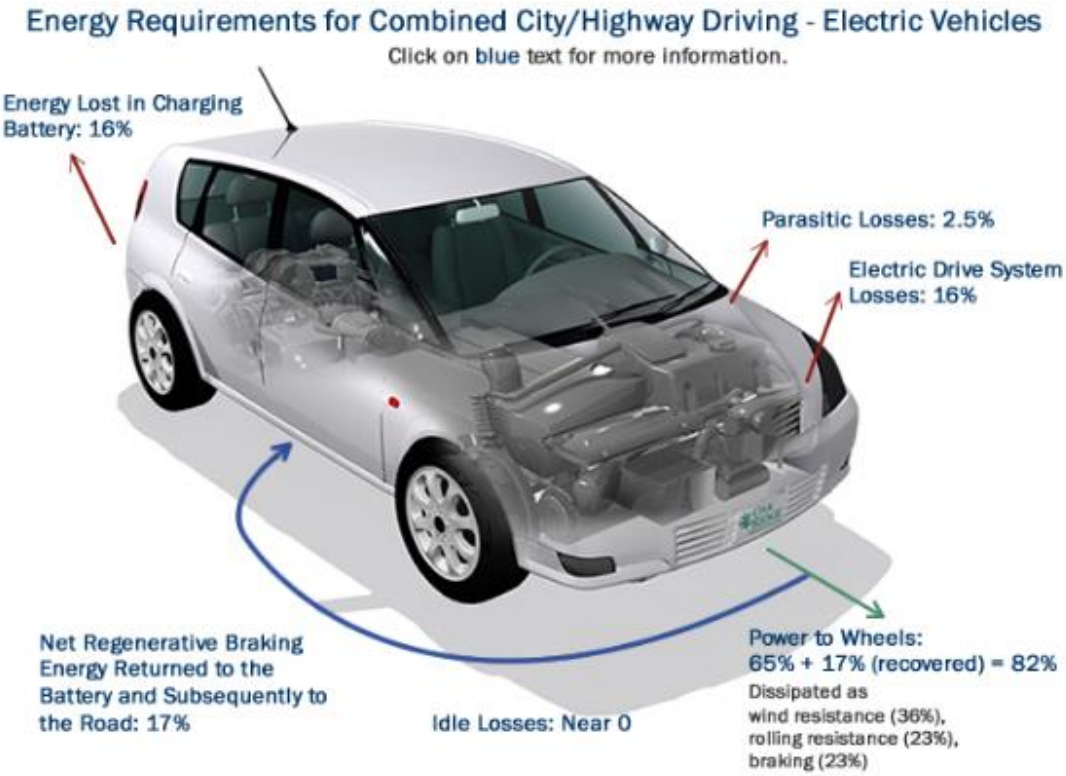

Figure 2-8: Energy input destination for a combined cycle in electric vehicles (US Department of Energy n.d.).

Without considering regenerative breaking and charging, the efficiency of electric vehicles is approximately 65%. Again, this estimation is reasonable since the efficiency of electric vehicles ranges, as mentioned earlier, from 71.5% to 75.3%. Taking regenerative breaking into consideration though, the efficiency would be as high as 82%, far superior than the 28% to 32% range of efficiency for diesel machines. This current method is used in Section 5.5 to estimate the heat generation for each electrical subcomponent in the Commander 5 EV.

3 Experimental Set-up

3.1 Introduction

The focus of the experiment is to evaluate heat transfer during charging and discharging of an individual battery cell and a battery module (multiple cells working together) in a range of simulated operating conditions. Calculation of the heat flux is based on the heat transfer equations for the processes of convection and radiation. Chapter 4 explains in detail the equations for the heat loss and generation in Lithium-iron Phosphate batteries. Heat conduction is neglected by using an insulating ceramic base between the battery set and the chamber surface. This is done to facilitate and minimize the number of equations used to calculate the heat loss of the batteries. The description of the set-up for the experiment is seen in Figure 3-1.

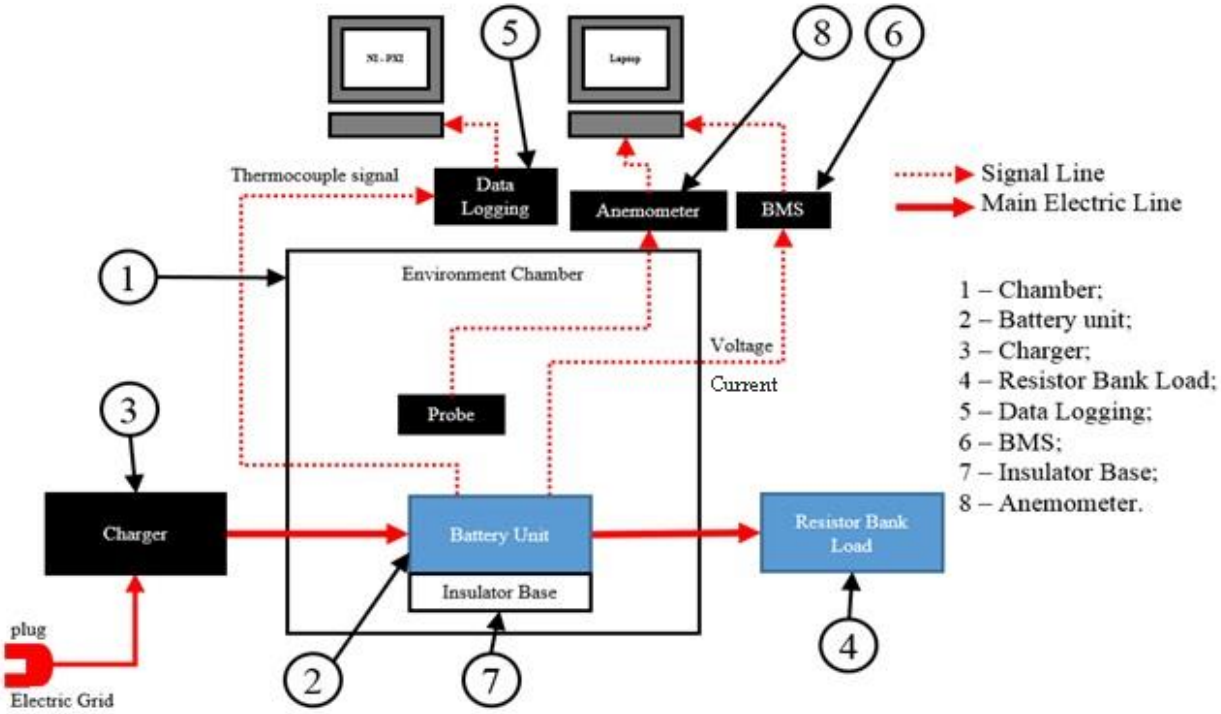

Figure 3-1: Schematic for the experimental set-up.

3.2 Physical Setup

To estimate the heat transfer and heat generation from the batteries during various states of charge, seven parameters were measured: cell temperature, chamber temperature (ambient temperature), cell voltage, cell open voltage, cell current, state of charge, and air velocity. K-type thermocouples attached to the battery surface read the cell temperature, while one K-type thermocouple inside the chamber read the environment temperature. These readings were sent to a data logging system, which recorded the results by means of a LabVIEW software. The BMS (Battery Management System), coupled directly to the positive and negative battery terminals, recorded the remaining variables except for the airflow speed. The BMS measures the cell voltage, open circuit voltage, and internal resistance, while the current sensor measures the current rate. The state of charge was estimated internally by using the Coulomb-counting method to evaluate the battery profile. All parameters measured and estimated for each second by the BMS, were provided in a single file at the end of the operation in the laptop. Finally, the anemometer situated vertically to the airflow direction, measured air speed inside the chamber (See Figure 3-2 and Figure 3-3).

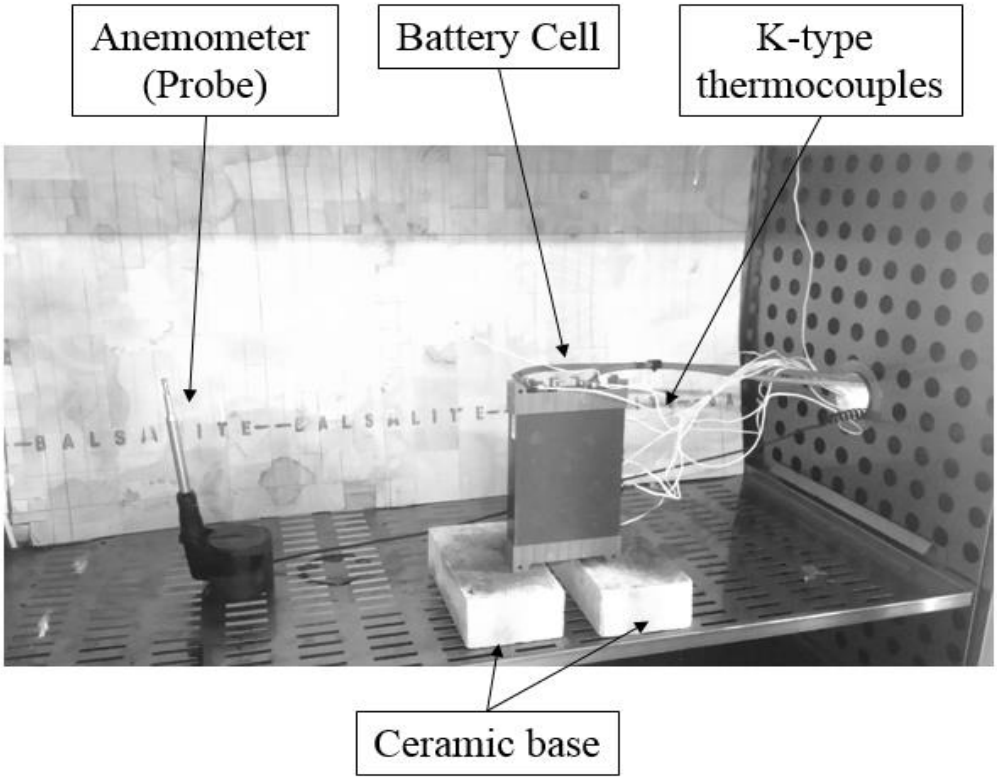

Figure 3-2: Battery heat loss experiment set-up for a single cell inside the chamber.

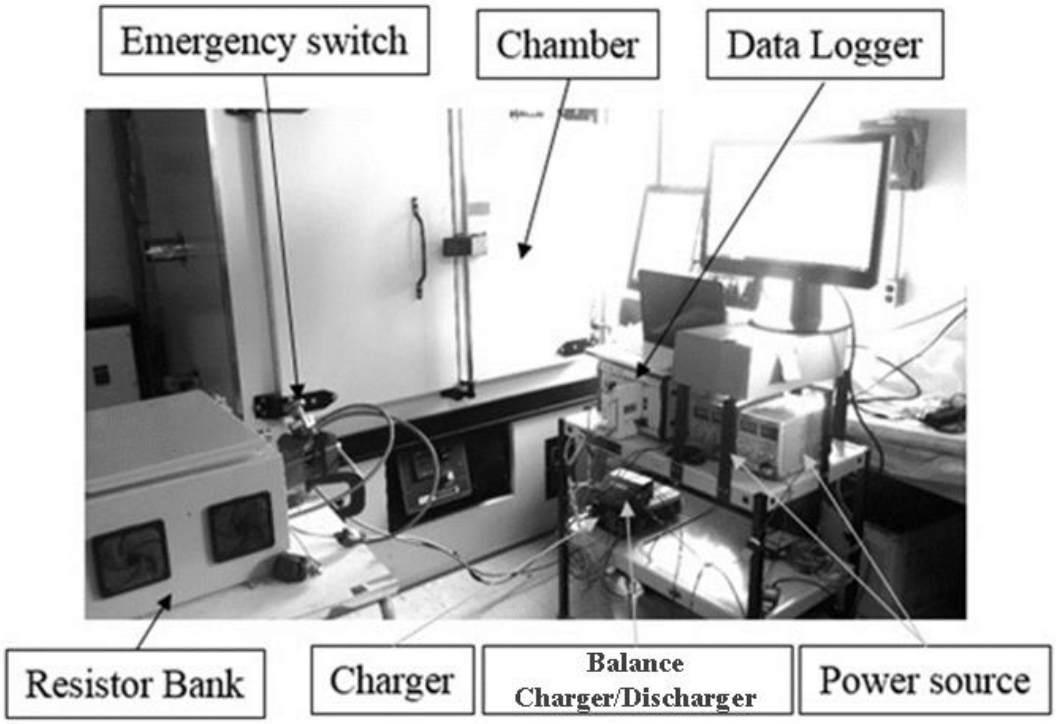

Figure 3-3: Battery heat loss experiment set-up.

3.2.1 Chamber

An industrial oven with an integrated, closed loop, temperature controller was used to simulate the operating environment of the batteries (See Figure 3-4). The required temperatures include 25°C, 30°C, 35°C, and 40°C. Two ports were located on each side of the chamber. The left port (from the front view of the chamber) served as the ventilation exhaust, while the right port was used for all necessary wiring connections. A single non-profiling ¼ DIN channel controls and adjusts the temperature based on temperature readings from a type J thermocouple located on the top interior of the chamber. On Table 3-1 is shown the main specifications of the chamber Oven Blue M DC 146.

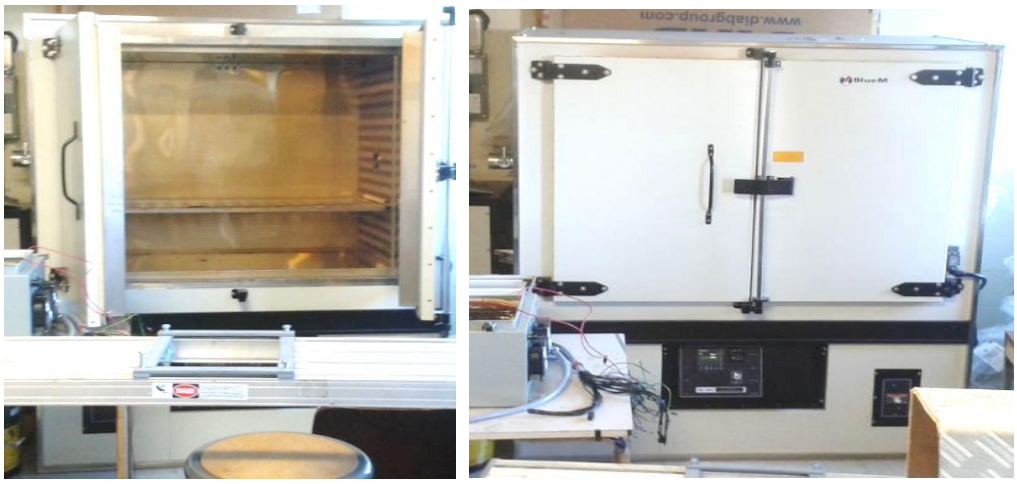

Figure 3-4: Front view of the industrial oven.

Table 3-1: Oven Blue M DC 146 series specifications.

Temperature range	15 (above room temp. to 350)	°C
Control	+0.5	°C
Uniformity	+/-2% of set-point	-
Resolution	Approx. 0.1%	W/m °C
Interior Dimension	(635 x 940 x 940)	(D x W x H) mm

3.2.2 Ceramic Support Bricks

Two high-porous refractory ceramic bricks were located between the metal base inside the chamber and the battery. The bricks were 125 mm apart from each other, providing space for the bottom thermocouple. The bricks that were employed are characterised by a low thermal conductivity, thus considerably reducing the effects of heat conduction at the contact points. This simplifies the heat loss calculation to convection and radiation. Table 3-2 presents the ceramic brick physical properties.

Table 3-2: Low Thermal Mass, Ceramic Brick (Carbon trust, 1993).

Thermal Conductivity	0.3 W/(mK)
Specific Heat	1000 J/(kgK)
Density	130 kg/m^3
Dimensions	(258 x 134 x 150) mm (L x W x H)

3.3 Battery Control Units

The following section presents the devices used in the experimental phase which are responsible for controlling the batteries in terms of charging and discharge rate.

3.3.1 Battery Balance Charger/Discharger

The charging system, as presented in Figure 3-5, converts AC input (ranging from 100VAC to 240VAC) to DC output. The voltage output ranges from 15VDC to 30VDC, with a maximum current capacity of 50A.

Figure 3-5: EFUEL PFC Heavy Duty 1200W/max 50A Power Supply.

The power supply was responsible for directing the electricity from the power grid to the Balance Charger/Discharger, see Figure 3-6.

Figure 3-6: Balance Charger/Discharger.

The Balance Charger/Discharger controlled the proper voltage and current to the battery. When used to charge battery modules, it ensured that the voltage of the cell was within the necessary voltage range, which for Lithium-iron phosphate batteries is generally between 2.8V and 3.6V. It operates a maximum of 20 NiCd/NiMH, or 8 Lithium-iron Phosphate cells connected in series, for a maximum of 40A charging. Its software can verify the voltage, the current, the state of charge, and the internal resistance in each cell. The unit also has the capacity to discharge batteries, but this feature was not

used during the experiment due to the limited current capacity. Instead, a resistor bank was used for discharging the batteries.

3.3.2 Resistor Load Bank

The resistor bank, presented in Figure 3-7, is composed of three 2.5Ω Ohmite C300K2R5E in the first column and nine 0.63Ω Ohmite C300KR63E in the remaining columns. In the experiment, 2.7 Ω of resistance was measured in the first column and 0.83 Ω in the other columns, with the wiring imposing an extra resistance of 0.02 Ω. These high-power resistors, which have a maximum capacity of 300 W capacity, can used under intermittent cycles. To protect against extreme temperature oscillations, the wires are embedded in ceramic with an enamel coating. Fans additionally were used to prevent excessive temperatures inside the resistor bank.

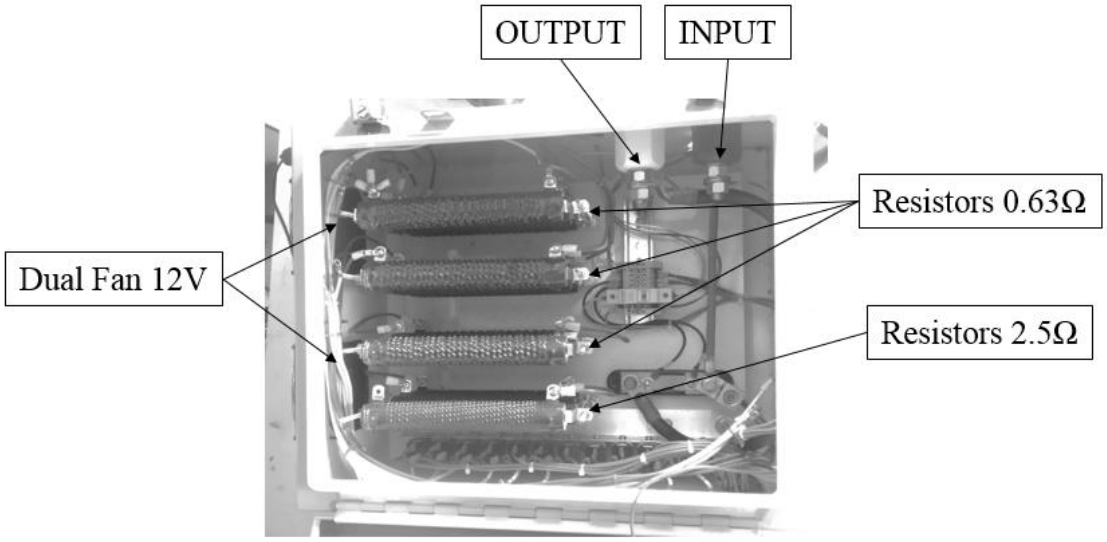

Figure 3-7: Resistor Load Bank.

The connecting wires in the resistor load bank may be rearranged for various setups equating to a range of effective resistances for the discharging processes. Figures 3-8 and 3-9 exhibit the set up for Flat and Uphill discharging respectively. The current target of the Flat condition is 17 amperes, which can be approximately achieved by using five 0.63Ω resistors in parallel.

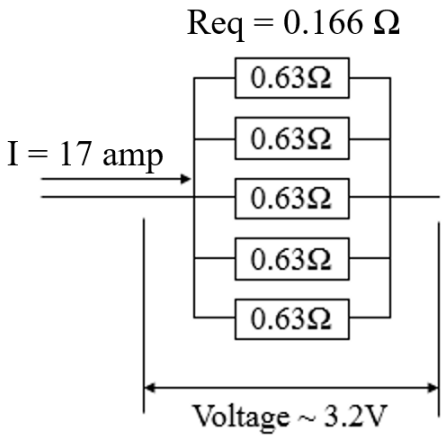

Figure 3-8: Arrangement of resistors for single cell analysis under Flat Condition.

To simulate the Uphill condition, two battery cells were connected in series and then connected to six 0.63Ω and three 2.5Ω resistors in parallel. An extra battery cell was used in series with the battery inside the chamber to closer achieve the current target of 44 amperes.

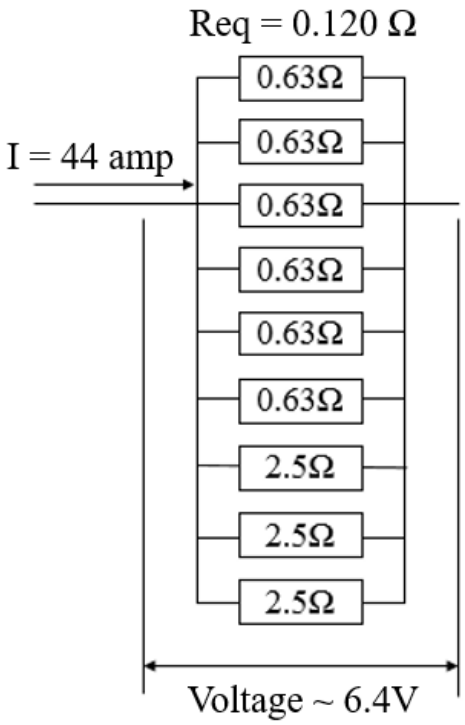

Figure 3-9: Resistor arrangement for single cell analysis under Uphill condition.

The same resistor arrangement was used for a module with 6 cells connected in series. The most suitable arrangement can be seen in Figures 3-10and 3-11, where the final current values are 14.5 amperes and 35 amperes for the Uphill and Flat conditions respectively. The limited number of resistors in the resistor bank caused a difference in current between the single cell and the module during the discharging process. The limitations of the charger caused similar deviations in the current value during the charging process. During the discharge process, the resistor bank is connected directly to the battery by means of an emergency switch.

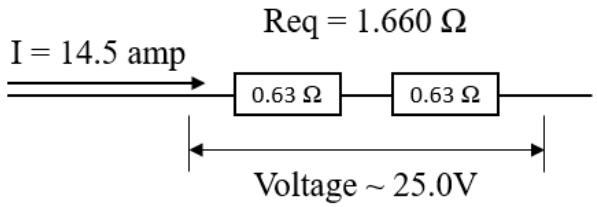

Figure 3-10: Arrangement of the resistors for a module analysis under Flat Condition.

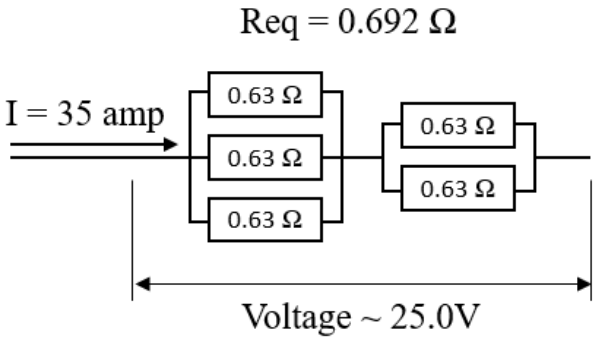

Figure 3-11: Resistors arrangement for module analysis under Uphill Condition.

3.4 Battery Systems

The experimental phase is divided into two parts, the heat transfer analysis of the single cell battery and the heat transfer of the battery module. The single cell analysis aims to provide a more complete description of the heat generation based on the temperature distribution over the battery cell,

and as for the module analysis, how this heat generation is affected when multiple cells are used closed to each other simultaneously.

3.4.1 Battery Unit

The experiments used the CALB CAM 72Ah battery cells. These batteries are based on Lithium-iron Phosphate chemistry, and they are the same used in the Commander 5EV. In comparison to other lithium battery chemistries, $LiFePO_4$ technology is safer to operate if abused. As well, not only has it got considerable specific energy and power, but it also can be used for a high number of cycles (see Table 3-3). These attributes make this a common choice for modern mining EVs. Figure 3-12 shows the discharge voltage curve as specified by the manufacturer under different rates of current, and Table 3-3 presents the battery specifications (CALB, 2014).

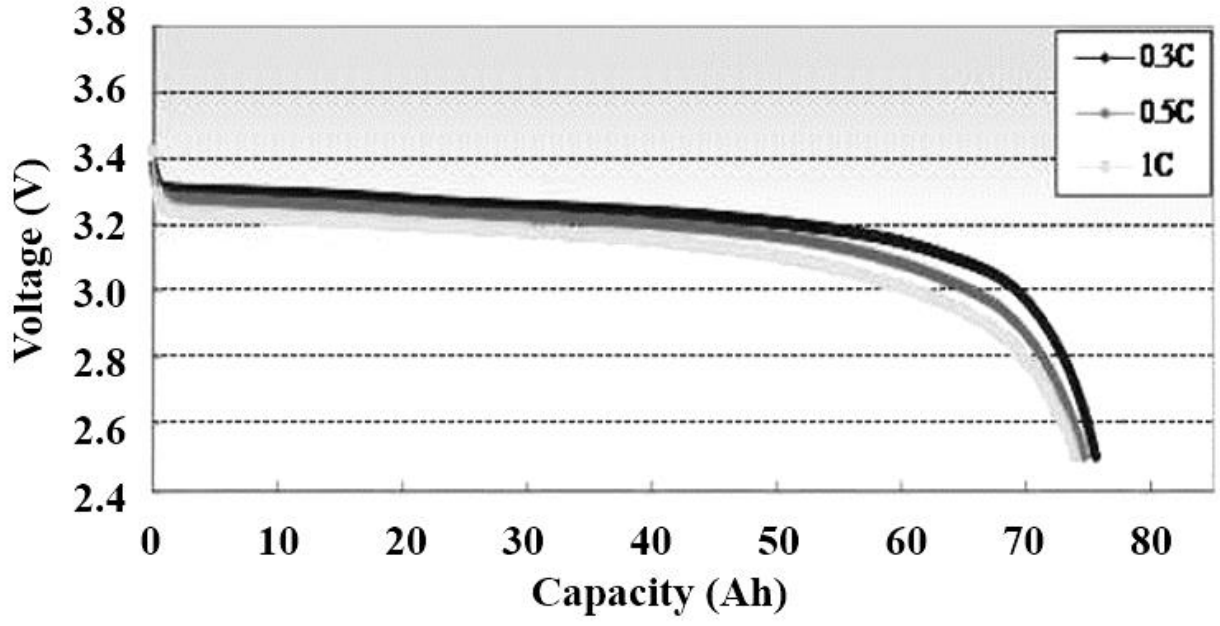

Figure 3-12: Discharge curves for CALB CAM 72Ah at 1C, 0.5C, and 0.3C (CALB, 2014).

Table 3-3: CALB CAM 72Ah specification (CALB, 2014).

Capacity	72 Ah	
Voltage	3.2 V nom	
Cycle Life	≥2000 Cycles	
Internal Resistance	≤1mΩ	
Charging (Constant Current-Constant Voltage)	Maximum Constant Charging Current	72 A
	CC To CV Voltage	3.65 V
Discharging	Maximum Constant Discharging Current	144 A
	Discharging Cut-off Voltage	2.5 V
	Pulse Discharge	576 A @ 10 s 288 A @ 30 s
Charge time	4 h nom, 1 h fast	
Weight	1.9 ± 0.1kg	
Dimensions	135 L × 29 W × 222H mm	
Charging Temperature	0 ~ 45 ℃	
Discharging Temperature	－20 ~ 50 ℃	
Ambient Humidity	＜70 %	
Shell Material	Aluminum alloy	

Externally, the battery cell has a prismatic geometry (Figure 3-13), in which its internal content is held by an aluminum alloy case 1 mm thick. A thin blue plastic layer surrounds the case, giving it an emissivity of 0.78 (Omega, accessed on April 5th, 2017). The two electric battery connectors (terminals) located at the top are made of different materials: aluminum and copper. The air-port vent prevents the pressure to build up inside the case, and it is located between the top connectors.

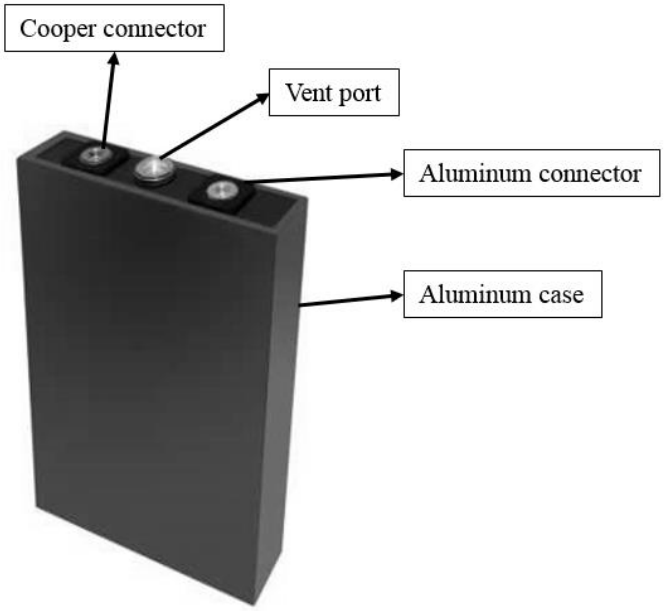

Figure 3-13: Single cell CALB CAM 72 Ah external view (CALB, 2014).

As for in Figure 3-14, it is presented the module with 6 cells connected in series, with a total voltage of approximately 19V, in the same arrangement used during the experiment.

Figure 3-14: One module of the battery pack with 6 cells with the plastic frame used in the EV.

3.4.2 Internal Structures

As for the internal structure of the Lithium-iron Phosphate battery cell, it is represented by the core, enclosed by the aluminum case, with an air gap between the top of the core and the top of the battery shell. In the air gap is located the aluminum, and copper extensions from the electrodes, which are physically connected to each top terminal. The battery core has 80 layers of the negative electrode, and 80 layers of the positive electrode for which each element is separated by the PP separator, with the polyethylene layer evolving the whole content (Figure 3-15 and Figure 3-16).

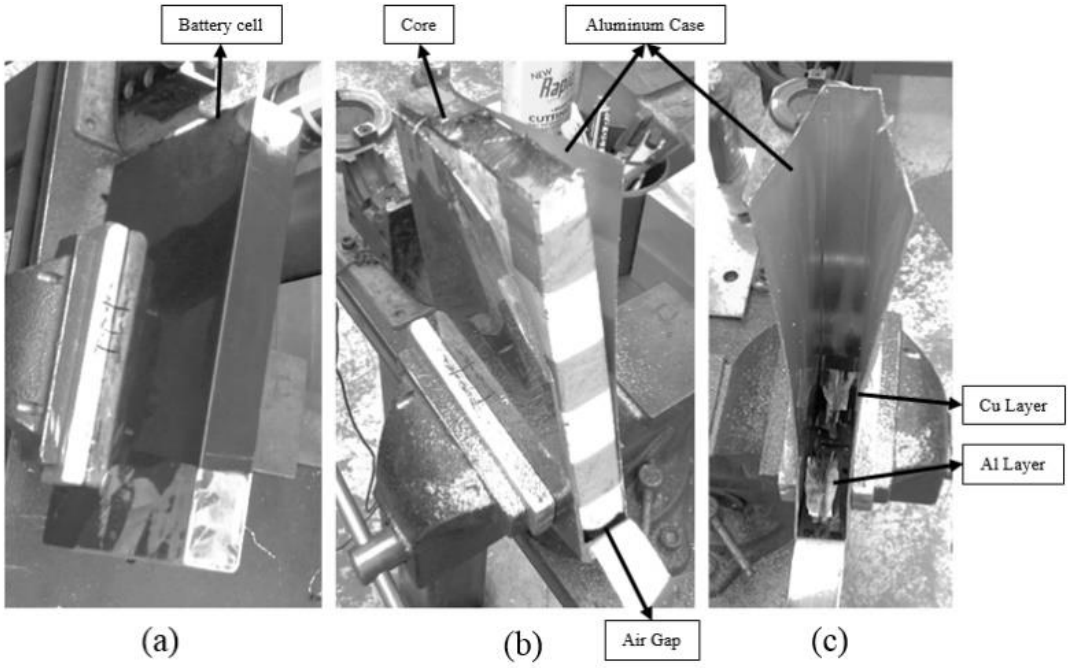

Figure 3-15: Internal components of the battery cell CALB CAM 72Ah. The opening stages can be seen from picture (a) to (c).

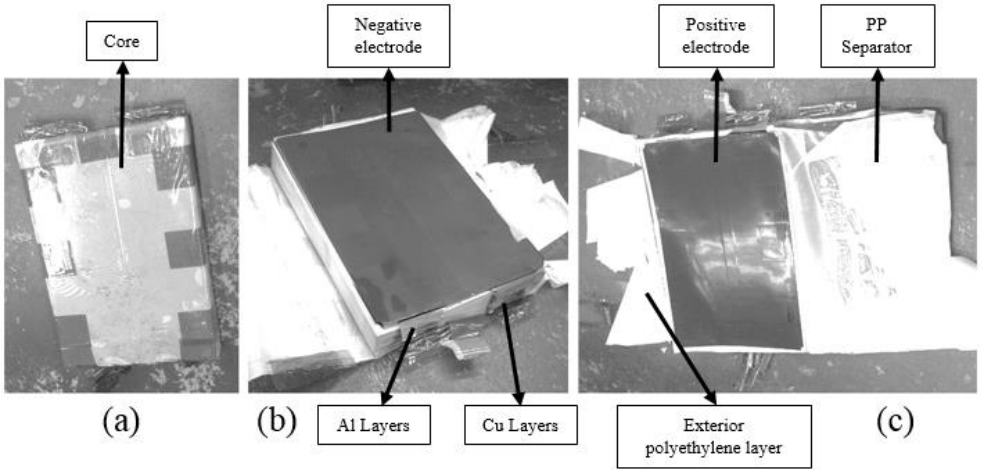

Figure 3-16: Internal Components of the battery core. The core is exposed in (a), and its contents in (b), and (c).

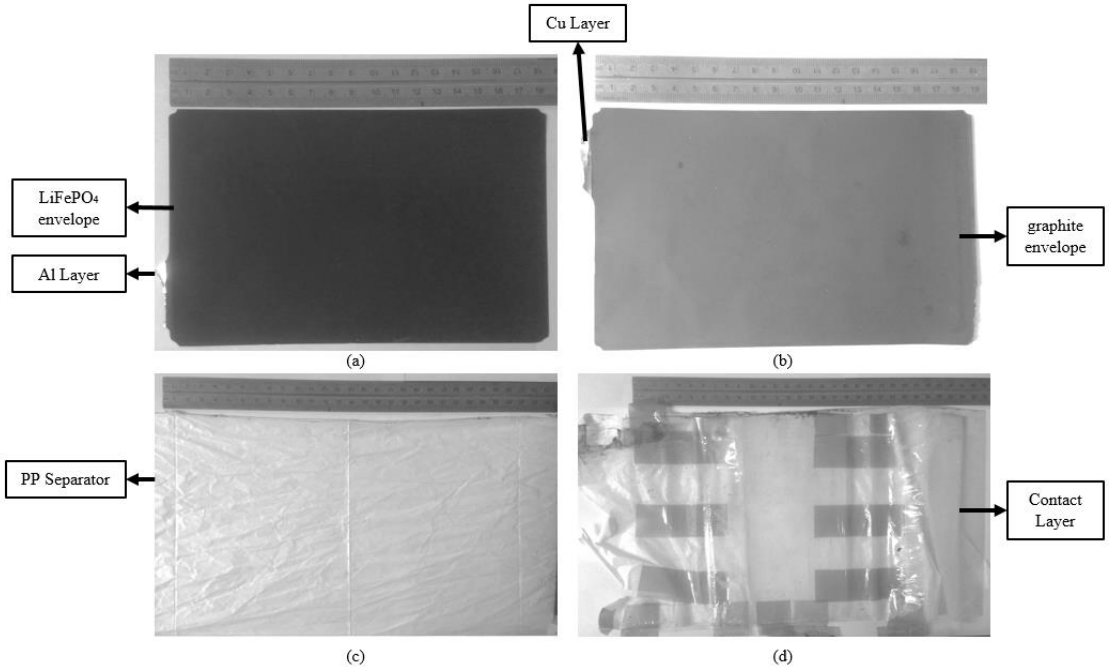

Figure 3-17: Battery core internal Layers. (a) – Positive Electrode, (b) – Negative Electrode, (c) – Separator, and (d) – Exterior Polyethylene / Contact Layer.

The Positive Electrode consists of an aluminum sheet, coated by LiFePO4, while the Negative Electrode is a sheet of copper, coated by graphite. Every electrode is placed parallel to each other inside

the core, with a PP Separator in between. Then, these electrodes can trap the liquid electrolyte inside them since they have porous structure. Table 3-4 presents physical and geometric properties for each material.

Table 3-4: Specification for the Layers inside the battery core (Chen, Wan, Wang, 2005).

Material	Thickness	Density	Heat Capacity	Thermal Conductivity	length	height
-	(mm)	(kg/m³)	(J/kg K)	(W/m K)	(mm)	(mm)
Aluminum foil	0.064	2702	903	238	100	165
Carbonaceous electrode	0.067	1347.33	1437.4	1.04	100	165
PP separator	0.036	1008.98	1978.16	0.3344	100	165
Lithium electrode	0.079	2328.5	1269.21	1.58	100	165
Copper foil	0.026	8933	385	398	100	165

Figure 3-18 presents the internal layout of the battery. In this schematic, the view of the terminals in the gap volume is omitted, to facilitate the visualization. In the battery core, each segment of PP separator, Positive electrode, PP separator again, and Negative electrode together, represents one pouch cell. A total of 80 pouch cells is compressed inside the case. It is the number of pouch cells that dictates the battery capacity for a single chemistry.

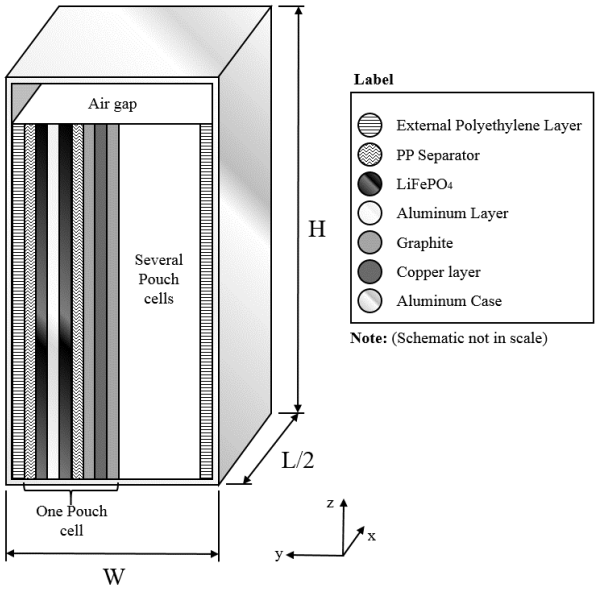

Figure 3-18: Internal Battery view – Schematic (H x L x D – 216.8 x 135.2 x 29.2 mm).

Figure 3-19 presents the terminals with a prismatic geometry. This is a simplified representation, since there are several layers of copper, or aluminum for the opposite side, compressed together, and attached to the top battery cells connectors, as can be seen in Figure 3-17. The dimensions for w', w", and h" are 8.5, 32, 28.8 mm, respectively. Additionally, these connectors are located at the center line, in the plane ZY, of the battery cell.

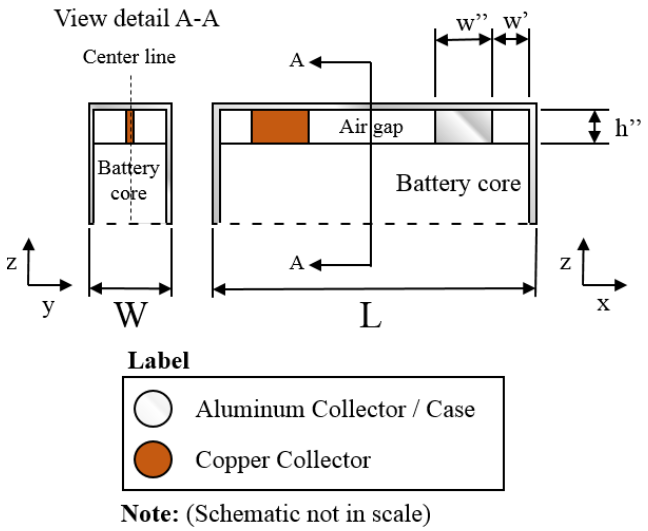

Figure 3-19: Terminal representation locate inside the air gap.

The CALB CAM 72 Ah is the actual battery cell selected as energy storage for the Commander 5EV. The machinery has a total of 50 modules, and each module has 8 battery cells. One of these modules is the one selected for this study, as shown in Figure 3-14, with 6 cells connected in series.

3.5 Instrumentation and Control

The Battery Management System, Data Logging System, Anemometer, and Thermal Camera are explained in detail in terms of features, usage requirements and the results provided by each device.

3.5.1 Battery Management System (BMS)

The BMS Jr manufactured by Orion, presented in Figure 3-20, not only obtains readings but also balances the battery pack. Capable of evaluating from one to sixteen Lithium-iron Phosphate chemistry cells in series with 48V nominal and 60V maximum, it measures the state of charge, discharge current limit, charge current limit, cell voltage, open cell voltage, and current. The CANBUS communication protocol is used to communicate with the BMS, meaning that the device also requires a can adapter. The BMS is powered by 12V input, which is supplied by the DC Power Supply AB5PS-D.

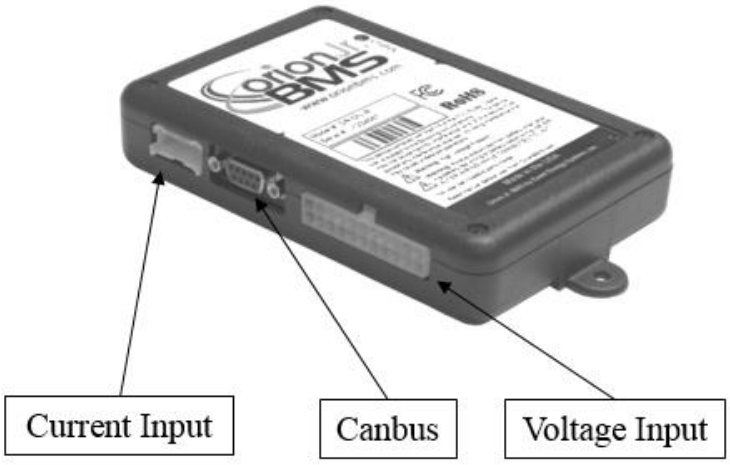

Figure 3-20: BMS Jr from Orion.

3.5.2 Data Logging System

A National Instruments PXIe-1082 data acquisition platform fitted with an NI TB-4353 front mounting isothermal terminal block used for thermocouple inputs (Figure 3-21) to obtain temperature readings. LabVIEW, the chassis software, recorded the temperature values sent from each K-type thermocouple.

Figure 3-21: PXIe-1082 chassis with NI TB-4353 front mounting terminal block attached.

K-type thermocouples were attached to the surface of the cells, according to the layouts presented in Figure 3-22 and Figure 3-23 for single cell and module respectively. For the single cell setup, thermocouples were placed in the centre of an area of interest on the front panel. The same was performed on the bottom and top surfaces, but the vent port locations required that thermocouple T9 was located on the side of the battery. The final temperature value used to calculate the heat loss is the average temperature reading of the front and sides of the area of interest. T10 was used to evaluate the temperature inside the chamber.

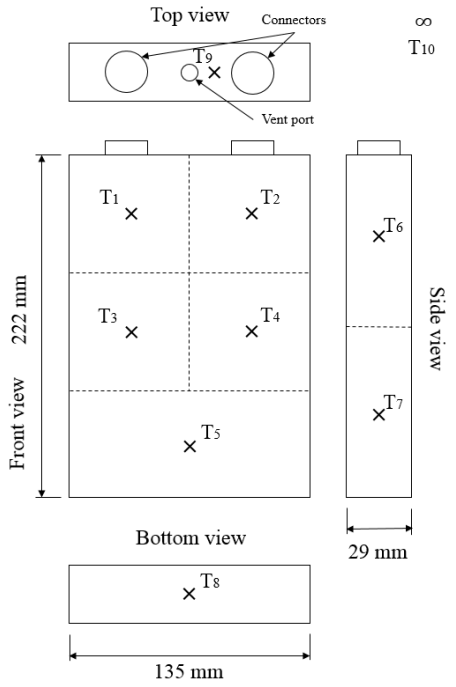

Figure 3-22: 10 K-type thermocouples location around the battery cell. Schematic not in scale.

In the module thermocouple arrangement, one thermocouple is in the centre of the front face of each cell, see Figure 3-23.

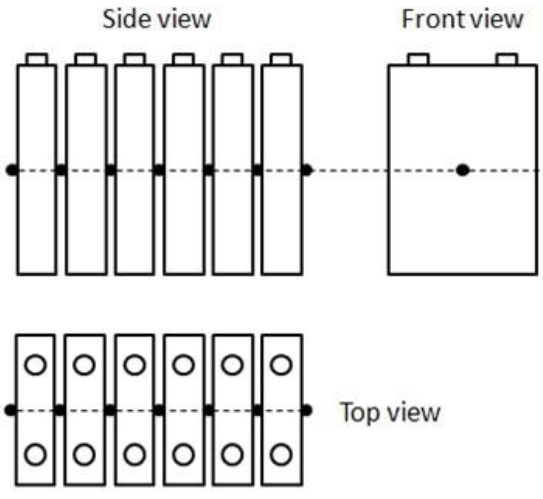

Figure 3-23: K-type thermocouples around the battery module. Schematic is not in scale.

Figure 3-24 shows that the thermocouples were located at the back of the battery cell to allow for clear thermal camera observation of the batteries.

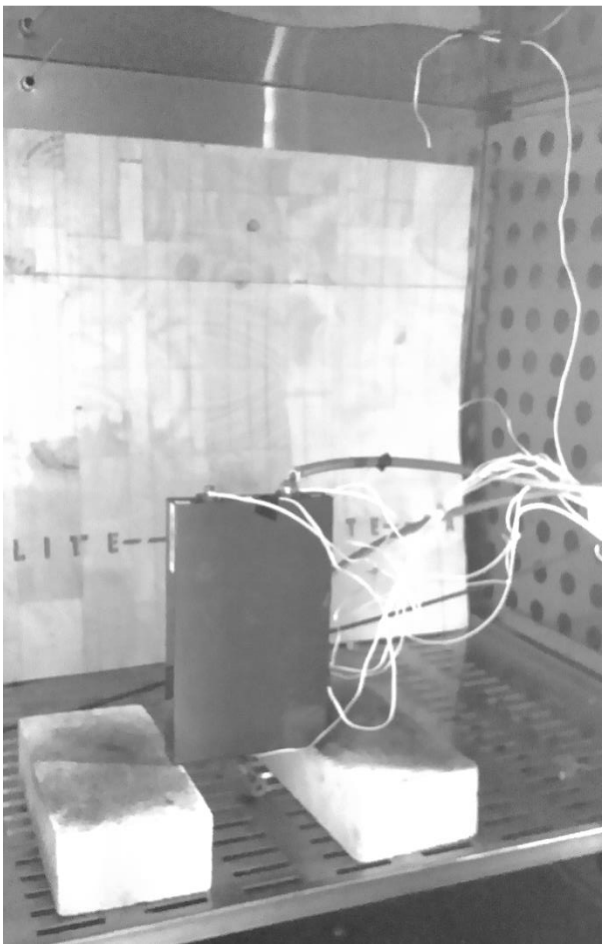

Figure 3-24: Setup for thermocouples and voltage tap connected around the battery cell.

3.5.3 Anemometer – TSI/Alnor 9545 VelociCalc Air velocity meter

The Anemometer probe, located inside the chamber adjacent to the battery cell, measures the air flow speed (Figure 3-25), as well as the mass flow, temperature, relative humidity, wet bulb, and dew point. The values measured are recorded in a data acquisition system.

Figure 3-25: Anemometer – TSI/Alnor 9545 VelociCalc and its probe stick (TSI, n.d.).

Table 3-5: Anemometer main specifications.

Range	0 to 30 m/s (+/- 0.015 m/s)
Resolution	0.01 m/s
Operating electronics	5° to 45°C
Operating probe	-10° to 60°C (+/- 0.3°C)
Resolution	0.1°C

3.5.4 Thermal Camera

A thermal camera (FLIR model E5 depicted in Figure 3-26) was employed to capture the temperature distribution of the battery surface. The image from the experiment was used to validate the simulation image. The infrared picture has also the advantage of providing a far more detailed result than the evaluation of the local temperature by a thermocouple. The downside of this methodology is that the image can only be obtained at the end of the procedure when the battery unit reaches its peak maximum temperature. This because photographs of the battery may not be taken during the experiment as this would require the chamber to be open, thus interfering with temperature reading results. Furthermore, it can be used to evaluate the temperature over surfaces with emissivities

within the range of 0.1 to 1 (see Table 3-5), which includes the battery cell, which has an emissivity estimated as 0.78, as mentioned earlier.

Figure 3-26: Thermal Camera – FLIR E5 (FLIR, n.d.).

Table 3-6: Thermal Camera – FLIR E5 main specifications.

IR resolution	120 x 90
Thermal sensitivity	<0.10°C
Temperature range	-20°C to 250°C (+/- 2°C)
Emissivity range	From 0.1 to 1

3.6 Experimental Procedure

The experimental procedure generally followed the sequence below:

1. Battery was placed inside the chamber and over the ceramic base;
2. Charging/Discharging cables were connected between the power supply and the resistor bank;
3. K-Thermocouples were attached to the battery surface and internally to the chamber at the top, and then connected to the Data Logging system;
4. Anemometer was placed inside the chamber and connected to the laptop;
5. BMS was connected to the negative and positive terminals of the battery;
6. BMS current sensor was attached to charger/discharger cable;
7. Chamber was set at the target temperature;
8. Waiting time until the battery reached temperature equilibrium with the chamber;
9. Charging process: Charging process was initiated by giving a command to the power-supply via laptop / Discharging process: Emergency bottom was opened allowing the battery to be discharged by the resistor banking;
10. The temperature was started being recorded by the thermocouple and the voltage/current by the BMS;
11. Once the desired SoC was reached accordingly to the BMS, the system was disengaged;
12. Recording for both temperature and current/voltage was terminated;
13. Chamber was opened, and a thermal picture of the battery/module was taken.

There are generally four modes of operation for the battery which result in heat generation: charging, downhill driving (regeneration charging), flat driving and uphill driving modes. These modes represent the basic conditions in which the Commander 5EV is going to be used underground. The current target for each mode is 16.9 amperes, 30.8 amperes, 17.0 amperes, and 42.3 amperes

respectively. These values were estimated by the electric motor manufacturer based on the power requirement for each condition. Experiments were conducted to simulate these operating conditions.

In the single cell experiment the battery was charged, for charging and downhill mode, at a current of 17.4 amperes, and 29.4 amperes on average respectively. The battery was then discharged in two different conditions, one at 17.0 amperes on average in a condition simulating driving over a flat surface, and the other at 44.1 amperes on average in an uphill simulation as though the vehicle is driving up the ramp. These values do not precisely match those from the target due to accuracy limitations from the resistor bank and the balance changer/discharger unit. Each driving condition is conducted in 25°C, 30°C, 35°C, and 40°C ambient temperature controlled by the oven chamber.

Table 3-7: Test matrix for single cell charging and discharging cases.

Usage Mode	Operating Condition	Current Rate	Ambient Temperature
Charging	Simulates battery charging when vehicle is not in use.	17.4 amperes	25°C, 30°C, 35°C, and 40°C
Downhill Charging	Simulates the regenerative breaking system when driving downhill.	29.4 amperes	25°C, 30°C, 35°C, and 40°C
Flat Discharge	Simulates the requirement for driving the machine over flat surface.	17.0 amperes	25°C, 30°C, 35°C, and 40°C
Uphill Discharge	Simulates the requirement for driving the machine upward on 20° amperes	44.1 amperes	25°C, 30°C, 35°C, and 40°C

In the module heat evaluation, 6 cells were connected in series to form a pack (See Figure 3-14). The pack was charged in charging and downhill modes and discharged in flat and uphill modes at 16.5 amperes, 31.0 amperes, 16.8 amperes, and 41.0 amperes respectively. As explained earlier, the slight difference between the target and the actual results were due to the same reasons as in the case of single cell experiment. The module was tested in the same range of ambient temperature as the single cell case. In both single cell and module experiment procedures, the module was charged/discharged within the range of 10% to 90% State of Charge (SoC). For the experimental results, see appendix A for single cell, and appendix B for module.

Table 3-8: Test matrix for module charging and discharging cases.

Usage Mode	Operating Condition	Current Rate	Ambient Temperature
Charging	Simulates module charging when vehicle is not in use.	16.5 amperes	25°C, 30°C, 35°C, and 40°C
Downhill Charging	Simulates the regenerative breaking system when driving downhill.	31.0 amperes	25°C, 30°C, 35°C, and 40°C
Flat Discharge	Simulates the requirement for driving the machine over flat surface.	16.8 amperes	25°C, 30°C, 35°C, and 40°C
Uphill Discharge	Simulates the requirement for driving the machine upward on 20° amperes	41.0 amperes	25°C, 30°C, 35°C, and 40°C

3.7 Experimental Results

The results for the evolution of the average surface temperature throughout the experiment for each case are presented below, Figures 27 to 34. The results for the same mode but for different ambient temperatures, 25°C, 30°C, 35°C, and 40°C are combined in the same graph to facilitate visualization of the impact of the ambient temperature on the temperature developed on the surface of the battery / module. In addition, it is worth mentioning that the graphs correlate the surface temperature with the state of charge, rather than the surface temperature over time, because each experiment exhibited different charge or discharge rate. Thus, the normalization of all the results based on SoC facilitates the understanding of the data obtained in the experiments.

Uphill Mode

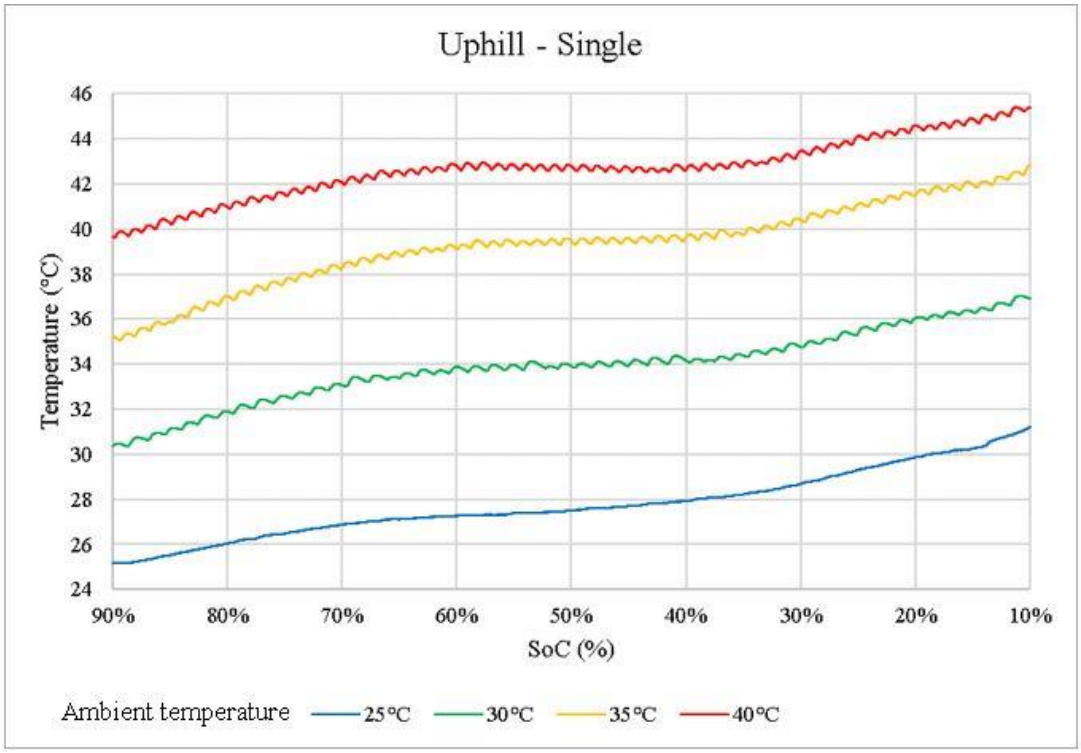

Figure 3-27: Experiment, battery surface temperature evolution, Uphill single-cell case.

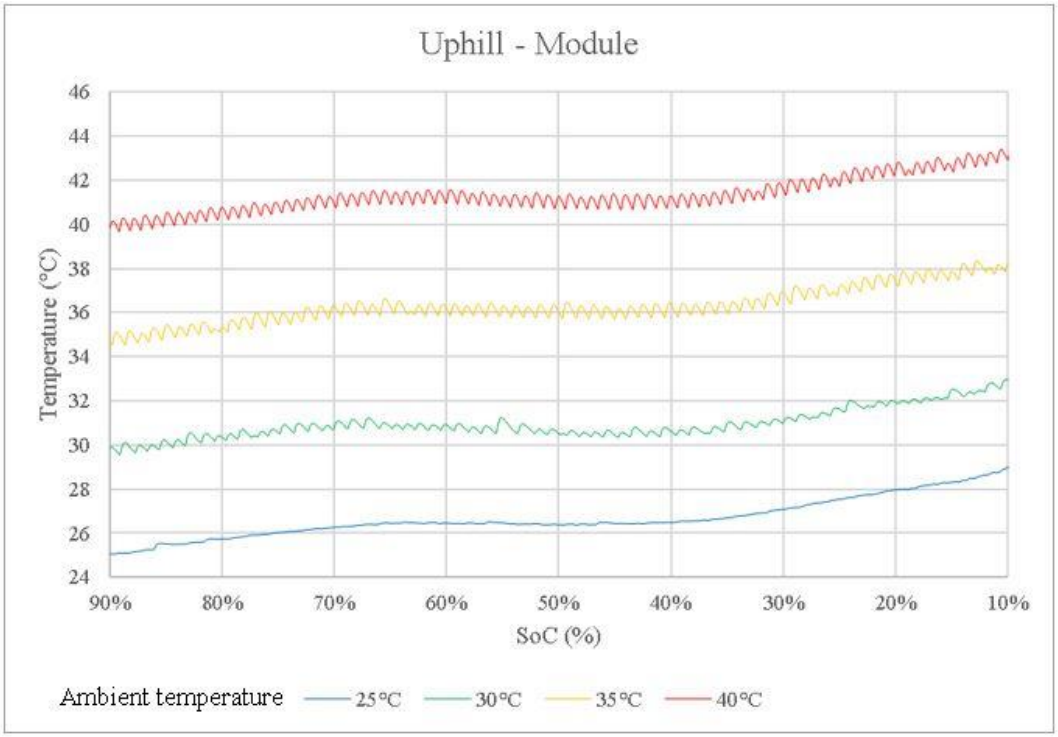

Figure 3-28: Experiment, battery surface temperature evolution, Uphill module case.

Flat Mode

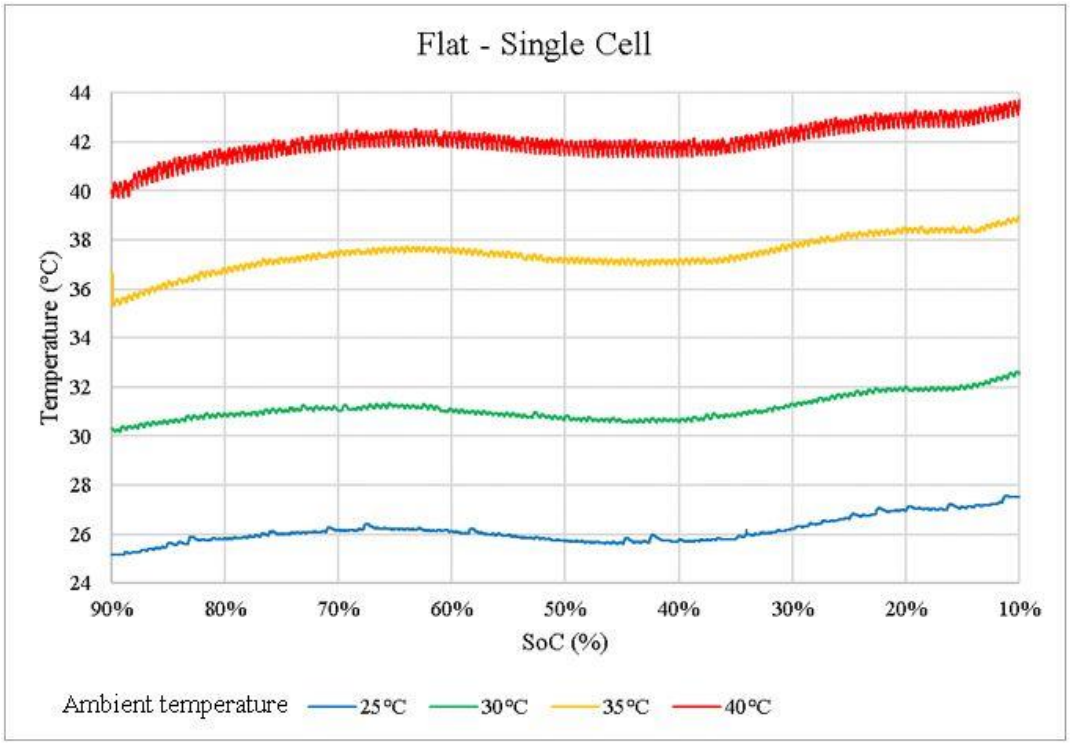

Figure 3-29: Experiment, battery surface temperature evolution, Flat single-cell case.

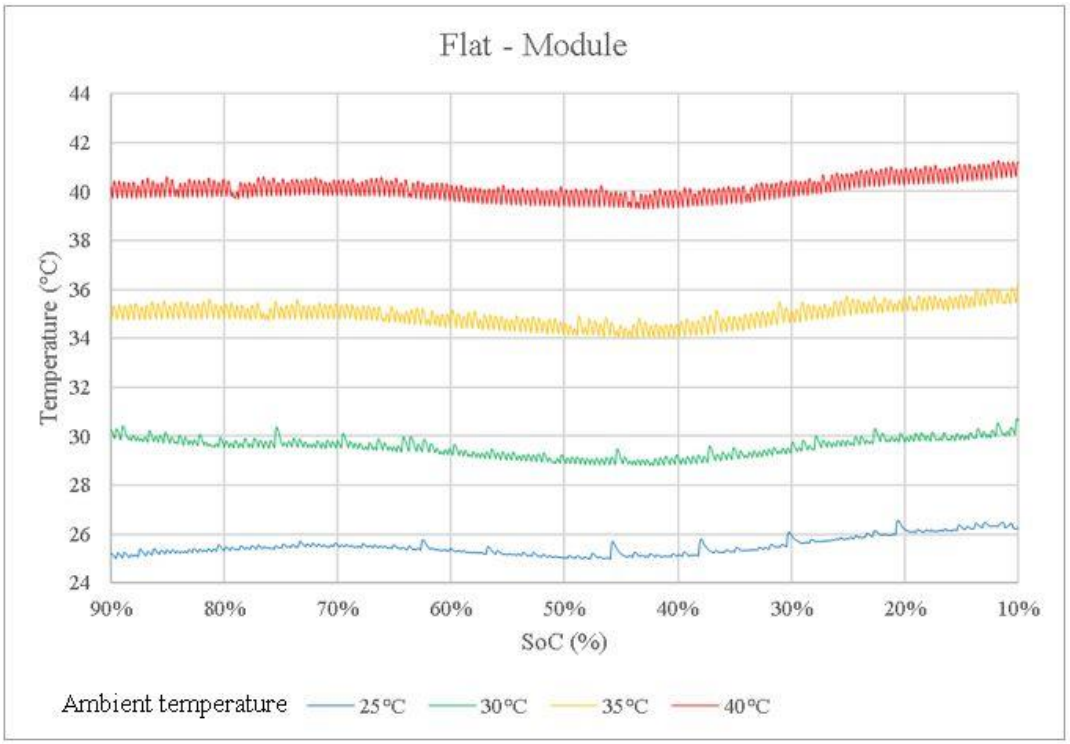

Figure 3-30: Experiment, battery surface temperature evolution, Flat module case.

Charging Mode

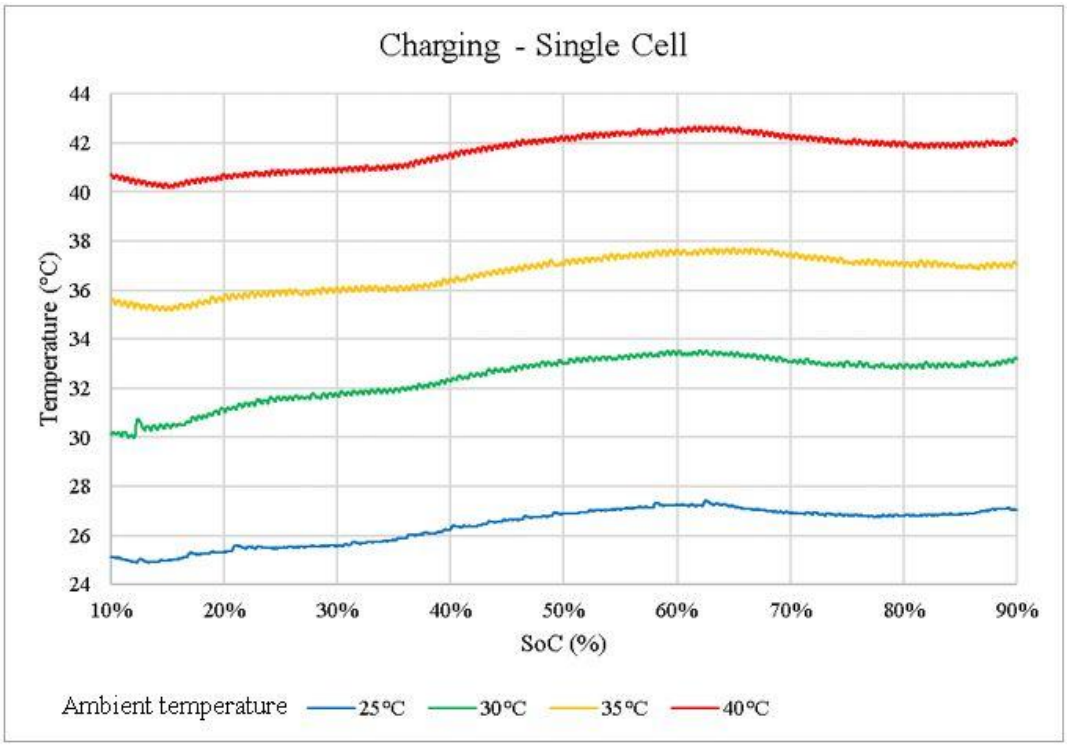

Figure 3-31: Experiment, battery surface temperature evolution, Charging single-cell case.

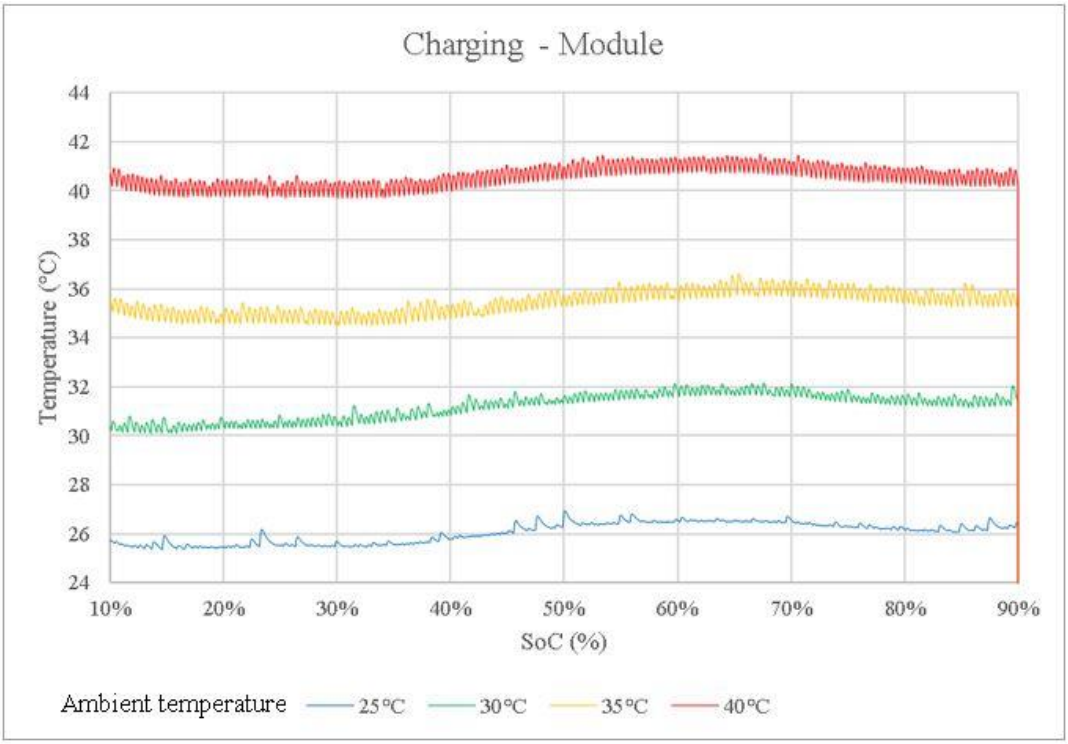

Figure 3-32: Experiment, battery surface temperature evolution, Charging module case.

Downhill Mode

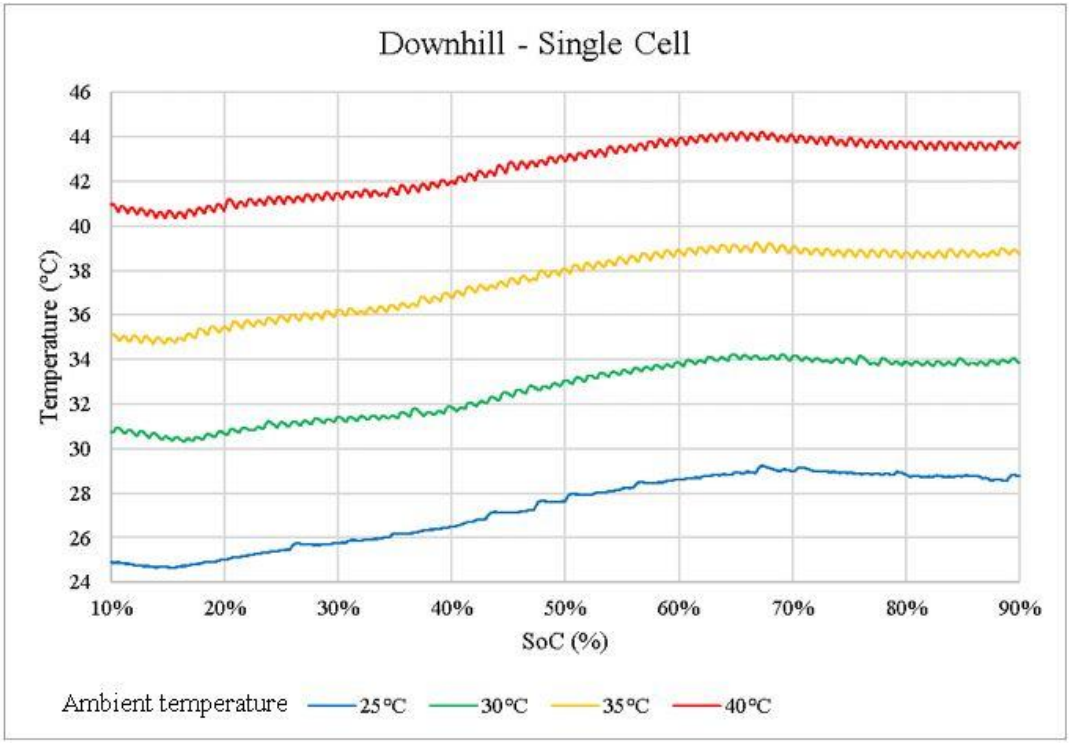

Figure 3-33: Experiment, battery surface temperature evolution, Downhill single-cell case.

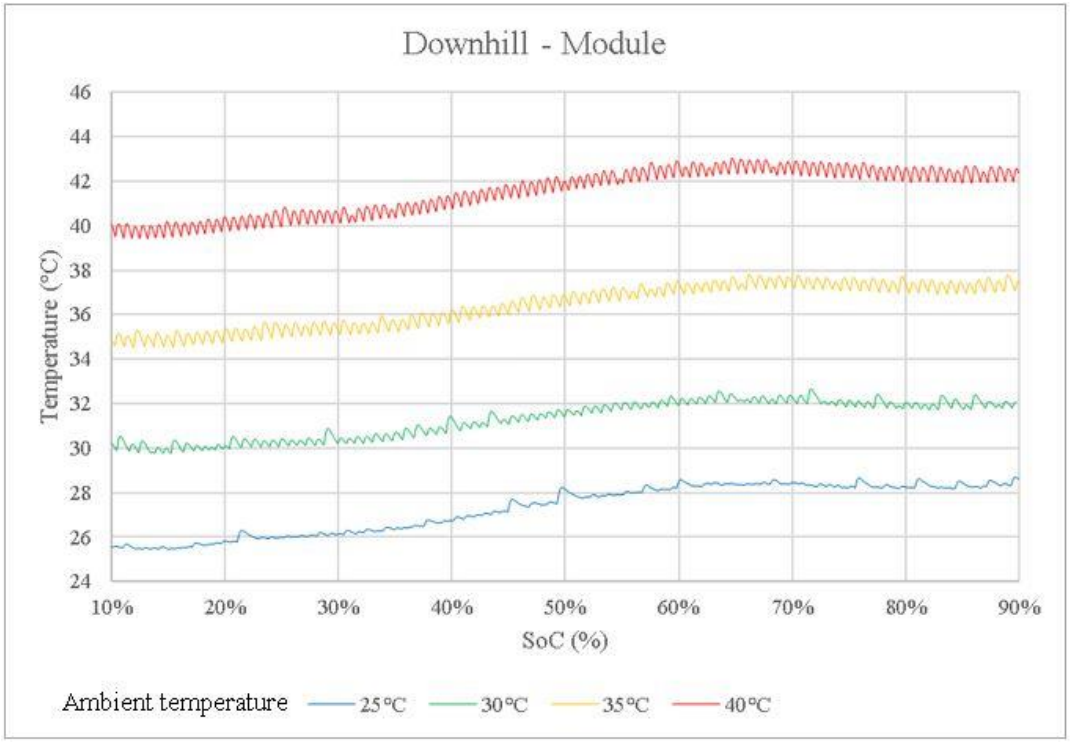

Figure 3-34: Experiment, battery surface temperature evolution, Downhill module case.

3.8 Discussion

As expected, the overall surface temperature of the battery increased during the experiment. The variation in the rate of increment in temperature is due to the second term in the heat generation equation for lithium battery cells. This second term referred to as the reversible entropy, discussed in detail in Section 4.3. The current as well as the difference between the voltage and the open voltage are virtually constant during the experiment.

The temperature coefficient required in equation (4-4) is obtained from a commercial Lithium-iron Phosphate battery cell (Forgez *et al*., 2010), whose respective curve can be seen in Figure 3-35. To not compromise the battery's life-span, the temperature coefficient curve is only used within the range of 10% to 90% SoC.

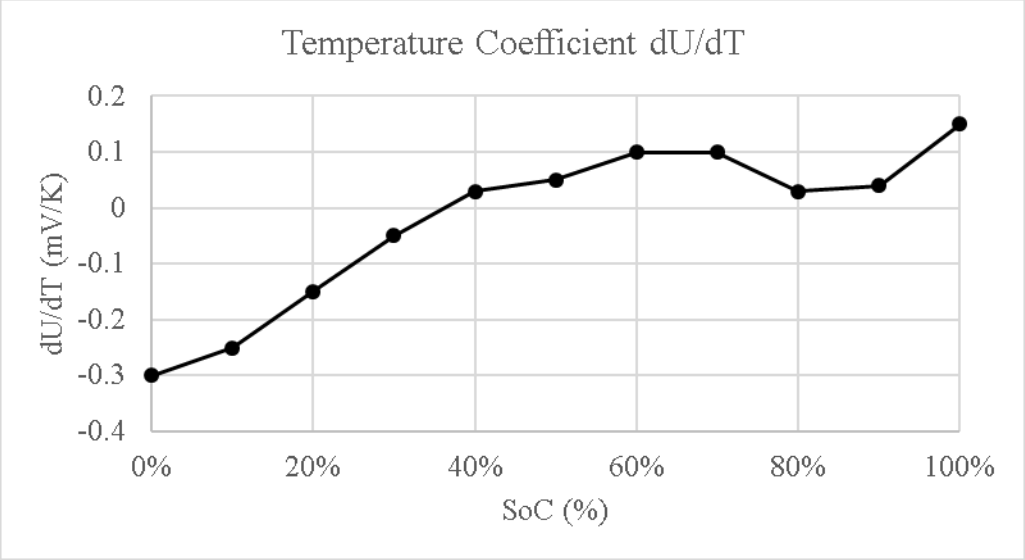

Figure 3-35: Temperature Coefficient curve adapted from (Forgez et al., 2010).

The average temperature evolution along the cell/battery module system generally follows the "shape" of the temperature coefficient curve (Figures 3-27 to 3-34). With regards to the charging processes (charging and downhill mode), the general average temperature surface curve follows a small decrement in the average surface temperature from 10% to 15% SoC, increasing over time until it

reaches a plateau around 60%, decreasing again until 80%, and increasing once more until 90% SoC has been achieved. We can deduce from equation (4-4) that since the Ohmic Heating term is assumed to be constant for this study curve, the heat generation variation is going to be dictated by the Reversible Entropic term. As for the discharging processes (Flat and Uphill modes), the SoC is decreased over time. This means that at the beginning of the process, the temperature is dramatically increased due to the high value for the temperature coefficient (Figures 3-22 to 3-25). Usually a plateau level is reached around 60% as a delay reflection of the lower temperature coefficient level, which stands around 80% SoC (Figure 3-30). After 40% SoC, the battery continuously increases its temperature dramatically because of the Ohmic Heat term, which has a considerably higher magnitude in comparison to the Reversible Entropic term, as can be seen in Table 3-9.

Table 3-9: Average Heat Generation in terms of Ohmic Resistance and Reversible Entropy.

Heat Generation term	Uphill	Downhill	Charge	Flat	unit
Ohmic Resistance	1.45	0.60	0.19	0.18	W/cell
Reversible Entropy	-0.07	0.05	0.03	-0.03	W/cell

The average surface temperature results in the current study showed that there is an agreement with the findings obtained in a prior study for both charging and discharging processes in the case where the chamber temperature is constant (Niculuta, 2011). In addition to this, it was observed that the magnitude of the ambient temperature was not enough to considerably affect the surface temperature increment of the battery/module for a given current level. In the case of the single cell, the average temperature increases for uphill, flat, charging and discharging cases, resulting in 7° C, 3° C, 2° C and 4° C increments in each mode, respectively. As in the case of the module, 3° C, 1° C, 2° C and 2° C increments occur for the same modes. These results show that the current level is the dominant factor in the development of the surface temperature of the battery/module.

Furthermore, even though both the battery and the module use similar current levels, which lead to similar heat generation, it did not translate into similar surface temperature because both cases

had different surface emissivity. For instance, the emissivity of the battery pack module is 0.78 (Omega, accessed on April 5th, 2017), versus 0.95 (Emissivity Values of Common Materials, 2007) of the electrical tape used to cover the single cell. The insulating effect is assumed to be insignificant because it has low thermal resistance (vinyl ester: 0.25W / mK, air 0.0262W / mK) (Thermal conductivity of common materials and gases, n.d.) and has a negligible thickness. This new emissivity value affected the amount of radiative heat loss emitted by the single battery, which comparable to the battery pack, produced a higher surface temperature consequently.

The understanding of temperature variation over time can be valuable in the daily use of these machines underground. As mentioned at the beginning of this section, the temperature increment is not constant and sometimes there is a possibility of a temperature decrease for a specific range of SoC, in which its surface temperature variation over time strongly depend on each battery chemistry. These are repeatable and consistent results, as expressed by Figures 3-22 to 3-29, which proves that the temperature coefficient is an important component that is needed to be addressed in the mathematical heat generation model. This knowledge can also be useful to proper size and operate the battery cooling system (if necessary), minimizing power consumption by the cooling pumps and to avoid thermal stresses of the battery.

4 Mathematical Treatment

4.1 Overview

The section describes the mathematical treatment which is used as a basis for the analysis of the battery thermal performance. The method, which is also followed by numerous other researchers, (Niculuta, 2012; Chen, Wan, Wang, 2005) divides the internal structure of the battery into different subdomains. This strategy allows direct mathematical and virtual modeling of the battery, given the specificity of each region and the equations which governs the heat transfer. See Figure 4-1 for the internal single battery model subdomains.

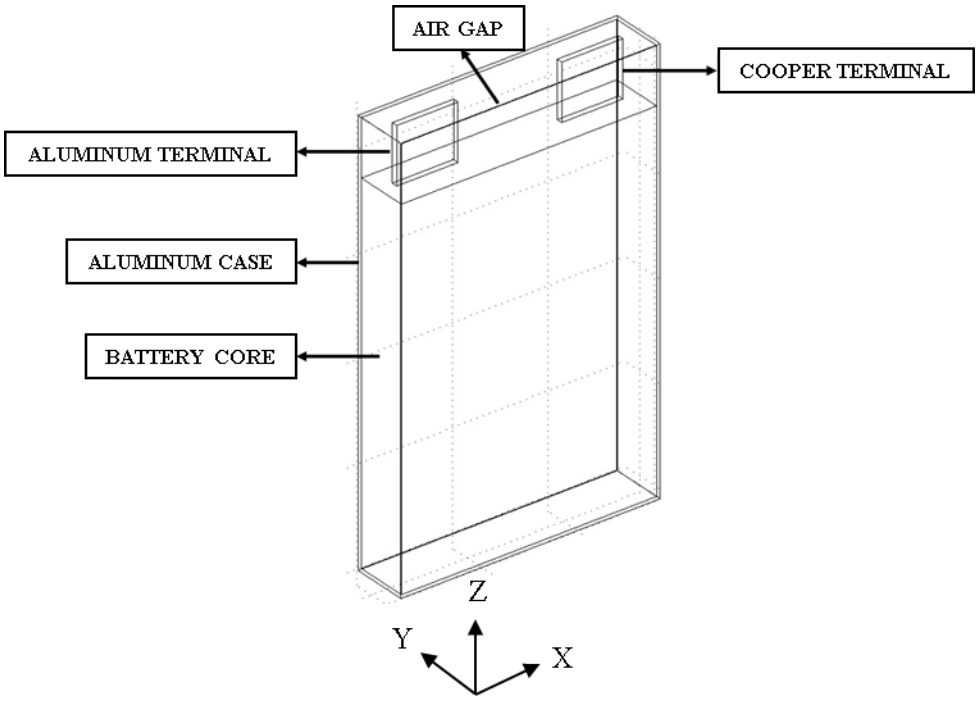

Figure 4-1: Battery subdomains and special parameters.

Most of the studies researched had divided the battery cell into three domains, the case, core, and the air gap (Niculuta, 2012) and (Chen, Wan, Wang, 2005). In this study, the battery connectors will be included as part of the evaluation as a mean to obtain a more accurate result. Inside the battery core, and under charging and discharging regimes, the transient heat is generated and propagated through three dimensions, as expressed by the energy balance equation (4-1). This equation describes the heat transfer from the battery core. The radiative heat term is not considered because it is assumed

that the internal layers are opaque. This heat is transferred through the internal layers, to the air gap at the top of the core, to the aluminum case, and then, it is released to the outside in the form of radiative and convective heat.

$$\rho Cp\ \frac{\partial T}{\partial t} = \frac{\partial}{\partial x}\left(k_x \frac{\partial T}{\partial x}\right) + \frac{\partial}{\partial y}\left(k_y \frac{\partial T}{\partial y}\right) + \frac{\partial}{\partial z}\left(k_z \frac{\partial T}{\partial z}\right) + Q \qquad (4\text{-}1)$$

ρ, Cp, k, and Q represent density, heat capacity, thermal capacity and heat generated in volumetric units respectively.

4.2 Physical Properties of the Core Domain

The battery core is composed by several thin layers of different materials as seen in Figure 3-16. When running a simulated model for heat transfer analysis, this level of detail can be excessively burden computational resources. For this reason, a common practice among those who study batteries from the thermal aspect is to simplify the internal structure into a single component, with a specific heat capacity and thermal conductivity (Niculuta, 2012; and Chen, Wan, Wang, 2005). The plane XZ is the one used as a reference for the equations because the layers are parallel to it. See Figure 4-2.

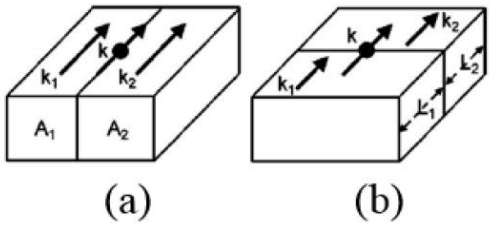

Figure 4-2: Effective thermal conductivity for parallel (a), and series (b) elements (Chen; Wan; Wang, 2005).

The battery orientation used for the calculation can be seen in Figure 4-1. Then, the calculation for the effective thermal conductivity normal to the plane XZ, or $k_{trans,}$ is given by equation (4-2 (a)); and for planes XY, and YZ, or $k_{long,}$ is given by equation (4-2 (b)). To calculate the equation (4-1), it is also required to obtain the effective ρ and Cp terms, in which both can be calculated through the

equations (4-2 (c)) and (4-2 (d)). *L* is the material thickness, *k* is its thermal conductivity, *A* is the layer front area in the plane XZ, *v* is the layer volume, and *i* is the index for each layer.

$$k_{trans} = \frac{\sum_i L_i}{\sum_i \left(\frac{L_i}{k_i}\right)} \qquad k_{long} = \frac{\sum_i (k_i A_i)}{\sum_i (A_i)} \qquad \rho = \frac{\sum_i \rho_i v_i}{\sum_i v_i} \qquad C_p = \frac{\sum_i C_{p,i} v_i}{\sum_i v_i} \qquad (4\text{-}2)$$

(a) (b) (c) (d)

From equations (4-2) and the values provided by Table 3-4, the parameters k_{trans}, k_{long}, ρ, and Cp are calculated, given 1.145 W/mK, 23.9 W/mK, 2133 kg/m³, and 1335 J/kgK. These final values are referred to CALB CAM72Ah.

4.3 Heat Generation from the Core Domain

The most detailed model available to describe the heat generated in lithium-ion battery cells was developed by Thomas and Newman (2003), and it is described in equation (4-3):

1st term 2nd term 3rd term 4th term

$$\dot{Q} = I\,(V - V_{oc}) + I\left(T\frac{\partial V_{oc}}{\partial T}\right) - \sum_i \Delta H_i^{avg} r_i - \int \sum_i \left(\bar{H}_j - \bar{H}_j^{avg}\right)\frac{\partial c_j}{\partial t}\,dv \qquad (4\text{-}3)$$

Ohmic Heating (Joules Effect) or Resistive Dissipation | Reversible Entropic Heat | Heat by the chemical reaction | Heat of mixing

This expression has four main terms: Ohmic heating (or resistive dissipation), reversible entropic heat, heat by chemical reaction and heat of mixing. Where $\dot{Q}$ is the heat generation over time; *I* is the current, which can be either positive (charging), or negative (discharging); *V* is the cell voltage; V_{oc} is the open-circuit potential or equilibrium cell voltage; *T* is the temperature, which in general is the average between the surface and the core; $\frac{\partial V_{oc}}{\partial T}$ is the temperature coefficient; ΔH_i is the enthalpy variation; r_i is the rate of reaction; $\bar{H}_j$ is the partial molar enthalpy of the materials *j*; c_j is the concentration of the

materials j; t is time; and v is the volume. Usually, the temperature coefficient is obtained experimentally through a complete discharging/charging process.

The fourth term represents the heat generated by the concentration variation across the electrolyte and the porous inside the internal layers as starting from the last component of equation (4-3). This value can be either positive or negative.

The third term considers the side reactions that can contribute to heat generation or consumption. So, as the fourth term, it can have positive or negative value. Since these reactions are commonly related to slow process such material aging, this term can also be neglected (Bernarda; Pawlikowski; Newman, 1985).

The formula ends up taking the shape of equation (4-4) through the elimination of the third and fourth terms from equation (4-3):

$$\underset{\substack{\text{Ohmic Heating (Joules Effect) or Resistive Dissipation}}}{\overset{1^{st}\text{ term}}{\dot{Q} = I\,(V - V_{oc})}} + \underbrace{I\left(T\frac{\partial V_{oc}}{\partial T}\right)}_{\text{Reversible Entropic Heat}}^{2^{nd}\text{ term}} \qquad (4\text{-}4)$$

This equation was originally developed by (Bernardi; Pawlikowski; Newman, 1985). The first term represents the Ohmic Heating from Joule`s effect, and other internal resistances. It has positive magnitude. The second term is the mathematical interpretation of entropy change due to electrochemical reactions. It can be either negative or positive. According to some sources (Pesaran; Vlahinos: Burch, 1997), and (Khasawneh, 2011) it always has a considerably lower magnitude when compared to the first term, and for complete charge and discharge, such as in EV applications for example, it can be ignored. However, in some other studies (Thomas, Newman, 2003; Forgez *et al.*, 2010; Niculuta, 2012), it is stated the opposite since they have the same magnitude as the Resistive Dissipation. Thus, this study follows the last approach in order to obtain more accurate results.

As pointed out by Niculuta (2012), the first term in equation (4-4) can be described as in equation (4-5).

$$\dot{Q}_{rd} = I\ (V - V_{oc}) = \ I^2 R \tag{4-5}$$

4.4 Collector Domain

The heat generation from the collectors, $\dot{Q}_{col}$, is given by equation (4-6):

$$\dot{Q}_{col} = \left(\frac{R\ I^2}{v}\right), \text{ where } R = r"h \tag{4-6}$$

The material resistance (*R*) is calculated based upon the material resistivity (*r''*), which is assumed to be 1.68x10^{-8} Ωm for copper, and 2.65x10^{-8} Ωm for aluminum (Giancoli, 1995). As for the remain parameters in the equation (4-6), *v* is the collector volume, and *h* is the collector height.

4.5 Air Gap Domain

The air inside the gap domain is static, or a solid like material. This allows the use of equation (4-1) for determining the energy balance. This is done to facilitate the simulation through the elimination of fluid dynamics mathematical modeling. Thus, the effective thermal conductivity is calculated as shown in equation (4-7).

$$k_{eff} = Nu_{gap} * k_{air} \tag{4-7}$$

It is assumed that the air gap is a vertical enclosure where occurs internal natural air convection from the bottom to the surrounding faces. Thus, equation (4-8) can be used as a mean to calculate the Nusselt value. 28.8mm is assumed to be the height of the air volume, and 27.3mm the depth (Incropera; DeWitt, 2002):

$$Nu_{gap} = 0.18\ \left(\frac{Pr}{0.2 + Pr} Ra_L\right)^{0.29} \tag{4-8}$$

Requirements for the use of equation (4-8) are listed in equation (4-9).

$$\begin{cases} 1 < \dfrac{H}{L} < 2 \\ 10^{-3} < Pr < 10^{5} \\ 10^{3} < \dfrac{Ra_L Pr}{0.2 + Pr} \end{cases} \tag{4-9}$$

Whereas for Rayleigh, *Ra*, the equation is given by (4-10):

$$Ra = \frac{g\beta(T_1 - T_2)L^3}{v"\alpha} Pr \tag{4-10}$$

Where L is the characteristic length, g is the gravitational acceleration, T_1 is the lower temperature surface, T_2 is top surface temperature, v is the volumetric thermal expansion coefficient, which is equal to $2/(T_1 - T_2)$, $v"$ is the kinematic viscosity, α is the thermal diffusivity, and Pr is the (dimensionless) Prandtl number, in which the values for the last two parameters are taking from the average temperature between the two plates.

4.6 Boundary Conditions

The heat transfer from the battery to the surrounding ambient environment occurs mainly through radiation and convection. In this study, the heat transfer due to conduction between the battery and the base support is assumed to be of negligible magnitude and not considered.

The heat transfer through Radiation and Convection is given by equations (3-11) and (3-12) respectively:

$$Q_{rad} = \epsilon\sigma A(T_s^4 - T_\infty^4) \tag{4-11}$$

$$Q_{conv} = h_{conv} A(T_s - T_\infty) \tag{4-12}$$

Where in equation (4-11) ϵ represents the surface emissivity, σ is the Stefan-Boltzmann constant, which is equal to 5.67 x 10^{-8} W/m². K, and A represents the surface area from where the heat

is being transferred from. For equation (4-12), h_{conv} is the convection heat transfer coefficient, which is calculated based on equation (4-13):

$$h_{conv} = \frac{Nu\, k_{air}}{L} \tag{4-13}$$

From which *L* is the characte1ristic length, and *Nu* is the Nusselt value.

4.7 Natural Convection

In this case, different correlations for the Nusselt calculation are used for each battery side. The equations for each face are as described below following the orientation seen in Figure 4-3 (Incropera; DeWitt, 2002).

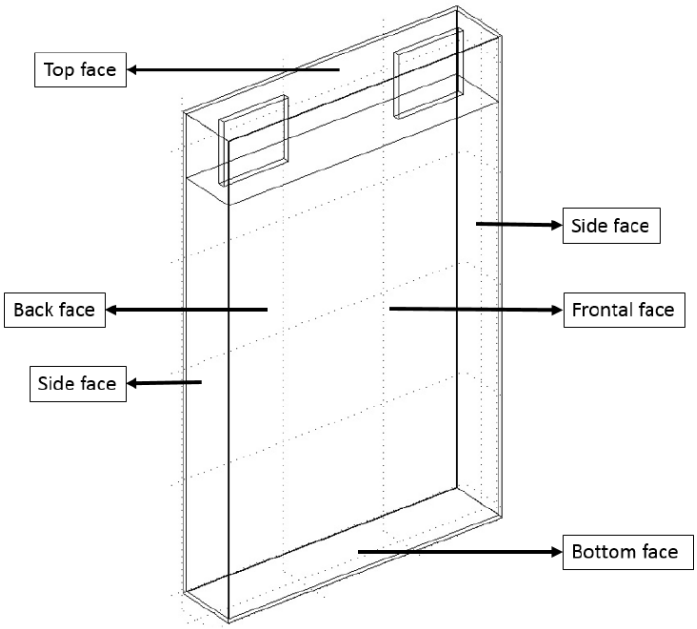

Figure 4-3: Battery faces schematic.

Frontal / Back / Sides Faces:

$$Nu = 0.68 + \frac{0.670\, Ra_L^{1/4}}{[1 + (0.492/Pr)^{9/16}]^{4/9}} \tag{4-14}$$

Here, the characteristic length, *L*, is the cell total height.

- Top Face

$$Nu = 0.54\ Ra_L^{1/4} \tag{4-15}$$

For the top surface, the characteristic length, *L*, is given by equation (4-16):

$$L = \frac{A_s}{P} \tag{4-16}$$

In which, *As* is the surface area, and *P* is its perimeter.

- Bottom Face

$$Nu = 0.27\ Ra_L^{1/4} \tag{4-17}$$

For the bottom surface, the characteristic length is calculated as described by equation (4-17) as well. For each surface side, the Rayleigh number is calculated the same manner as given by equation (4-18):

$$Ra = \frac{g\beta(T_s - T_\infty)L^3}{v"\alpha} Pr \tag{4-18}$$

Where *L* is the characteristic length, g is the gravitational acceleration, T_s is the surface temperature, T_∞ is the environment temperature, β is the volumetric thermal expansion coefficient, which is equal to $2/(T_s - T_\infty)$, *v"* is the kinematic viscosity, α is the thermal diffusivity, and *Pr* is the (dimensionless) Prandtl number. The values for the thermal diffusivity and Prandtl number are taken from the average temperature between the surface and the environment.

4.8 Forced Convection

The methodology used is the same as developed by Ellison (1969) for forced convection. In this method, the heat transfer coefficient *hc* is calculated based on a function for the average temperature between the surface and the environment, as described by equation (4-19):

$$hc = f\sqrt{\frac{V}{L}} \tag{4-19}$$

Where V is the air velocity, and L is the characteristic length, whereas the values for f, the temperature difference coefficient, is given by Table 4-1:

Table 4-1: Sample values for Temperature Difference Coefficient (Ellison, 1969).

T(K)	f
273.15	3.963703
298.15	3.873619
323.15	3.783535
348.15	3.748887
373.15	3.721169

5 Simulation and Experimental Results

5.1 Overview

The general goal of this section is to complement the experimental results described in Chapter 3 through calculation and simulation of the test conditions. The section will examine surface temperature distribution and average surface temperature over time for the single battery and the multi-cell battery modules subjected to different environmental temperatures and electrical duty cycles. The methodology is like what was done by other researchers working in this issue including (Niculuta, 2012; Chen, Wan, Wang, 2005). The simulation is based on the heat flux and heat generation equations for lithium battery cells, the mathematical basis for these calculations are described in the previous section. Parameters such as voltage, open voltage, current, cell temperature, and environment temperature were obtained from the experiment for each second and used as input for the simulation, see Figure 5-1. Heat generation and heat loss in the experiment are calculated based on these same parameters, which are imported into the model via spread-sheets. Due to the inevitable damage to the batteries, and the safety measures imposed on the experiment, it was not possible to insert a thermocouple inside of each cell (Forgez *et al*, 2010). Instead, this value is estimated based on the results extracted from the simulation itself. Once the contribution of the battery is calculated, then it is possible to address the total heat impact of the machinery by adding the thermal impact of the battery pack with the remain electrical components of the Commander 5EV.

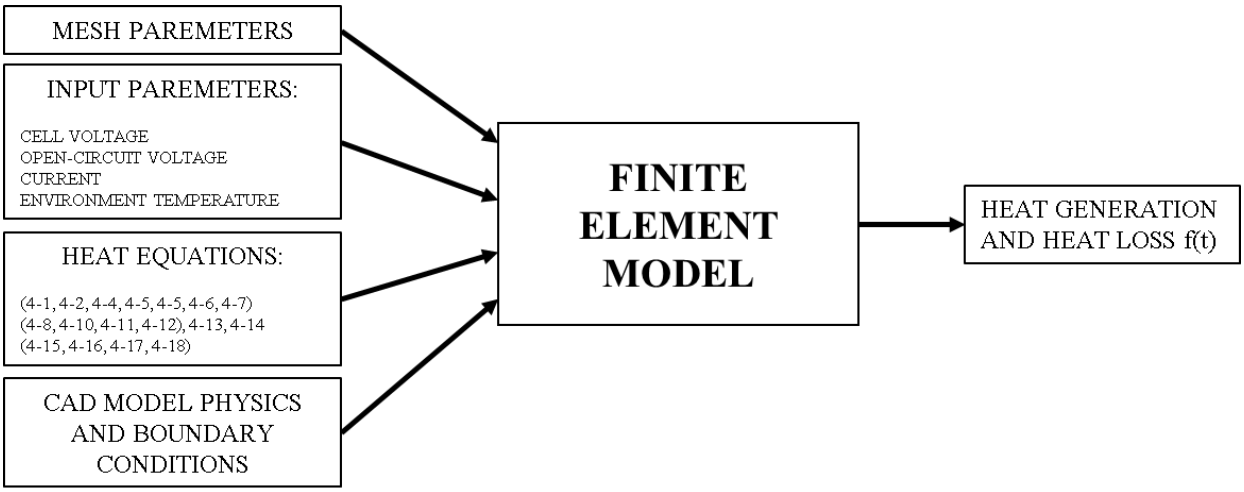

Figure 5-1: Block diagram of the FEA model.

In the actual battery, there are multiple layers (also known as the pouch cells) of dissimilar materials…For the modeling, a simplification that was introduced by previous researchers (Niculuta, 2012; Chen, Wan, Wang, 2005) is used to optimize the simulation. It involves the representation of the multiple layers of pouch cells as a single structure (referred here as the battery core) (See Chapter 3.4.2) in which the material properties can summarize into a single component as described by equations 4.2. After combining all pouch cells together, the resulting structure is anisotropic with regards to heat transfer.

5.2 Methodology

Simulations for this work were conducted using the Finite Element Modeling (FEM) software COMSOL MULTIPHYSICS (version 3.5a) using the heat transfer pack for 2D and 3D environments. COMSOL is a well-known, robust, and powerful software which allows the user to incorporate physical equations to better describe a phenomenon, such the heat generation in lithium battery cells.

5.3 Single Cell Analysis

The single cell the FEM model employed a 3D mesh size with a total of 17023 tetrahedral elements presented in Figure 5-2. Special attention was given to the thickness of the aluminum battery

case, hence, the dense mesh. For this analysis, assumed that a negligible amount of heat is transferred at the base of the model. In all the remain surfaces, only radiative and convective heat transfer occurs. The mesh is considerably denser in the center of the frontal and back face to better describe the heat flow on these regions. The battery cell modeled for the FEM simulations is the CALB CAM 72Ah (previously described in section 3.4.1 and 3.4.2), see Figure 4-2 and Figure 4-3.

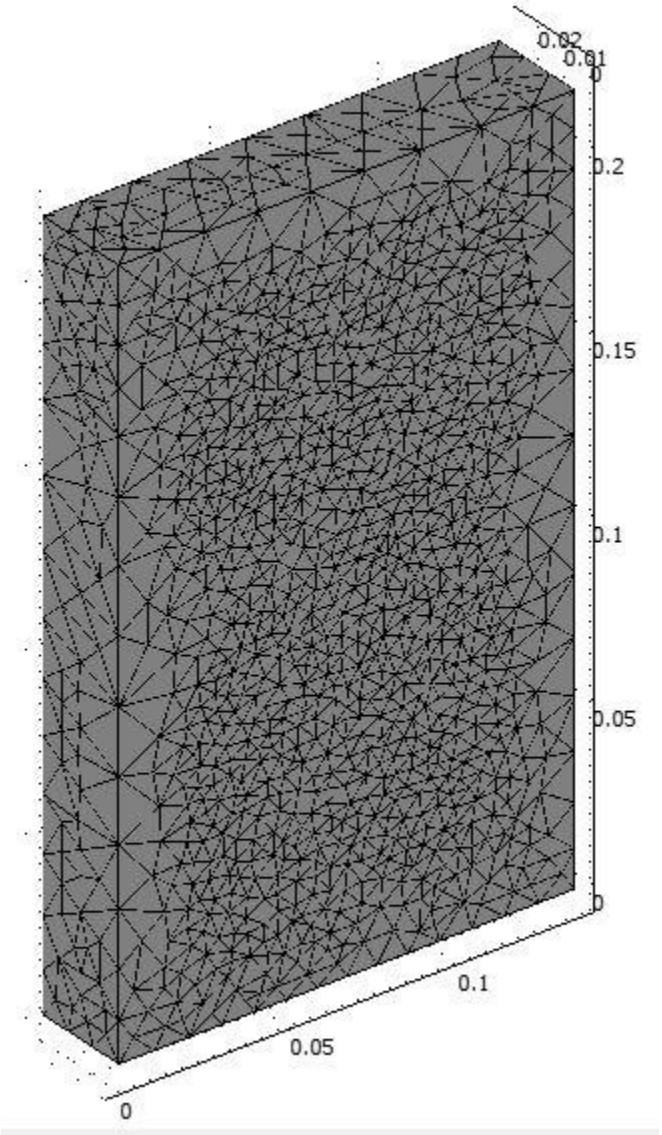

Figure 5-2: Mesh Distribution for the CAD single cell model.

5.3.1 Important Considerations about the Simulation and the Experiment

The simulations were conducted using the same ambient temperature conditions and battery parameters (Voltage, open-circuit voltage, current) from the experimental work described in Chapter 3. When the battery was tested inside the chamber, the air temperature was set at mean value throughout the operation. During the experimental test described in Chapter 3, the environmental chamber temperature control unit worked to maintain a steady environmental temperature during the test. As stated earlier, due to limitations on the ability of the heating system to keep maintaining a perfectly steady temperature, some temperature fluctuation was observed. It is important to note that the simulations described in this section used the actual observed ambient temperatures in during the experimental work rather than the setpoint. This measure is intended to reflect a more representative result of the experiments.

Prior to calculating the convective heat transfer from the battery surfaces, it was first required to determine if the air flow regime is laminar (natural convection) or turbulent (forced convection). This was performed by determining the Reynolds number (Re). If this number is higher then 5×10^5, then air flow regime is turbulent, otherwise it is laminar. This parameter is calculated based on equation 5-1.

$$Re = \frac{vl}{V} \tag{5-1}$$

v = velocity of the fluid;
l = characteristic length;
V = air kinematic viscosity.

For the thermal test chamber used in the experiment test, room temperature air is drawn in to a heating compartment from the outside, then it is preheated with resistive heating elements, blown inside the test chamber, and finally expelled to the outside again. According to measurements taken with an anemometer, the airflow inside the chamber never exceeded 0.3 m/s. This resulted in a

Reynolds value always lower than 280 for the side of the battery side and 2550 for the front of the battery. Corresponding to these Reynolds values, the set of equations for natural convection were used to calculate the convective heat transfer.

As can be seen in equation (4-4), the battery internal temperature is required for the heat generation calculation. The core temperature was measured in another study (Niculuta, 2012) by internally inserting a thermocouple in a single experiment. The average between the core and surface temperatures was thus used as a constant in the reversible entropy heat term. This methodology is problematic because it does not consider the temperature difference between the core and the surface over time. However, a solution proposed for this issue was to estimate the internal temperature based on the temperature difference between the core and the battery`s surface obtained in the simulation.

Section 5.3 provides summarised results only for the Uphill, Flat, Charge, and Downhill cases in 40°C ambient temperature. The results for scenarios involving 25°C, 30°C, and 35°C are provided in Appendices A and B, including graphs and visual simulations.

5.3.2 Uphill Scenario

The simulation demonstrates the discharge from 90% to 10% SOC within 78 min on average for the single cell Uphill scenario. As was in the experiment, the simulation is conducted in 25°C, 30°C, 35°C, and 40°C, with currents of 44.3 amperes, 44.3 amperes, 43.7 amperes, and 44.2 amperes used in each case respectively. After the discharge process, the battery temperature gradually decreases until it again reaches the thermal equilibrium within the test chamber again. This response reflects what would be expected in the actual case.

The results of the FEM simulation are presented in Figure 5-3 below. It presents the surface temperature distribution after discharging at the ambient temperature of 40°C. The temperature

difference between the side and the front surfaces is negligible, but there exists a temperature difference of 1°C between the upper section, where the air gap is located, and the lower section, where the core is located. The figure also presents the heat generated by the battery terminals inside the air gap. The copper terminal, located at the internal top right, has a higher surrounding temperature than the aluminium terminal at the internal top left, since the copper material has higher thermal conductivity.

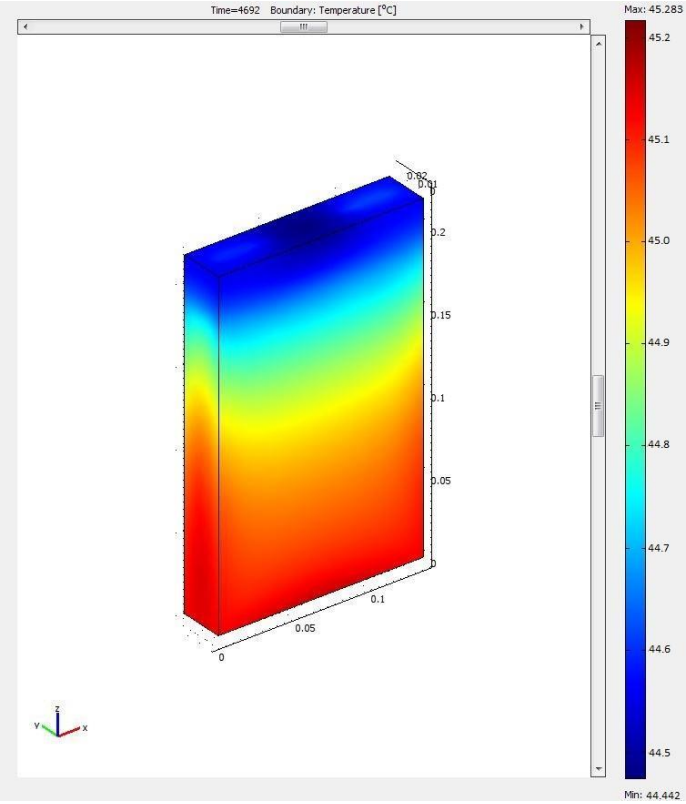

Figure 5-3: Final visual simulation of the temperature distribution along the external battery surface for 44.2A discharging. Total running time of 78 minutes.

Figure 5-4 presents the observed temperature distribution of the cell during the period of peak heat generation (5 W) at the completion of the process for the Uphill condition at 40°C, resulting in an

average of 1.45W. As well, the mean value increases consistently in heat loss at an average of 0.50W/cell[2].

Figure 5-4: Experimental temperature distribution on the external battery surface for 44.2A discharging. Total running time of 78 minutes.

In Figure 5-5, the heat loss result is approximated using a 6th degree polynomial fit. This provides a smoothed result minimizing the effects of the chamber temperature fluctuations.

[2] The thermal image presents a region with lower temperature in the upper right side, which is the result of the insulation tape not being attached directly to the surface on the cell. This tape is holding the thermocouple in place and that does not mean that the temperature surface is reduced on the surface of the battery in this region.

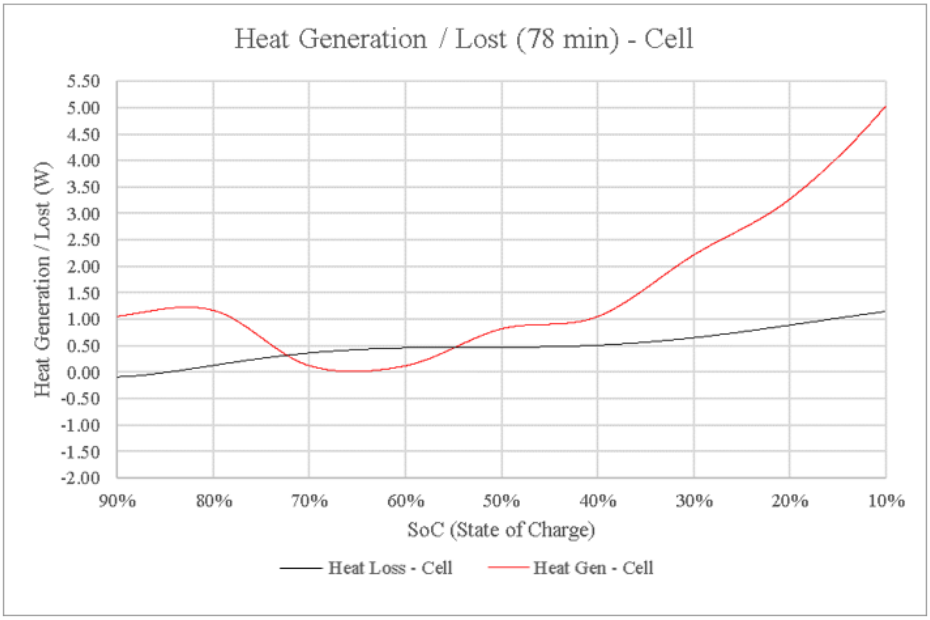

Figure 5-5: Experimental Heat generated and lost during battery discharge for the Uphill condition.

It was observed that the lower portion of the cell, particularly the sides and the base, produced the highest temperature in the cell as presented in Figure 5-3, this result is in agreement with what was observed in the experimental case (Figure 5.4). A cooler portion was also observed in the top section of the battery which coincided exactly with the position of the air gap, see Figure 3-18. Knowing that the temperature distribution around the cell is not homogeneous, the temperature curve described in Figure 5-6 is related to the weighted arithmetic mean of the temperature from each thermocouple in relation to the area of the surrounding region as pointed out in Figure 3-22. According to the simulation, the battery cell surface temperature ranges from 45.3°C to 44.4°C at the completion of the process. The average temperature for the whole simulation varies within a 6°C range, independently from the chamber temperature, during the Uphill discharging process.

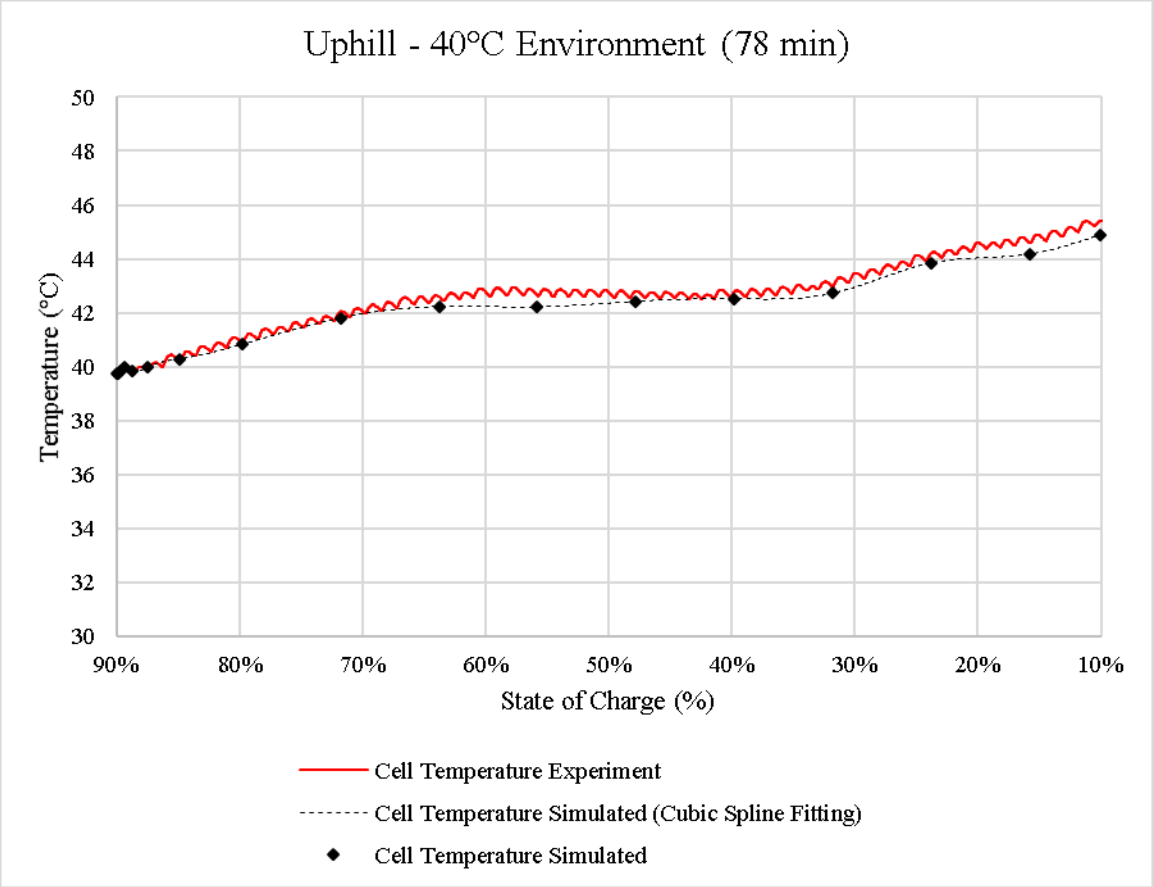

Figure 5-6: Simulated temperature and Experimental temperature obtained at the centre of the front face during Uphill discharging at 40°C.

As explained earlier, because the temperature inside the chamber oscillates around a mean value, this also affects the temperature of the surface of the cell (Figure 5-6). Nevertheless, since the frequency for the temperature variation is sufficiently high in comparison to the experiment length, the result is not compromised.

The most significant impact on heat generation from the battery pack is the Ohmic Heating term equation (4-4). This term is the magnitude of the heating produced during battery charging or discharging which then impacts the current level and creates the difference between voltage and open voltage (Figure 5-7). Consequently, the overall impact of the reversible Entropic term is almost negligible. The average Ohmic Heating term is 1.52W on average, while the Reversible Entropic term

is -0.06W on average (Figure 5-8). However, the Reversible Entropy term has the most significantly long-term impact on the total heat generation.

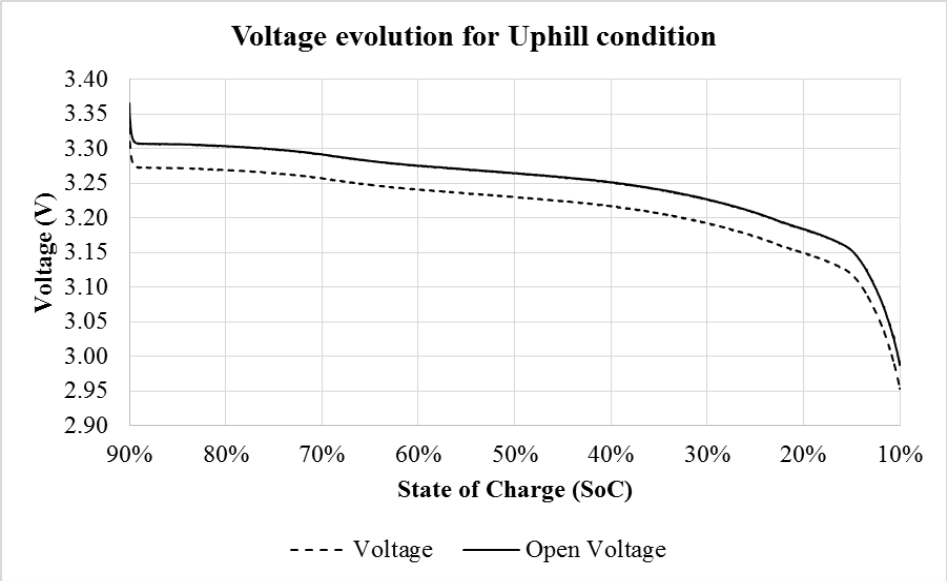

Figure 5-7: Voltage and Open-voltage during Uphill discharging at 40°C.

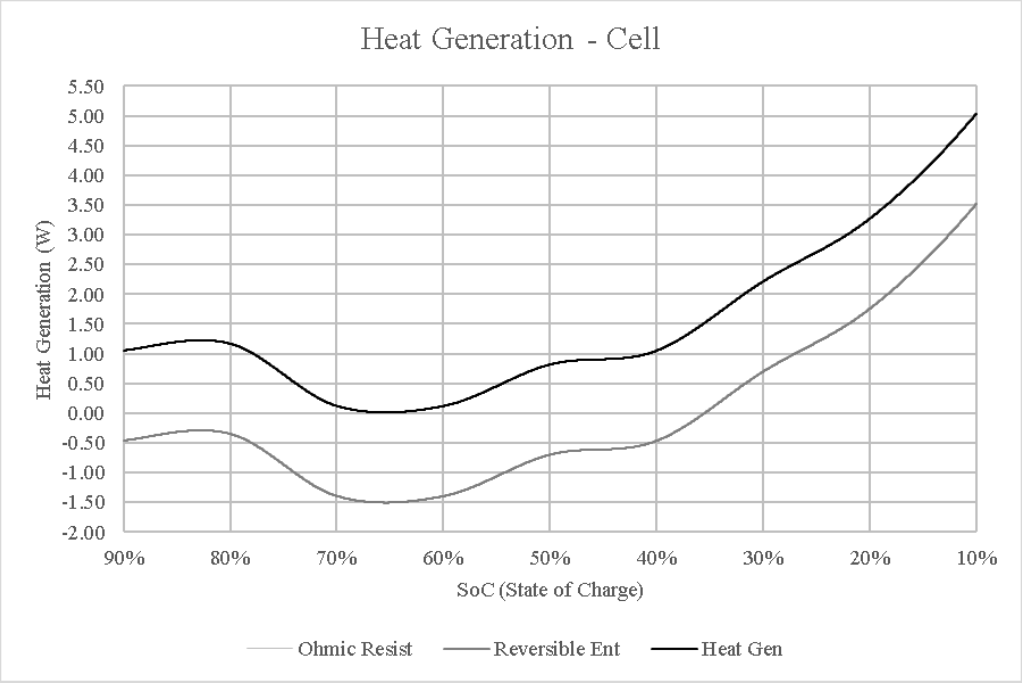

Figure 5-8: Heat generation Comparison between the Ohmic Heating term and the Reversible Entropic term for Uphill 40°C.

5.3.3 Flat scenario

The Flat condition (representing the battery duty while the EV is driving on flat ground) requires approximately 205 minutes to discharge from a state of charge of 90% to 10%. The experiment was conducted in ambient temperatures of 25°, 30°C, 35°C, and 40°C with average discharge currents of 17.3 amperes, 16.9 amperes, 16.9 amperes and 16.7 amperes respectively. Figure 5-9 shows the thermal distribution on the surface of the battery cell at the completion of the process, which is considerably more homogeneous than the last scenario, having a maximum surface temperature variation of 0.5°C. As for Figure 5-10, it presents the temperature distribution over the battery surface at the end of the process.

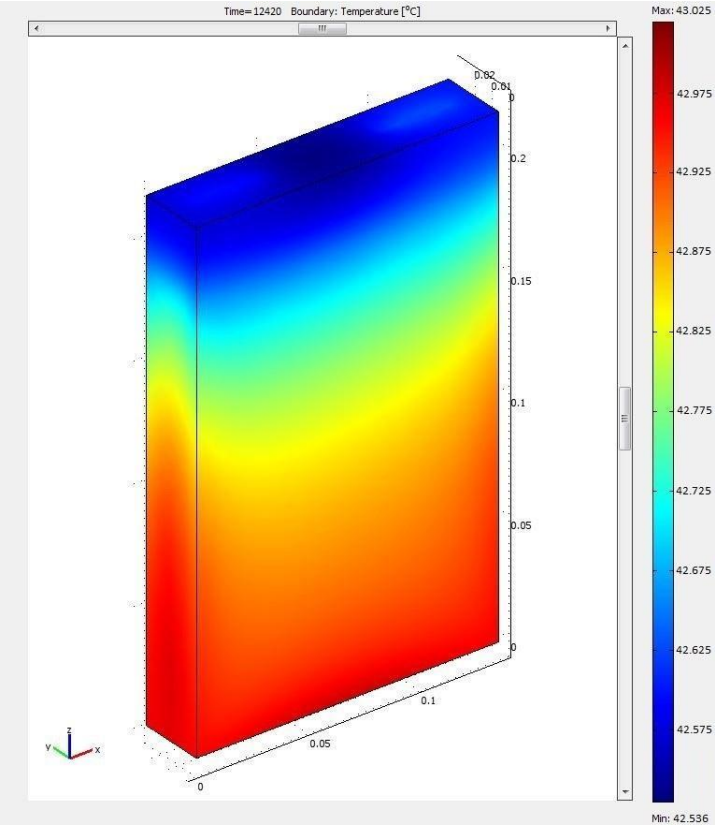

Figure 5-9: Final visual simulation of the temperature distribution along the external battery surface for 16.9A discharging. Total running time of 205 minutes.

Figure 5-10: Experimental temperature distribution on the external battery surface for 16.9A discharging. Total running time of 205 minutes.

The maximum heat generated at the completion of the process is almost 1.5W, which is nearly 0.4W of heat loss. However, the average value for the whole process is 0.16W of heat generated and 0.15W of heat lost (Figure 5-11). The heat accumulation, less than in the Uphill condition, produces a reduced temperature increment of 3.5°C (Figure 5-12).

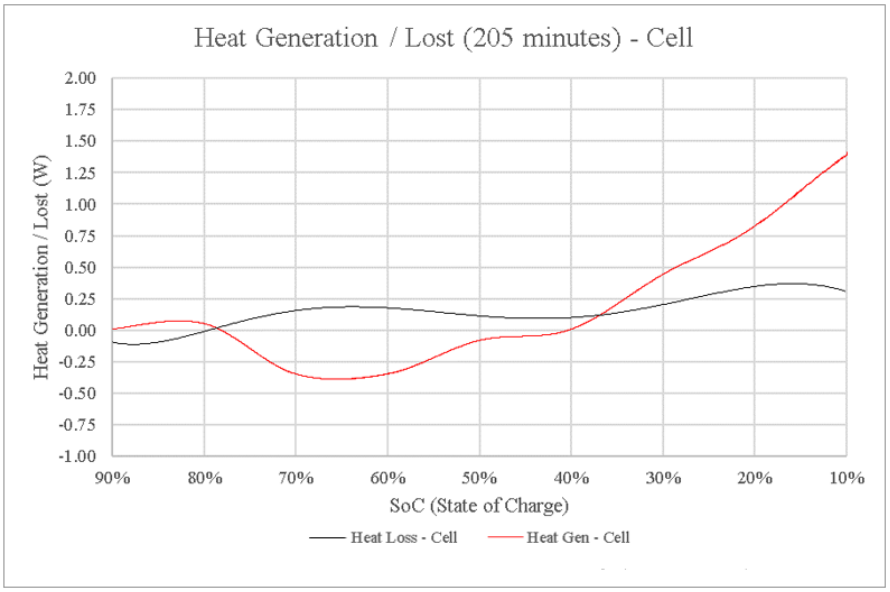

Figure 5-11: Experimental Heat generated and lost during battery discharge for the Uphill condition.

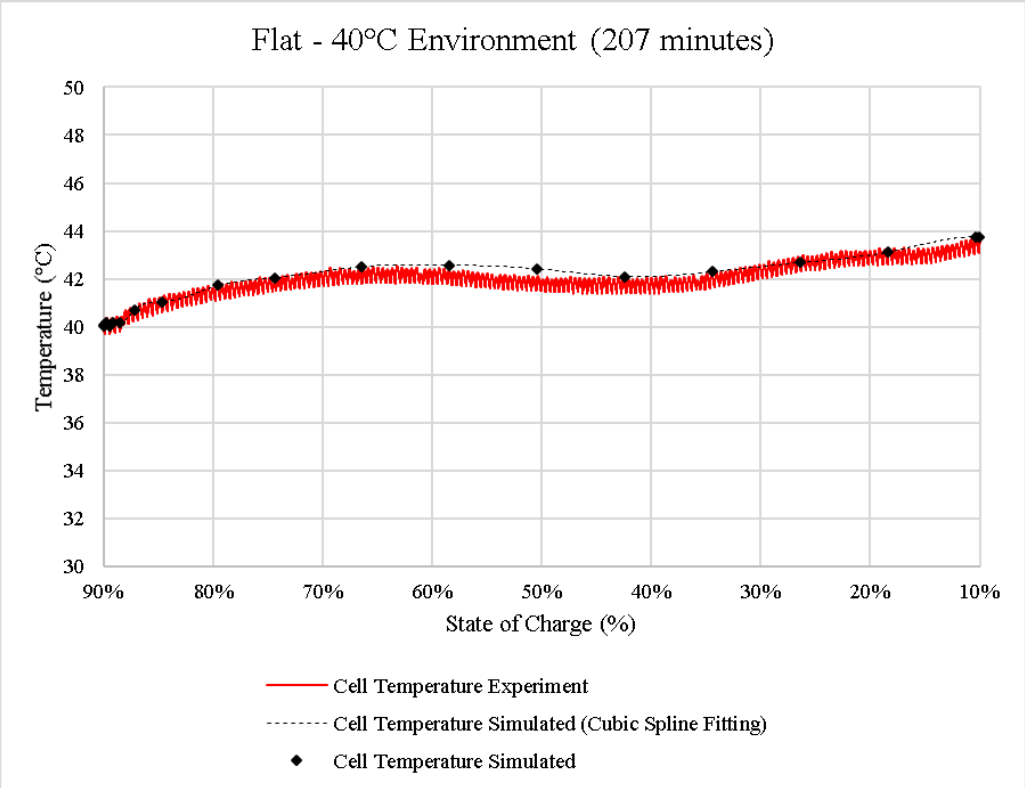

Figure 5-12: Simulated temperature and Experimental temperature obtained at the centre of the front face during flat discharging at 40°C.

The temperature decreases during the middle of the process as seen in the temperature curve in Figure 5-12, unlike in the previous case when the temperature remained constant between 60% to 40%. This results in a negative heat generation of 80% to 40% SoC. The final average cell temperature is approximately 43.3°C in the experiment and 43.75°C in the simulation, which shows that both methods provide similar results (Figure 5-12).

5.3.4 Charging scenario

The for the batteries used in this work, the charging process typically required 195 minutes to be completed from 10% to 90% SoC. The Charging scenarios are conducted in 25°C, 30°C, 35°C, and 40°C using currents of 16.7 amperes, 16.5 amperes, 18.4 amperes, and 17.8 amperes respectively. The

variations in these charging currents are due to imprecisions in the charging rate selection at the power supply. Figure 5-13 presents the surface temperature distribution at the completion of this scenario. The distribution varies within the range of approximately 1°C. Even though the Charging and Flat processes have similar current rates 39.5% more heat is generated and 41.1% more heat is lost on average during the charging process. Figure 5-14, it presents the surface temperature distribution over the battery surface at the end of the process.

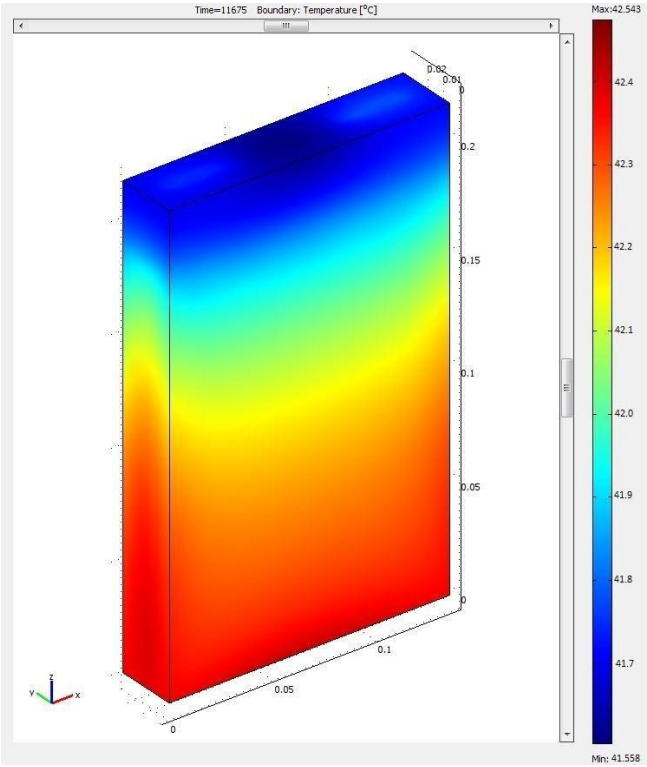

Figure 5-13: Final visual simulation of the temperature distribution along the external battery surface for 16.7A discharging. Total running time of 195 minutes.

Figure 5-14: Experimental temperature distribution on the external battery surface for 17.8A discharging. Total running time of 195 minutes.

During this process, heat generation reaches a peak at approximately 65% SoC with 0.84W (Figure 5-15), as well as a maximum mean heat loss average of 0.4W. Average heat generation and heat lost is 0.23W and 0.22W respectively. Even though heat generation is considerably higher in this scenario than the Flat discharge case, the temperature difference in the experiment reached a peak of 2.5°C (see Figure 5-17). Figure 5-16 shows the curve for the difference between the open circuit voltage and the nominal voltage. This difference is an important component in the Ohmic Heating term in equation (4-4). Comparing Figure 5-7 to Figure 5-16, the voltage difference is considerably reduced in the case of the charging mode. This difference may be a result of the current level used in the experiment.

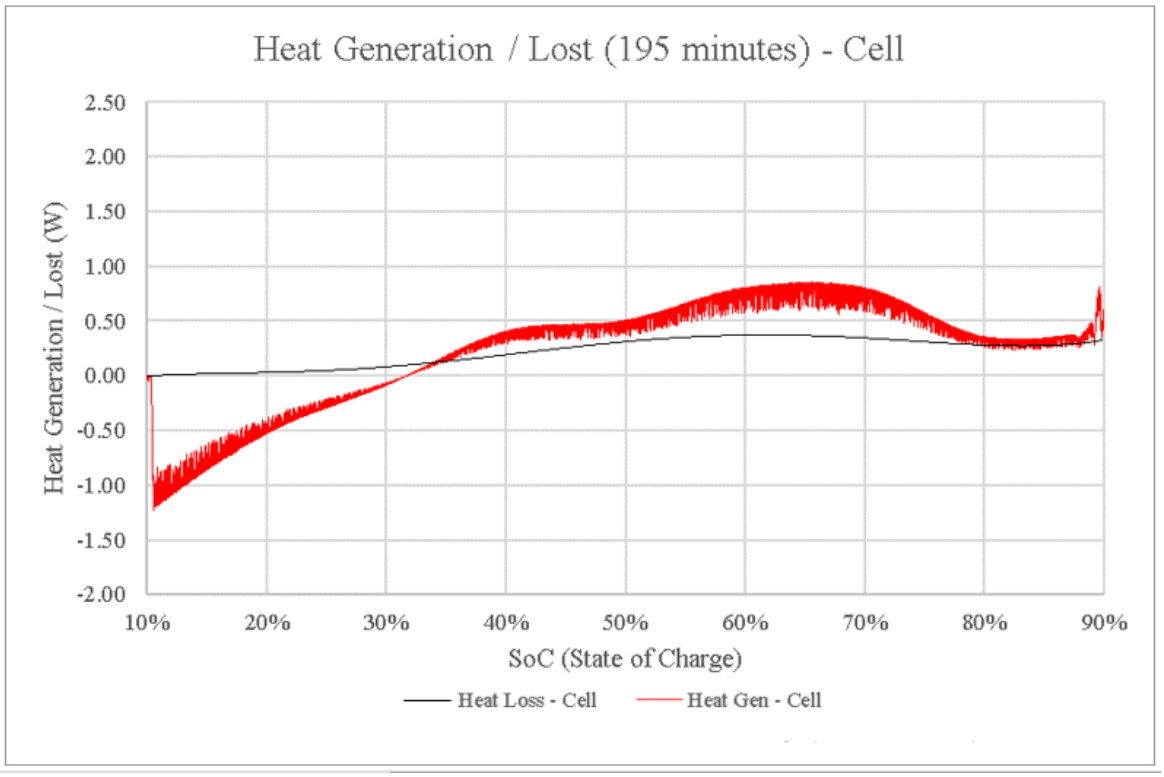

Figure 5-15: Experimental heat generated and lost during battery charging for the charge condition.

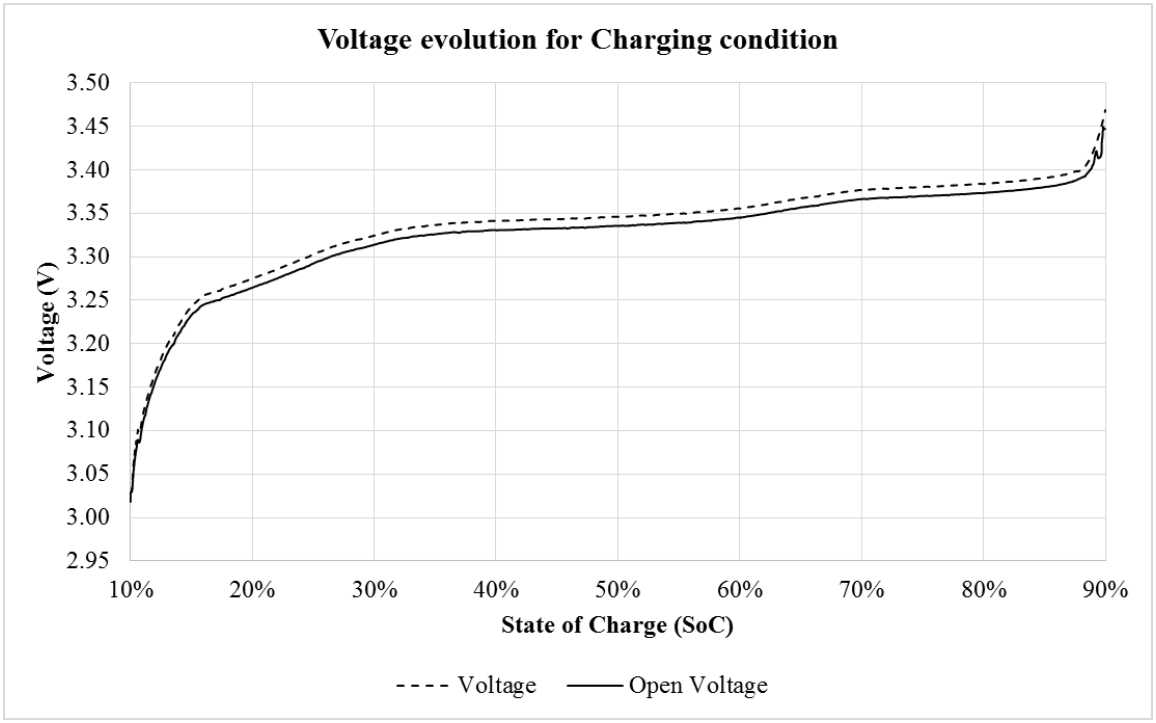

Figure 5-16: Voltage and Open-voltage during charging at 40°C.

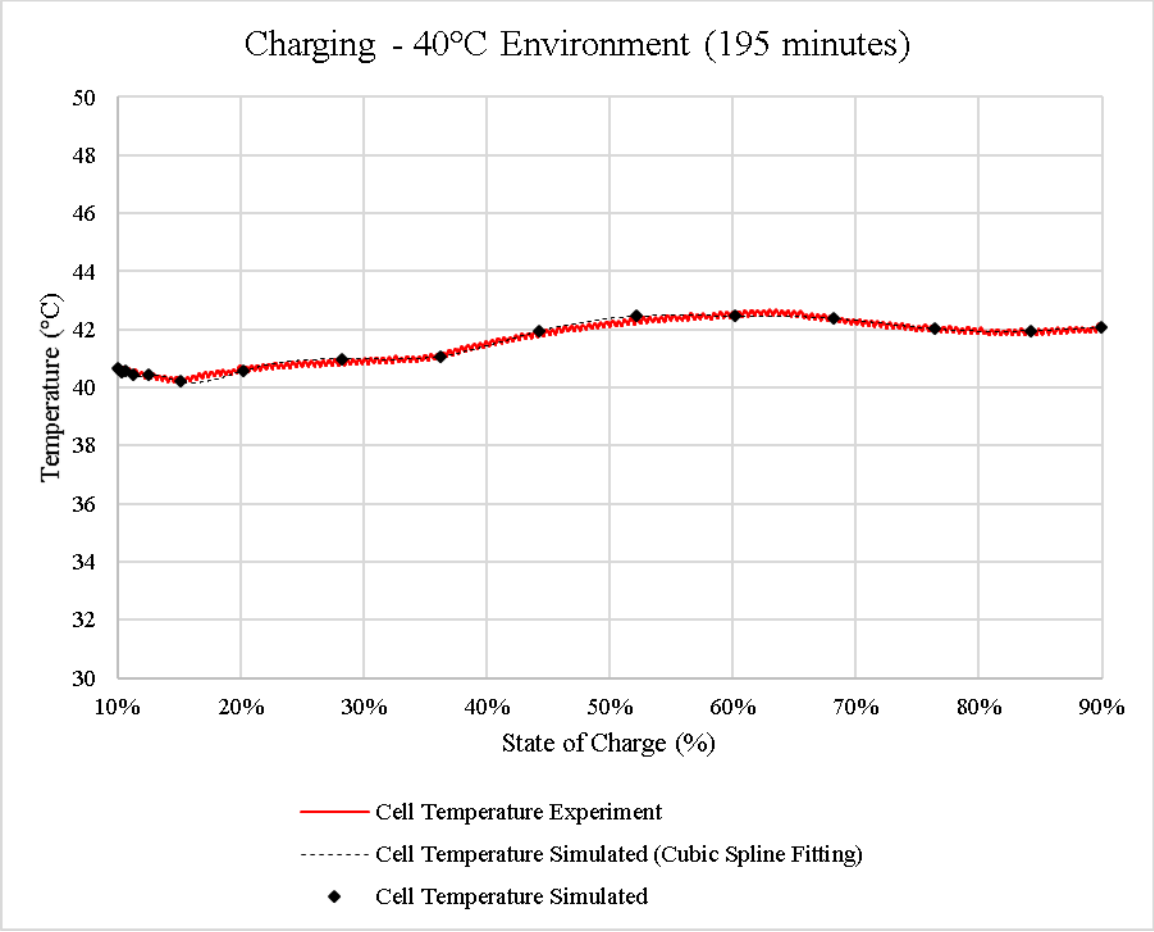

Figure 5-17: Simulated temperature and Experimental temperature obtained at the centre of the front face during charging at 40°C.

5.3.5 Downhill scenario

As mentioned before, in electric vehicles downhill driving charges the battery pack through the regenerative braking system. This process requires 114 minutes on average to be completed (to charge a battery from a SOC of 0% to 100%). The experiment was conducted in 25°C, 30°C, 35°C, and 40°C with currents of 30.9 amperes, 31.0 amperes, 31.0 amperes, and 31.0 amperes. In Figure 5-18, the maximum temperature gradient is 0.5°C, which is lower than the previous case, where the temperature reaches 1°C during charge since the experiment length is only half the charging time. The temperature distribution in the lower portion of the cell, including the lower sides and bottom, is similar in all the

ambient cases. On the upper portion however, the aluminum and copper connectors create a different heat pattern. As for Figure 5-19, it presents the temperature distribution over the battery surface at the end of the process.

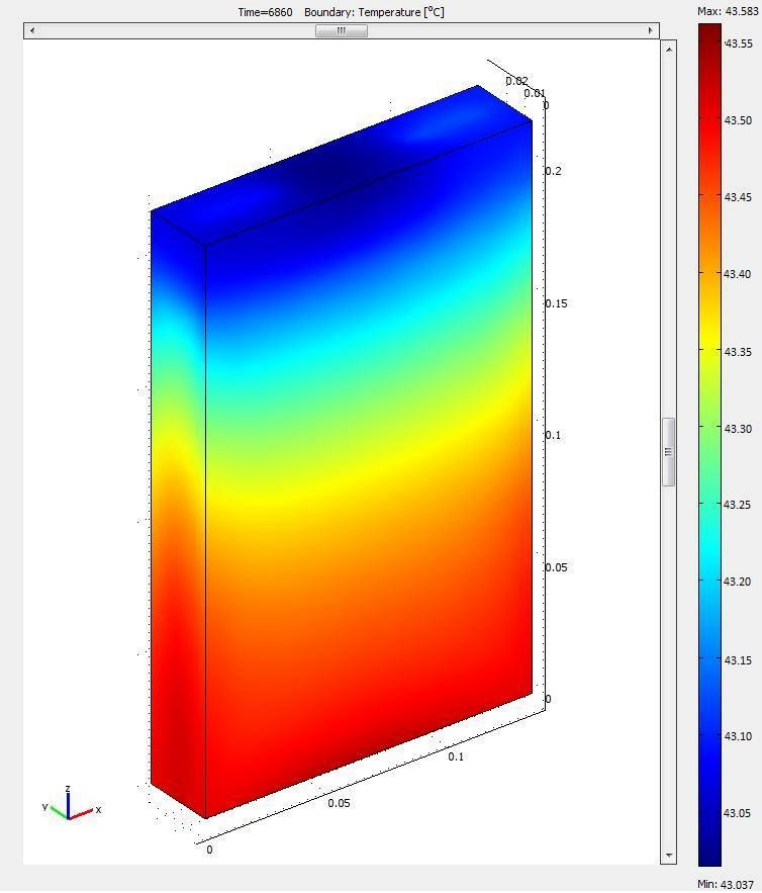

Figure 5-18: Final visual simulation of the temperature distribution along the external battery surface for 31.0A charging. Total running time of 114 minutes.

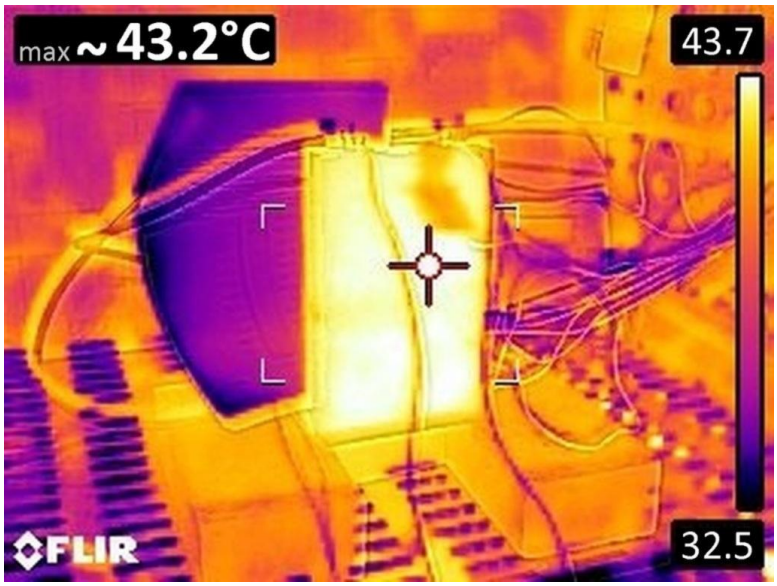

Figure 5-19: Experimental temperature distribution on the external battery surface for 31.0A charging. Total running time of 114 minutes.

The heat generation reaches maximum peak at 65% SoC with 1.67W (Figure 5-20), two times higher than during the charging, while the maximum heat loss decreases to 70% SoC with 0.5W. The maximum temperature difference between the beginning and the completion of the experiment is 3.5°C (Figure 5-21), 1°C higher than during Charging mode. In both Charging and Downhill modes, the heat generating term commences as a negative number and increases over time. This results in a delay in the temperature increase on the battery surface.

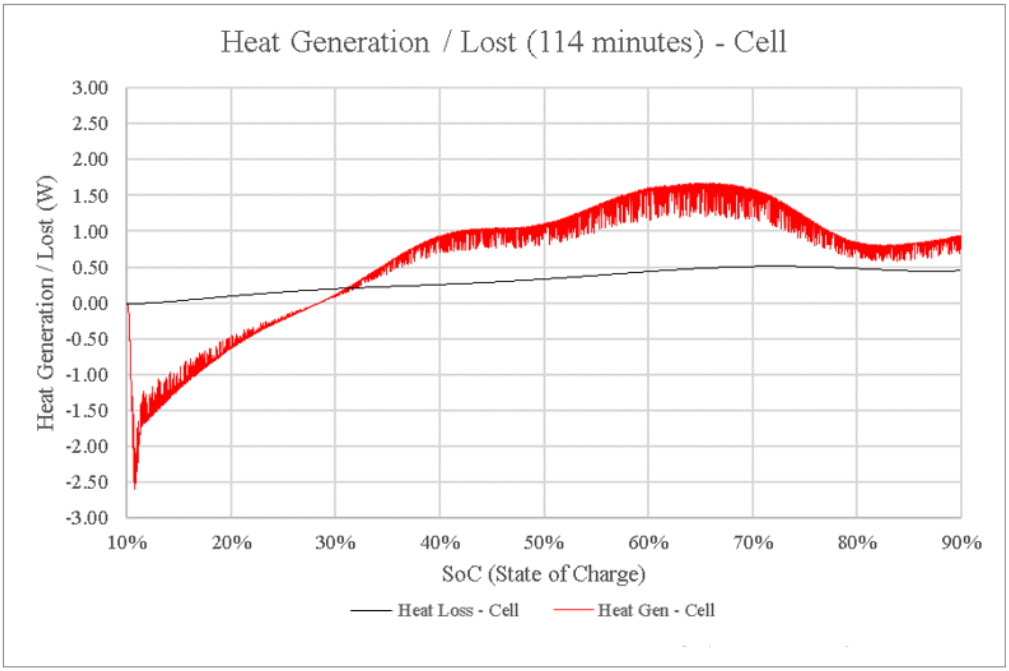

Figure 5-20: Experimental Heat generated and lost during battery charging for the Downhill condition.

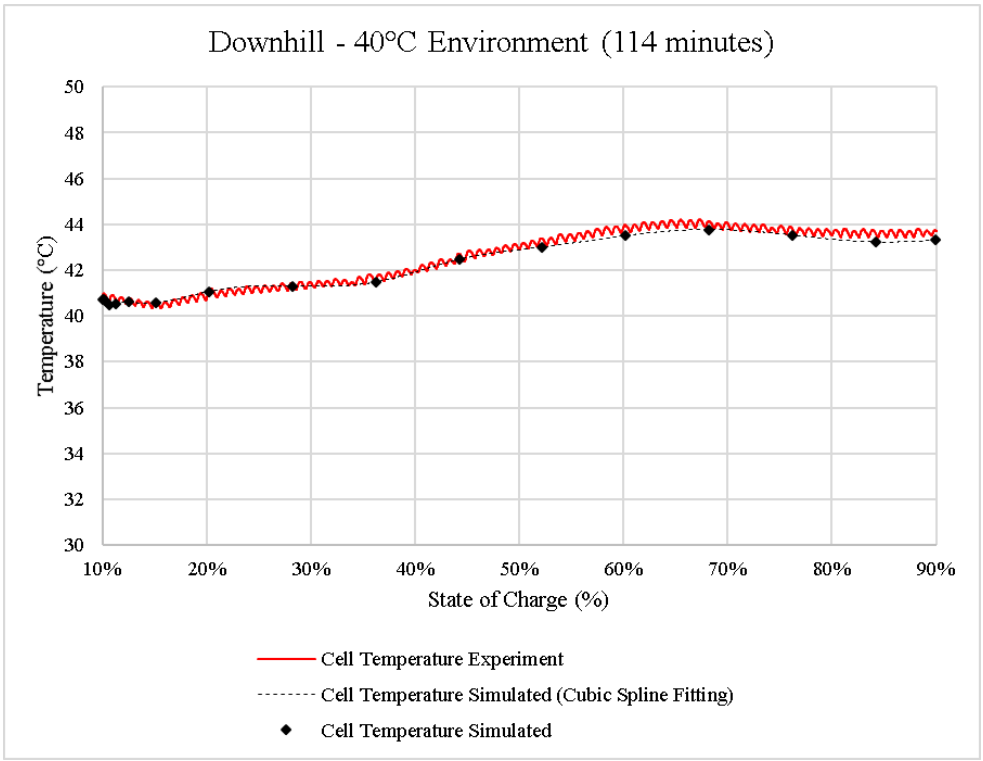

Figure 5-21: Simulated temperature and Experimental temperature from the centre of the front face during downhill charging at 40°C.

5.3.6 Single cell – Conclusion

The previous section regarding the single cell case presented results for the discharging and charging conditions for 40°C ambient temperature. Here, Table 5-1 summarises all the results obtained for the single cell study case for the other ambient temperatures (25°C, 30°C, 35°C and 40°C). The Charging, Downhill, Flat, and Uphill modes used current averages of 17.3 amperes, 29.4 amperes, 16.9 amperes, and 44.1 amperes and generated heat of 97.3 W, 251.9 W, 58.9 W, and 564.1 W respectively. Based on the results presented in Table 5-1, and Figures 5-22 until 5-25, the current level impacts battery cell heat generation. By contrast, the environment temperature does not significantly impact heat generation.

Table 5-1: Average Heat lost and generated from the battery pack for each environment temperature.

Parameter	**25°C**	**30°C**	**35°C**	**40°C**	**Scenario**
Heat Gen (W)	580.7	586.5	506.8	582.6	Uphill
Heat Loss (W)	199.4	176.1	126.3	199	
Current (amp)	44.3	44.3	43.7	44.2	
Heat Gen (W)	57.8	56.5	55.7	65.5	Flat
Heat Loss (W)	54.7	50.7	50.1	60.5	
Current (amp)	17.3	16.9	16.9	16.7	
Heat Gen (W)	104.9	94	97.4	93.2	Charging
Heat Loss (W)	99.2	88.2	91.7	87.7	
Current (amp)	16.7	16.5	18.4	17.8	
Heat Gen (W)	265.8	241.9	252.8	246.9	Downhill
Heat Loss (W)	158.3	165.7	166.2	125.6	
Current (amp)	29.7	28.4	29.8	29.8	

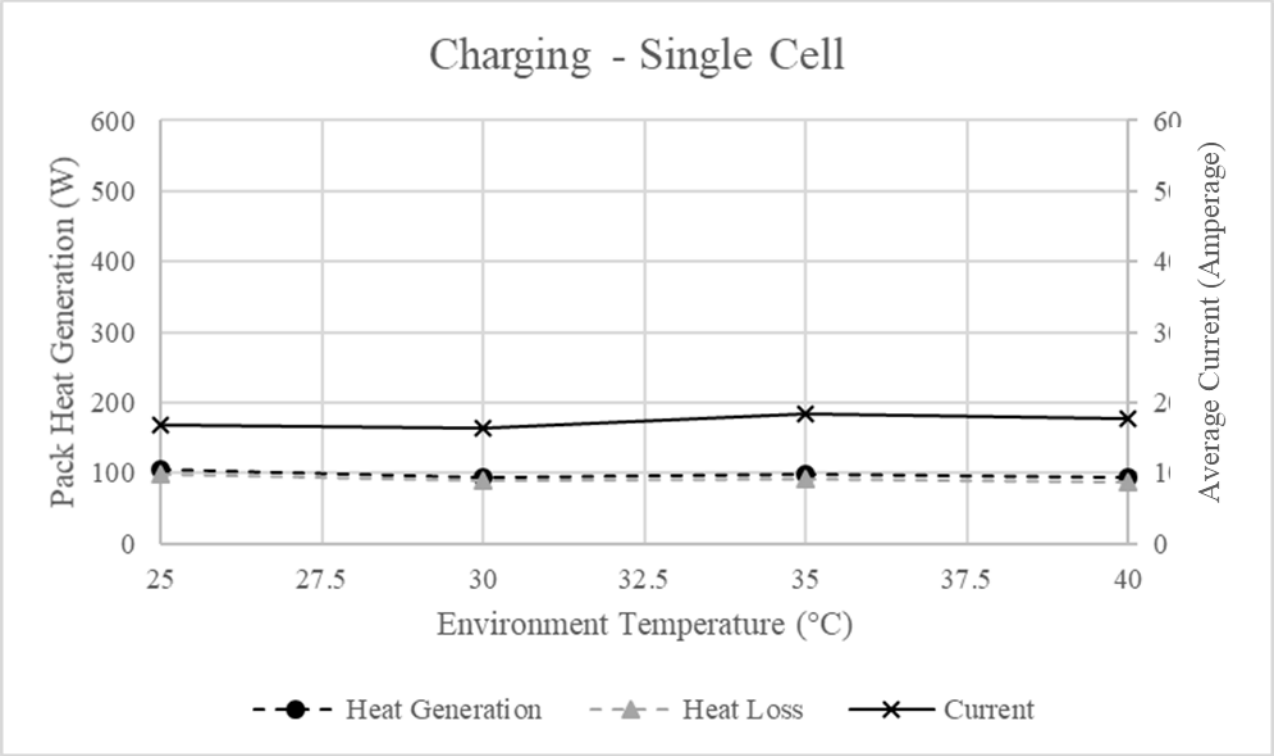

Figure 5-22: Average current and pack heat generated during Charging mode.

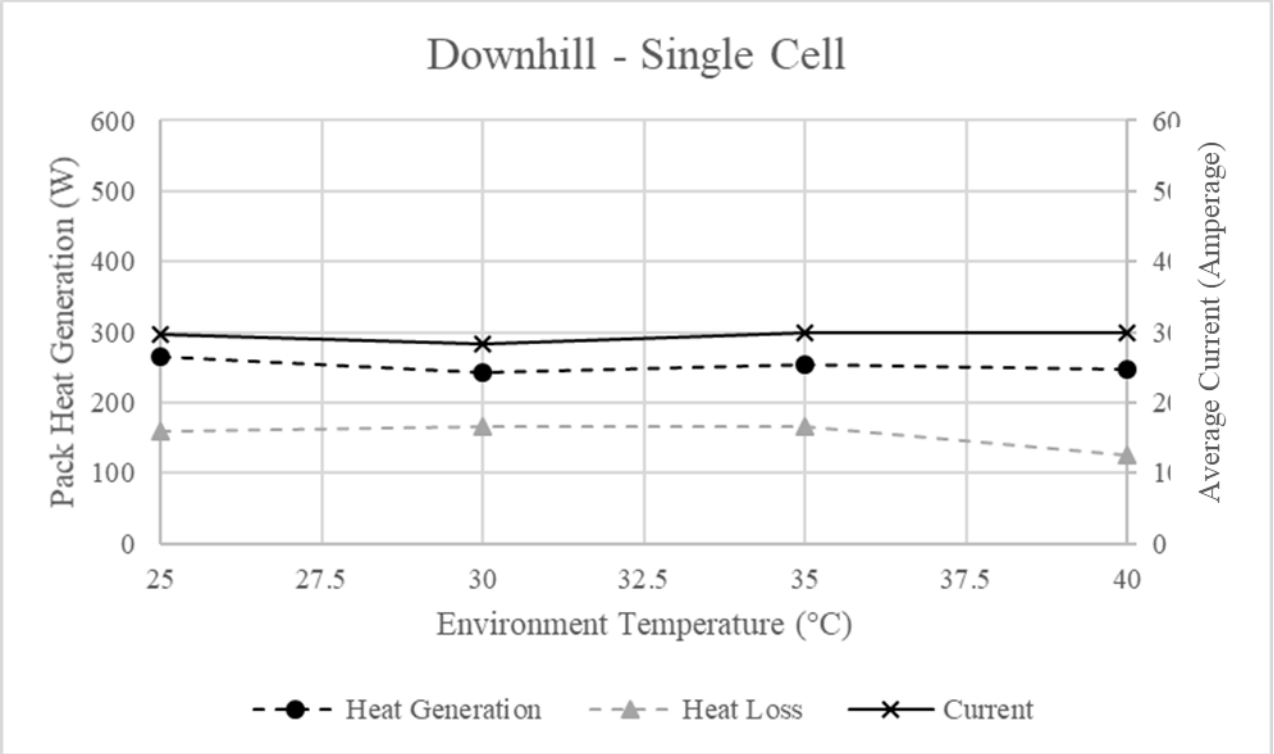

Figure 5-23: Average current and pack heat generated during Downhill mode.

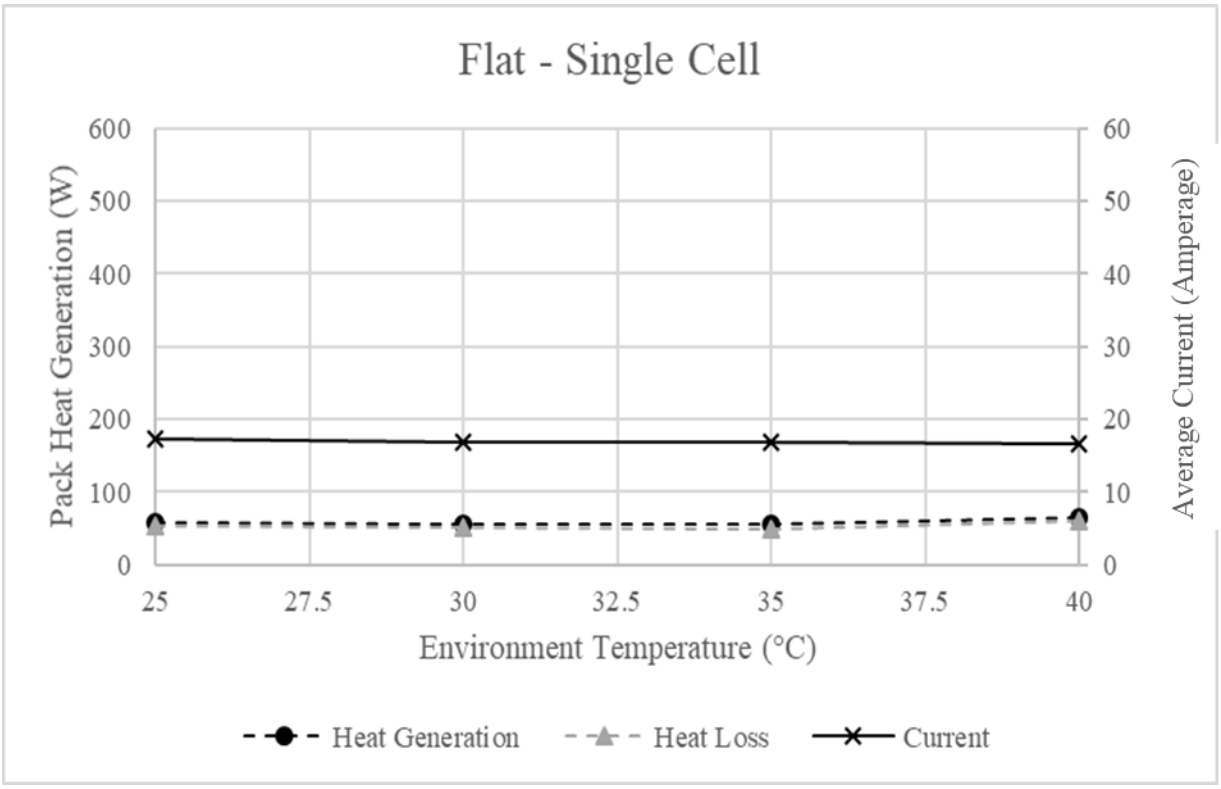

Figure 5-24: Average current and pack heat generated during Flat mode.

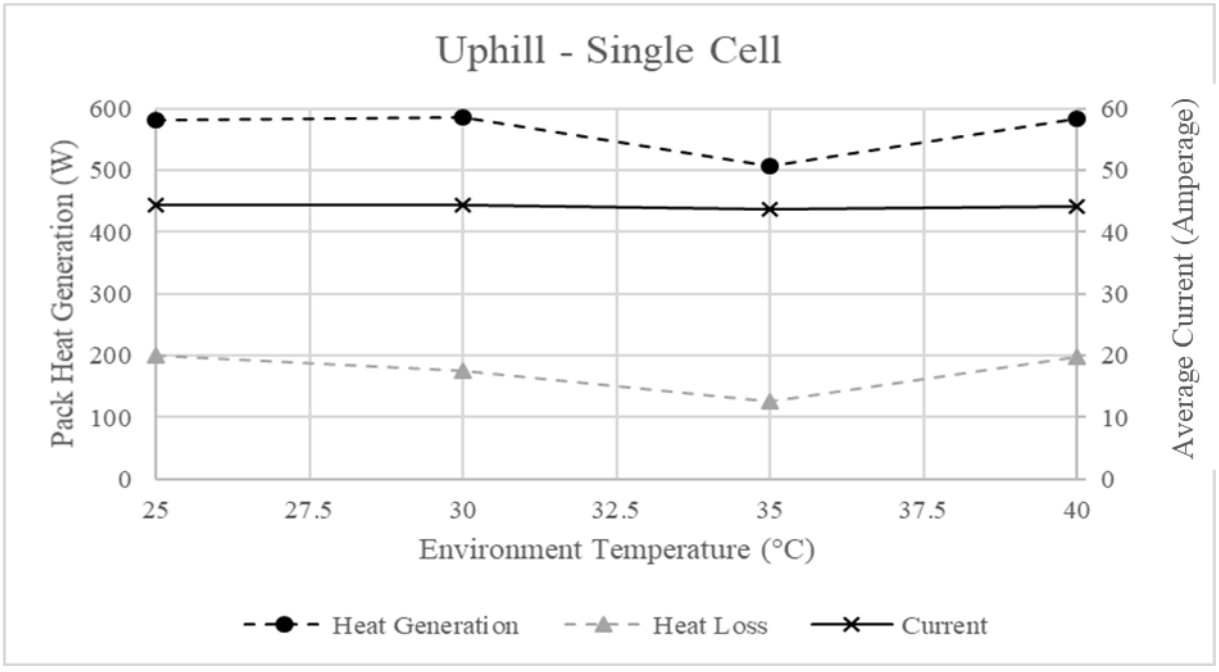

Figure 5-25: Average current and pack heat generated during Uphill mode.

In the discharging cases, increasing the current by 2.6 times (from 16.9 amperes in the Flat scenario and 44.1 amperes in the Uphill case) also increases the average heat generation by 9.6 times (from 58.9 W to 564.1 W for the whole pack). An increment of 70% in the absolute magnitude of the current from the Charging to the Downhill mode increases heat generation by 2.6 times. Furthermore, the charging process generates 1.65 times more heat even though, in absolute numbers, the current for charging is 1.02 times higher than that used during discharging Flat.

As can be seen in Table 5-1, the environmental temperature has limited effect on heat generation in Lithium-iron Phosphate battery cells because of the magnitude of the environmental temperature. Instead, the gap between voltage and open circuit voltage, the current level used, and the chemical reaction inside the core all contribute considerably more to heat generation. The strongest impacts though on heat generation are the values of the current and the difference between the battery voltage and the open-circuit voltage equation (4-4). Typically, an increase in the current level increases the difference. In the Charging, Downhill, Flat, and Uphill cases, these differences are typically 0.012V, 0.020V, 0.009V and 0.033V respectively.

The current level also indirectly affects heat loss by increasing the amount of heat transferred from the core to the outer layers. The speed of heat propagation from the core of the cell depends on the heat capacity (1350 J/kgK) and the thermal conductivity in the *y* direction (1.145 W/mK), as seen in Figure 3-18. However, since thermal conductivity in the *xz* directions is higher (23.9 W/mK), heat tends to flow more easily in these directions. The difference between the heat loss and the heat generated causes heat to accumulate inside the battery. Thus, heat will continuously be released into the environment after the charging or discharging process is completed.

5.4 Module Analysis

For the multi-cell battery module, 15623 tetrahedral elements were used in the mesh to describe the cross-sectional 2D plane as presented in Figure 5-26. The mesh is refined in the areas representing the case and the air gap between each cell. Each cell is modeled with the core in the middle, the aluminum case around it, and an air gap between the cells. Around the cell, it is assumed that convection and radiative heat can occur[3].

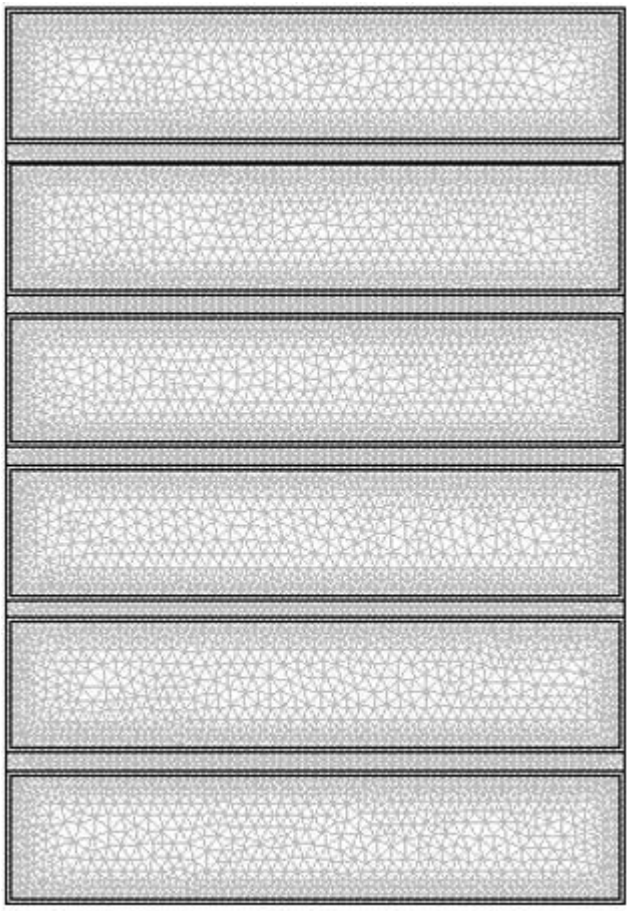

Figure 5-26: Mesh Distribution for the CAD multi-cell model.

[3] For further information about the mathematical Heat Transfer and Heat Generation equations used in the FEM in each domain of the model, and boundary conditions, see Chapter 4.

The results for the heat generation study of the module are reported for the case of Uphill 40°C, since overall, the findings in this section are somewhat similar to the ones for the single cell case. In the Commander 5 EV, each module has eight Lithium-iron Phosphate cells connected in series. Due to the limitations of the number of cells available for the experiment, six cells instead were connected in series. In the vehicle, a total of fifty modules are used, which are distributed between the front and back of the machine. The use of modules allows for convenient maintenance. Since the computer which runs the simulations has limited memory capacity, a 2D model is used to run the simulations instead of a 3D model. The simulation uses the meridional cross section plane of the module, which is located halfway down from the top of the battery cell. This region has not got the highest temperature of the cell surface, which instead is more likely to be observed in the lower part of the cell due to the core location. The model is designed with a 4mm thick air gap between each cell. The simulation inputs, as seen in Figure 5-1, come from the data collected during the experimental phase. One of these parameters is the surface temperature, which is obtained using thermocouples located on the center of each cell face.

The Uphill 40°C operating mode was chosen for the module simulation since this condition resulted in the highest heat generation for the single cell case. For the other scenarios, see Appendix B. Moreover, due to limitations of the power supplies and resistor load bank, the module was charged and discharged with slightly different currents than the ones used during the single cell experiment. The currents used were on average 16.5 amperes (4.9% higher), 31.0 amperes (5.3% lower), 16.8 amperes (0.7% higher), and 41.0 amperes (7.2% lower), and they are referred to charging, Downhill, flat, and Uphill.

The widest temperature difference on the surface of the module in the Uphill 40°C scenario was observed to be approximately 1°C. As expected, the highest temperatures are reached in the cells located in the interior of the module. The virtual model accurately presents these temperature results

obtained from this experiment (Compare Figure 5-27, Figure 5-28, and Figure 5-29). The temperature is increased by 3°C during the experiment as can be seen in Figure 5-28. In this scenario, heat generation reached a peak of 4.22W/cell and an average of 1.29W/cell (Figure 5-29).

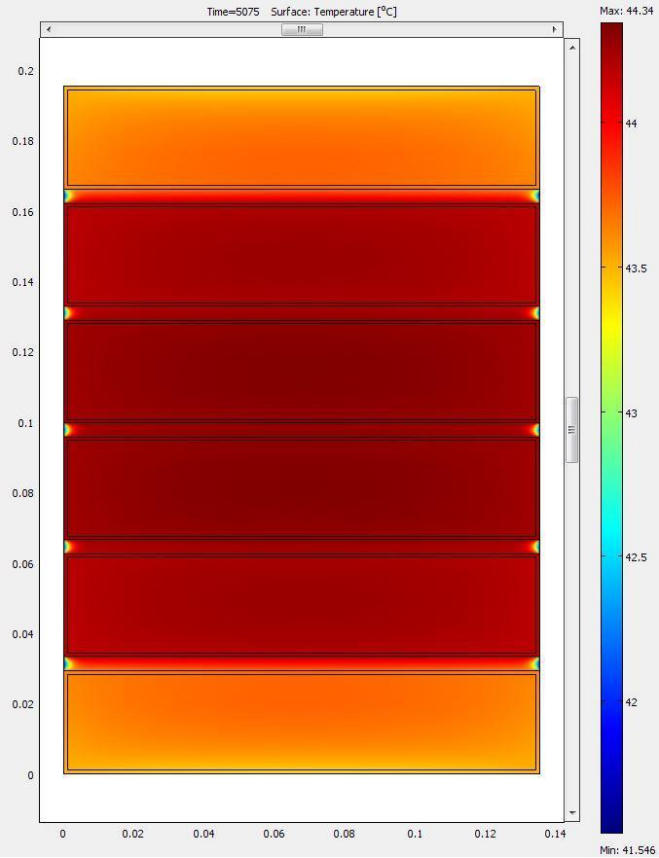

Figure 5-27: Temperature distribution in the meridional section of the module during Uphill operation at 40°C.

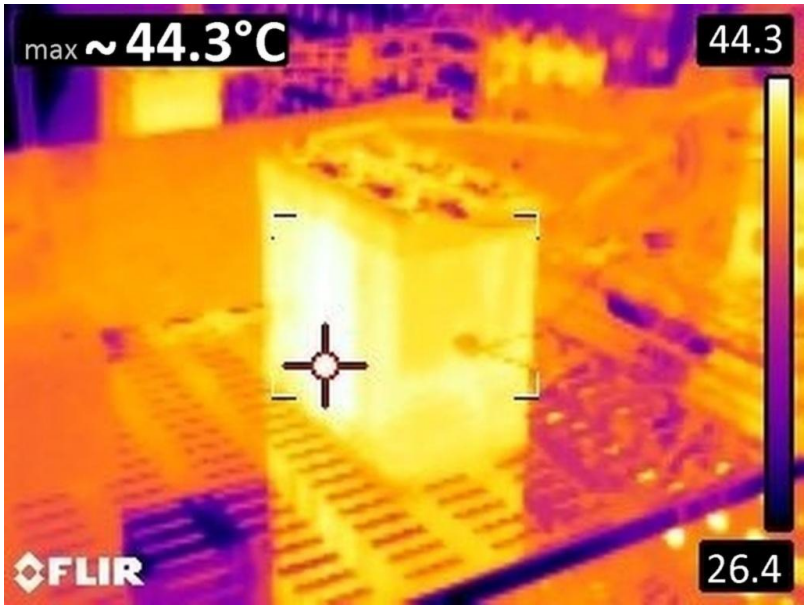

Figure 5-28: Experimental temperature distribution on the module during Uphill operation at 40°C.

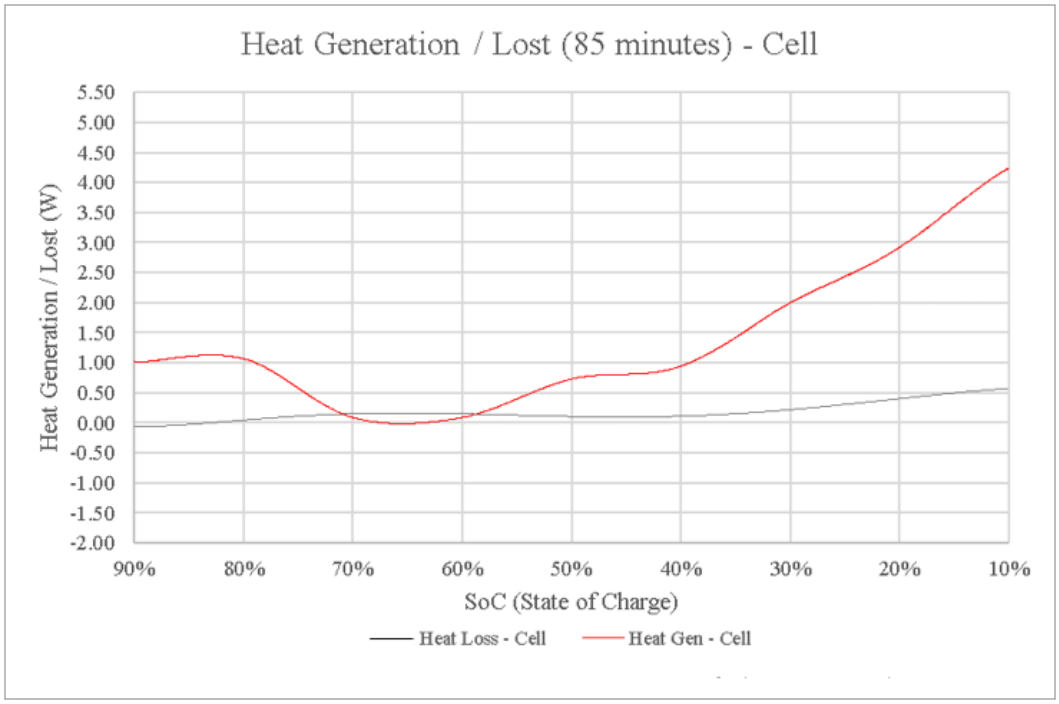

Figure 5-29: Experimental Heat generated and lost during module discharging calculated per cell for the Uphill condition.

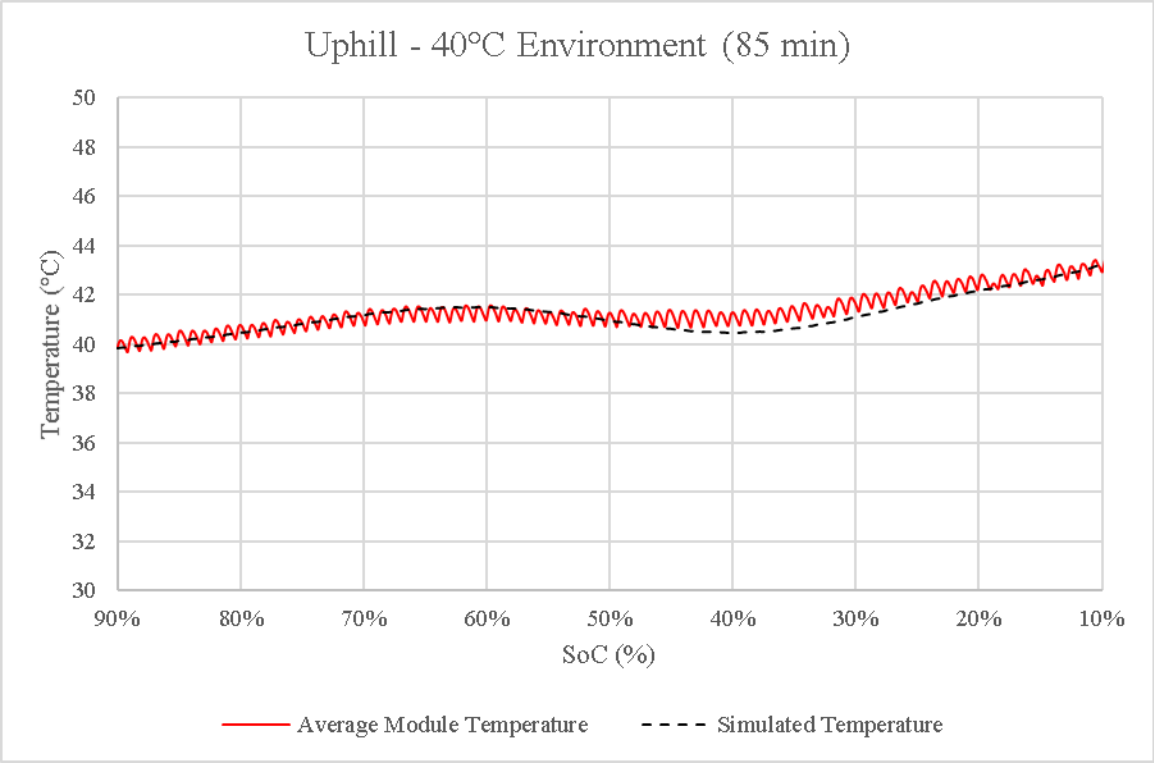

Figure 5-30: Simulated temperature and Experimental temperature discharging at 40°C.

Table 5-2 presents the average heat generated and lost calculated during the experiment in each scenario fusing the modules.

Table 5-2: Average Heat lost and generated from the battery pack for each environment temperature.

Parameter (module)	**25°C**	**30°C**	**35°C**	**40°C**	**Scenario**
Heat Gen (W)	546.5	569.5	527.7	517.7	Uphill
Heat Loss (W)	137.2	110.1	87.4	71	
Current (amperes)	41.1	41.1	40.9	40.9	
Heat Gen (W)	56.2	55.8	55.5	55.7	Flat
Heat Loss (W)	21.7	27	6.2	6.9	
Current (amperes)	16.8	16.8	16.8	16.8	
Heat Gen (W)	80	80.3	80.2	80.9	Charging
Heat Loss (W)	56.5	41.8	42.3	34.7	
Current (amperes)	16.5	16.5	16.5	16.5	
Heat Gen (W)	276.6	264.4	263.1	256.5	Downhill
Heat Loss (W)	130.1	125.5	99.4	103.4	
Current (amperes)	30.9	31	31	31	

The results contained in Table 5-2 confirm that charging processes typically generate more heat than discharging processes that proceed at the same rate, and that the heat generated is not considerably influenced by the ambient temperature. Furthermore, even though heat is generated at the same level as in the single cell case, heat loss is lower since the cell is covered with black tape which increases emissivity of the cells.[4]

5.5 Estimation of Overall Machinery Heat Generated

This section calculates the heat emission from each component in the electric vehicle (Commander 5EV), except for the battery pack, which is evaluated in depth in Chapter 4. The major heat emitting components that are evaluated include two electric motors, two motor controllers, a hydraulic motor (which controls the steering and the brakes), a motor controller for the hydraulic pump, a DC/DC converter, and two chargers. The vehicle also includes an enclosed cab with a heat and air conditioning (HVAC) which, in addition to being responsible for creating a comfortable environment inside the cab, is also required for the cooling system. Heat losses from these components is presented in Figure 2-8, except for the charger and electric motors. This current study also assumes the idle losses to be zero, even though there is a small drive shaft connecting the electric motor to its respective driving axle.

Electric motor losses are correlated to internal frictions between the movable parts and to the electric losses (based on $P = I^2R$). These losses can be summarized into the electric motor efficiency curve provided by the manufacturer, see Figure 5-31.

[4] Black tape was used to secure the thermocouples to the cells. In order to have a consistent emissivity for the entire cell, and therefore have a consistent infra-red temperature measurement, it was decided that a consistent surface finish was desirable, therefore the entire cell was covered in a single layer of tape.

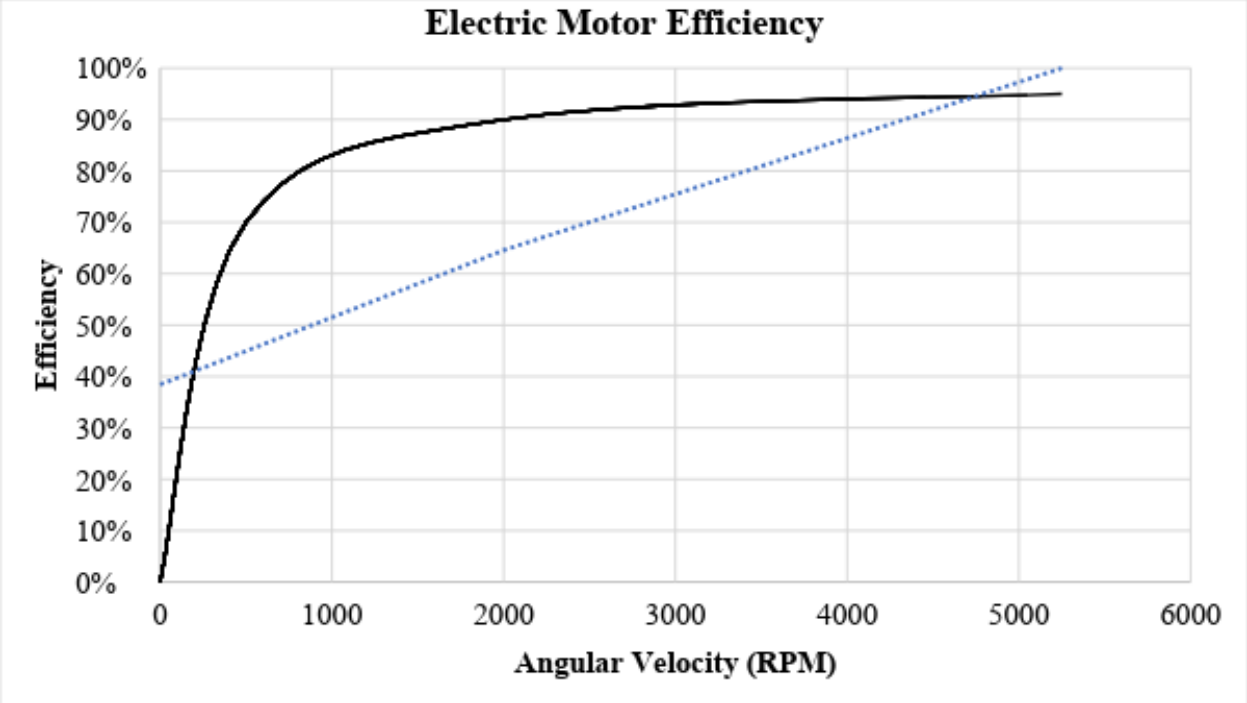

Figure 5-31: Simulation for the losses in the electric motor used in the Commander 5 EV during nominal operation (~200 amperes), courtesy of the manufacturer.

The manufacturer of the electric motors estimates that both motors require 22 kW, 53 kW, and 40 kW of power consumption for driving on Flat, Uphill, and Downhill conditions respectively. Table 5-3 shows the expected power consumption, RPM, and vehicle speed for each driving scenario, and the resulting total loss for the electric motor.

Table 5-3: Result for each electric motor losses for different driving scenarios.

Grade	***vehicle speed (KPH)***	***Torque (N.m)***	***shaft speed (RPM)***	***Power (kW)***	***Efficiency (%)***	***Total Losses (W)***
Flat (0%)	32.8	322	3823	**11**	94%	697.1
Uphill (20%)	15.8	355	1846	**27**	86%	3811.8
Downhill (-20%)	12.0	-355	1396	**20**	83%	3495.8

The current value is used to calculate the losses for both the electric motor and the motor controller. The motor controller manufacturer has provided the curve for the power loss of this component, which can be seen in Figure 5-32.

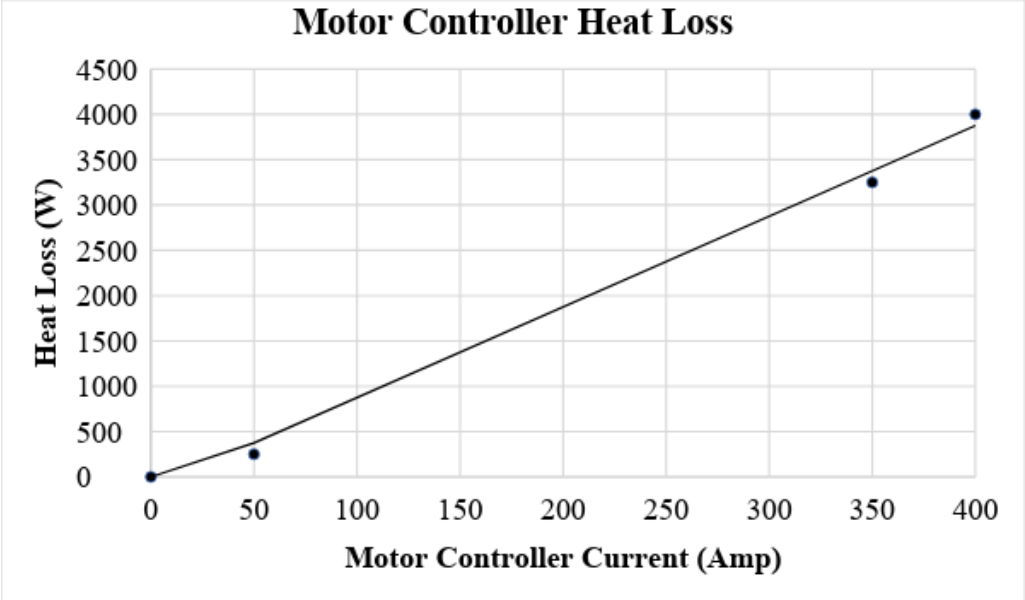

Figure 5-32: Motor controller heat loss curve.

The average electric current used for Flat, Uphill, and Downhill conditions are 68, 169, and 123 amperes respectively, giving 711 W, 2269 W, and 1488 W of total energy loss as presented in Table 5-4.

Table 5-4: This table summarizes the power loss estimation of each major component in the Commander 5EV.

Component	**Quantity**	**Flat**	**Uphill**	**Downhill**	**Charging**	
Electric Motor	2	1394	7624	6992	0	Watts
Motor Controller	2	321	894	641	0	Watts
Pump	1	476	476	476	0	Watts
Motor Controller Pump	1	75	75	75	0	Watts
DC/DC	1	140	140	140	0	Watts
Charger	2	0	0	0	2200	Watts
Batteries	1	55.8	540.4	265.1	80.4	Watts
Total without A/C	-	**2.5**	**9.7**	**8.6**	**2.3**	kW
A/C	1	250	250	250	0	Watts
Total with A/C	-	**2.7**	**10.0**	**8.8**	**2.3**	kW
Heater	1	5	5	5	0	kW
Total with heater	-	**7.5**	**14.7**	**13.6**	**2.3**	kW

Another component that needs to be included for heat evaluation is the hydraulic electric motor pump, dedicated to brakes and steerage. The pump heat loss calculation is based on the nominal power requirement of 6.3kW at 325V. The curve for the total heat losses, which is the sum of the moving and electrical losses, is presented in Figure 5-33. The rotation of the shaft at 4500 RPM and at 20 amperes results in a heat loss of 568W.

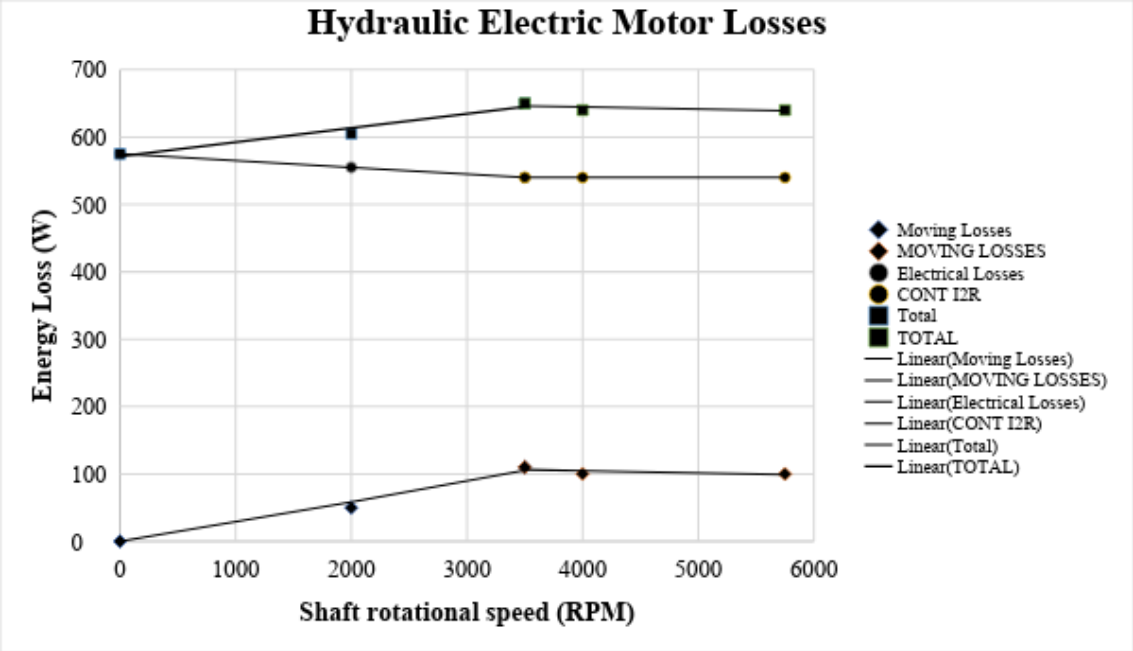

Figure 5-33: Simulation for the losses in the hydraulic electric motor used in the Commander 5 EV during nominal operation (~20 amperes), courtesy from the manufacture.

As well, a DC/DC converter is required in the vehicle to convert battery power from 325V to a lower voltage for vehicle accessories (24Vdc). With a current of 2kW with 93% efficiency, it generates 140W in heat loss. The machine is also equipped with an HVAC system, which is used for the air conditioner and heater. The air conditioner has a capacity of 35000Btu/hr. The heater is rated at 5kW, if all this energy is converted to electric heat. The system utilises two electric compressors that each use 2.5kW and have 95% efficiency, resulting in a total of 250W of heat loss. Finally, the charger, according to the manufacturer, is rated at 11kW which is divided between two units that have each

90% efficiency at nominal condition, producing a total heat loss of 1100W. It is important to note that when on charge mode, the other major components are not be accessible, as seen in Table 5-4.

The total heat produced by the Commander 5EV can be estimated based on the values presented in Table 5-4, while the results for the total heat generated by the battery pack heat generated is displayed in Table 5-5, and it is presented in the graphic form in Figures 5-34, 5-35,5-36 and 5-37. The average battery heat expressed in this section is obtained from the module scenario (the single cell case has different emissivity in comparison to the original batteries due to the use of black electrical tape), and its results are extrapolated for the battery system. As for the remain components, some of the calculations are based on the rated power, and some others on the device efficiency. Both are summarised on Table 5-4. In the power loss calculation, the transmission loss is not included since, in the case of the Commander 5EV, each electric motor is connected directed to each axle via a small drive shaft. This power loss can be assumed to be negligible.

Table 5-5: Total Heat generated by the Personnel Carrier Truck with no use of the air conditioner.

Parameter	**25°C**	**30°C**	**35°C**	**40°C**	**Scenario**
Heat Gen (kW)	10.3	10.3	10.3	10.3	Uphill
Battery Heat fraction	5.30%	5.50%	5.10%	5.00%	
Power (kW)	53.4	53.4	53.1	53.1	
Efficiency	80.70%	80.70%	80.70%	80.70%	
Heat Gen (kW)	2.5	2.5	2.5	2.5	Flat
Battery Heat fraction	2.20%	2.20%	2.20%	2.20%	
Power (kW)	21.8	21.8	21.9	21.9	
Efficiency	88.50%	88.50%	88.50%	88.50%	
Heat Gen (kW)	2.36	2.36	2.36	2.36	Charging
Battery Heat fraction	3.40%	3.40%	3.40%	3.40%	
Power (kW)	21.4	21.4	21.4	21.4	
Efficiency	89.00%	89.00%	89.00%	89.00%	
Heat Gen (kW)	8.87	8.85	8.85	8.84	Downhill
Battery Heat fraction	3.10%	3.00%	3.00%	2.90%	
Power (kW)	40.2	40.3	40.3	40.2	
Efficiency	77.90%	78.00%	78.10%	78.00%	

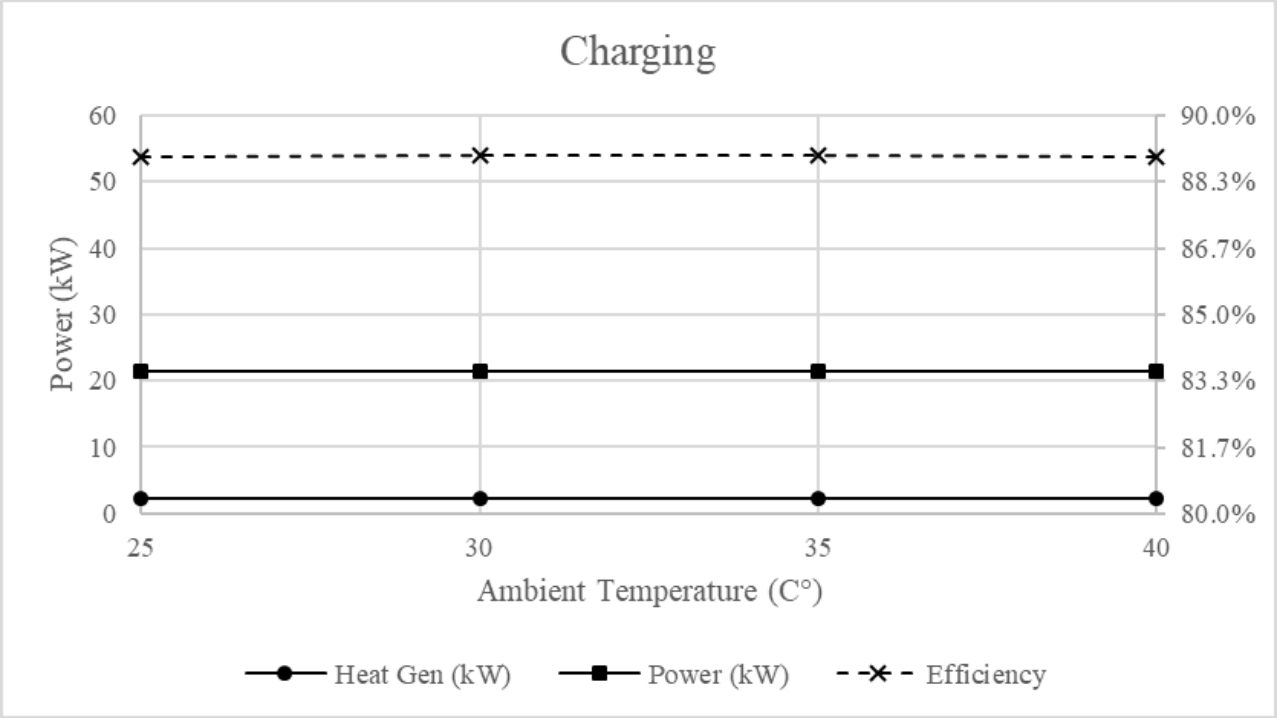

Figure 5-34: Estimation of the machinery average efficiency under Charging regime.

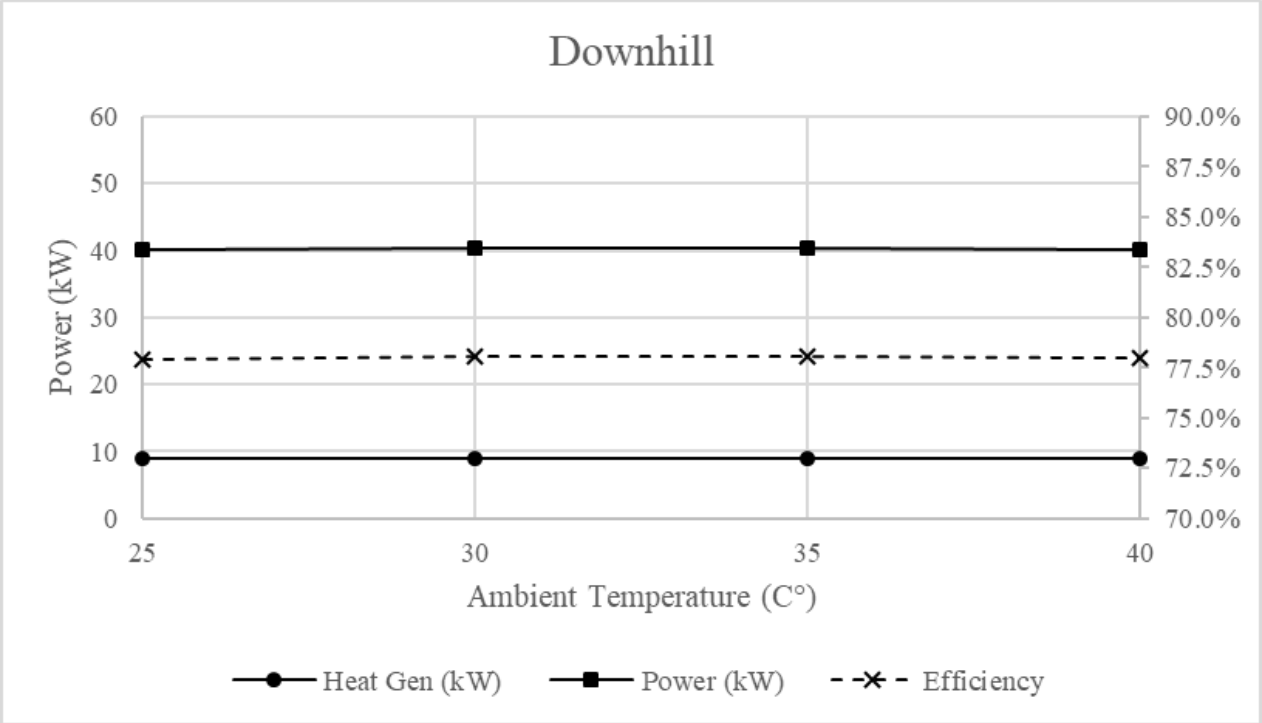

Figure 5-35: Estimation of the machinery average efficiency under Downhill regime.

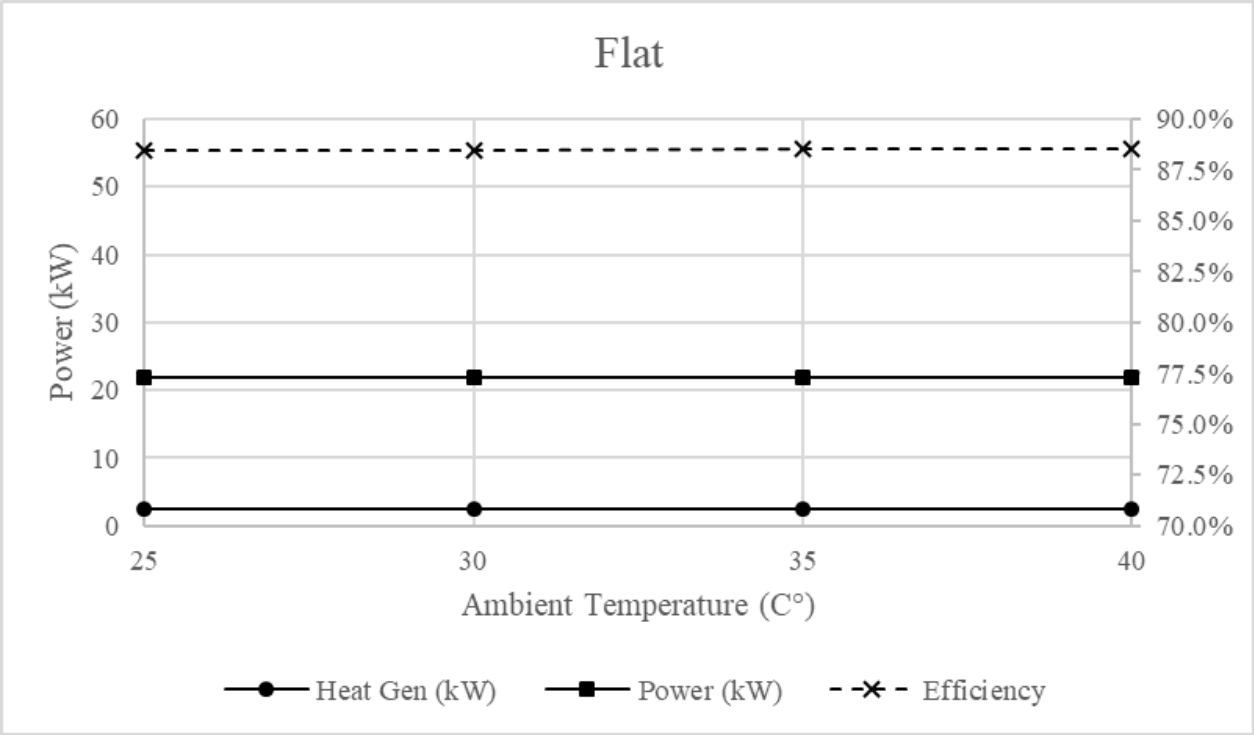

Figure 5-36: Estimation of the machinery average efficiency under Flat regime.

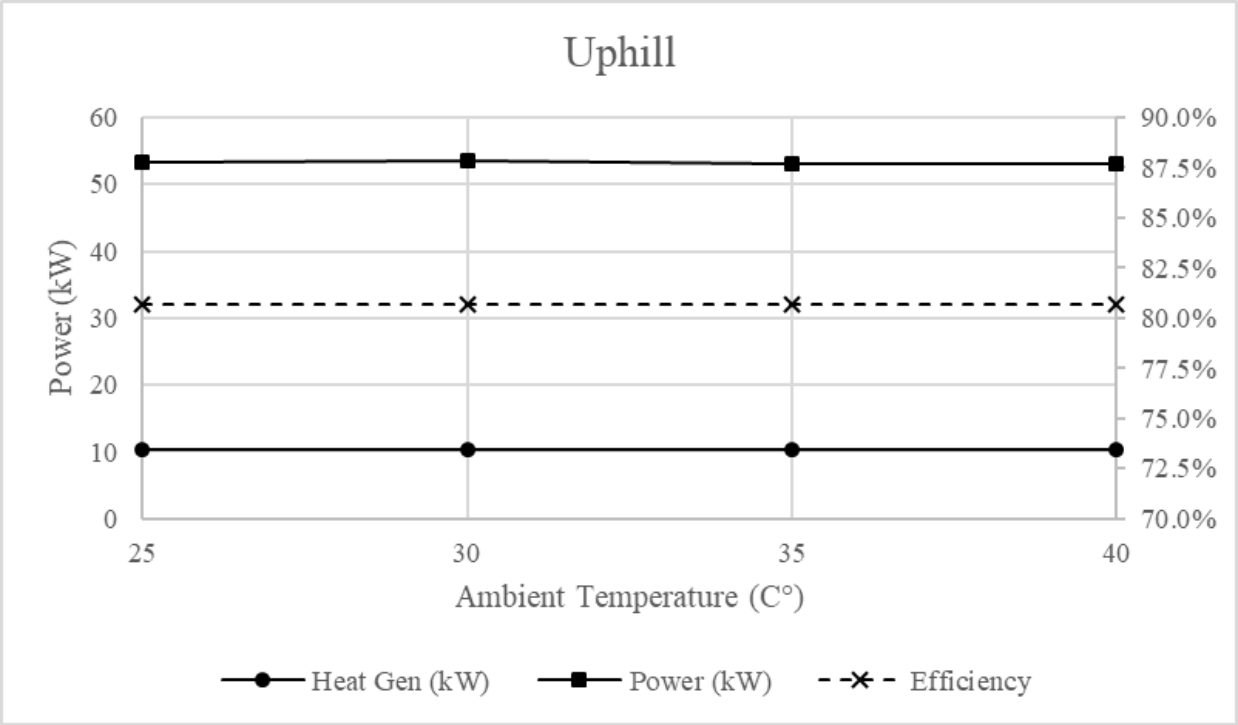

Figure 5-37: Estimation of the machinery average efficiency under Uphill regime.

Figure 2-8 shows that the efficiency of an electric vehicle ranges from 65% (if there is no regenerative braking), and 82% (when there is regenerative braking). However, in this calculation, the charging efficiency is included. Nonetheless, if it is assumed only the parasitic losses, which includes cooling and electric devices, and the electric drive system losses, which count the losses in the electric motor and the transmission, the efficiency increases to 81.5% (without regen) and 98.5% (with regen). In the case of the Commander 5 EV, the average overall efficiencies estimated for the whole vehicle are 89.0% (Charging), 78.0% (Downhill), 88.5% (Flat), and 80.7% (Uphill) when the air-conditioning and heater is not under usage (see Table 5-5).

Table 5-5 presents the average machine`s efficiency for each charging/discharging condition, and for different environment temperature. Relative to the other components of the system, the battery pack is a very efficient device, since its heat generated comprehend no more than 6% of the total heat developed, being 3.4%, 3.0%, 2.2%, and 5.3% of the total for charging, Downhill, flat, and Uphill mode, respectively. In these calculations, it is assumed that all the components are being used simultaneously, except during charging (see Table 5-4). For this reason, the efficiency drops between Charging and Downhill modes. As for the discharging current, when is increased, the machine`s efficiency is slightly decreased. The average efficiency for Charging, Downhill, Flat, and Uphill are 89.3%, 83%, 85.6%, and 84.8% respectively.

As a side note, it is included Table 5-6 about the average efficiency under air conditioning usage.

Table 5-6: Total Heat generated by the Personnel Carrier Truck with air conditioner usage.

Parameter	**25°C**	**30°C**	**35°C**	**40°C**	**Scenario**
Heat Gen (kW)	10.5	10.6	10.5	10.5	Uphill w/ A/C
Battery Heat fraction	5.20%	5.40%	5.00%	4.90%	
Power (kW)	53.4	53.4	53.1	53.1	
Efficiency	80.30%	80.20%	80.20%	80.20%	
Heat Gen (kW)	2.8	2.8	2.8	2.8	Flat w/ A/C
Battery Heat fraction	2.00%	2.00%	2.00%	2.00%	
Power (kW)	21.8	21.8	21.9	21.9	
Efficiency	87.30%	87.30%	87.40%	87.40%	
Heat Gen (kW)	2.36	2.36	2.36	2.36	Charging w/ A/C
Battery Heat fraction	3.40%	3.40%	3.40%	3.40%	
Power (kW)	21.4	21.4	21.4	21.4	
Efficiency	89.00%	89.00%	89.00%	89.00%	
Heat Gen (kW)	9.12	9.1	9.1	9.09	Downhill w/ A/C
Battery Heat fraction	3.00%	2.90%	2.90%	2.80%	
Power (kW)	40.2	40.3	40.3	40.2	
Efficiency	77.30%	77.40%	77.40%	77.40%	

Although the use of air conditioning in electric vehicles decreases considerably the efficiency of the machine, since it consumes 10.26kW, its heat impact is barely noticeable due to the compressor high efficiency (95%). When in use, the system efficiency drops in 0.8%, 1.3%, and 0.6% for Downhill, Flat, and Uphill respectively.

The impact of air conditioning usage is considerably lower when compared to the heater, as can be seen in Table 5-7. However, it is unlikely that heaters will be used with a frequently in underground environment. The side effect of using HVAC system is that the machine`s range is severe impact by it. This information can be inferred by the efficiency reduction, especially when the heat is in operation.

Table 5-7: Total Heat generated by the Personnel Carrier Truck with heater usage.

Parameter	25°C	30°C	35°C	40°C	Scenario
Heat Gen (kW)	15.3	15.32	15.28	15.27	Uphill w/ heater
Battery Heat fraction	3.60%	3.70%	3.50%	3.40%	
Power (kW)	58.4	58.4	58.1	58.1	
Efficiency	73.80%	73.80%	73.70%	73.70%	
Heat Gen (kW)	7.52	7.52	7.52	7.52	Flat w/ heater
Battery Heat fraction	0.70%	0.70%	0.70%	0.70%	
Power (kW)	21.8	21.8	21.9	21.9	
Efficiency	65.60%	65.60%	65.70%	65.70%	
Heat Gen (kW)	2.36	2.36	2.36	2.36	Charging w/ heater
Battery Heat fraction	3.40%	3.40%	3.40%	3.40%	
Power (kW)	21.4	21.4	21.4	21.4	
Efficiency	89.00%	89.00%	89.00%	89.00%	
Heat Gen (kW)	13.87	13.85	13.85	13.84	Downhill w/ heater
Battery Heat fraction	2.00%	1.90%	1.90%	1.90%	
Power (kW)	40.2	40.3	40.3	40.2	
Efficiency	65.50%	65.60%	65.70%	65.60%	

From Table 5-7, the efficiency decreases expressively under Downhill, Flat, and Uphill regime to 65.6%, 65.6%, and 73.8%, respectively, which represents a decrement on the efficiency in relation to Table 5-6 in 16.1% on average.

Another important point is that the regenerative brake only charges the battery if the state of charge is below 90%. This limit is set to not damage the Lithium-iron Phosphate batteries, since crossing it can induce to memory effect, which reduces the battery life span. Driving the machine from the top to the bottom of the mine, starting with nearly completed battery capacity, can lead to cross this limit under the Downhill driving process. If it does, the machine has a backup system which directs the current from the battery to a resistor mounted at the back of the machine. This resistor is coupled to a back radiator through a water line, and it is rated at 25kW. Since during Downhill, 40.3 kW can be produced on average, the braking resistors have the capacity to slow down the machine by

transforming 25 kW of kinetic energy into thermal heat. Thus, it is highly recommended to not charge the machine at the top of the shaft if the intention is to drive it down the mine.

6 Conclusions

The goal of this study is to evaluate heat generated from battery cells that are designed to be used in electric vehicles and how the thermal signature is influenced by both the driving/charging condition and the ambient temperature. These topics and questions are important for the mining industry in operating electric mining underground vehicles. From the mining perspective, the movement towards EVs technologies is a way to mitigate the heat generated by diesel engines, which is generally the third major source of heat, and to provide a healthier work environment for miners with no diesel particulate matter or hazardous gases emitted. Indeed, financial savings in mining operation and a healthier environment in accordance with the most recent mining regulations can be achieved when underground machines emit a lower rate of heat.

Electric machines are becoming a viable alternative to traditional diesel vehicles. Higher efficiency, high torque at low RPM, reduced motor size, reduced mechanical complexity, and lack of hazardous emissions are among their benefits. Currently, the costs of acquisition and operation are currently moderately higher than for diesel units with similar bucket capacity. Furthermore, electric machines have reduced range, have a longer charging time, and require charging infrastructure, all consequences of the low energy capacity of current battery pack models. Yet, this may change soon. With new improved cell chemistries being introduced to the market, EVs are becoming a realistic substitute to current IC engines in underground mine operations.

From the mine operator's perspective, one of the EVs' strongest advantage beside the aspect of no emissions is the considerably lower heat impact on the immediate environment in comparison to IC vehicles. Current methods used to estimate heat impact involve an approximate estimation of heat generation based on the general assumption of the efficiency value. These

methods do not describe changes in the heat load as shaped by different driving and charging requirements. These strategies can cause misleading assumptions that can either overestimate or underestimate the total heat generation. Another strategy estimates that the heat generation of these machines is equal to the power consumption when not working against gravity. This strategy is also equivocal since vehicles are typically used in underground mines up and down slopes, and some other machines, such as scoop trams, almost always work against gravity. All of these considerations must be raised if there is an intention to properly evaluate the heat impact of electric machines in underground environments.

However, calculating the efficiency of the machine is a valid strategy to determine how heat generation is affected by different driving conditions and environmental temperatures. This study primarily evaluates the battery pack as it is a critical component in EVs. The heat generation of the other electrical components is estimated based their efficiencies and rated powers. The study consists of two analysis focusses: the single cell and the module. One of the purposes of the model study is to specify interference between individual cells. In both cases, the cells are tested in situations typically found in a mining environment, being Charging, Downhill, Uphill, and Flat conditions, all of which are tested in 25°C, 30°C, 35°C, and 40°C ambient temperatures. The thermal impact is calculated based on the heat generated by the Lithium-iron Phosphate cells, and the heat released to the environment through radiation and convection.

The results show that there is a considerable difference between the heat generated and the heat lost for high discharging/charging currents. This is a consequence of the low thermal conductivity in the battery core. Furthermore, the heat flux has a preferable direction, but due to the magnitude of the temperature gradient around the battery cell, these temperature differences for each face are not expressive. This difference between the heat generated and the heat loss is

expressed by the heat accumulated, which is released into the environment after the process of charging/discharging. For this reason, analysing the heat generation is the most advantageous approach to evaluate the impact of machines operating in their intended environment.

The findings of this study show that the current level has a more significant impact on the battery heat generation than the environmental temperature found in underground mines. The heat generated by the single cell under the Downhill operating condition is 2.6 times higher on average than during the Charging condition, and the Uphill condition produces 9.6 times more heat on average than the Flat mode. The Charging, Downhill, Flat, and Uphill scenarios use current levels of 17.3 amperes, 29.4 amperes, 16.9 amperes, and 44.1 amperes, producing heat averages of 97.3 W, 251.9 W, 58.9 W, and 564.1 W respectively. However, the heat generation varies considerably over time because of the reversible entropic term, which can be positive or negative depending on the state of charge and the current level. The study also determined that the battery produces 39.5% more heat during the Charging process than the Flat discharge, even though in both scenarios the battery has a similar absolute current rate. By contrast, for the extreme case of Uphill mode at 40°C, there is a minor temperature difference of only 0.5°C between the external cells in the module with the ones located in the middle.

The analysis of the heat generated by the Commander 5 EV, a personnel carrier mining electric truck designed by Tracks and Wheels, shows that the battery pack, with 400 cells in total, does not generate more than 6% of the overall heat generated by the vehicle. On average it produces 3.4%, 3.0%, 2.2%, and 5.3% of the heat in the Charging, Downhill, Flat, and Uphill modes respectively. The average total heat generated and the efficiency for the vehicle in the aforesaid scenarios are respectively 2.4 kW (89.0% efficiency), 8.9 kW (78.0%), 2.5 kW (88.5%),

and 10.3 kW (80.7%). This means that higher current levels generally reduce the efficiency of the machine.

There are a multitude of areas that could serve as fertile ground for future work. Future studies can use the results of this work to optimize the usage of electric vehicle in underground mines. These aspects can include: optimal paths for electrical machine usage, the most suitable charging locations, and the financial gains from the substitution of diesel machines by their electric counter parts.

In addition, future studies may expand the range of temperature and current. The temperature range between 25°C and 40°C has no considerable impact on the thermal signature of Lithium-iron Phosphate battery cells, however, there is a possibility the conclusions may differ for temperatures under 25°C and above 40°C. Furthermore, the current level requirements vary with each electrical machine. It is important to increase their scope since each electrical machine has different current requirements. By increasing their range, the findings can be applied to different machines used underground. Another important point is the investigation of the difference between using a constant environmental temperature and the actual measured temperature in the simulation.

Overall, the proposed ideas for future work may expand the scope of understanding of both heat generation and heat loss of electric vehicles in underground mine.

7 References

Al Hallaj S., Maleki, H., Hong, J.S., and Selman, J.R. (1999), *Thermal modeling and design considerations of lithium-ion batteries*. J. Power Sources, 83, 1.

Anon (2014)**;** JoyGlobal P&H, Generation 2 Wheel Loader Product Overview, *P&H Mining Equipment Inc., Milwaukee, USA.*

AUSIMM. 2012. *Cost Estimation Handbook*. 2nd ed. The Australian Institute of Mining and Metallurgy. Carlton, Victoria.

Barnes D., Miller A. (2005). *Fuelcell-Powered Front-End Loader Mining Vehicle*. Retrieved on April 12, 2018, from https://www.hydrogen.energy.gov/pdfs/progress05/viii_a_6_barnes.pdf.

Bandhauer, T.M., Garimella, S., & Fuller, T.F. (2011). *A Critical review of Thermal Issues in Lithium-Ion Batteries*. Journal of the Electromechanical Society, 158(3). Doi:10.1149/1.3515880.

Baz-Dresch JJ, Bickel KL, Watts WF (1993). *Evaluation of catalyzed diesel particulate filters in an underground metal mine.* Minneapolis, MN: US Department of the Interior, Bureau of Mines, RI 9478.

Bernardi D., Pawlikowski E., Newman J. (1985) *A General Energy Balance for Battery Systems*, Journal of the Electrochemical Society, 132, pp. 53-63.

Betounay M.C. (2012). *The Green Mining Vehicle-Green Energy Road Map*. April 12, 2018, from http://www.mdec.ca/2012/S4P3-Young.pdf

Buchmann, I. (2016, February 21). *BU-205: Types of Lithium-ion*. Retrieved March 02, 2016, from http://battery university.com/learn/article/types_of_lithium_ion.

Burke J. (2017). GMSG Recommended Practices for Battery Electric Vehicles in Underground Mining. Accessed on 11th April 2018 from http://www.globalminingstandards.org/wp-content/uploads/2017/04/20160726_UG_Mining_BEV-GMSG-WG-v01-r01_published.pdf

CALB, China Aviation Lithium Batteries. (2014). *CAM72F I, Aluminum alloy shelled, rechargeable Lithium-iron Phosphateion phosphate energy cell.* Retrieved from: https://evwest.com/support/CAM72FI%20Final.pdf

Calisir T., Baskaya S., Yazar H. O., & Yucedag S. (2015). *Experimental Investigation of Panel Radiator Heat Output Enhancement for Efficient Thermal use Under Actual Operating Conditions, EDP Sciences.*

Carder D.K. (1999). *Performance evaluation of exhaust after-treatment devices used for emissions control on diesel engines employed in underground coal mines* [Thesis]. Morgantown, WV: West Virginia University, Department of Mechanical and Aerospace Engineering.

Catenacci, M., Verdolini, El, Bosetti, V., Fiorese, G., & Ameli, N. (2012). Going Electric: Survey on the Future of Battery Technologies for Electric Vehicles. *SSRN Electronic Journal SSRN Journal*.

"Cat Loader Powered by Hydrogen Fuel Cells" (2007). Sudbury Mining Solutions Journal.

Chan, C. C. (2007). The State of the Art of Electric, Hybrid, and Fuel Cell Vehicles. *Proceedings of the IEEE Proc. IEEE, 95*(4), 704-718.

Chen, D., Jiang, J., Kim, G., Yang, C., & Pesaran, A., (2016). Comparison of different cooling methods for Lithium-iron Phosphateion battery cells. *Applied Thermal Engineering*, 94, 846-854. Doi:10.1016/j.applthermaleng.2015.10.015

Chen, S., Wan, C., & Wang, Y. (2005). Thermal analysis of lithium-ion batteries. *Journal of power Sources*, 140(1), 111-124, doi:10.1016/j.jpowsour.2004.05.064

CIPEC (2005): "*Benchmarking the Energy Consumption of Canadian Underground Bulk Mines.*" Canadian Industry Program for Energy Conservation. Natural Resources Canada, 2005.

Deglon, P. & Hemp, R.,(1980). *Second International Mine Ventilation Congress: Reno, NV, November 4-8, 1979.* New York, NY: Society of Mining Engineers of American Institute of Mining Metallurgical, and Petroleum Engineers. 532.

Demers M., Labelle D., Wilson R. and Matikainen O. (2010, October 5). *Hybrid Underground Loader – 2010 Project Update*, presentation given at the MDEC 2010 Conference, Toronto, Ont., Canada.

De Souza E., Cost Saving Strategies in Mine Ventilation (2015). Accessed on 1st February, 2018. http://www.airfinders.ca/wp-content/uploads/2015/05/Cost-Saving-Strategies-in-Mine-Ventilation.pdf

Diesel to Electric: What is the Future of Mining? (2016, June). Accessed on 11th April 2018. http://www.skidsteers.net.au/BlogPostView.asp?BlogPostID=22

Electrical Motors and Heat Loss. (n.d.). Retrieved March 15, 2016, from http://www.engineeringtoolbox.com/electrical-motor-heat-loss-d_898.html

Emissivity Values of Common Materials (2007) Retrivied October 10, 2017, from http://support.fluke.com/find-ales/Download/Asset/3038318_6251_ENG_A_W.PDF.

EPA – United State Environmental Protection Agency. (2002). *A Comprehensive Analysis of Biodiesel Impacts on Exhaust Emissions, Draft Technical Report*. (EPA420-P-02-001). Washington, DC: U.S. Government Printing Office.

Enderlin, W., (1973), *Evaluating Underground Heat Sources in Deep Mines*, M. S. thesis, Mont. Coll. Minl. Sci. Tech., Butte; also *USBM, O.F.R.*,Research Contract No. GO 122137, June. 78-86.

Ellison G.N., Thermal Computational for Electronic Equipment, Van Nostrand Reinhold, New York, 1969.

Fleet, M. (2012); Personal communication on "Hybrid Drive Electric Mining Loaders", *Longview, Texas, USA*

FLIR (n.d.) Retrieved July 17, 2018 from https://www.flir.com/products/e5/

Forbush S. (2001). *Diesel emissions reduction program. Unpublished paper presented at the Mining Diesel Emissions Conference*, Markham, Ontario, Canada, November 7.

Forgez, C., Vinh Do D., Friedrich G., Morcrette M., and Delacourt C.. (2010). *Thermal Modeling of a Cylindrical LiFePO4/graphite Lithium-ion Battery*. Journal of Power Sources 195.9: 2961-968. Web.

Fuel Cell Research Lab (nd). *Fuel Cell Hybrid Bus Program.* Retrieved July 17, 2018 from

http://www.me.udel.edu/research_groups/prasad/research/fcb.html

"Fuel Cell Technology" (2001). Retrieved April 12, 2018 from https://www1.eere.energy.gov/hydrogenandfuelcells/tech_validation/pdfs/fcm04r0.pdf

Garcia-Valle, R., & Lopes, J. A. P. (2013). *Electric Vehicle Integration into Modern Power Networks*. New York: Springer.

Gautam, D., Musavi, F., Edington, M.m Eberl, W., & Dunford, W. G. (2011). "An automotive on-board 3.3 kW battery charger for PHEV application." (2011) *IEEE Vehicle Power and Propulsion Conference*.

Giancoli, Douglas C., Physics, 4th Edition, Prentice Hall, (1995).

Greenhill, N. & Knights, P. (2013). *Conceptual Feasibility of Battery Powered Loaders in Underground Mines. Thesis*, Universidad Técnica Federico Santa María, Valparaíso, Chile.Griffiths, D. J. (1999). *Introduction to electrodynamics*. Upper Saddle River, NJ: Prentice Hall.

Halim, A., Kerai, M. (2013). *Ventilation Requirements for 'Electric' Underground Hard Rock Mines - A Conceptual Study*. Australian Mine Ventilation Conference, Adelaide.

Hartman, H. L., Mutmansky, J. M., & Wang, Y. J. (1982). *Mine ventilation and air conditioning*. New York: Willey. 561-593.

Hartman, H.L., Mutmansky, J.M., Ramani, R.V., and Wang, Y.J., (1997). *Mine Ventilation and Air Conditioning, Third Edition.* John Wiley & Sons, New York, U.S.A., 730 p.

Hodkinson, R., & Fenton, J. (2000). Current EV design approaches. *Lightweight Electric/Hybrid Vehicle Design*, 3-28.

Hosni, M.H., Jones, B.W., and Xu, H. (1999). *Experimental results for heat gain and radiant/convective split from equipment in buildings*. ASHRAE Transactions 105(2): 527-42.

Hsu, J. S. (2000). A Machine Approach for Field Weakening of Permanent-Magnet Motors. *SAE Technical Paper Series*.

Hughes, A. (2006). *Electric motors and drives: Fundamentals, types, and applications*. Amsterdam: Elsevier/Newnes.

Hussain, I. (2003). *Electric and hybrid vehicles: Design fundamentals.* Boca Raton, FL: CRC Press.

Hussain, I. (2011). *Electric and hybrid vehicles: Design fundamentals*. Second Edition. Boca Raton, FL: CRC Press.\

Incropera, Frank P., and David P. DeWitt (2002). *Fundamentals of Heat and Mass Transfer*. New York: J. Wiley. Print.

Jacobs, W. (28 October, 2013). *Electric LHDs in Underground Hard Rock Mining: A Cost/Benefit Analysis*. School of Mechanical and Chemical Engineering University of Western Australia.

Jacobs, W., Hodkiewicz, M. R., & Braunl, T. (2014). *A cost-benefit analysis of electric loaders to reduce diesel emissions in underground hard rock mines*. 2014 IEEE Industry Application Society Annual Meeting.

Jang J.C., Rhi S.H. (2010). *Battery Thermal Management System of Future Electric Vehicles with Loop Thermosyphon*. In: *US-Korea conference on science, technology, and entrepreneurship* (UKC).

Jensen, S. (2013). Electric Underground. Retrieved April 11, 2018, from https://www.oemoffhighway.com/electronics/article/11224086/electrification-of-underground-mining-equipment

Khasawneh, H. J. (2011). *Analysis of Heat-Spreading Thermal Management Solutions for Lithium-Ion Batteries*, Master's Thesis.

Klein H, Lox E, Kreuzer T, Kawanami M, Ried T, Bächmann K (1998). *Diesel particulate emissions of passenger cars: new insights into structural changes during the process of exhaust after-treatment using diesel oxidation catalysts.* Warrendale, PA: Society of Automotive Engineers, SAE paper 980196.

Kumar, L., & Jain, S. (2014). Electric propulsion system for electric vehicular technology: A review. *Renewable and Sustainable Energy Reviews, 29,* 924-940.

Leitman, S., & Brant, B. (2009). *Build your own electric vehicle*. New York: McGraw-Hill.

Leonida, C. (2017, June). Battery electric: The death of diesel underground? *MiningMagazine*, 48-54.

Nensen, P., & Lundkvist, A. (2005). From 167 GWH to 72 GWH - *Ventilation on Demand in LKAB's Iron Ore Mine*, Malmberget. Proc IPPC Conference, Innovative Energy Efficiency Examples of Different Industrial Secotros - Energy Efficiency in the Cement, Metal and Petrochemical Industry.

Niculuta, M.C. (2011). *Battery Cell Thermal Measurements Activity Report*.

Niculuta, M.C. (2012). *Thermal Analysis of a LiFePO 4 Battery Pack*, Master's Thesis.

Norris, J. (2013): Personal Comunication with Ozdogan M. and Ozdogan H., *P&H LeTourneau Factory., Texas, U.S.A.*

Marks, J R, (2012). *Airflow specification for metal and non-metal mines*, in Proceedings of 14th US/North American Mine Ventilation Symposium (eds: F Calizaya and M Nelson), pp 191-195, (University of Utah: Salt Lake City).

Marinov, A., & Valchev, V. (2009). Power loss reduction in electronic inverters trough IGBT-MOSFET combination. *Procedia Earth and Planetary Science, 1*(1), 1539-1543.

McGINN, S. (2007). Controlling diesel emissions in underground mining within an evolving regulatory structure in Canada and the United States of America: in *Queensland Mining Industry Health & Safety Conference*, 2007 Step Change to a Safety Future, Townsville, 11 pp. Retrieved March 27, 2016, from <http://www.qrc.org.au/conference/_dbase_upl/mcginn_Controlling%20Diesel%20Emissions.pdf>

McPherson, M. J. (1993). *Subsurface ventilation and environmental engineering*. London: Chapman & Hall. 289, 370-382, 523-582

Menéndez-Díaz, A., Ordóñez-Galán, C., Bouza-Rodríguez, J. B., & Fernández-Calleja, J. J. (2014). Thermal analysis of a stoneware panel covering radiators. *Applied Energy, 131*, 248-256.

Miller, A. R., van den Berg G., Barnes D.L., Eisele R.I., Tanner D.M., Vallely J.M., and Lassiter D.A. (2012). Fuel Cell Technology in Underground Mining. The Southern African Institute of Mining and Metallurgy.

MK Powered. (2010). *Sealed Valve Regulated (SVR) Gelled Electrolyte Lead-acid Batteries: Technical Manual*. Retrieved on March 24th, 2016, from <http://www.mkbattery.com/pdf/technical_manual.pdf>

Monem, M. A., Trad, K., Omar, N., Hegazy, O., Mantels, B., Mulder, G., Bossche P., Mierlo, J. V. (2015). "Lithium-ion Batteries: Evaluation Study of Different Charging Methodologies Based on Aging Process." *Applied Energy, 152*, 143-155.

Moore, P. 2010. *Plugging the Gap Underground. Mining Magazine*, November, 40-46.

Mollenhauer, K., & Tschöke, H. (2010). *Handbook of diesel engines.* Berlin: Springer. 420-425.

OMEGA. (n/a). Emissivity of Common Materials. Retrieved on April 5th, 2017, from https://www.omega.com/literature/transactions/volume1/emissivityb.html

Ozdogan, M., and Ozdogan H. (2015); *Diesel-Electric Mining Loaders – A Case Study*, IMCET 2015, Antalya, Turkey.

Norton P, Vertin K, Clark NN, Lyons DW, Gautam M, Goguen S, *et al*. [1999]. *Emissions from buses with DDC 6V92 engines using synthetic diesel fuel.* Warrendale, PA: Society of automotive Engineers, SAE paper 1999-01-1512.

Paas N (1999). *Dry system technology management system. In: Proceedings of the Mining Diesel Emissions Conference* (Markham, Ontario, Canada).

Paraszczak, J., Laflamme, M., Fytas, K. 2013. *Electric load-haul-dump machines: real alternative for diesels?* CIM Journal, 4(1), 13-19.

Paraszczak, J., Svedlund, E., Fytas, K., & Laflamme, M., a, (2014). Electrification of loaders and trucks: A step towards more sustainable underground mining. *International Conference on Renewable Energies and Power Quality (ICREPQ'14). Cordoba, Spain.*

Paraszczak, J., Svedlund, E., Fytas, K., & Laflamme, M., b, (2014). Feasibility of Using Electric Trucks in Deep Metal Mines. *International Conference on Mine Planning and Equipment Selection. Dresden, Germany*.

Pesaran A.A. (2001). Battery Thermal Management in EVs and HEVs Issues and Solutions. *Advanced Automotive Battery Conference*, Las Vegas, Nevada.

Pesaran A.A. (2002). Battery Thermal Models for Hybrid Vehicle Simulations, *Journal of Power Sources*, 110 377-382.

Pesaran A. A., Vlahinos A., and Burch S. D.. (1997). *Thermal Performance of EV and HEV Battery Modules and Packs,* 14th Electric Vehicle Symposium.

Pignon, J.. (2005). Diesel Engines: Design and Emissions. *Johnson Matthey Technology Review, a journal published by Johnson Matthey Plc, 49,* (3), 119-121.

Rao Z., Wang S (2011). A Review of Power Battery Thermal Energy Management. *Renewable and Sustainable Energy Reviews*. 15 4554-4571.

Quilliam, J. H. (1974). The Ventilation of South African gold mines. *Cape Town: Chamber of Mines of South Africa*. 82-92.

Regan, R. (2008). Guideline for the Management of Diesel Engine Pollutants in Underground Environments. *Mine Safety Operations Division, New South Wales Department of Primary Industries*. Retrieved March 27, 2016, from < http://www.resourcesandenergy.nsw.gov.au/__data/assets/pdf_file/0011/419465/MDG-29.pdf>

Regan, R. (2013, June 14). Safety Bulletin - Diesel Emissions in Mines. Retrieved March 27, 2016, from <http://www.resourcesandenergy.nsw.gov.au/__data/assets/pdf_file/ 0005/469454/SB13-03-Diesel-emissions-in-mines.pdf>

Righettini G. and Mousset-Jones P. (2004). *Ventilation Savings with Fuel Cell Vehicles A Cost-Benefit Analysis for Selected U.S. Metal/Non-Metal Mines,* 2004.

Ryan M. & Rakochy D. (2012, October 2-4). *Considerations when deciding between and electric Loader and a diesel Loader.* Paper presented at MDEC – Mining diesel emissions council, Toronto, ON. Retrieved March 15, 2016, from <http://www.mdec.ca/2012/S4P2-Rakochy.pdf>

SAE Hybrid Committee (2011). *SAE Charging Configurations and Ratings Terminology: Technical specification*. Retrieved March 03, 2016, from <http://www.sae.org/smartgrid/chargingspeeds.pdf>

Samba, A. (2016). Battery Electrical Vehicles-Analysis of Thermal Modelling and Thermal Management (Doctoral dissertation). Retrieved on April 10, 2017, from http://hal.archives-ouvertes.fr/tel-01298416/document

Sandivik. (2010). *LH514E: Technical specification*. Retrieved March 24, 2016, from <http://www.miningandconstruction.sandvik.com/sandvik/5100/SAM/Internet/cl01023.nsf/Alldocs/Products%2a5CLoad%2aand%2ahaul%2amachines%2a5CUnderground%2aloaders%2a%2a28LHDs%2a29%2a2ATORO%2a1400E/$FILE/Technical%20specification%20Sandvik%20LH514E-06.pdf>

Santiago, J. D., Bernhoff, H., Ekergård, B., Eriksson, S., Ferhatovic, S., Waters, R., & Leijon, M. (2012). Electrical Motor Drivelines in Commercial All-Electric Vehicles: A Review. *IEEE Trans. Veh. Technol. IEEE Transactions on Vehicular Technology, 61*(2), 475-484.

Sayadi A. R., Lashgari A., & Paraszczak J. (2012). *Hard-rock LHD cost estimation using single and multiple regressions based on principal component analysis*, Tunnelling and Underground Space Technology 133-141.

Schatz R., Nieto A., Dogruoz C., and Lvov S. (2015). *Using modern battery systems in light duty mining vehicles, International Journal of Mining*, Reclamation and Environment, 29:4, 243-265, DOI: 10.1080/17480930.2013.866797

Schnakenberg, G. H., & Bugarski, A. D. (2002). *Review of technology available to the underground*

mining industry for control of diesel emissions (United States of America, U.S. Department of Health and Human Services). Pittsburgh, PA: U.S. Dept. of Health and Human Services, Public Health Service, Centers for Disease Control and Prevention, National Institute for Occupational Safety and Health, Pittsburgh Research Laboratory.

Sengupta, M. (1990). *Mine environmental engineering.* Boca Raton, FL: CRC Press. 21-23.

Smil, V. (2010). *Prime Movers of Globalization: The History and Impact of Diesel Engines and Gas Turbines.* USA: Massachusetts Institute of Technology.

Soylu, S. (2011). *Electric vehicles: the benefits and barriers*. Rijeka: In Tech.

Suberu, M. Y., Mustafa, M. W., and Bashir, N. (2014). "Energy Storage Systems for Renewable energy Power Sector Integration and Mitigation of Intermittency". *Renewable and Suitainable Energy Reviews 35*: 499-514.

Takahashi M., Tobishima S., Takei K., and Sakuari Y. "Characterization of Lithium-iron Phosphateiron phosphate as the cathode material for rechargeable Lithium-iron Phosphatebatteries". *Journal of Power Sources, 97-98*: 508-511, 2001.

Takano Y., Takeno M., Hoshi N., Chiba A., Takemoto M., Ogasawara S., and Rahman M. A., "Design and analysis of a switched reluctance motor for next generation hybrid vehicle without PM materials," in *Proc. IPEC*, 2010, pp. 1801–1806.

The carbon trust. Energy Efficiency Office, UK Government. *Good Practice Guide 76-Continuous Steel Reheating Furnaces: Specification Design and Equipment. 1993*. Retrieved on May 24, 2017, from www.thecarbontrust.co.uk/energy/pages/home.asp

Thermal Conductivity of common Materials and Gases (n.d.) Retrieved August 12, 2018, from https://www.engineeringtoolbox.com/thermal-conductivity-d_429.html

Thomas K. E. and Newman J. (2003). *Thermal Modeling of Porous Insertion Electrodes* Journal of the Electrochemical Society 150 (2) A176-A192.

Tollinsky N., *Electric Vehicle Purpose-built for Deep Mining*. January 27, 2017. Sudbury Mining

Solutions Journal. Retrieved on March 19, 2018, from http://www.sudburyminingsolutions.com/electric-vehicle-purpose-built-for-deep-mining.html.

TSI (n.d.) Retrieved on August 8, 2018, from https://www.itm.com/images/products/cache/tsi-alnor/datalogger/9545/main/tsi-alnor_9545_datalogger.jpg

Valicek, P. *Fuel cell technology in underground mining (2014).* The 6th International Platinum Conference, 'Platinum–Metal for the Future', The Southern African Institute of Mining and Metallurgy.

Varaschin, J., & De Souza, E. (2015, June 20). *The 15th North American. Economics of diesel fleet replacement by electric mining equipment*. Symposium conducted at the meeting of Mine ventilation Symposium, Blacksburg, VA.

Varaschin J. (2016), *The Economic Case for Electric Mining Equipment and Technical Considerations Relating to their Implementation*. Master's Thesis.

Vergne, J.N., (2008). *Hard rock miners handbook*. Ed. Edmonton: Stantec Consulting Ltd, 174.

Victoria A. Fisher, M.P.H (July, 2012). *Diesel Exhaust Exposure in Miners Linked to Lung Cancer*. Retrieved November 30, 2017, from https://dceg.cancer.gov/news-events/linkage-newsletter/2012-07/research-publications/diesel-exhaust

Vo, T. T., Chen, X., Shen, W., & kapoor, A. (2015). "New charging strategy for lithium-ion batteries based on the integration of Taguchi method and state of charge estimation." *Journal of Power Sources, 273*, 413-422.

West, J. (1994). DC, induction, reluctance and PM motors for electric vehicles. *Power Engineering Journal, 8*(2), 77-88.

Where the Energy Goes: Gasoline Vehicles, US Department of Energy. Retrieved on July 19, 2017, from https://www.fueleconomy.gov/feg/atv.shtml#data-sources

Where the Energy Goes: Electric Cars, US Department of Energy. Retrieved on July 19, 2017, from https://www.fueleconomy.gov/feg/atv-ev.shtml#data-sources.

Wood, A. (2014); Personal Communication with Ozdogan M. and Ozdogan H., *Joy Global (UK) Surface Limited, Wigan, England*

Wood, a. (n.d.); Electric Drive Mining Class Wheel Loaders as Primary Production Tools. Retrieved on April 4, 2018, from https://www.academia.edu/11694100/Electric_Drive_Mining_Class_Wheel_Loaders_as_Primary_Production_Tools

Woof M., "Technology for Underground Loading and Hauling Systems Offers Exciting Prospects," Eng. Min. J., vol. 206, no. 3, p. 32, 2005.

World Health Organization, International Agency for Research on Cancer. (June 12, 2012). *IARC: DIESEL ENGINE EXHAUST CARCINOGENIC* [Press release]. Retrieved November 30, 2017, from https://www.iarc.fr/en/media-centre/pr/2012/pdfs/pr213_E.pdf

Yong, J. Y., Ramachandaramurthy, V. K., Tan, K. M., & Mithulananthan, N. (2015). A review on the state-of-the-art technologies of electric vehicle, its impacts and prospects. *Renewable and Sustainable Energy Reviews, 49*, 365-385.

Yonghuang Y. (2015). A Study on the Thermal Behavior and Capacity Recovery of Lithium-ion Batteries and Their Thermal Management Using Heat Pipes. (Doctoral dissertation). Retrieved on April 11, 2017, from http://pqdtopen.proquest.com/doc/1761646424.html?FMT=AI

Zeraoulia, M., Benbouzid, M. E., & Diallo, D. (2006). Electric Motor Drive Selection Issues for HEV Propulsion Systems: A Comparative Study. *IEEE Trans. Veh. Technol. IEEE Transactions on Vehicular Technology, 55*(6), 1756-1764.

8 Appendix A – Single Cell Study Results

In the current appendix is presented the results for the single cell case during 25°C, 30°C, and 35°C ambient temperature. The case for 40°C is excluded in this chapter since it is already mentioned during section 5.3. Some of the results obtained from the infrared camera might be slightly divergent from the thermocouples. This can be caused by uncertainties in the camera measurement, capture range, and the fact that the chamber needs to be open to capture the picture. The maximum temperature obtained in the thermal imaging is the maximum temperature in the target area, as for the temperature scale, it is the result of the temperature range in the whole field of view.

8.1 Charging – 25°C

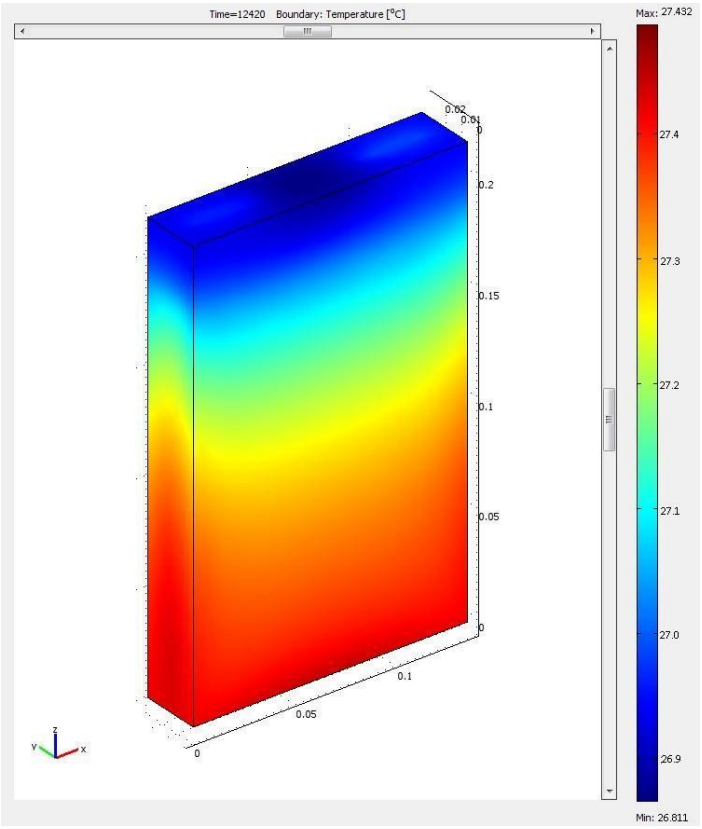

Figure 8-1: Final visual simulation of a temperature gradient along the external battery surface for 16.7A charging. Total running time of 207 minutes.

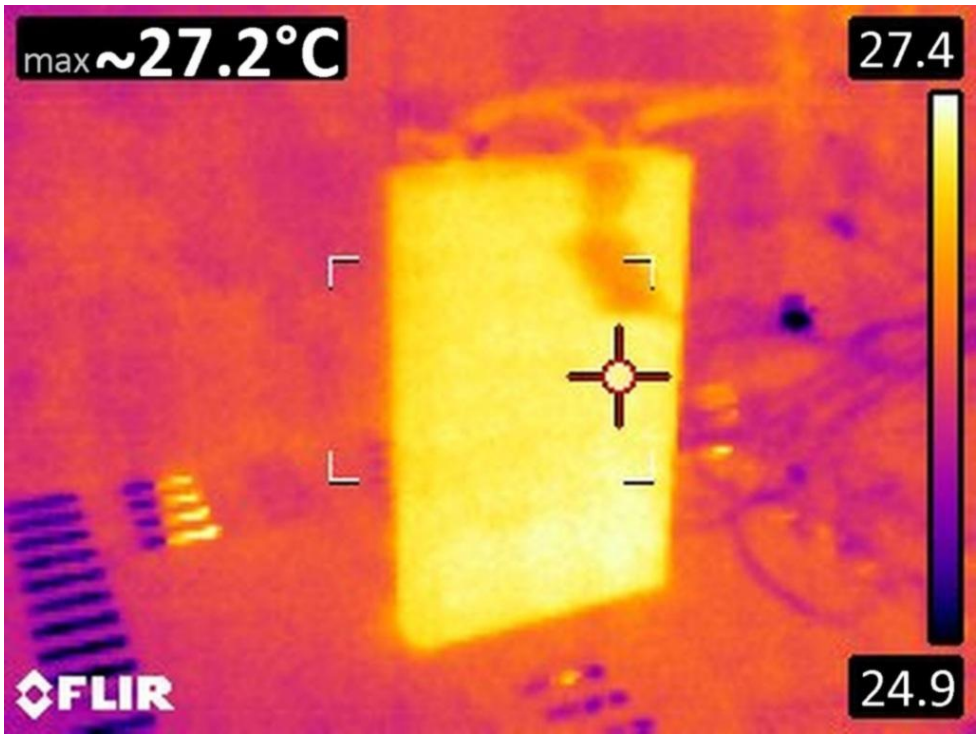

Figure 8-2: Thermal picture from the battery at 207 minutes for 16.7A charging, 25°C ambient.

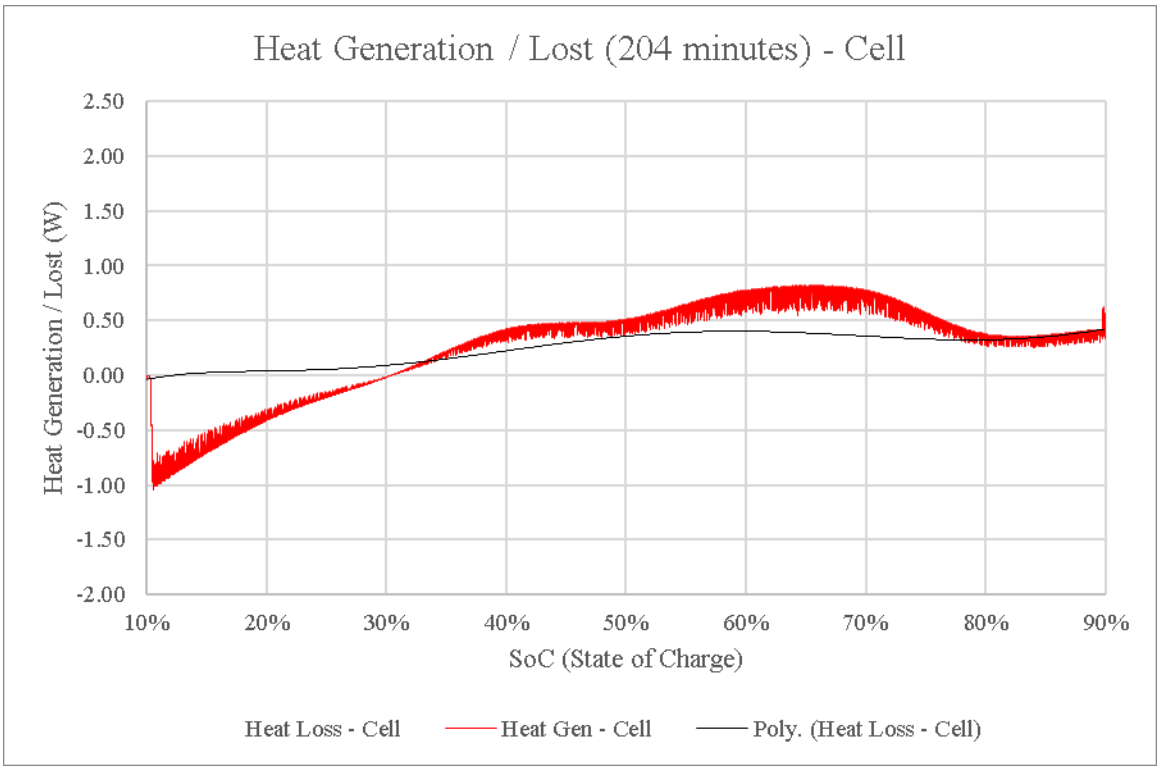

Figure 8-3: Experimental Generated heat and Lost during battery charge for the charging condition.

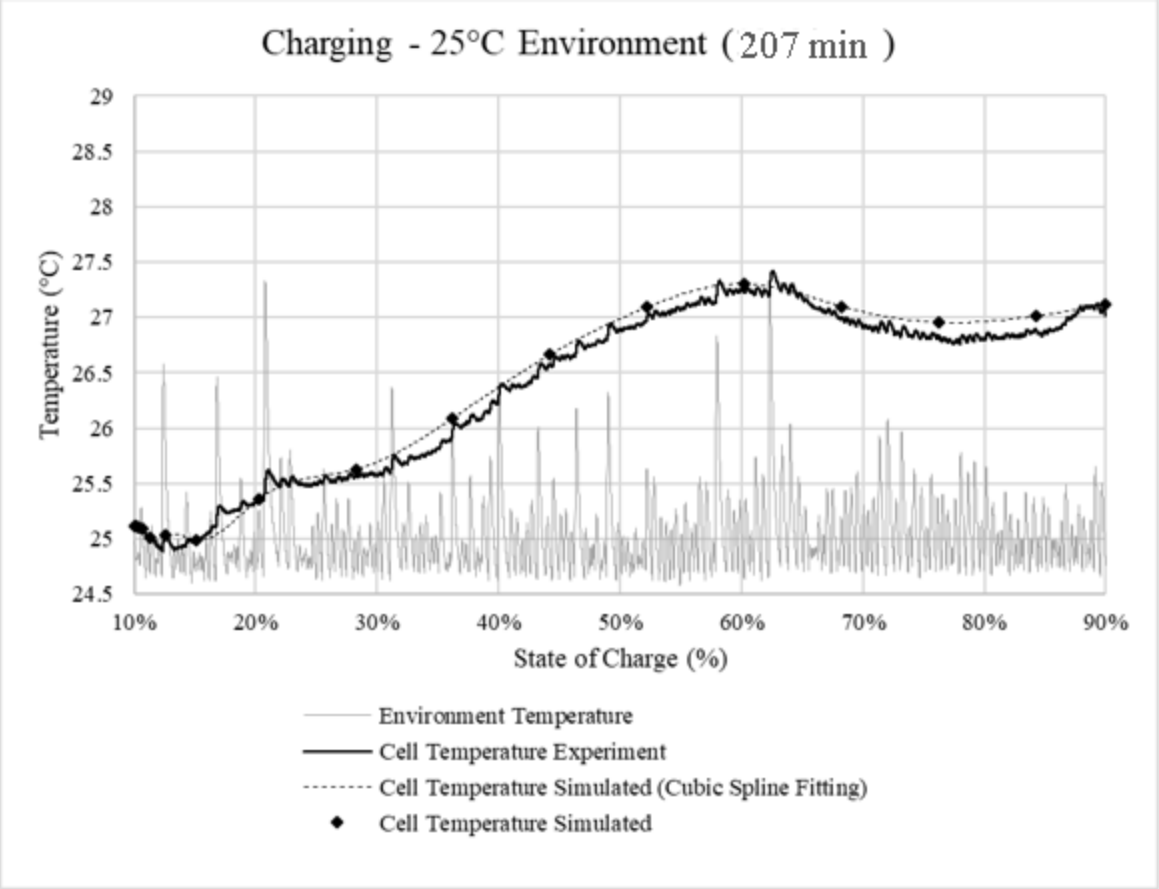

Figure 8-4: Simulated temperature and Experimental temperature obtained during charging at 25°C.

8.2 Charging – 30°C

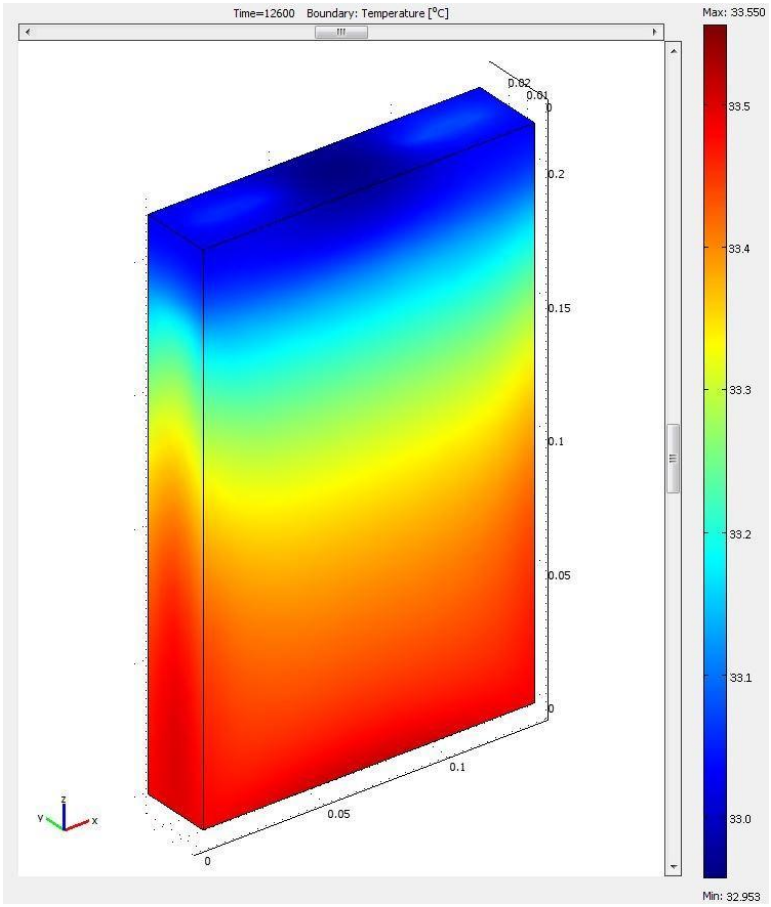

Figure 8-5: Final visual simulation of a temperature gradient along the external battery surface for 16.5A charging. Total running time of 210 minutes.

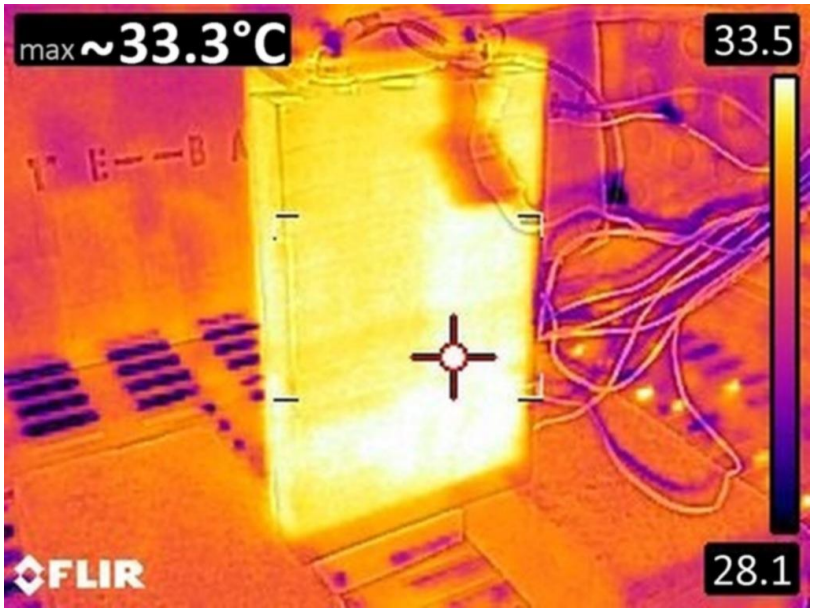

Figure 8-6: Thermal picture from the battery at 210 minutes for 16.5A charging, 30°C ambient.

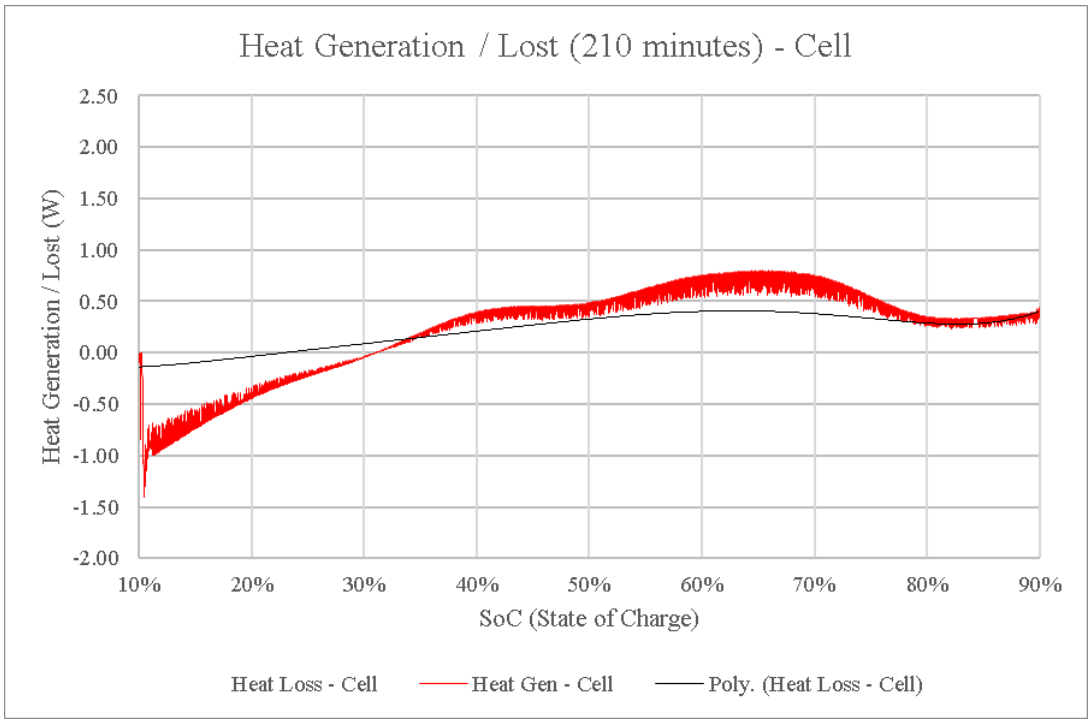

Figure 8-7: Experimental Generated heat and Lost during battery charge for the charging condition.

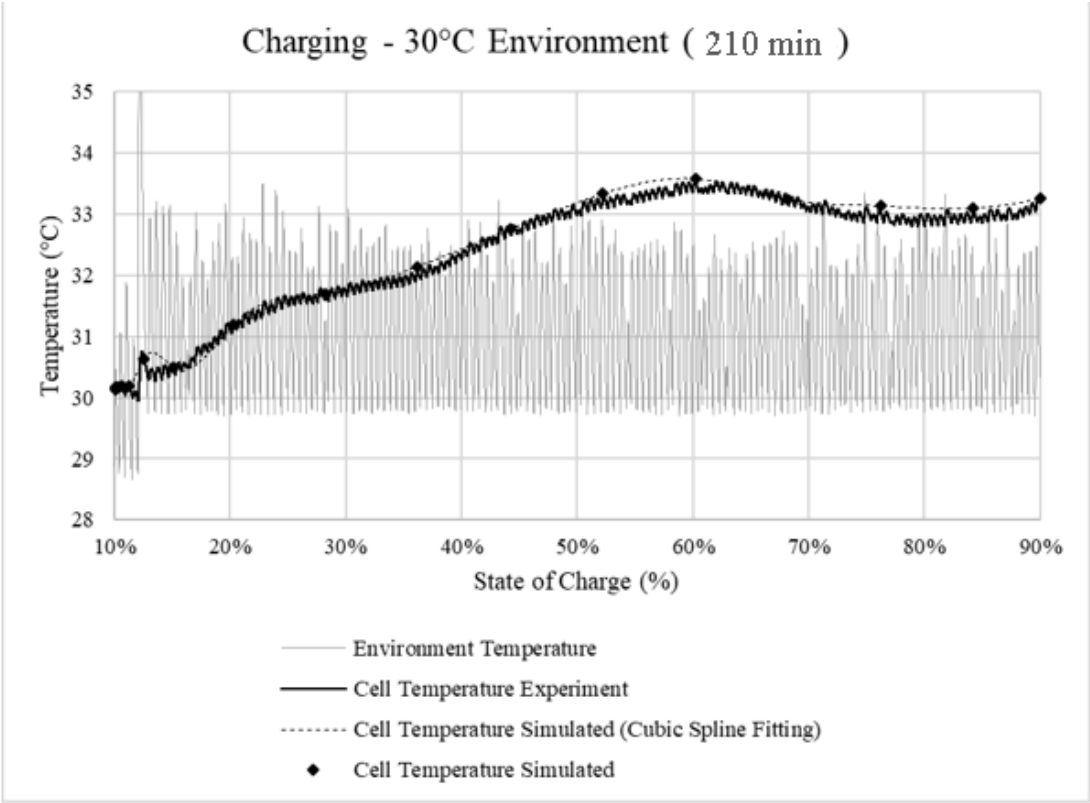

Figure 8-8: Simulated temperature and Experimental temperature obtained during charging at 30°C.

8.3 Charging – 35°C

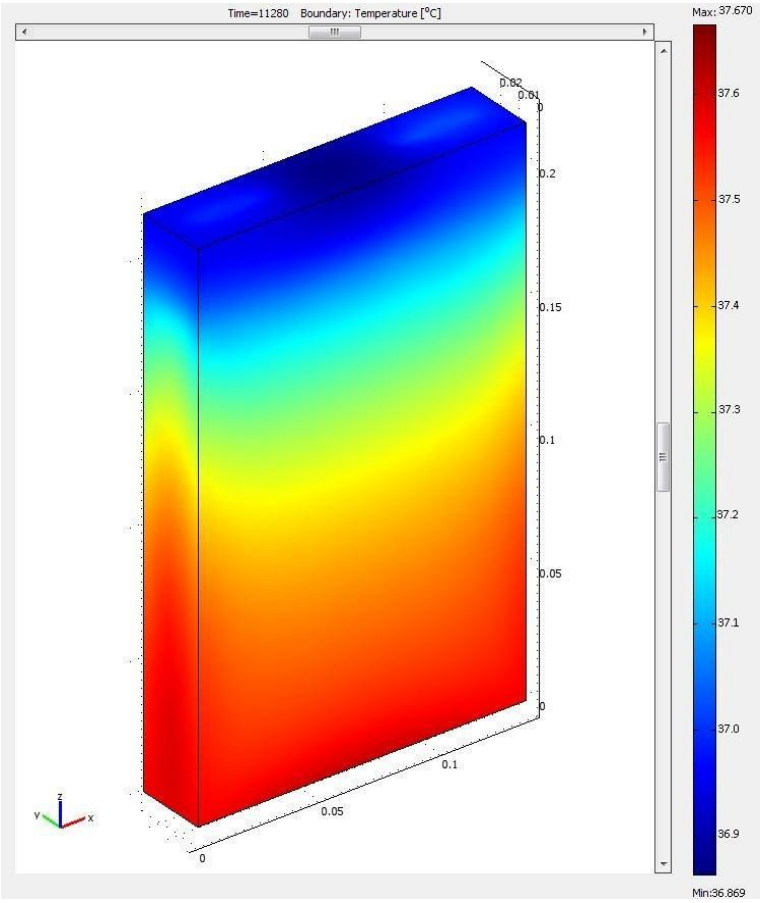

Figure 8-9: Final visual simulation of a temperature gradient along the external battery surface for 18.4A charging. Total running time of 188 minutes.

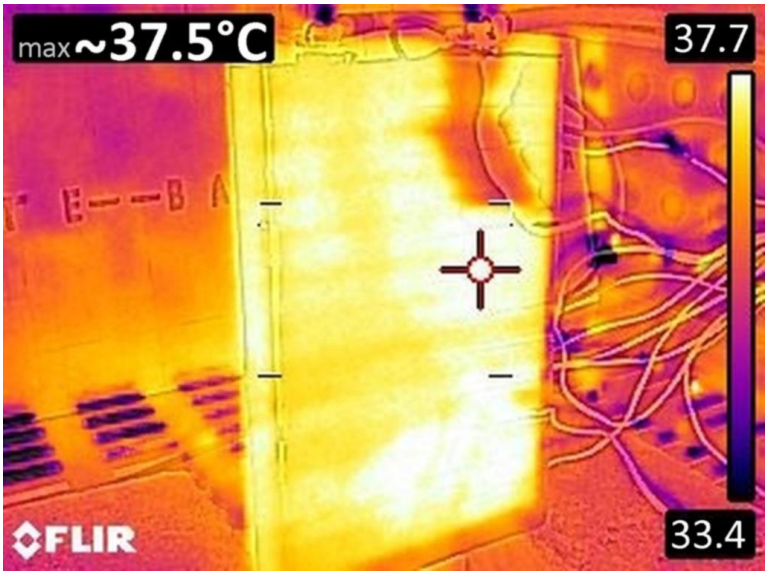

Figure 8-10: Thermal picture from the battery at 188 minutes for 18.4A charging, 35°C ambient.

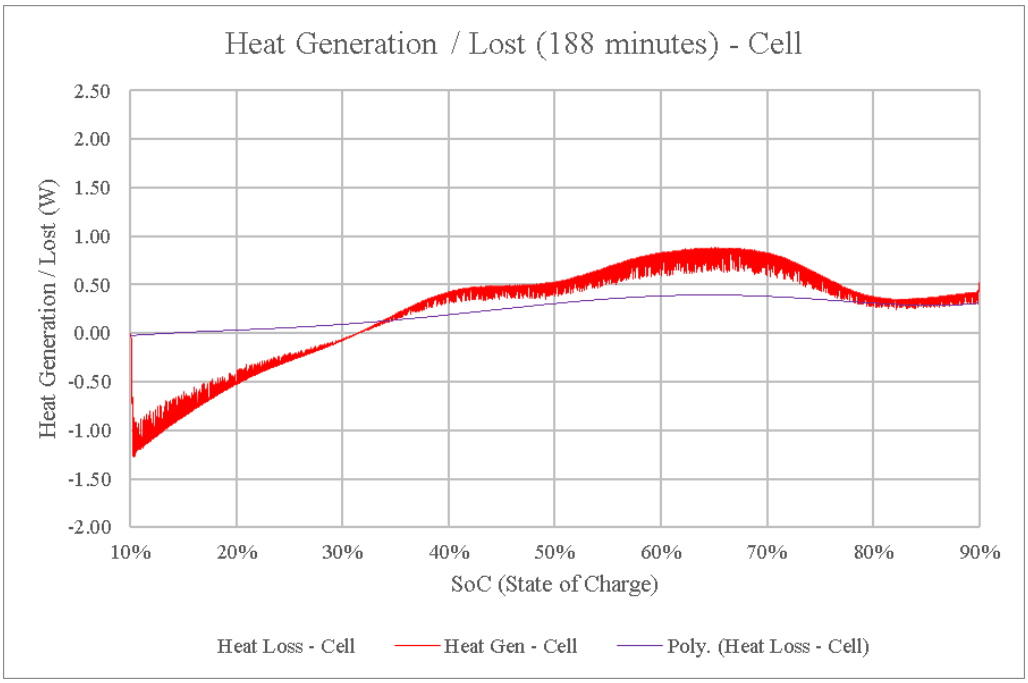

Figure 8-11: Experimental Generated heat and Lost during battery charge for the charging condition.

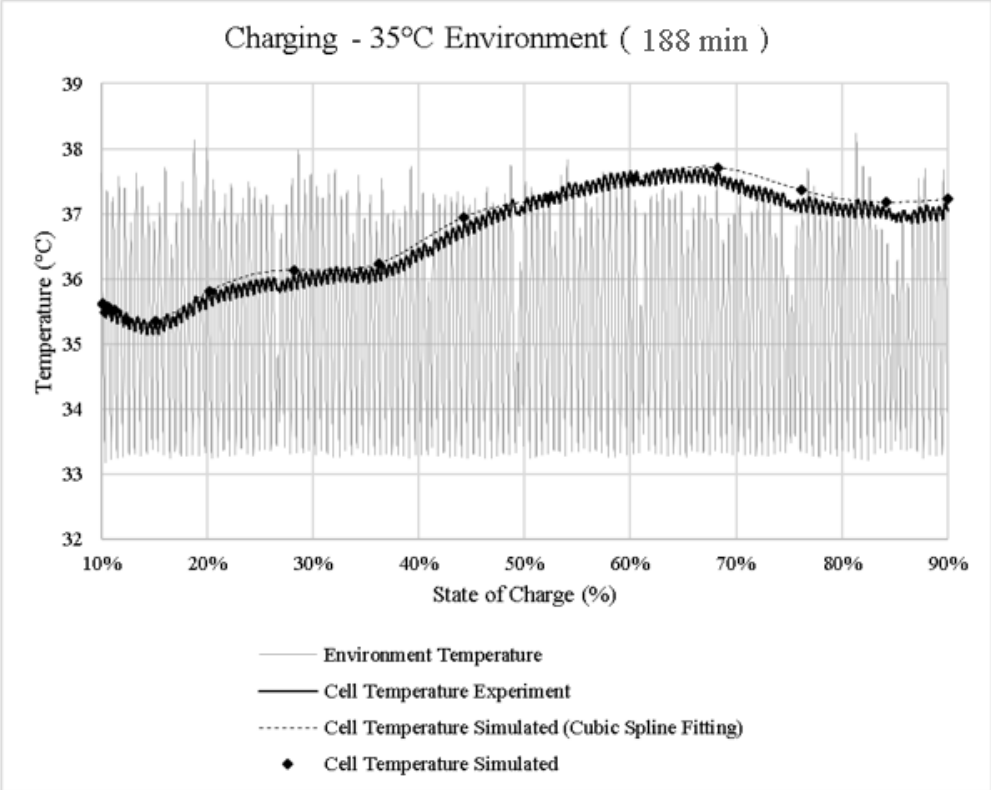

Figure 8-12: Simulated temperature and Experimental temperature obtained during charging at 35°C.

8.4 Downhill – 25°C

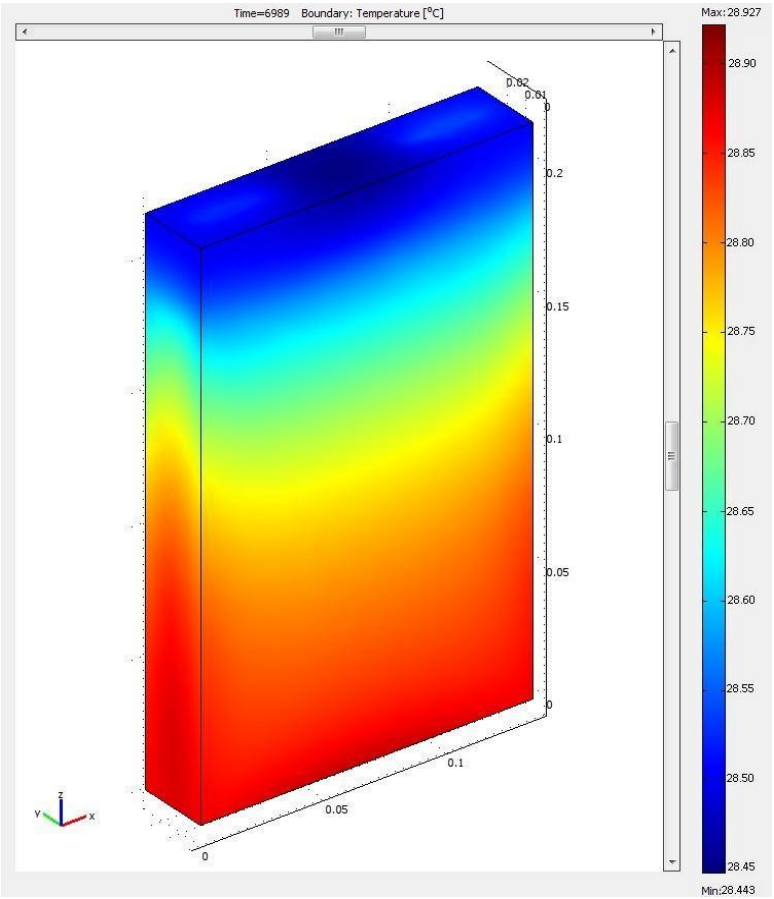

Figure 8-13: Final visual simulation of a temperature gradient along the external battery surface for 29.7A Downhill. Total running time of 116 minutes.

Figure 8-14: Thermal picture from the battery at 116 minutes for 29.7A charging, 25°C ambient.

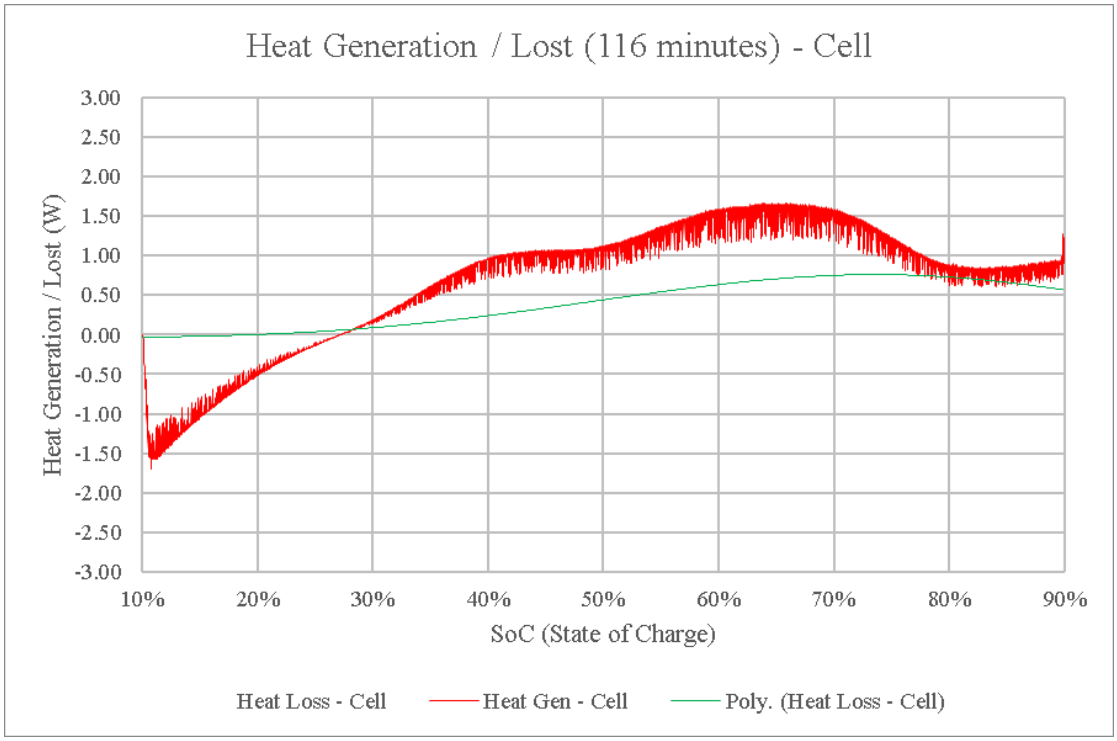

Figure 8-15: Experimental Generated heat and Lost during battery charge for the Downhill condition.

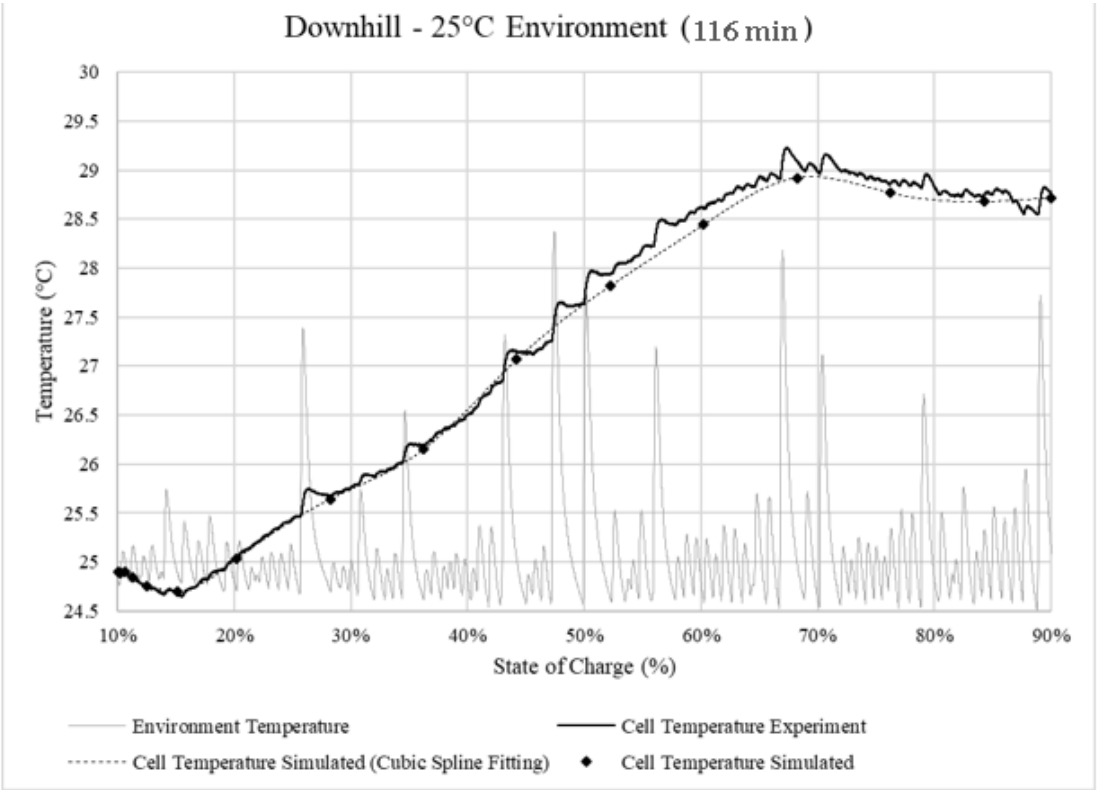

Figure 8-16: Simulated temperature and Experimental temperature obtained during Downhill at 25°C.

8.5 Downhill – 30°C

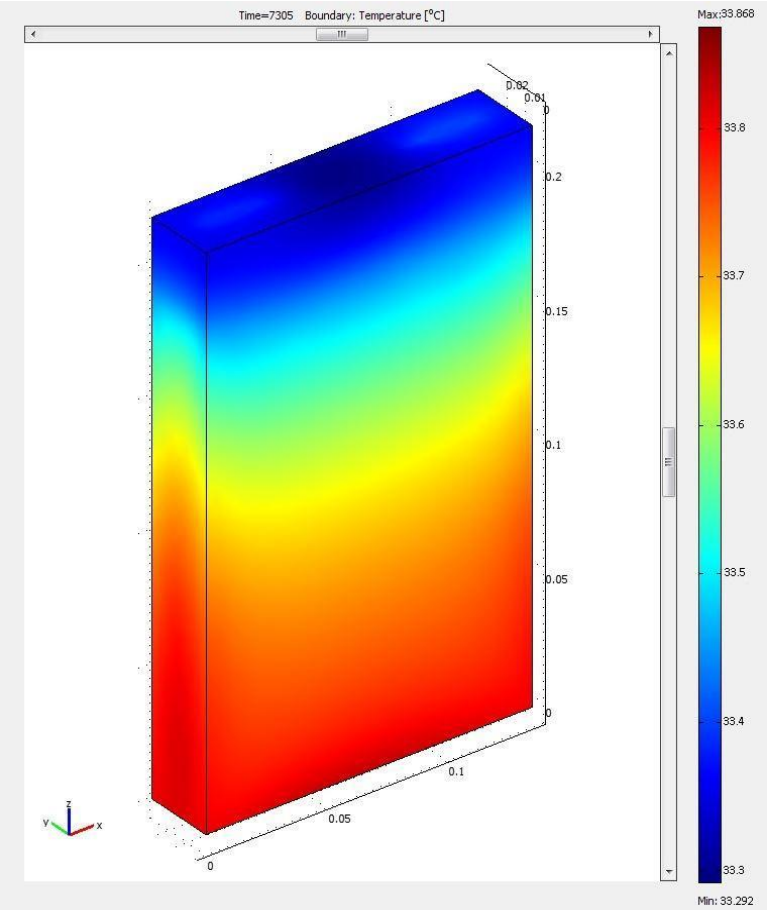

Figure 8-17: Final visual simulation of a temperature gradient along the external battery surface for 28.4A Downhill. Total running time of 122 minutes.

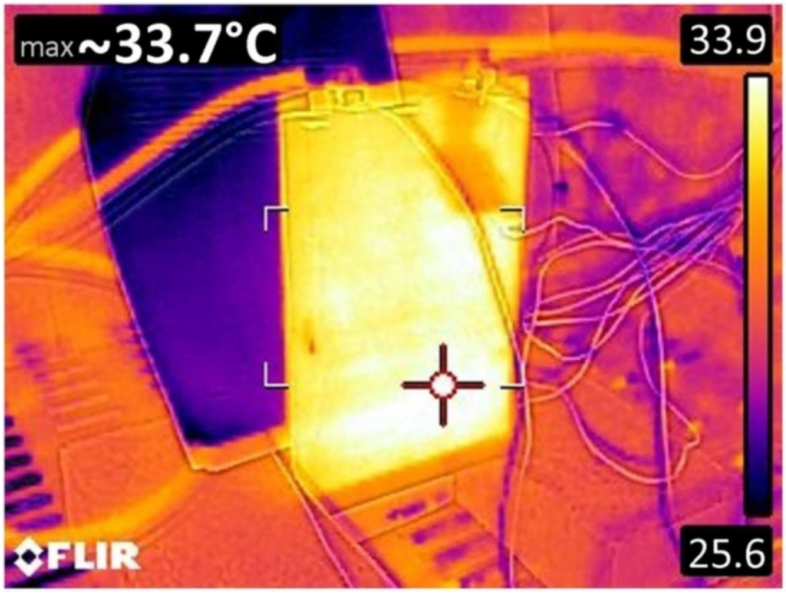

Figure 8-18: Thermal picture from the battery at 122 minutes for 28.4A charging, 30°C ambient.

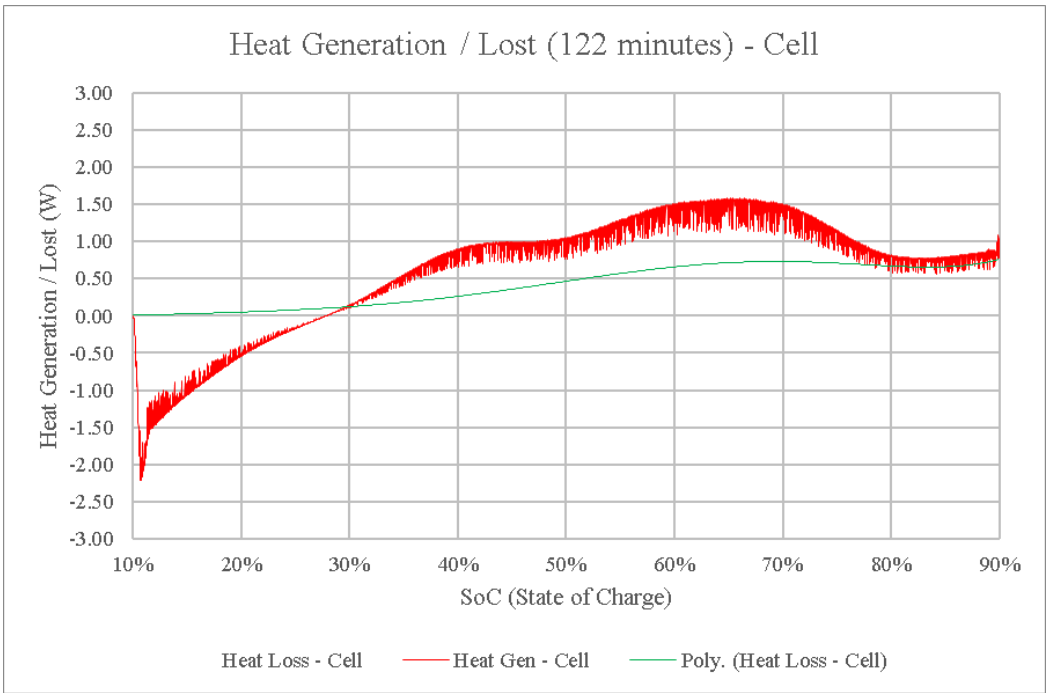

Figure 8-19: Experimental Generated heat and Lost during battery charge for the Downhill condition.

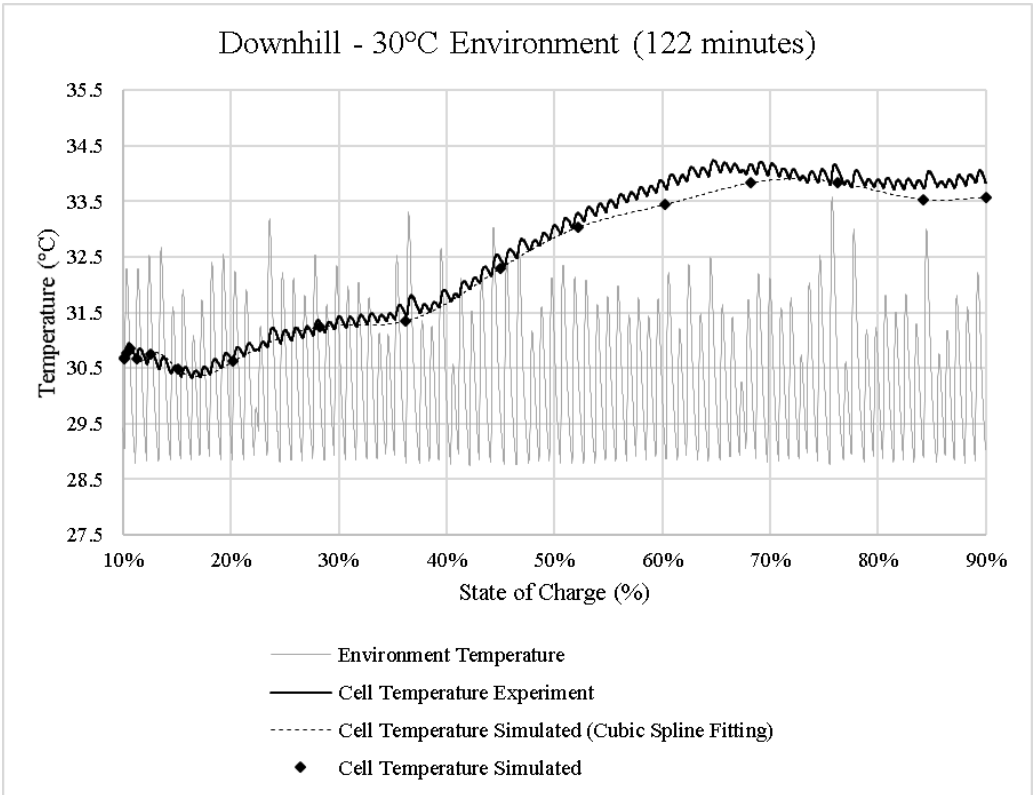

Figure 8-20: Simulated temperature and Experimental temperature obtained during Downhill at 30°C.

8.6 Downhill – 35°C

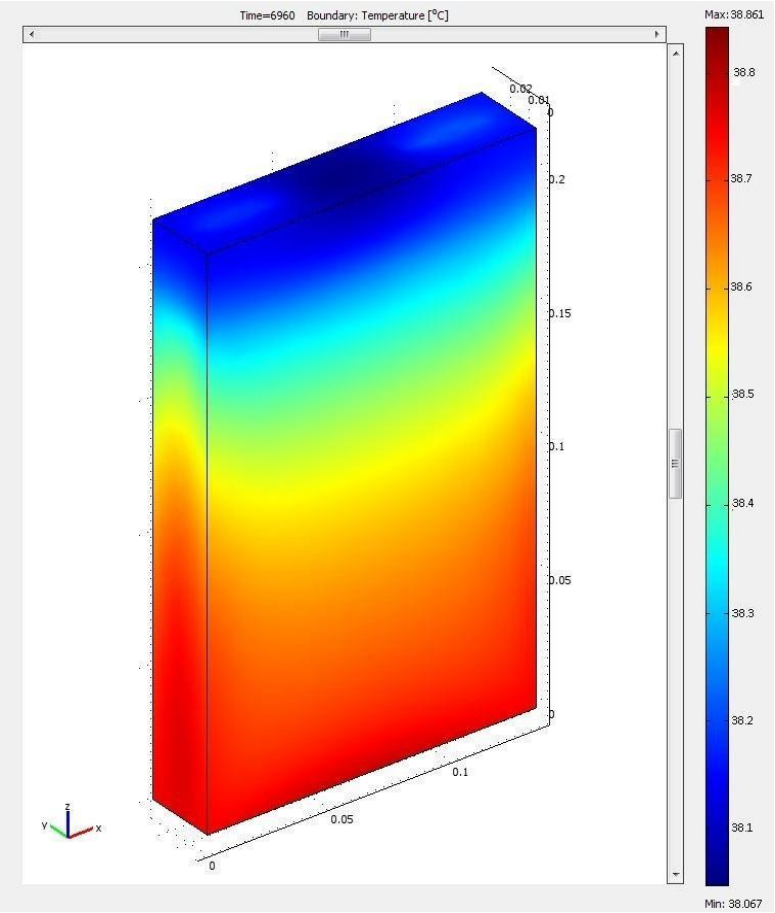

Figure 8-21: Final visual simulation of a temperature gradient along the external battery surface for 29.8A Downhill. Total running time of 116 minutes.

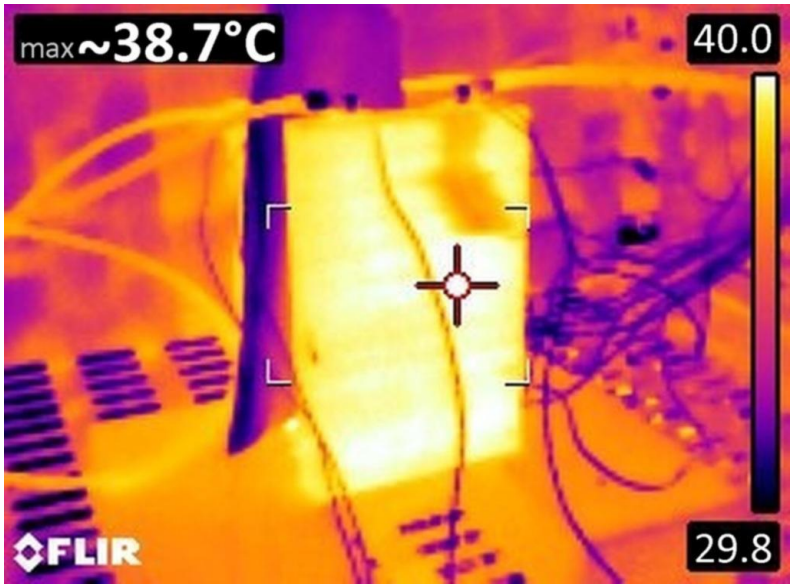

Figure 8-22: Thermal picture from the battery at 116 minutes for 29.8A charging, 35°C ambient.

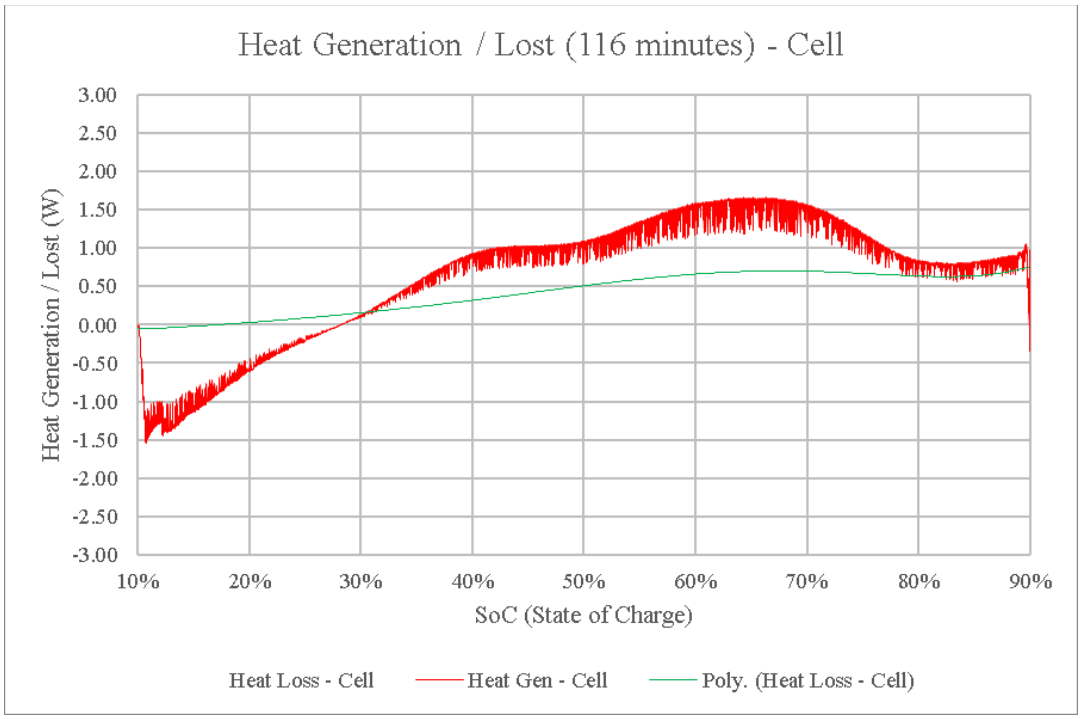

Figure 8-23: Experimental Generated heat and Lost during battery charge for the Downhill condition.

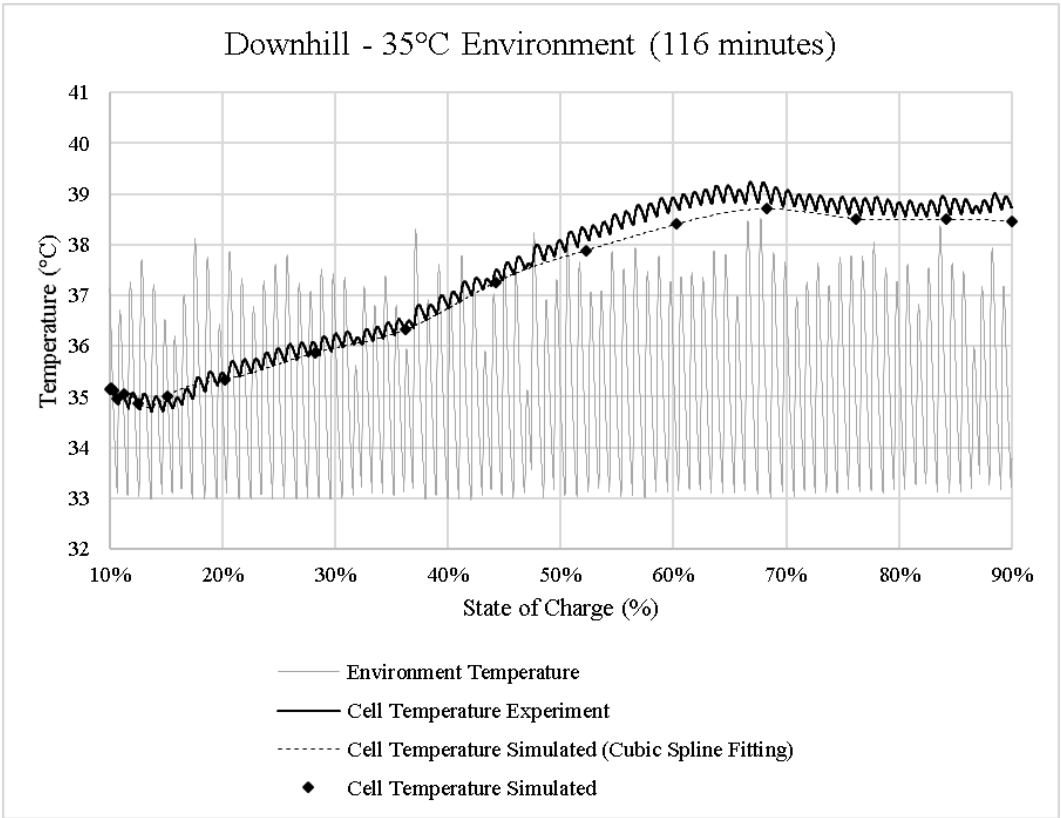

Figure 8-24: Experimental Generated heat and Lost during battery charge for the Downhill condition.

8.7 Flat – 25°C

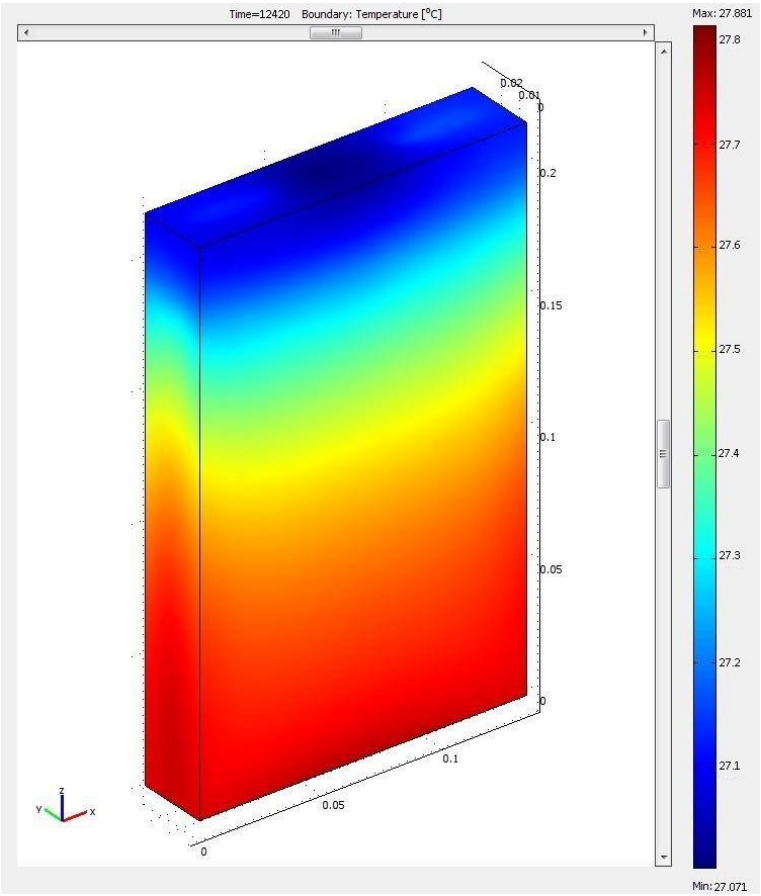

Figure 8-25: Final visual simulation of a temperature gradient along the external battery surface for 17.2A discharging. Total running time of 200 minutes.

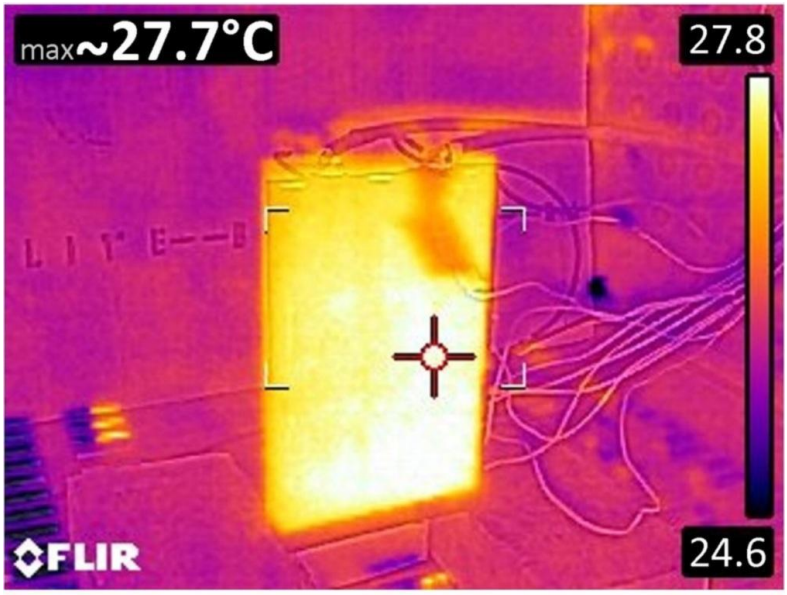

Figure 8-26: Thermal picture from the battery at 200 minutes for 17.2A discharging, 25°C ambient.

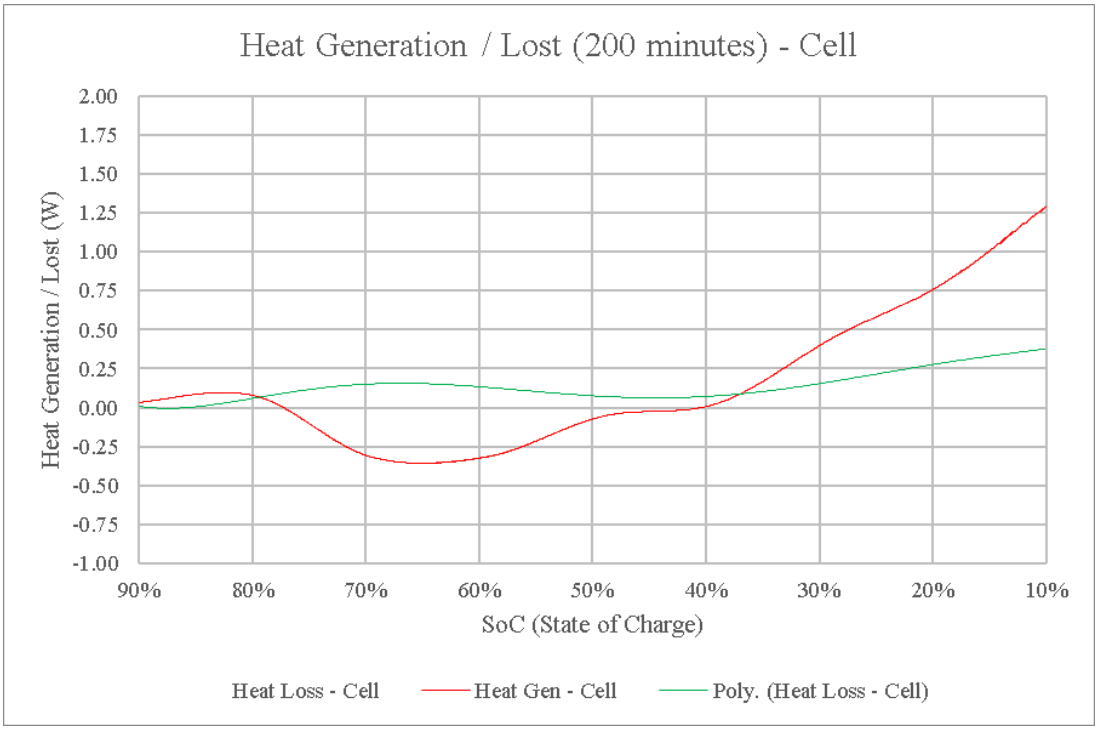

Figure 8-27: Experimental Generated heat and Lost during battery discharge for the flat condition.

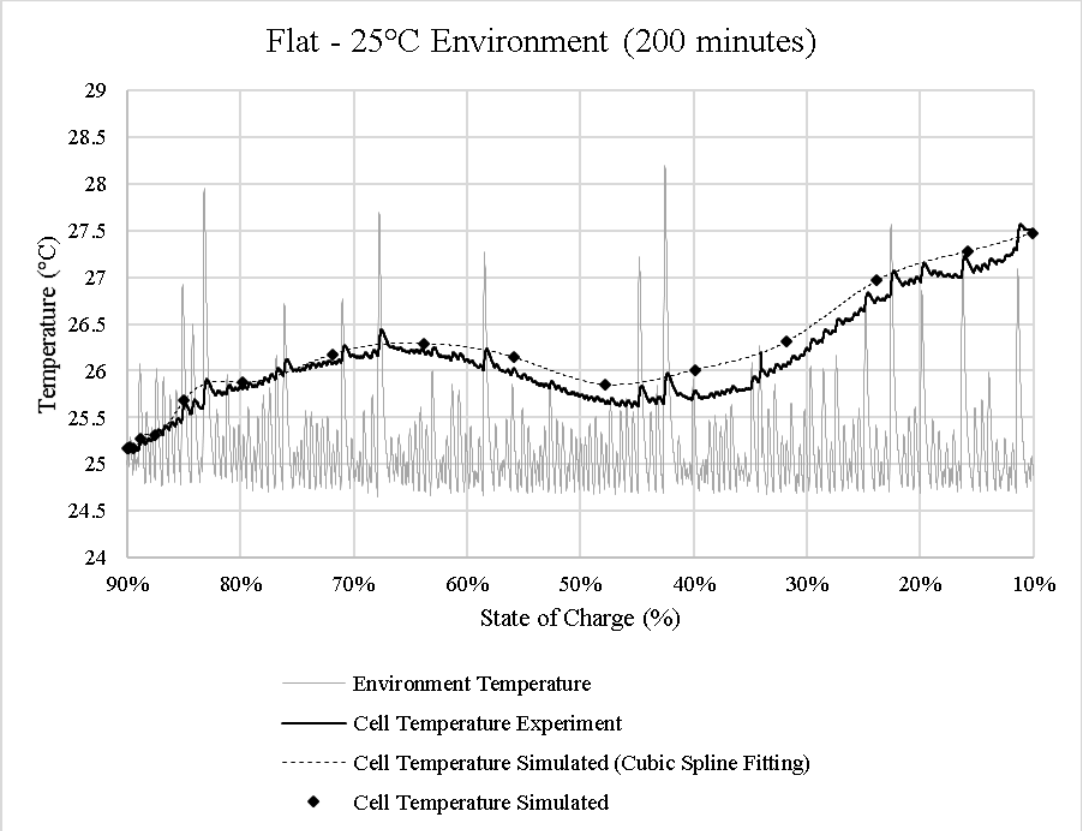

Figure 8-28: Experimental Generated heat and Lost during battery discharge for the flat condition.

8.8 Flat – 30°C

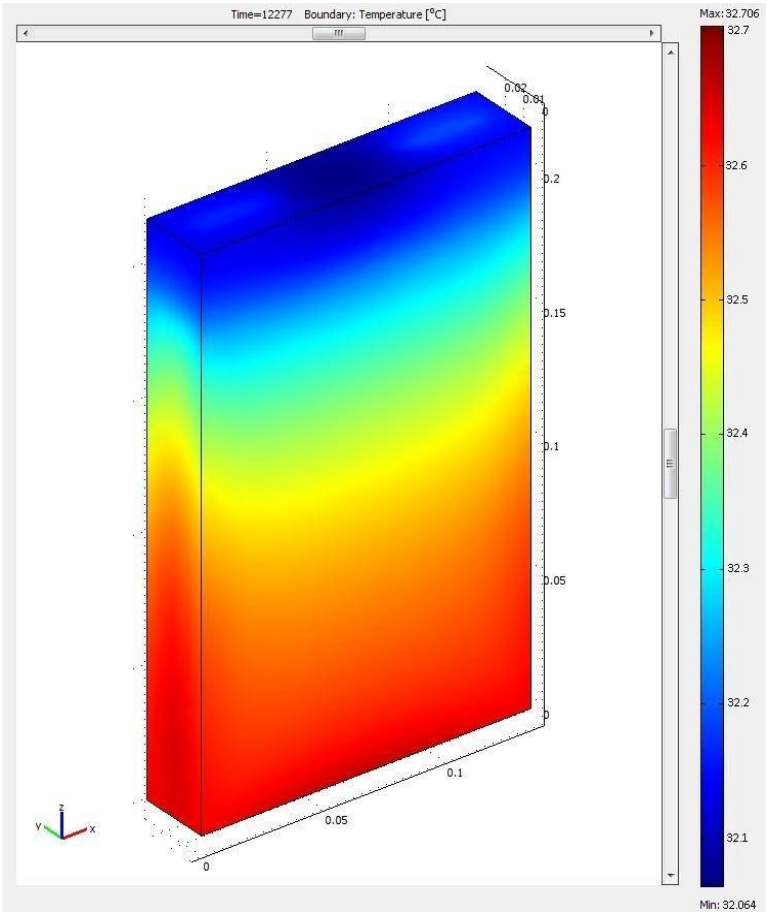

Figure 8-29: Final visual simulation of a temperature gradient along the external battery surface for 16.9A discharging. Total running time of 205 minutes.

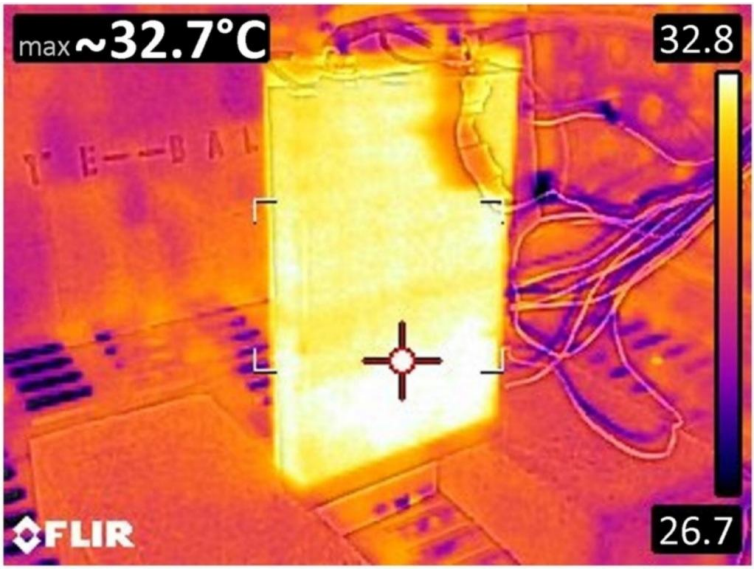

Figure 8-30: Thermal picture from the battery at 205 minutes for 16.9A discharging, 30°C ambient.

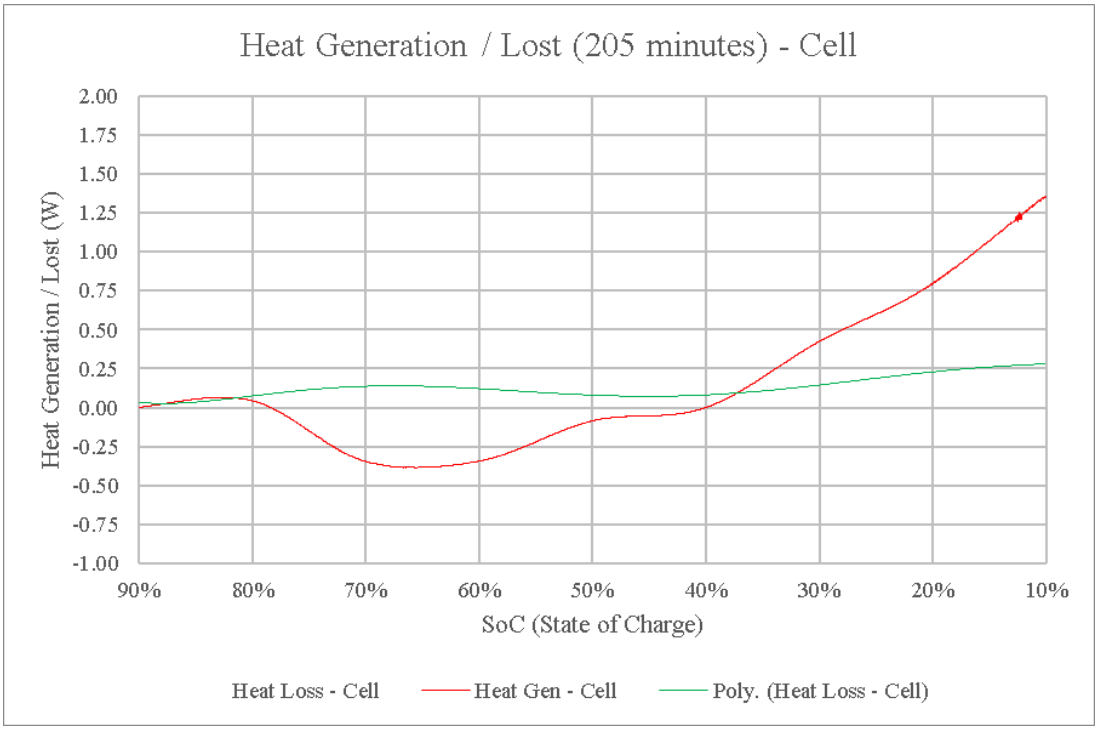

Figure 8-31: Experimental Generated heat and Lost during battery discharge for the flat condition.

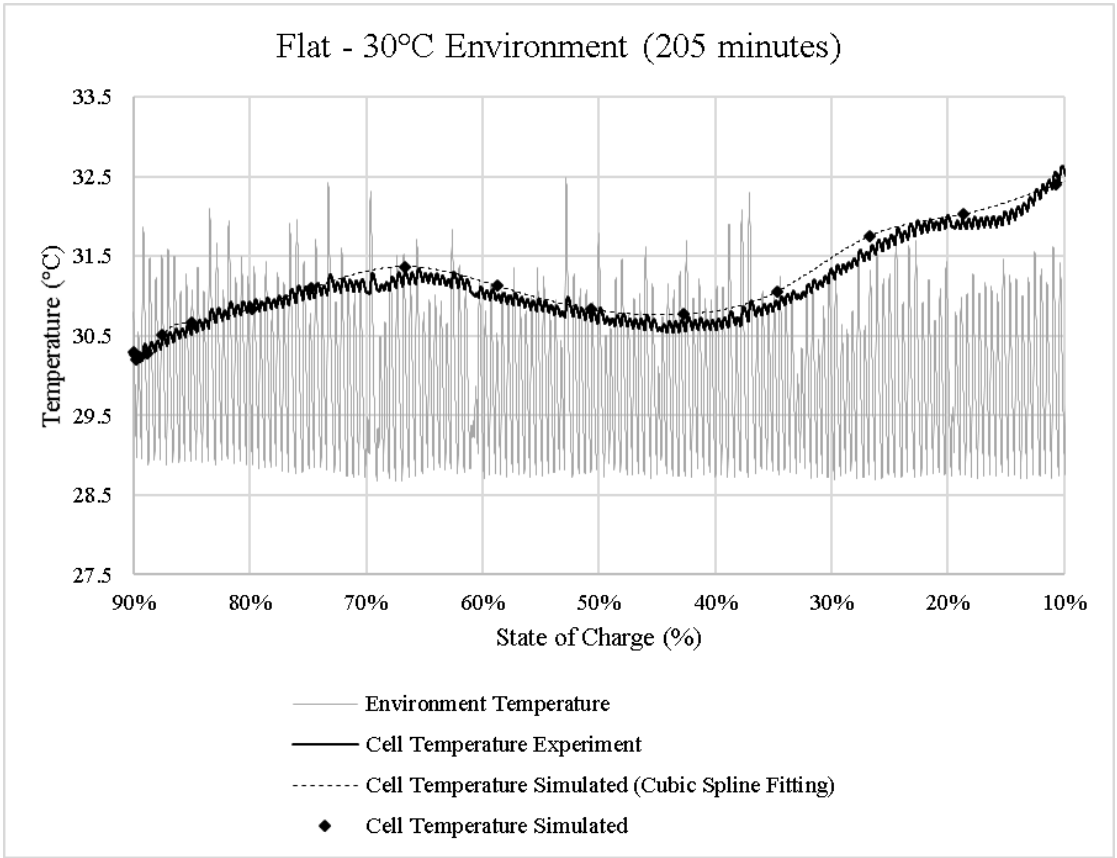

Figure 8-32: Experimental Generated heat and Lost during battery discharge for the flat condition.

8.9 Flat – 35°C

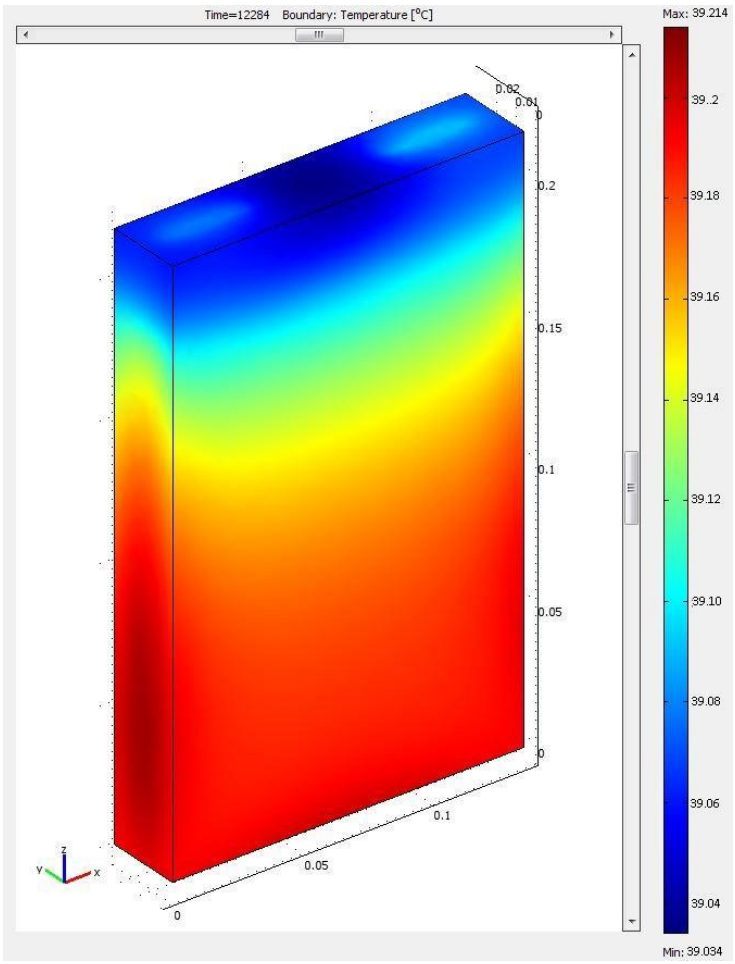

Figure 8-33: Final visual simulation of a temperature gradient along the external battery surface for 16.9A discharging. Total running time of 205 minutes.

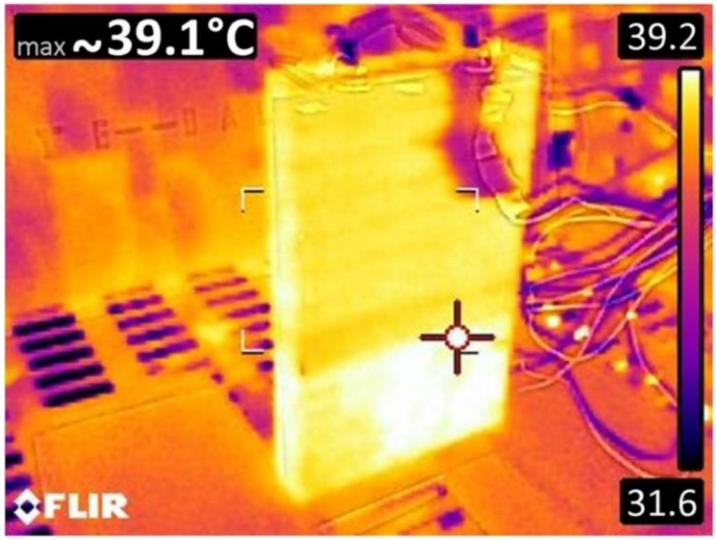

Figure 8-34: Thermal picture from the battery at 205 minutes for 16.9A discharging, 35°C ambient.

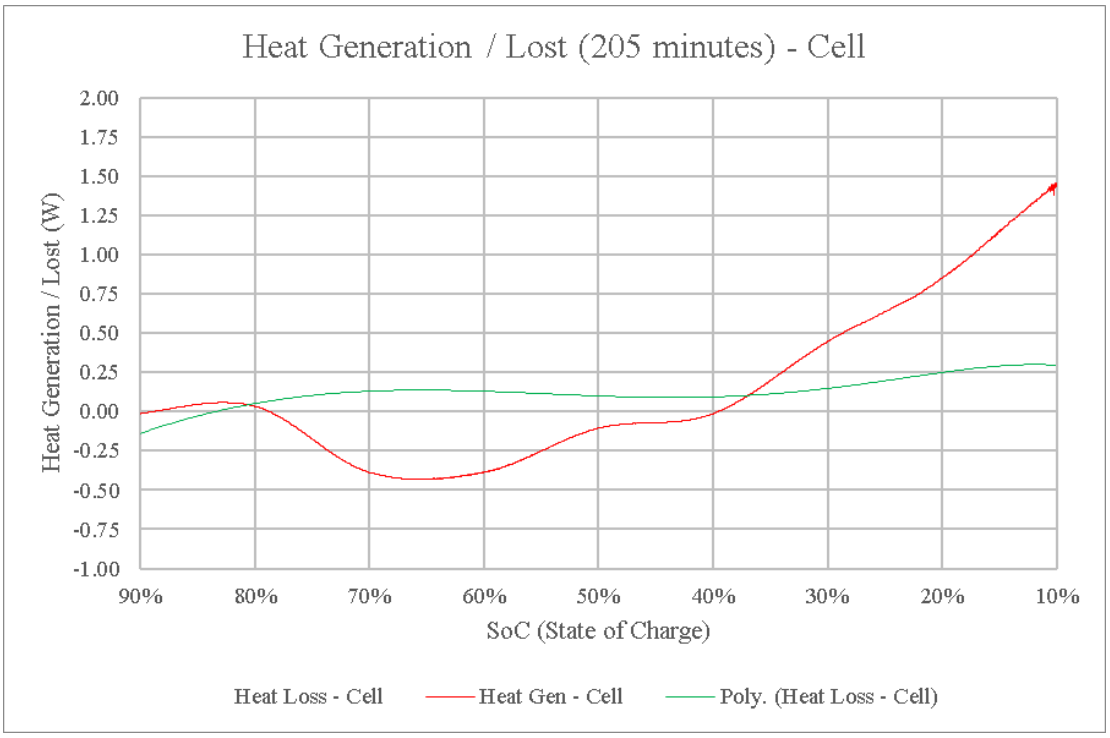

Figure 8-35: Experimental Generated heat and Lost during battery discharge for the flat condition.

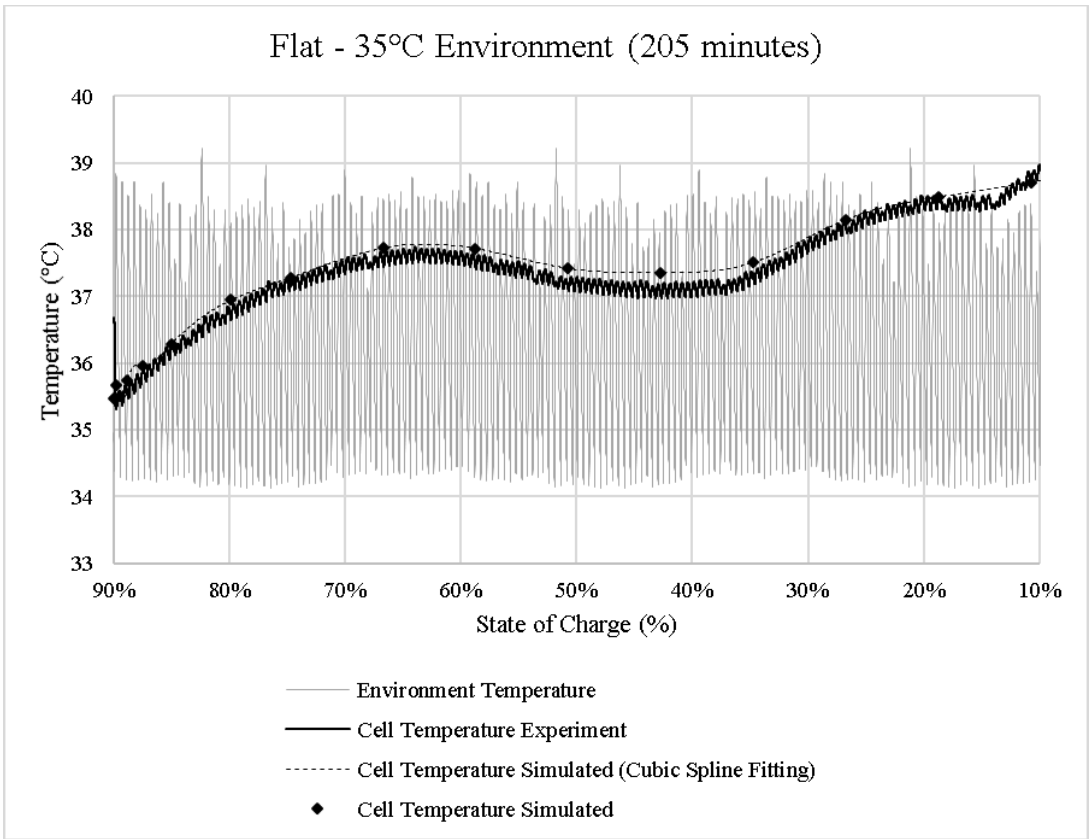

Figure 8-36: Simulated temperature and Experimental temperature obtained during discharging at 35°C.

8.10 Uphill – 25°C

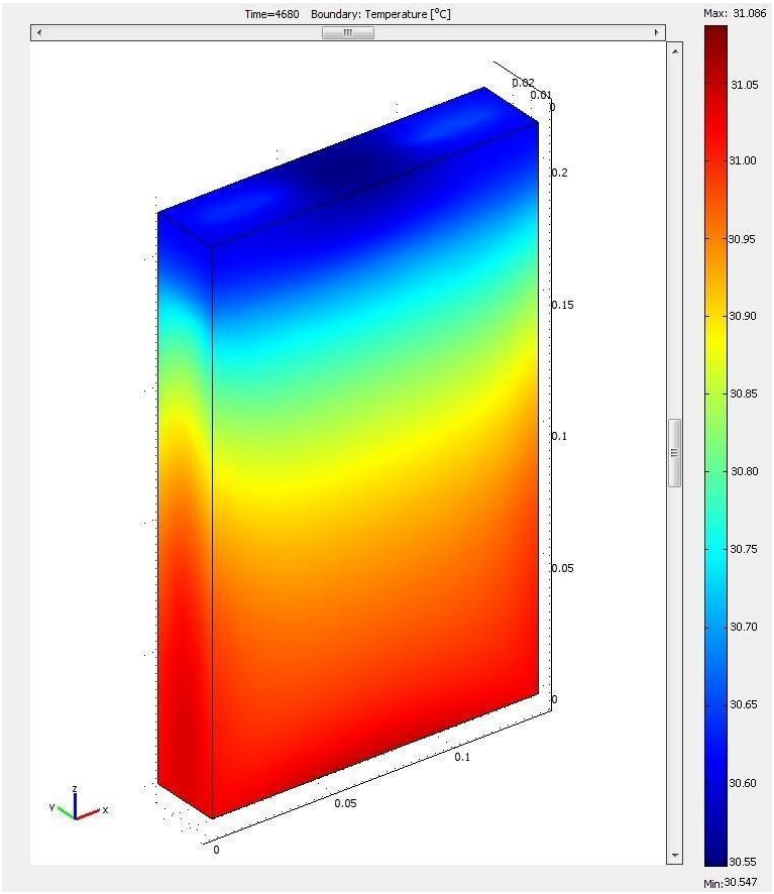

Figure 8-37: Final visual simulation of a temperature gradient along the external battery surface for 44.3A discharging. Total running time of 78 minutes.

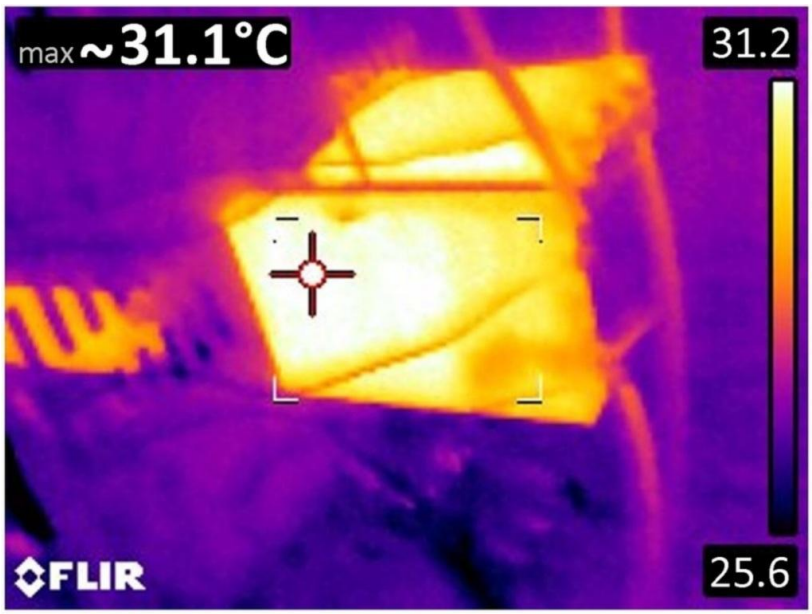

Figure 8-38: Thermal picture from the battery at 78 minutes for 44.3A discharging, 25°C ambient.

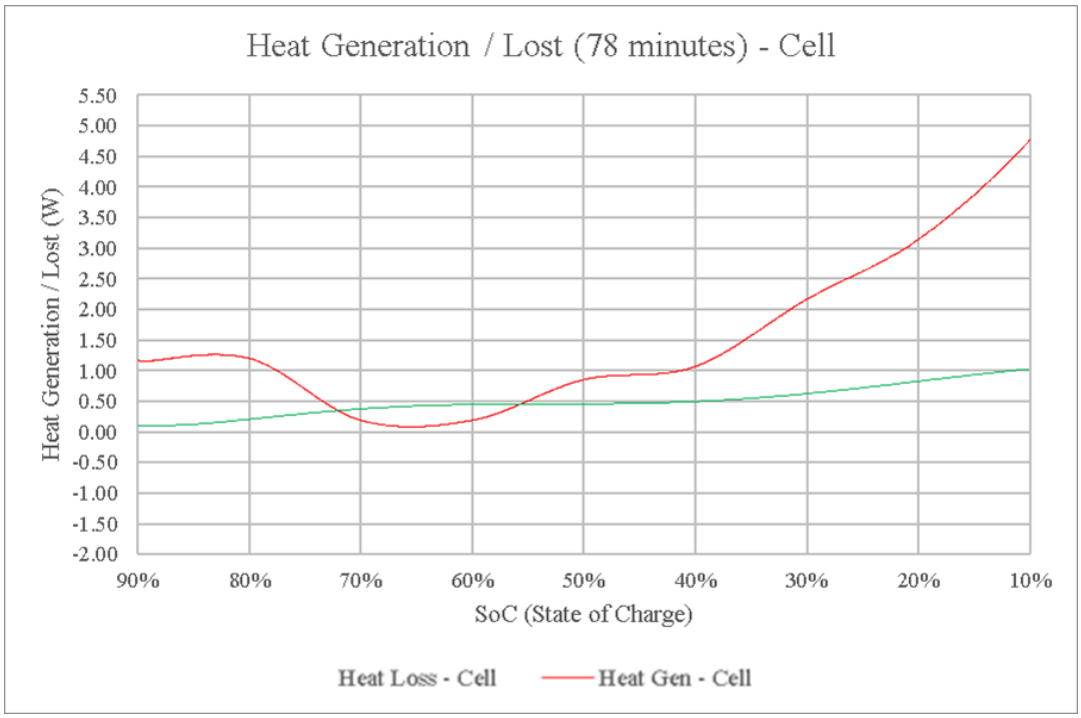

Figure 8-39: Experimental Generated heat and Lost during battery discharge for the Uphill condition.

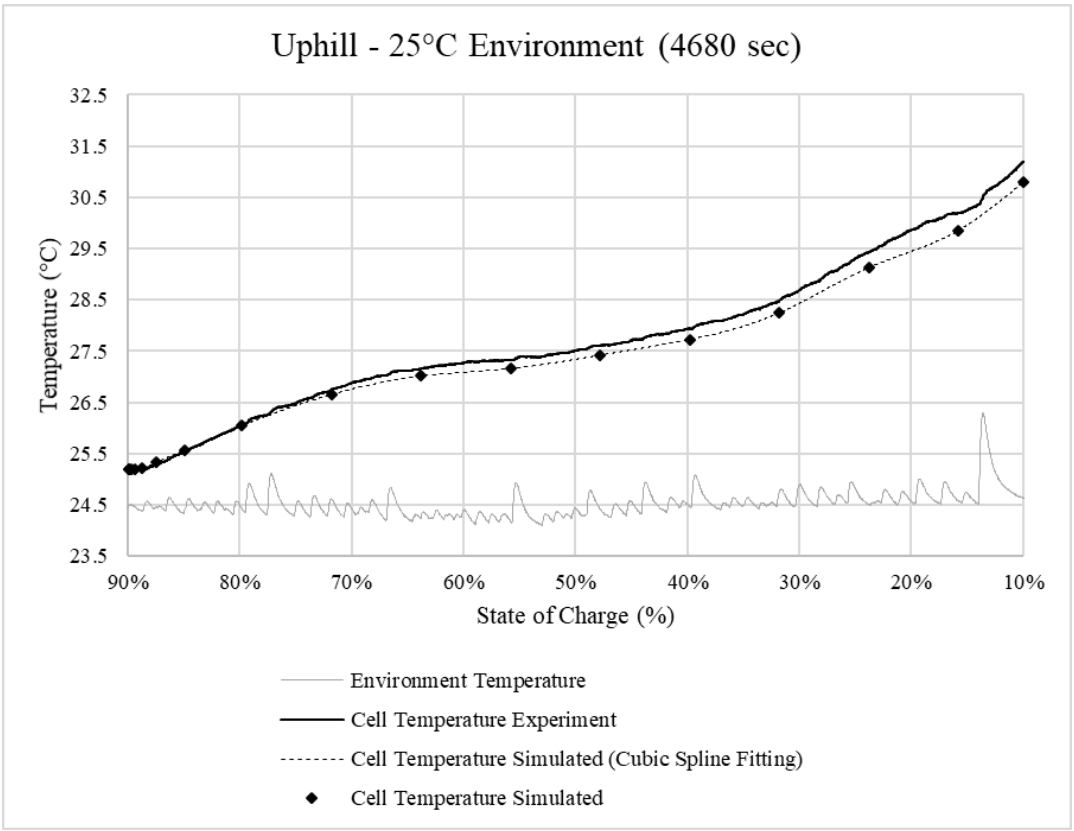

Figure 8-40: Simulated temperature and Experimental temperature obtained during discharging at 25°C.

8.11 Uphill – 30°C

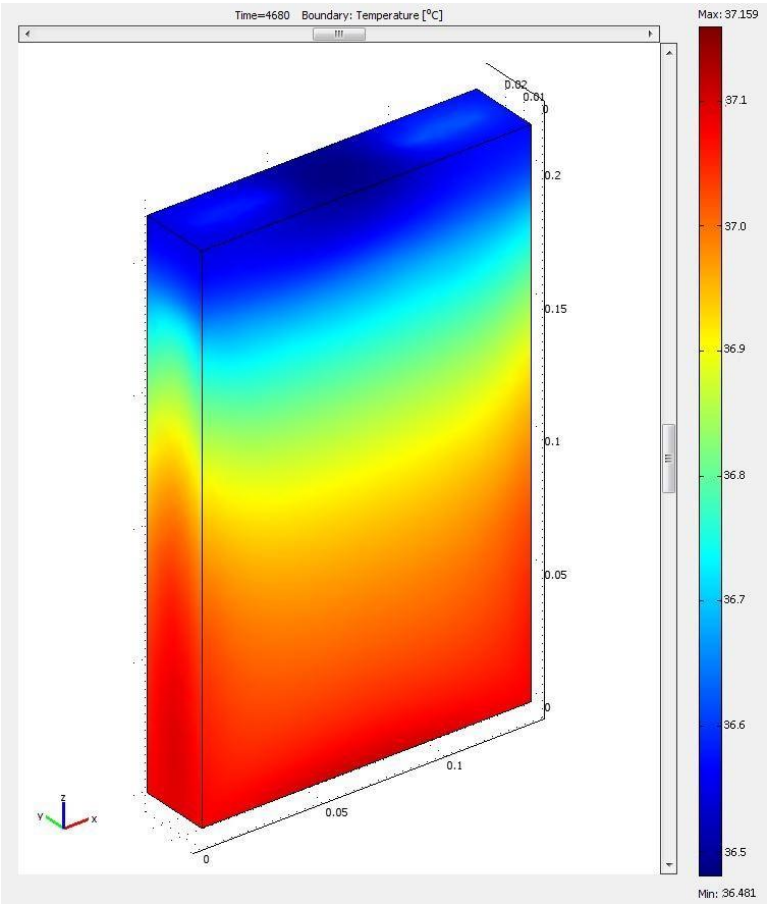

Figure 8-41: Final visual simulation of a temperature gradient along the external battery surface for 44.3A discharging. Total running time of 78 minutes.

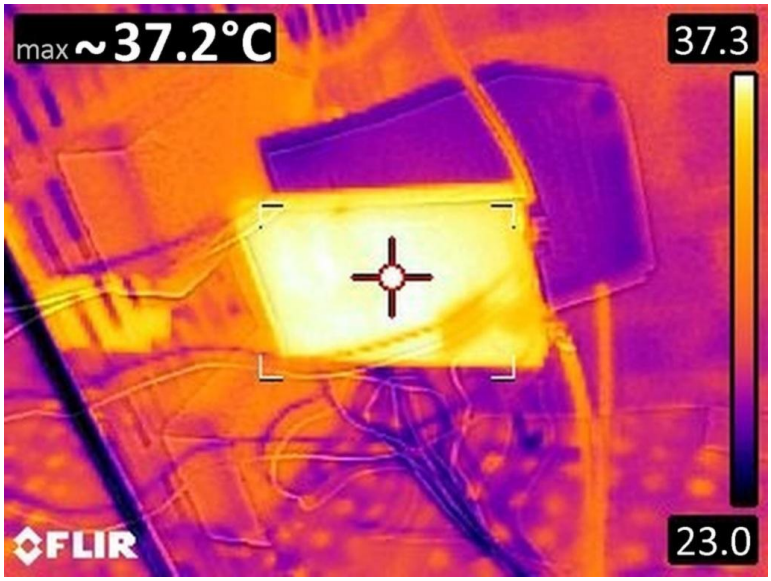

Figure 8-42: Thermal picture from the battery at 78 minutes for 44.3A discharging, 30°C ambient.

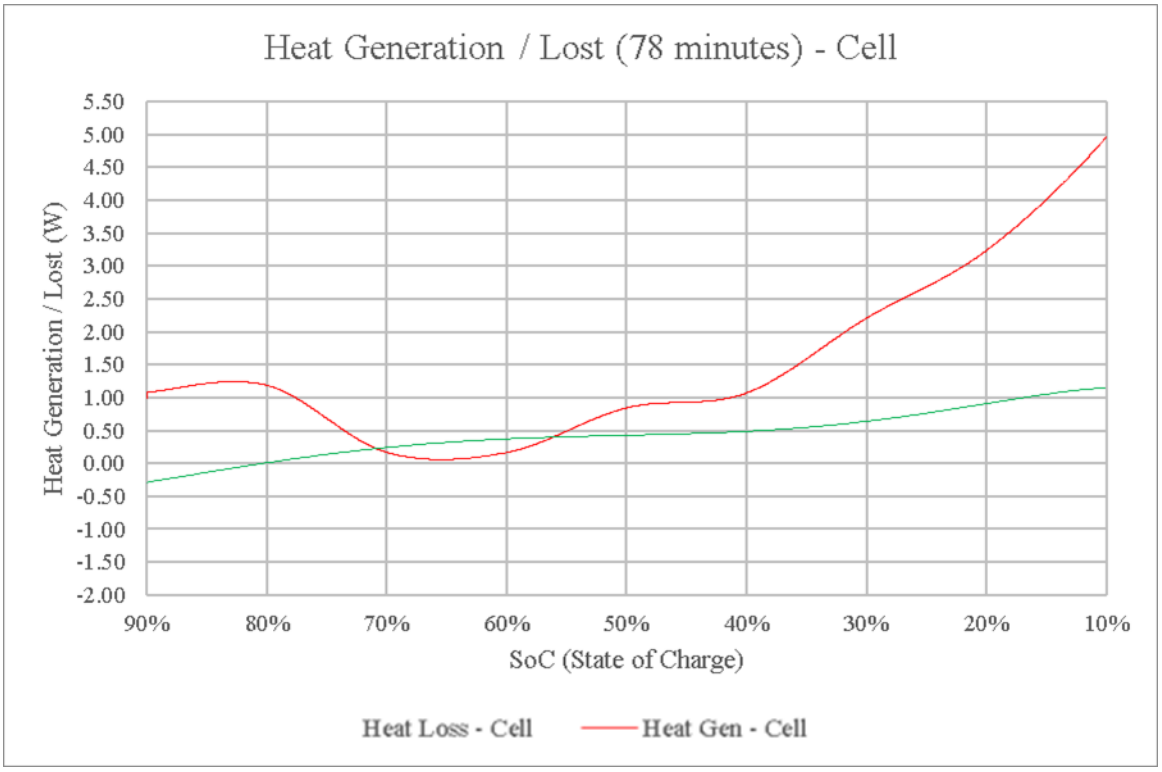

Figure 8-43: Experimental Generated heat and Lost during battery discharge for the Uphill condition.

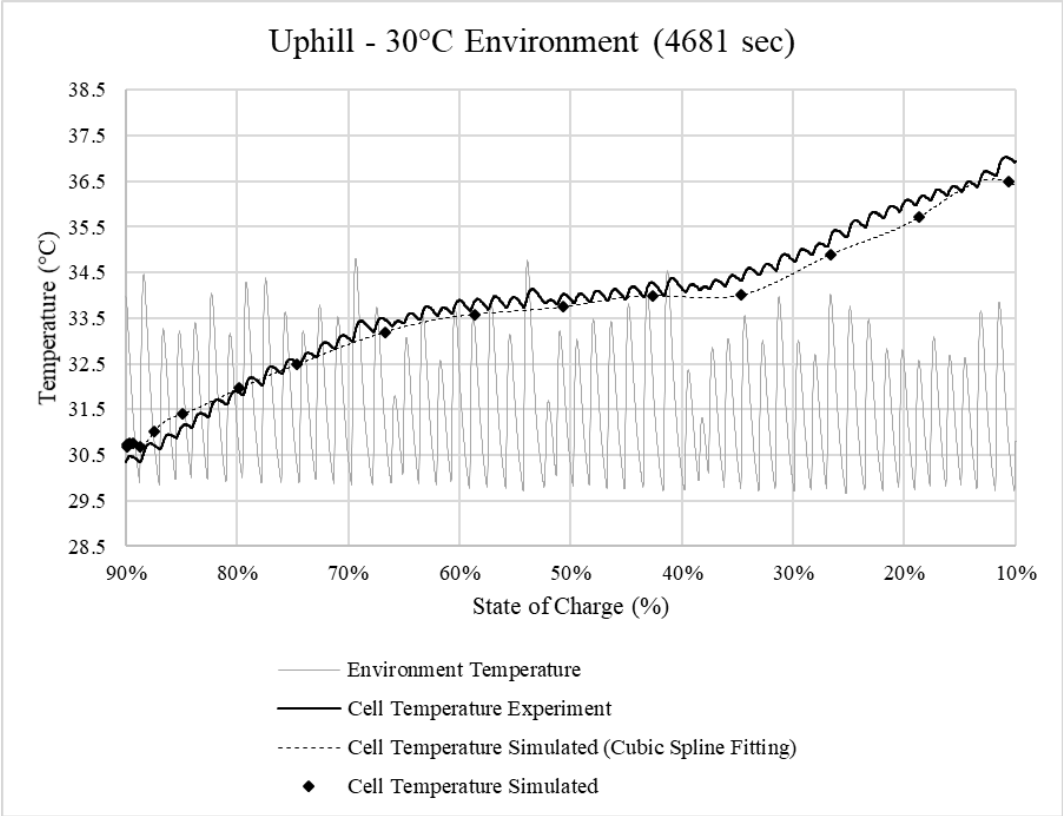

Figure 8-44: Simulated temperature and Experimental temperature obtained during discharging at 30°C.

8.12 Uphill – 35°C

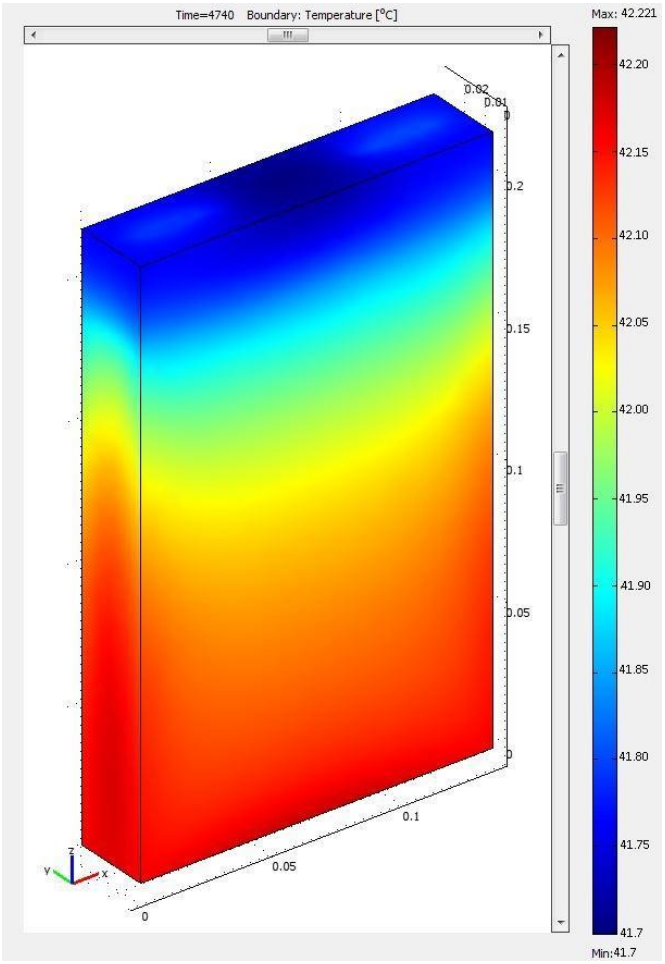

Figure 8-45: Final visual simulation of a temperature gradient along the external battery surface for 43.7A discharging. Total running time of 79 minutes.

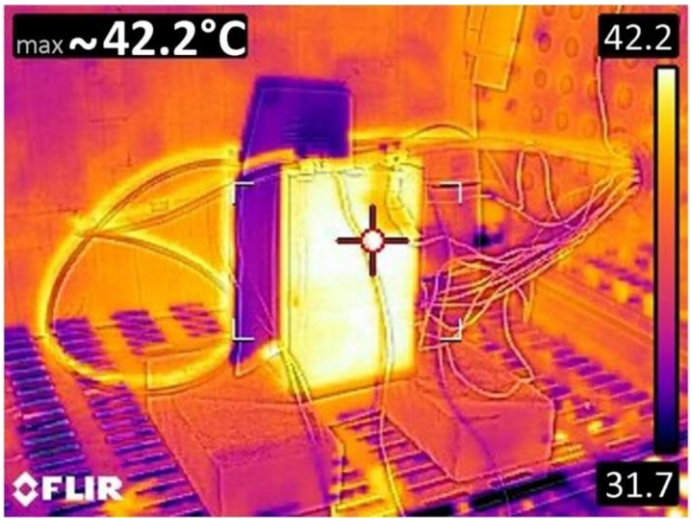

Figure 8-46: Thermal picture from the battery at 79 minutes for 43.7A discharging, 35°C ambient.

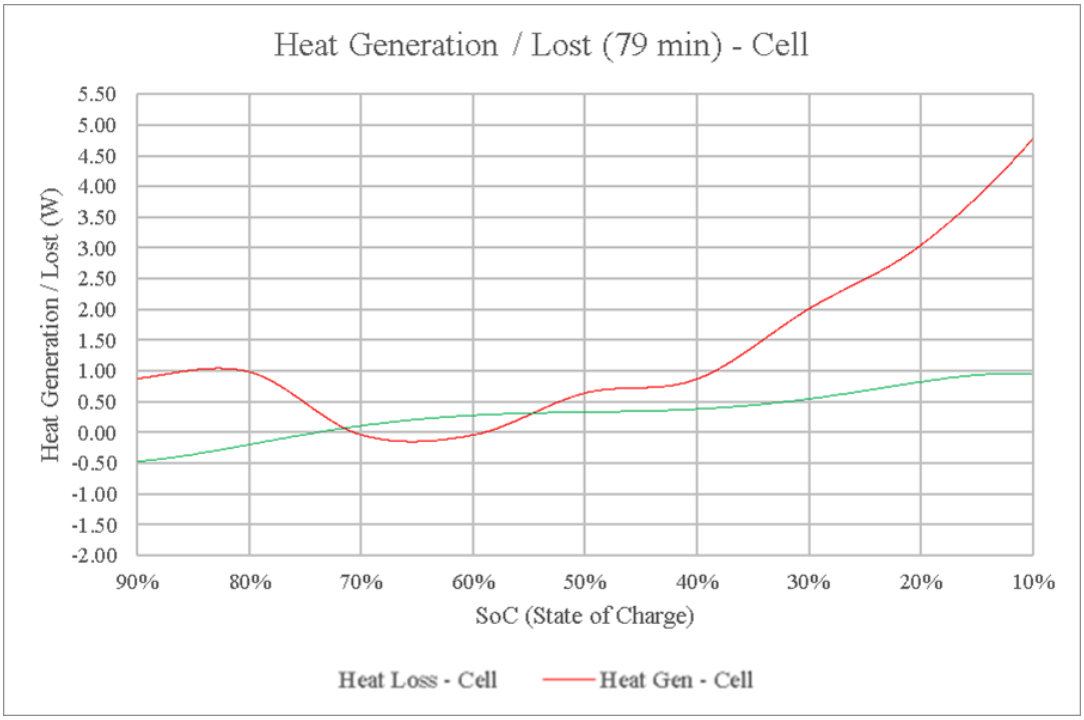

Figure 8-47: Experimental Generated heat and Lost during battery discharge for the Uphill condition.

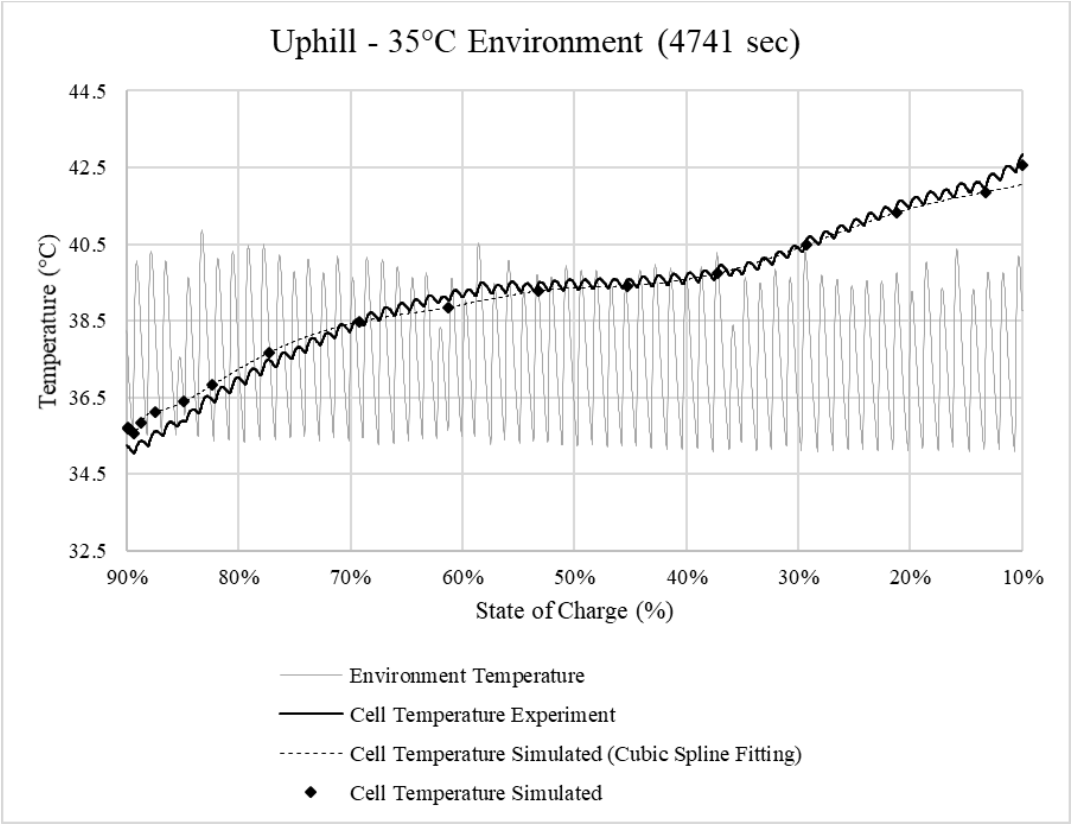

Figure 8-48: Simulated temperature and Experimental temperature obtained during discharging at 35°C.

9 Appendix B – Module Case Study Results

As for the appendix A, the results here presented refer to the module case, related to the charging, Downhill, flat, and Uphill modes, and for ambient temperature (25°C, 30°C, 35°C, and 40°C). The graph results provided are related to the average between the cells in the module. The module is the result of 6 cells connected in series and operated simultaneously. For the whole battery pack in the unit, the cell heat results need to be multiplied by 400, the total amount of cells. The maximum temperature obtained in the thermal imaging is the maximum temperature in the target area, as for the temperature scale, it is the result of the temperature range in the whole field of view.

9 Charging – 25°C

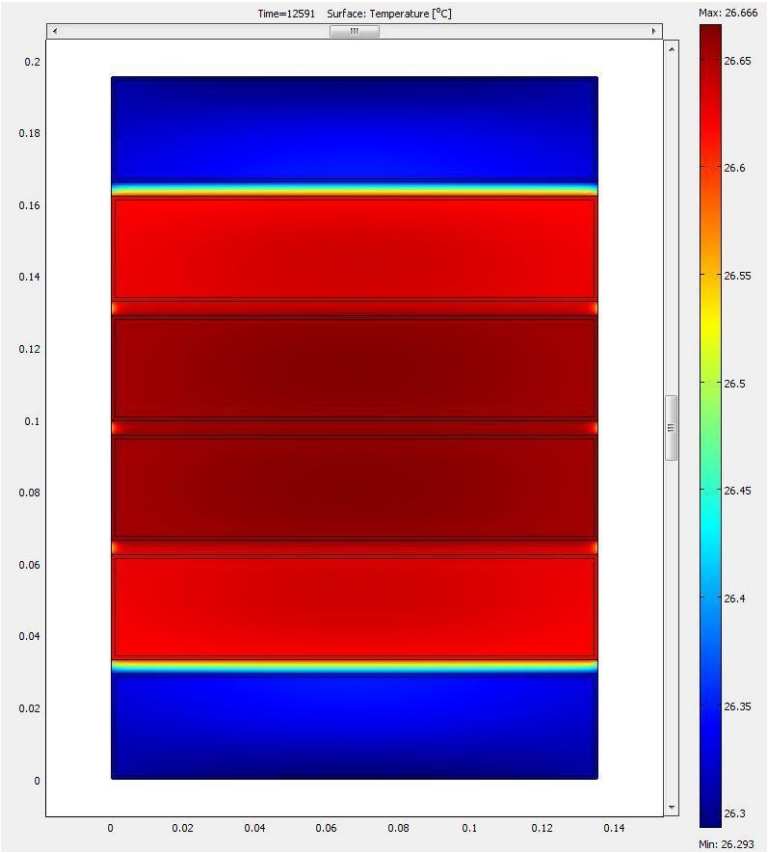

Figure 9-1: Final visual simulation of a temperature gradient along the external battery surface for 16.5A charging. Total running time of 210 minutes.

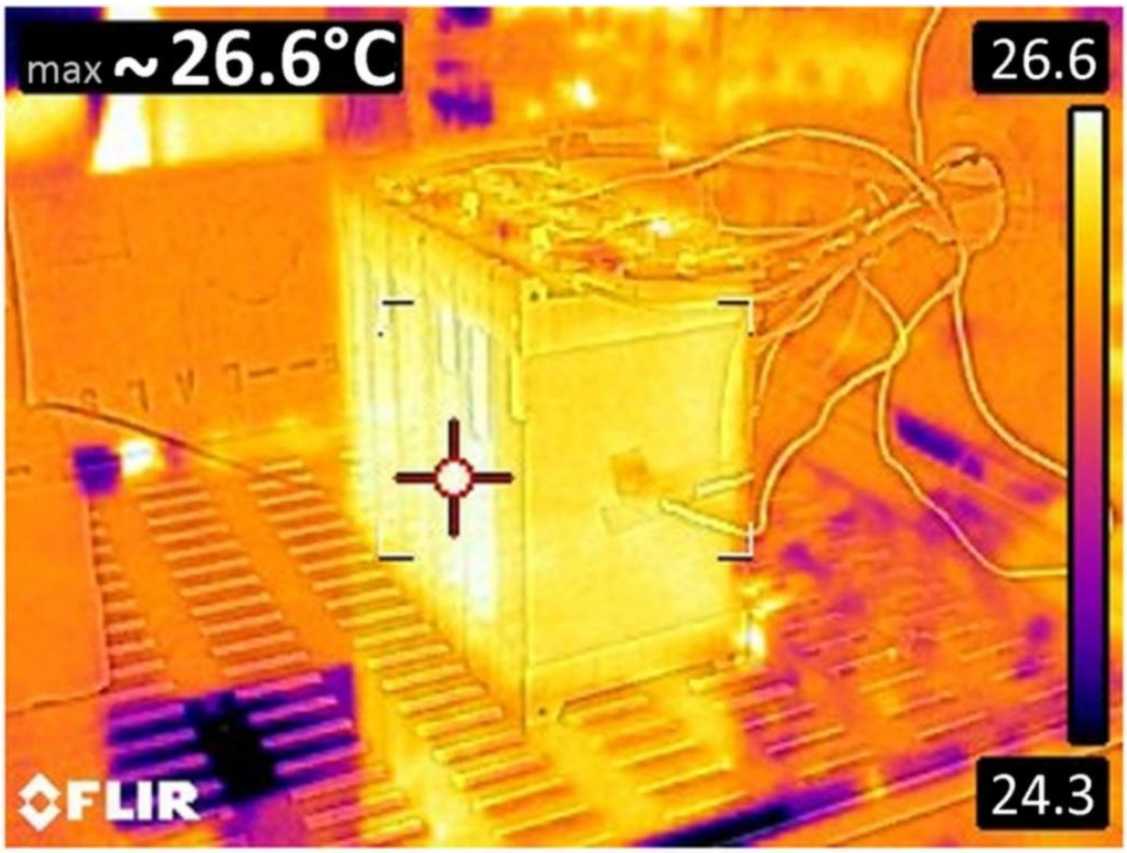

Figure 9-2: Thermal picture from the battery at 210 minutes for 16.5A charging, 25°C ambient.

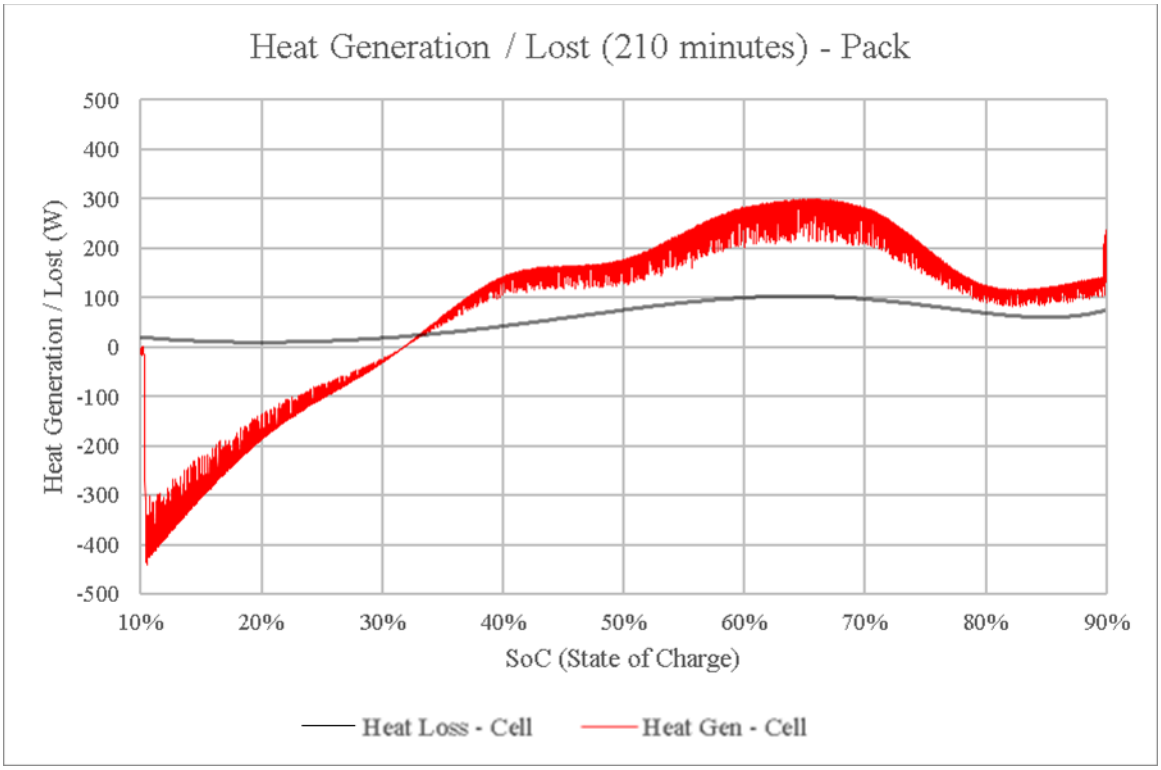

Figure 9-3: Experimental Generated heat and Lost during battery charge for the charging condition.

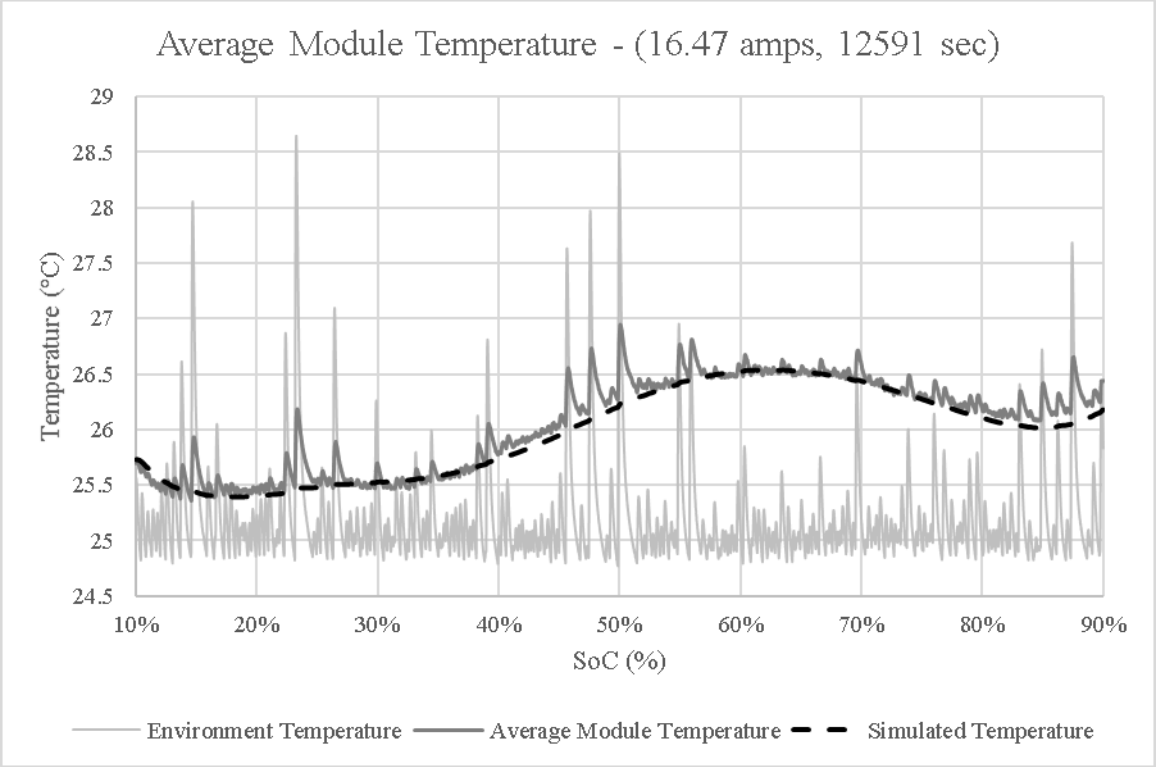

Figure 9-4: Simulated temperature and Experimental temperature obtained during charging at 25°C.

9.1 Charging – 30°C

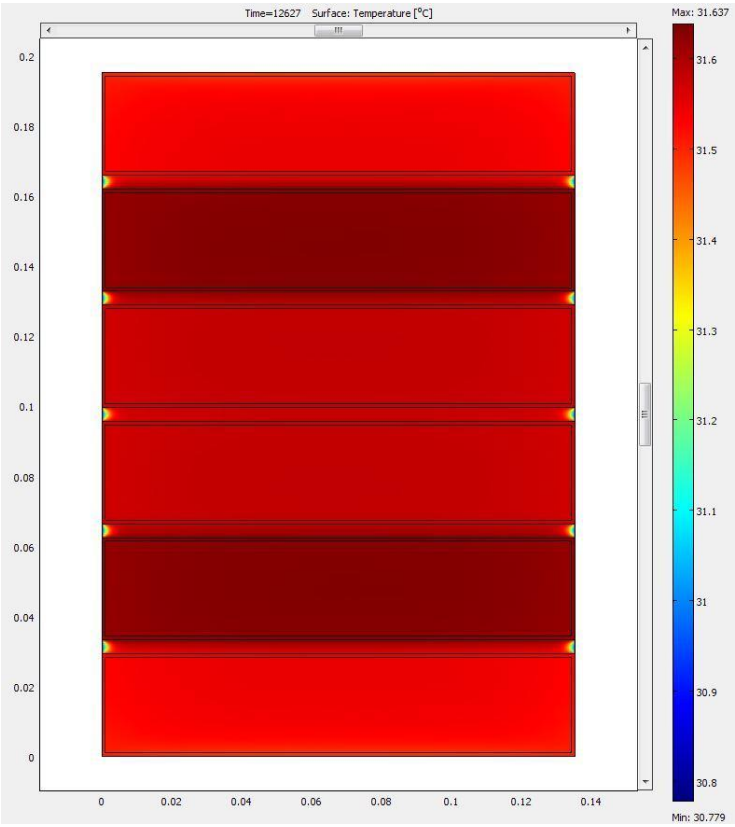

Figure 9-5: Final visual simulation of a temperature gradient along the external battery surface for 16.4A charging. Total running time of 210 minutes.

Figure 9-6: Thermal picture from the battery at 210 minutes for 16.4A charging, 30°C ambient.

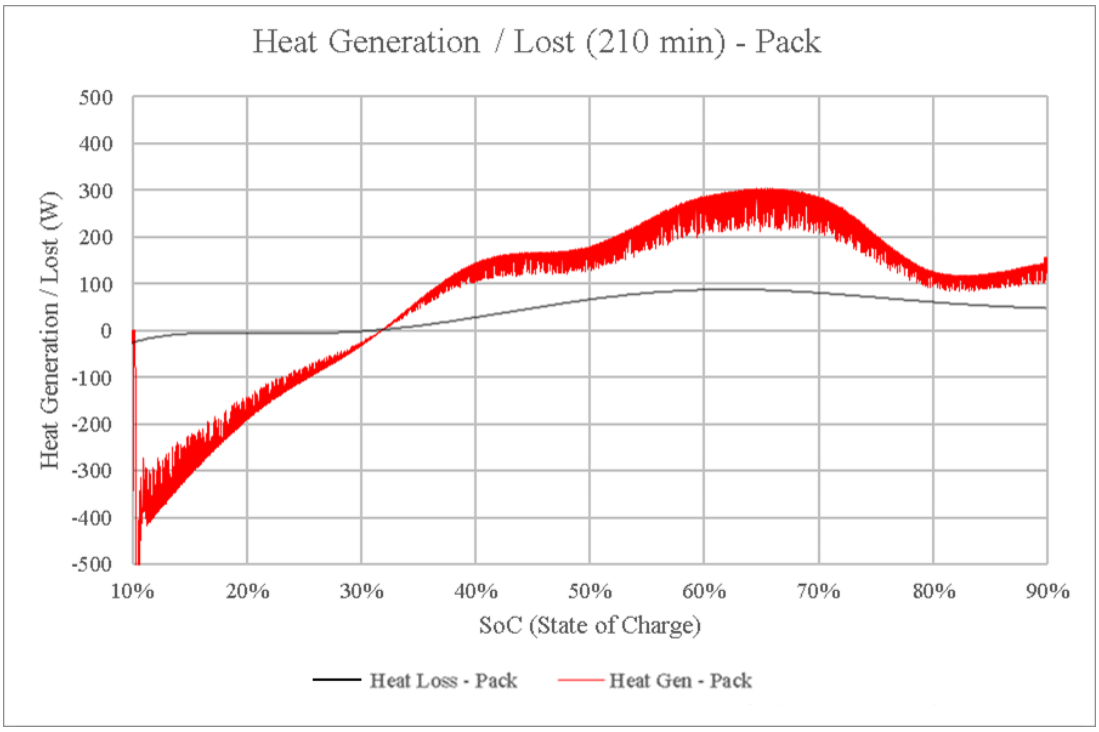

Figure 9-7: Experimental Generated heat and Lost during battery charge for the charging condition.

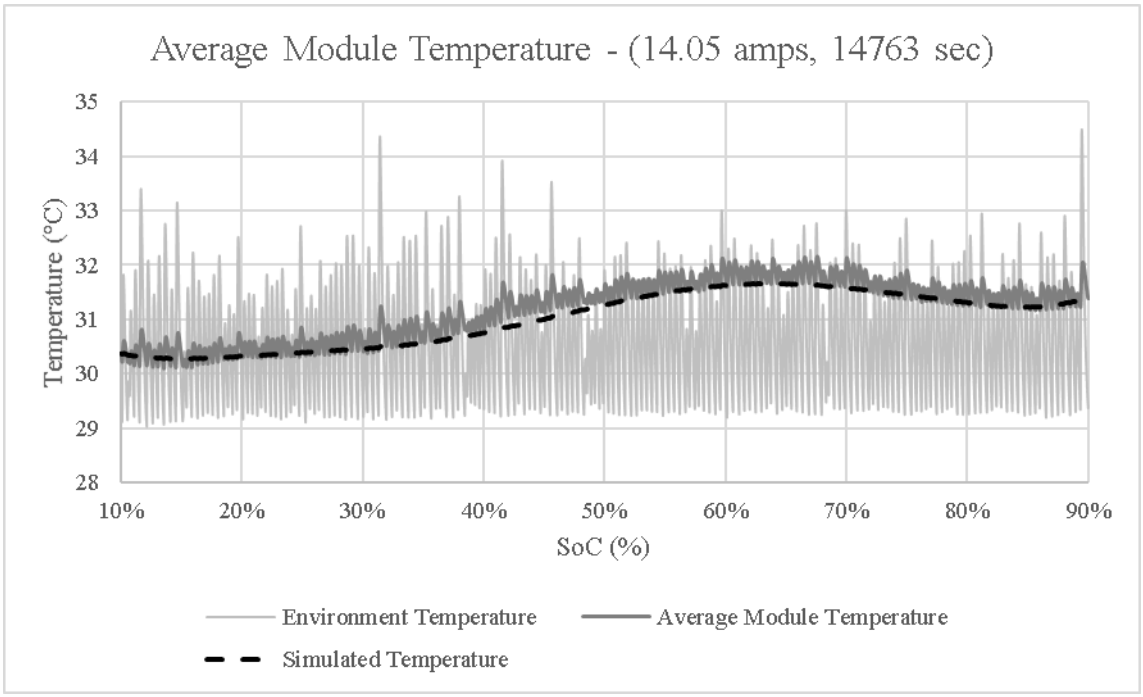

Figure 9-8: Simulated temperature and Experimental temperature obtained during charging at 30°C.

9.2 Charging – 35°C

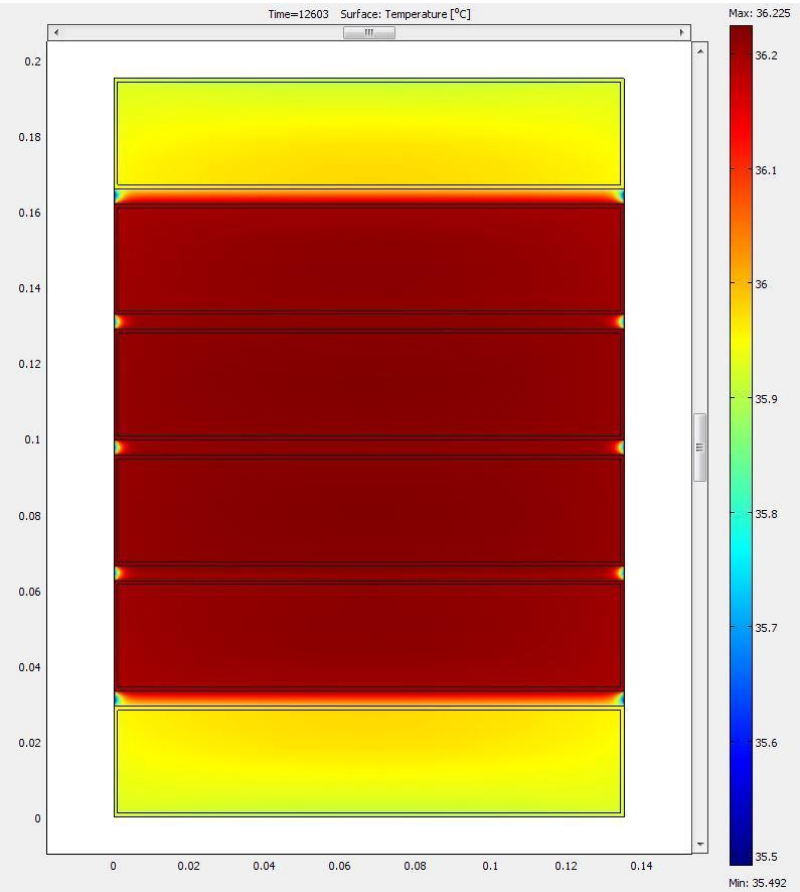

Figure 9-9: Final visual simulation of a temperature gradient along the external battery surface for 16.5A charging. Total running time of 210 minutes.

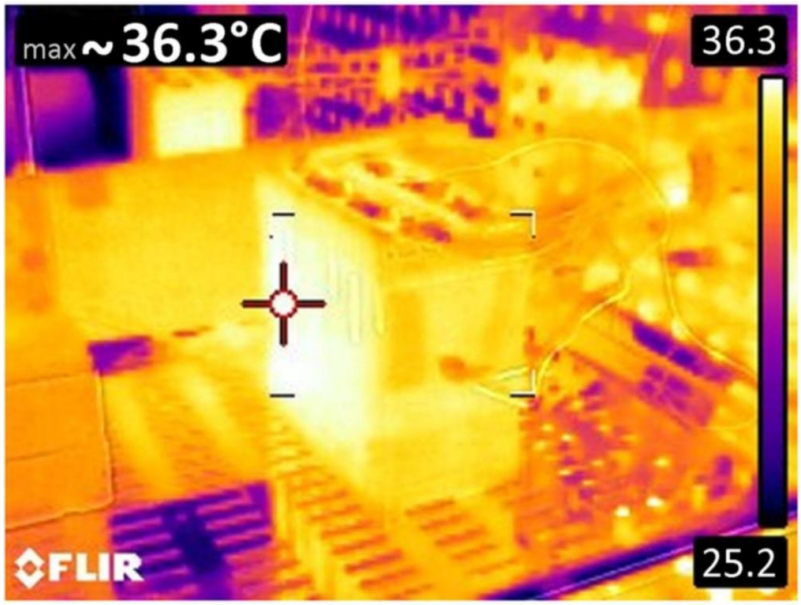

Figure 9-10: Thermal picture from the battery at 210 minutes for 16.5A charging, 35°C ambient.

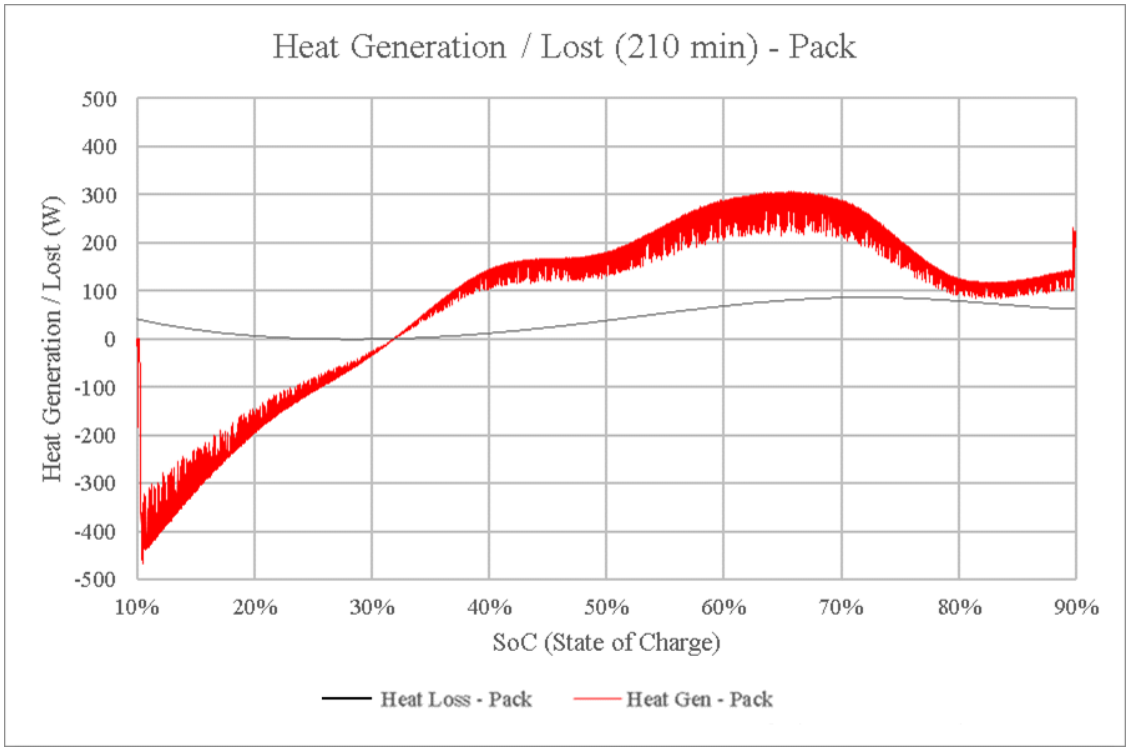

Figure 9-11: Experimental Generated heat and Lost during battery charge for the charging condition.

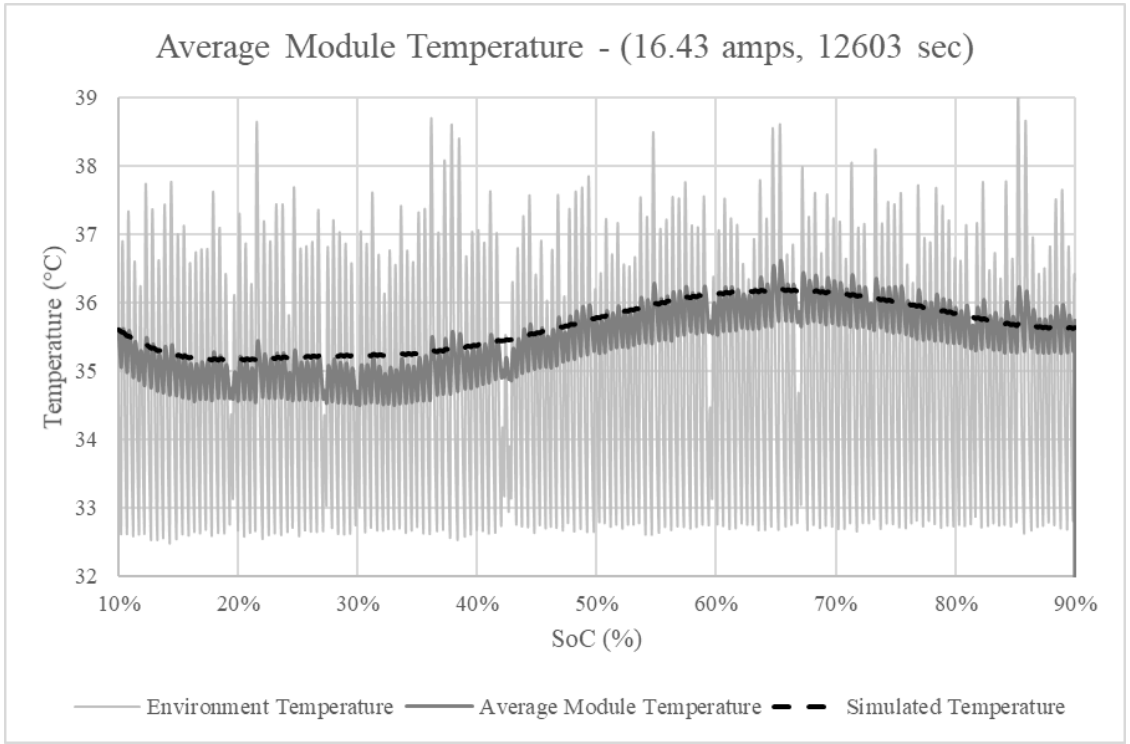

Figure 9-12: Simulated temperature and Experimental temperature obtained during charging at 35°C.

9.3 Charging – 40°C

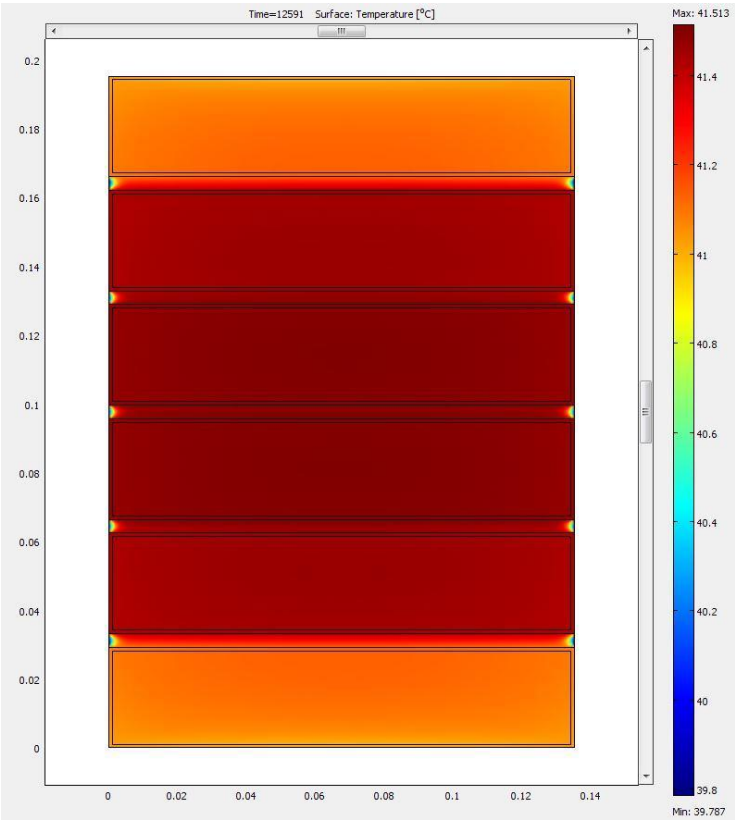

Figure 9-13: Final visual simulation of a temperature gradient along the external battery surface for 16.5A charging. Total running time of 210 minutes.

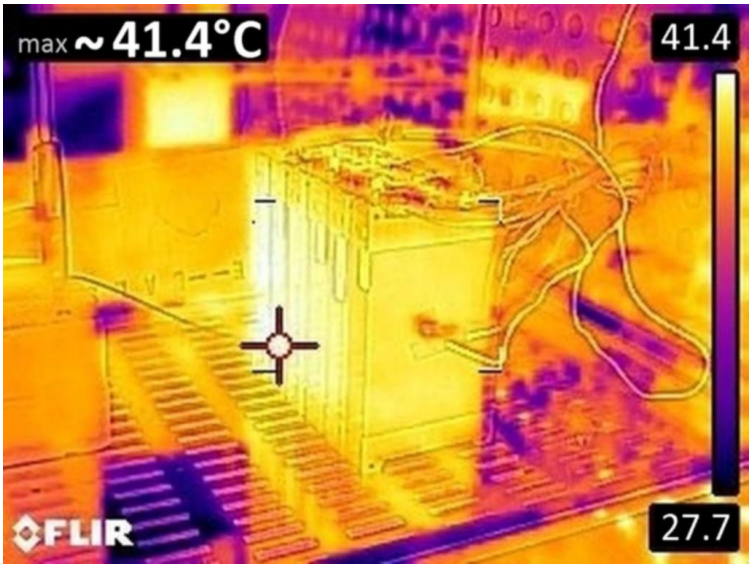

Figure 9-14: Thermal picture from the battery at 210 minutes for 16.5A charging, 40°C ambient.

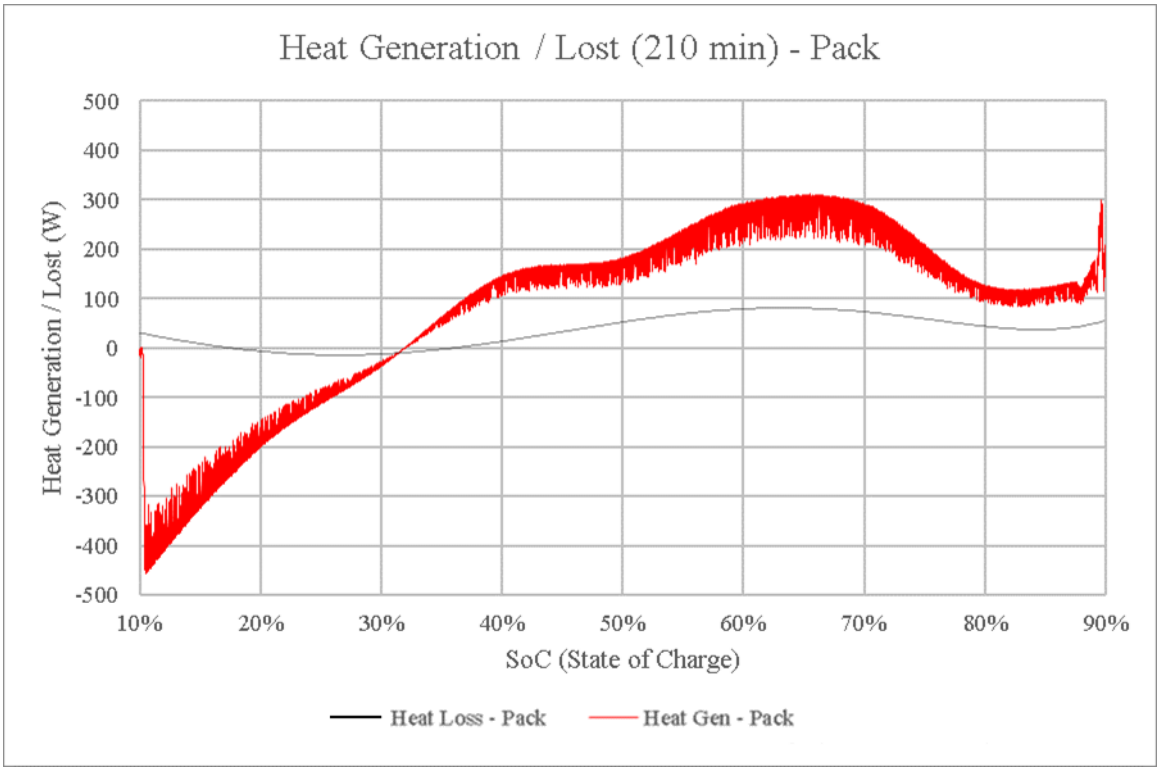

Figure 9-15: Experimental Generated heat and Lost during battery charge for the charging condition.

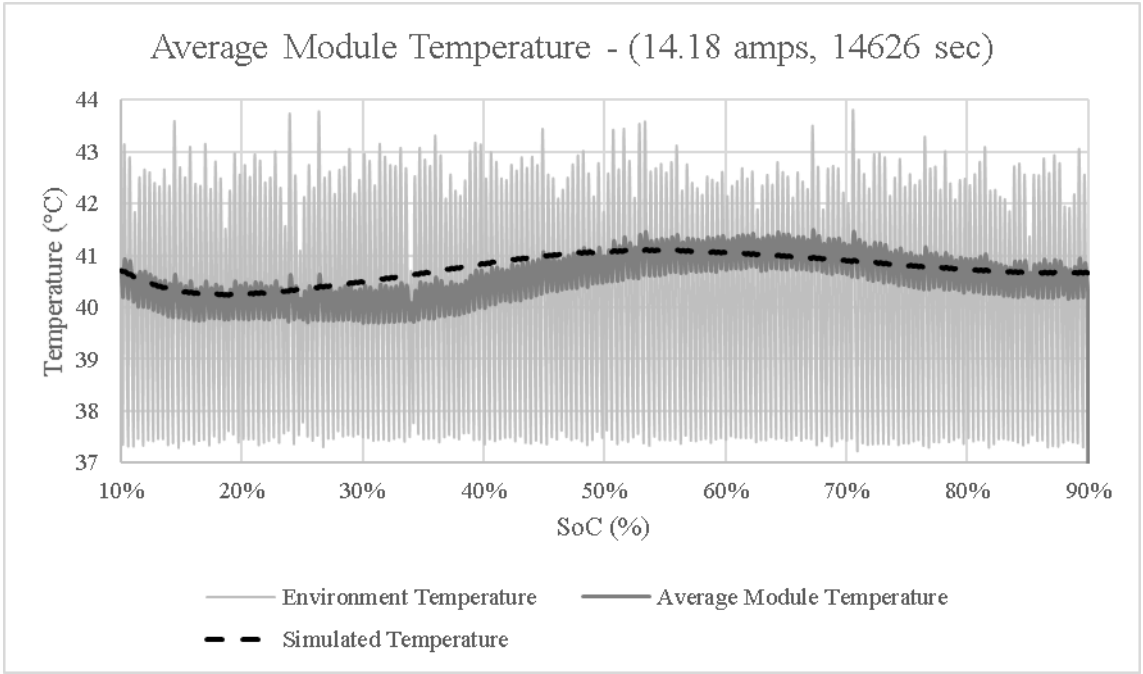

Figure 9-16: Simulated temperature and Experimental temperature obtained during charging at 40°C.

9.4 Downhill – 25°C

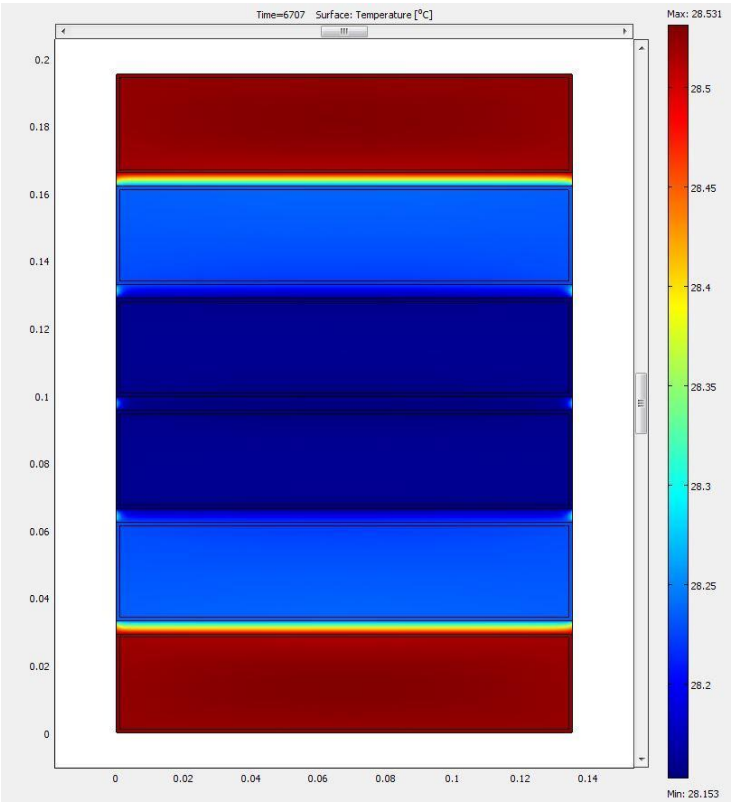

Figure 9-17: Final visual simulation of a temperature gradient along the external battery surface for 30.9A discharging. Total running time of 112 minutes.

Figure 9-18: Thermal picture from the battery at 112 minutes for 30.9A charging, 25°C ambient.

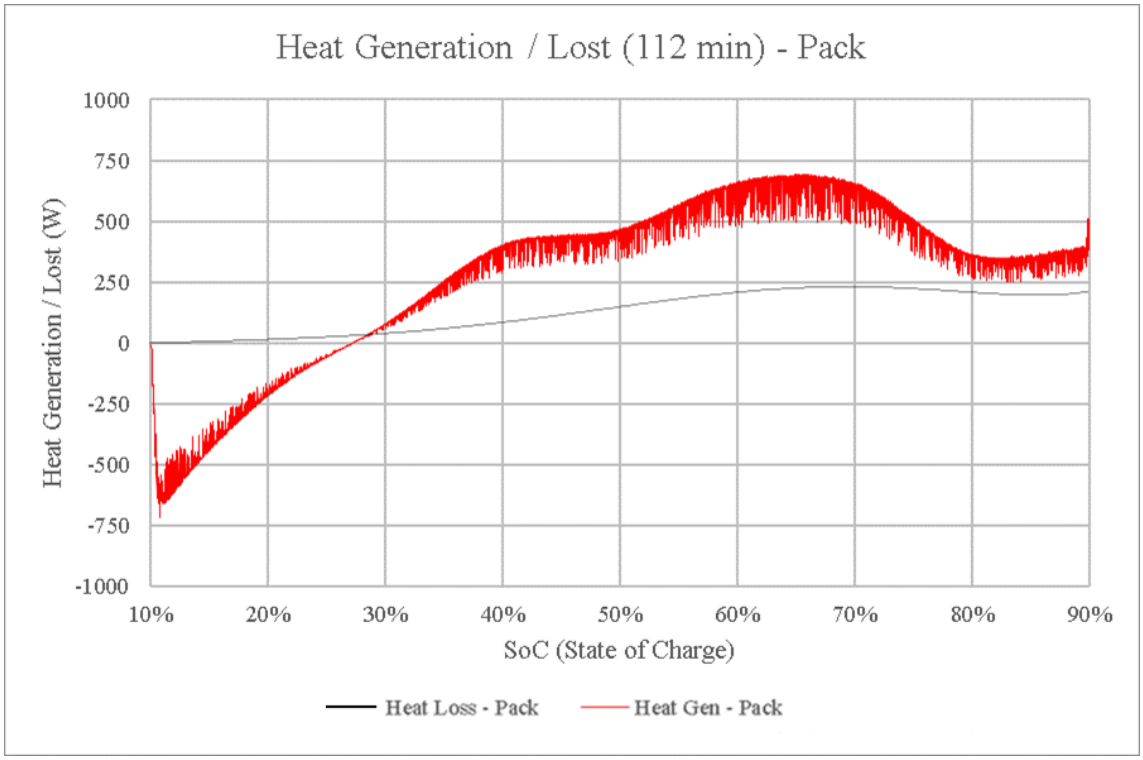

Figure 9-19: Experimental Generated heat and Lost during battery discharge for the Downhill condition.

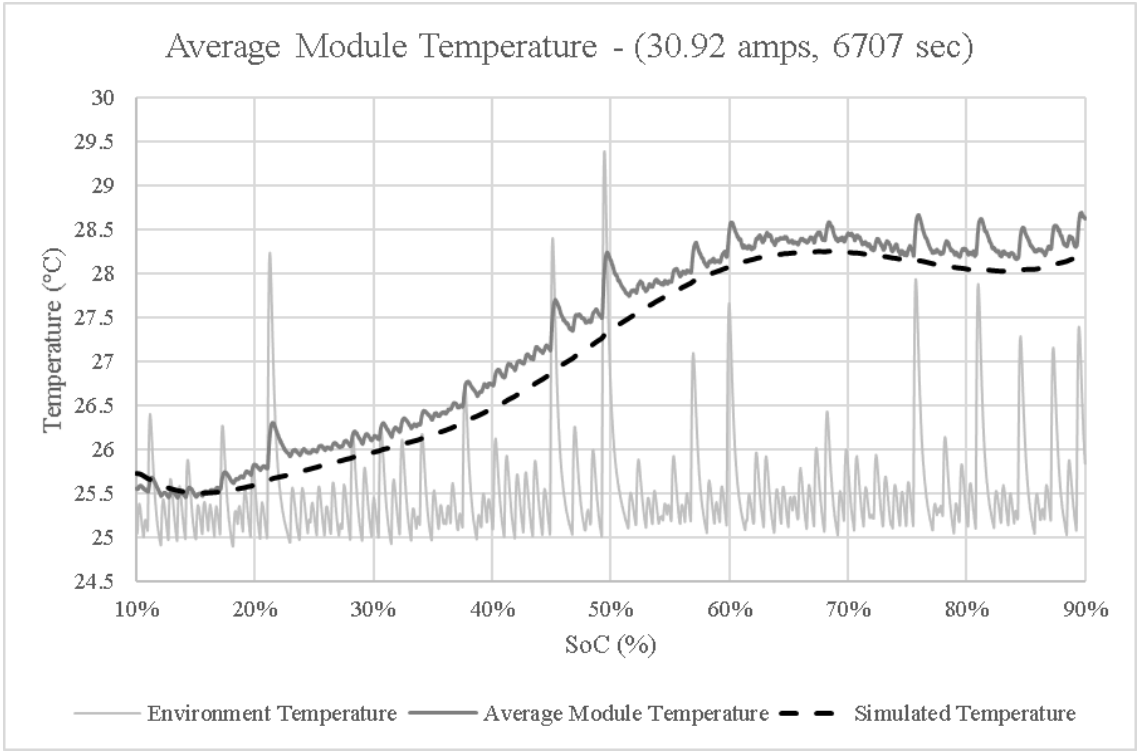

Figure 9-20: Simulated temperature and Experimental temperature obtained during discharge at 25°C.

9.5 Downhill – 30°C

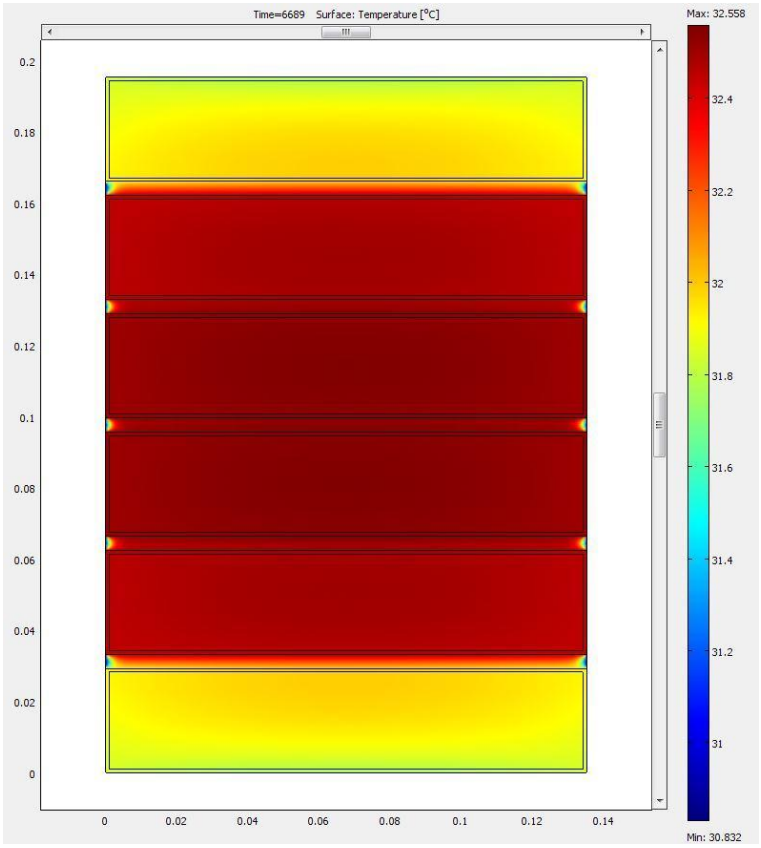

Figure 9-21: Final visual simulation of a temperature gradient along the external battery surface for 31.0A charging. Total running time of 111 minutes.

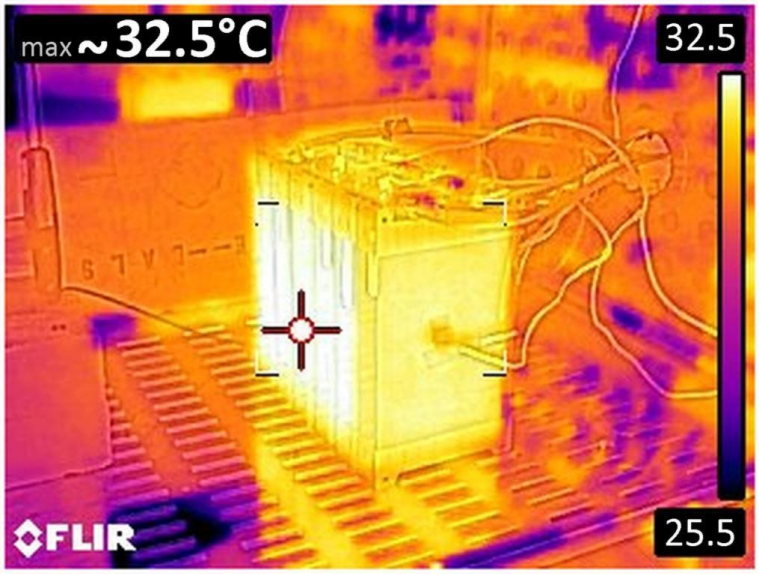

Figure 9-22: Thermal picture from the battery at 111 minutes for 31.0A charging, 30°C ambient.

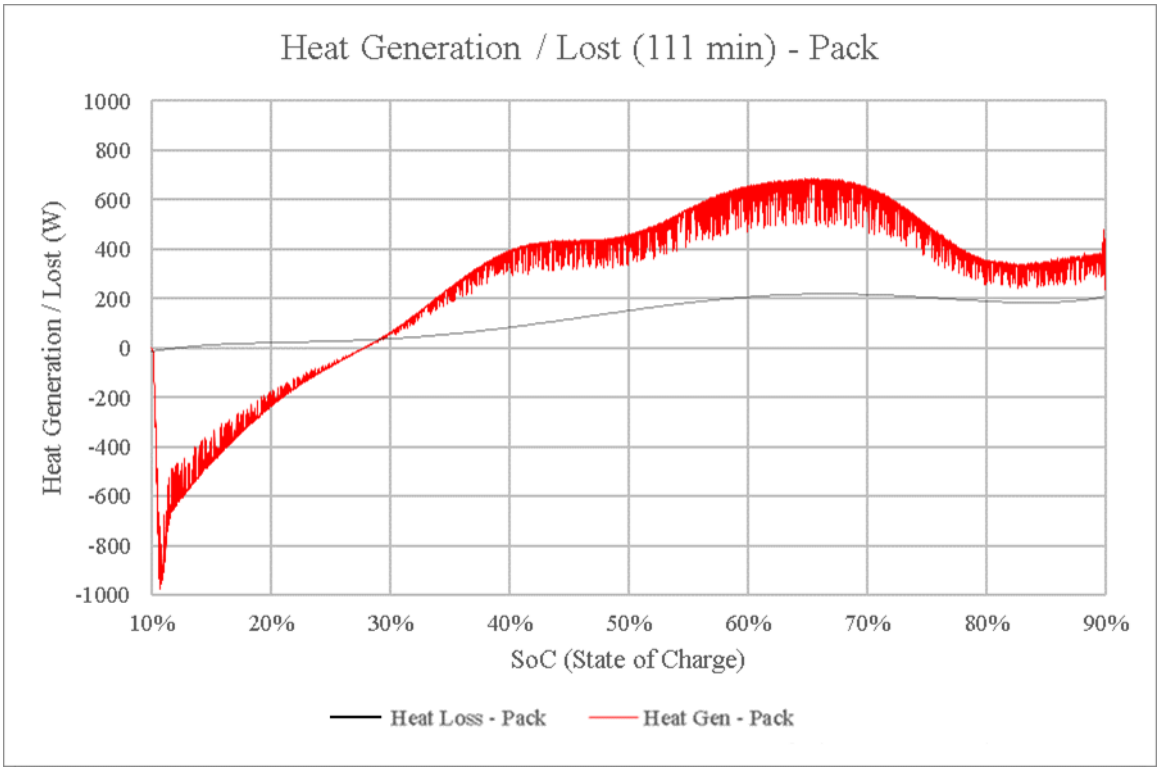

Figure 9-23: Experimental Generated heat and Lost during battery charge for the Downhill condition.

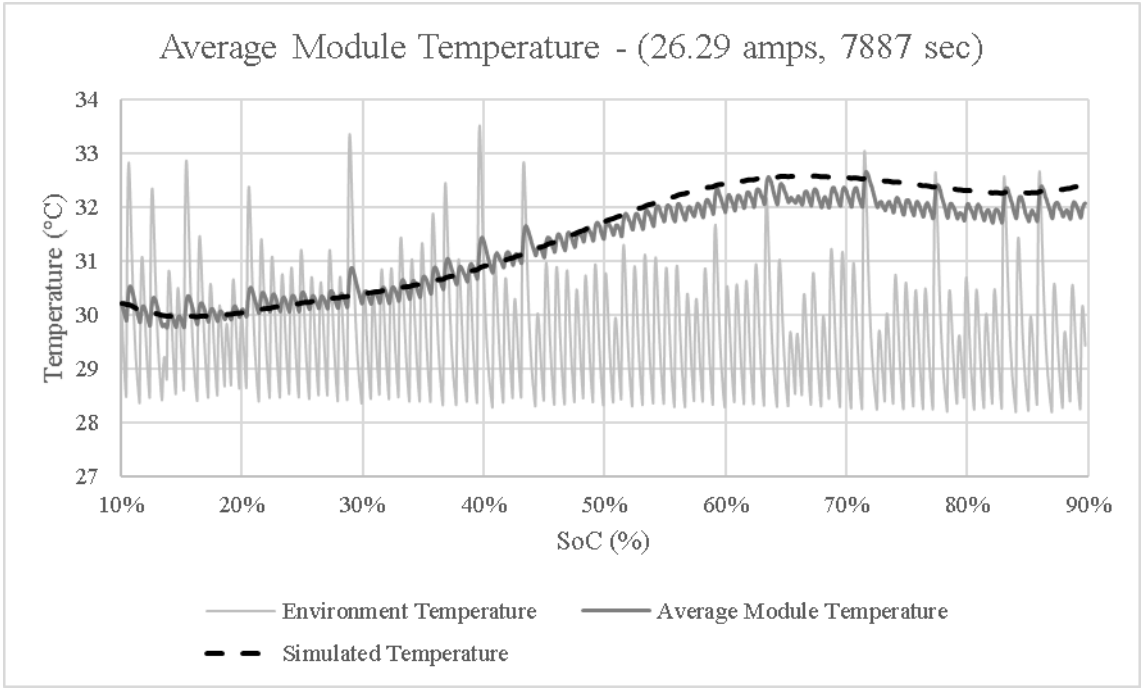

Figure 9-24: Simulated temperature and Experimental temperature obtained during charging at 30°C.

9.6 Downhill – 35°C

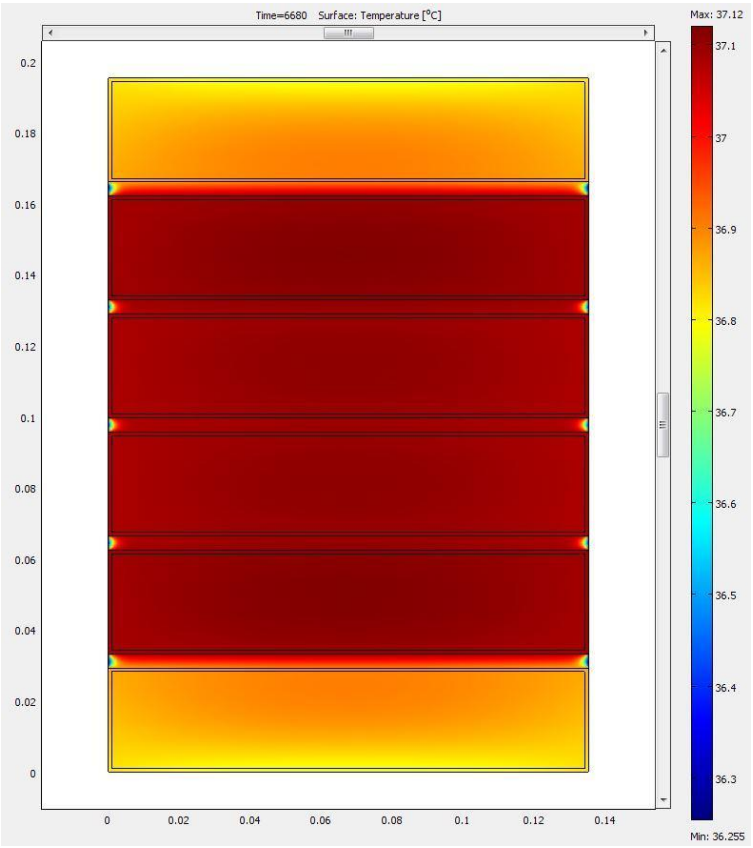

Figure 9-25: Final visual simulation of a temperature gradient along the external battery surface for 30.1A charging. Total running time of 111 minutes.

Figure 9-26: Thermal picture from the battery at 111 minutes for 31.0A charging, 35°C ambient.

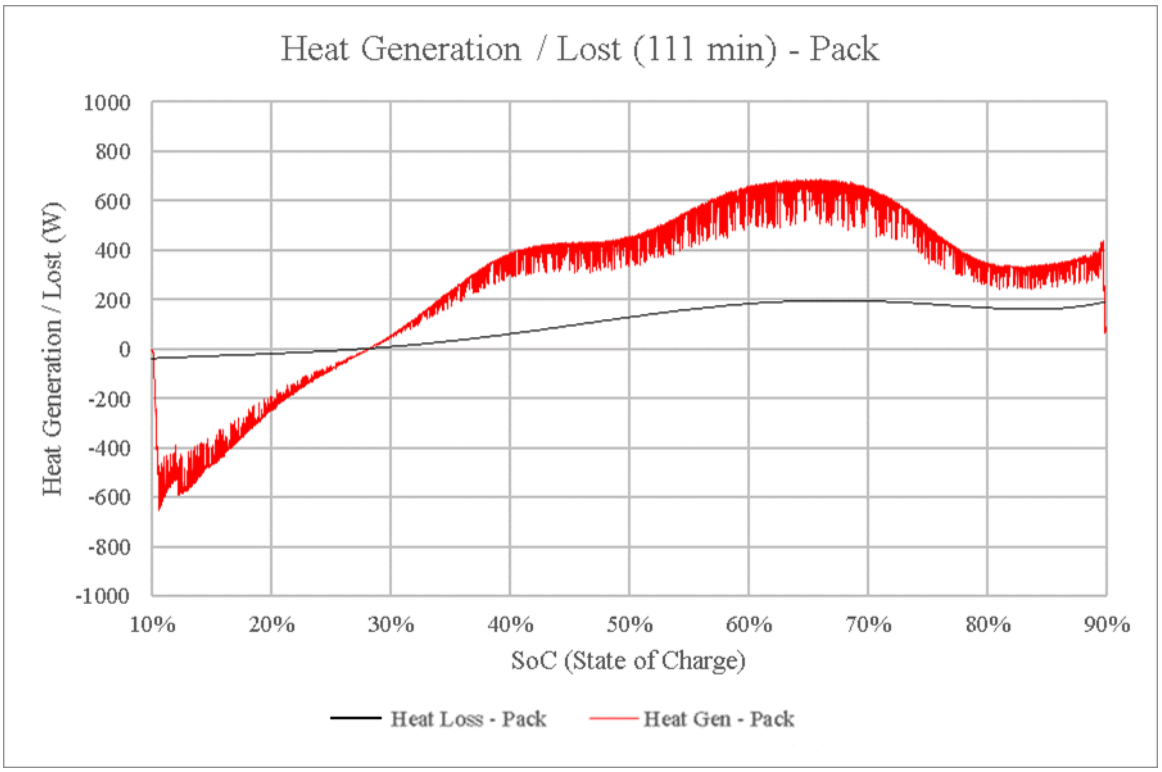

Figure 9-27: Experimental Generated heat and Lost during battery charge for the Downhill condition.

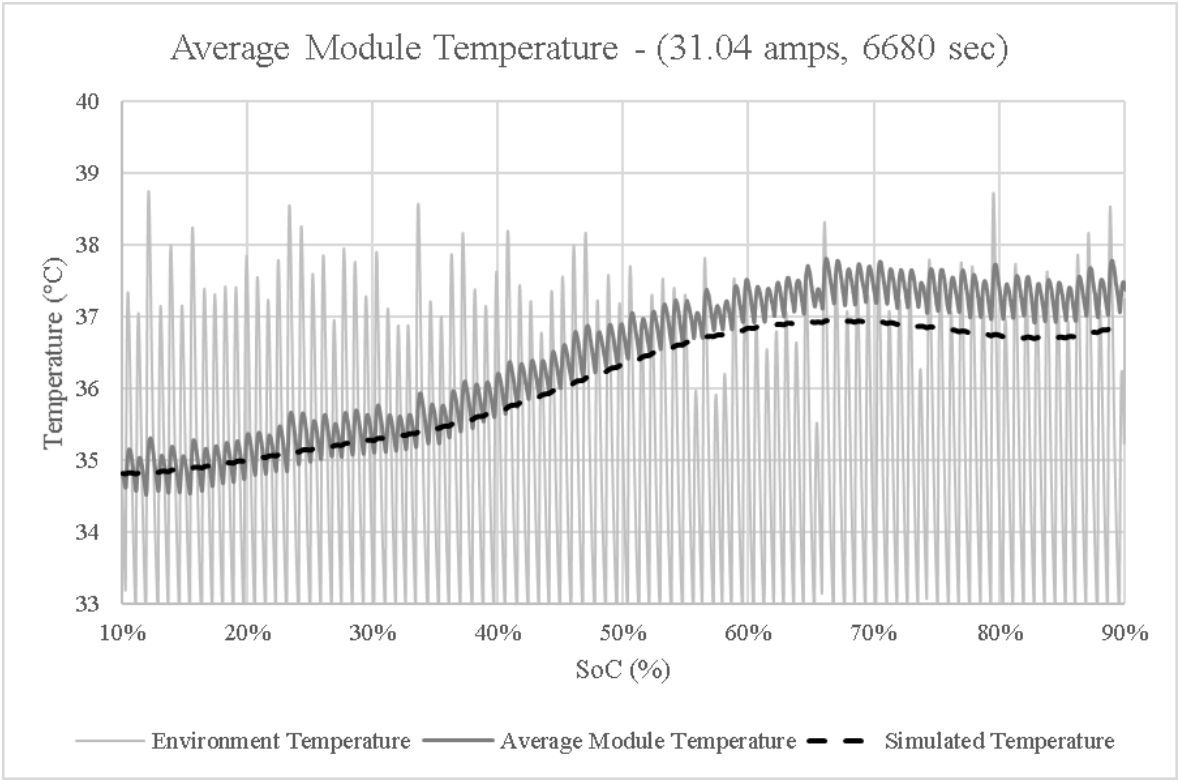

Figure 9-28: Simulated temperature and Experimental temperature obtained during charging at 35°C.

9.7 Downhill – 40°C

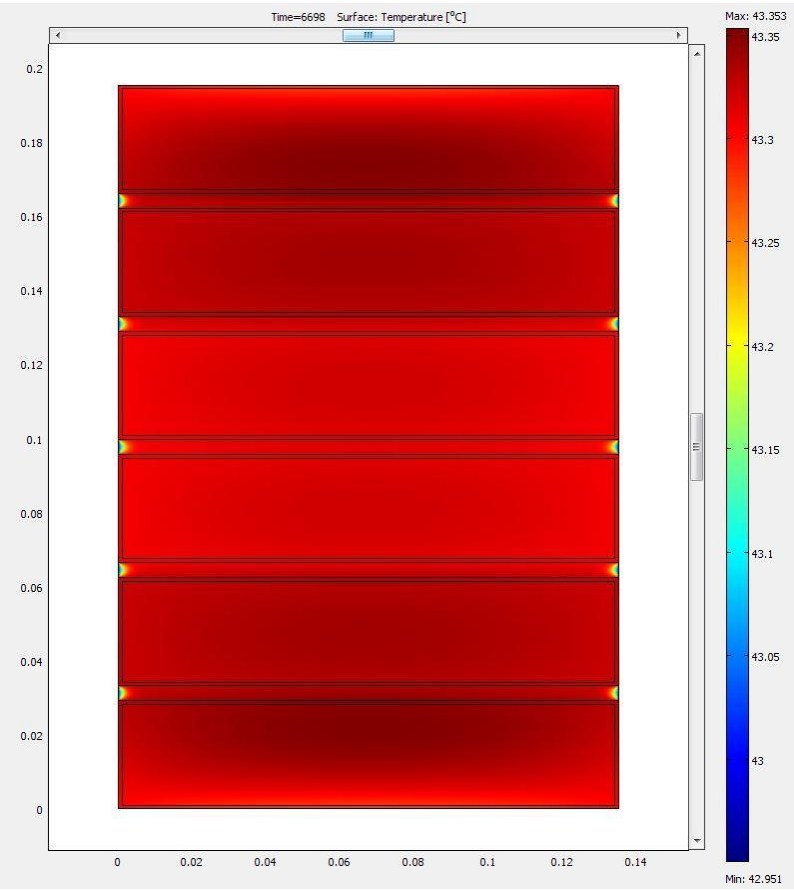

Figure 9-29: Final visual simulation of a temperature gradient along the external battery surface for 31.0A charging. Total running time of 111 minutes.

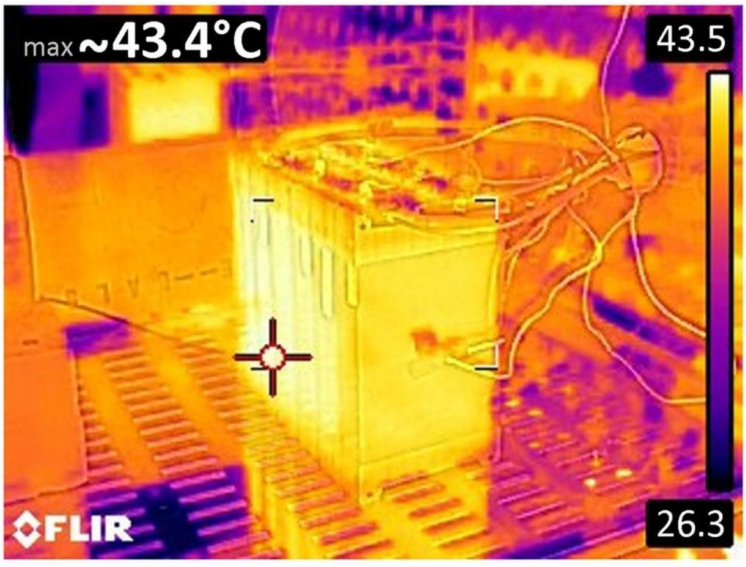

Figure 9-30: Thermal picture from the battery at 111 minutes for 31.0A charging, 40°C ambient.

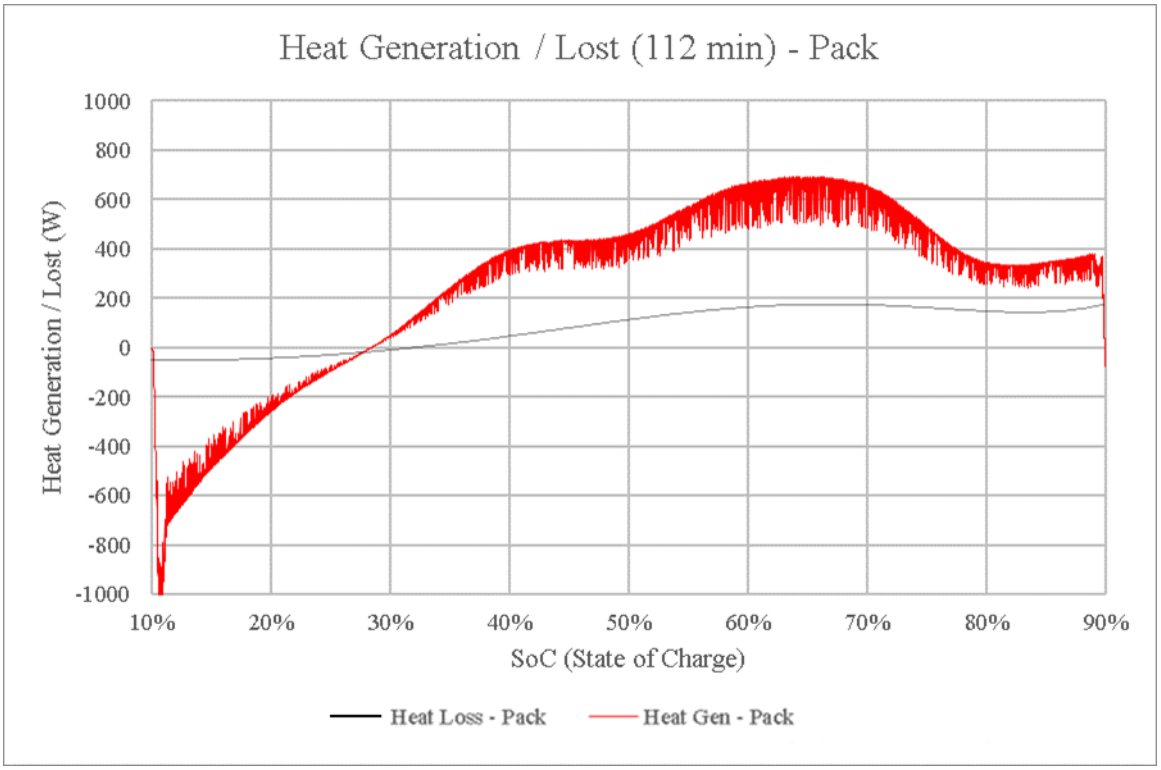

Figure 9-31: Experimental Generated heat and Lost during battery charge for the charging condition.

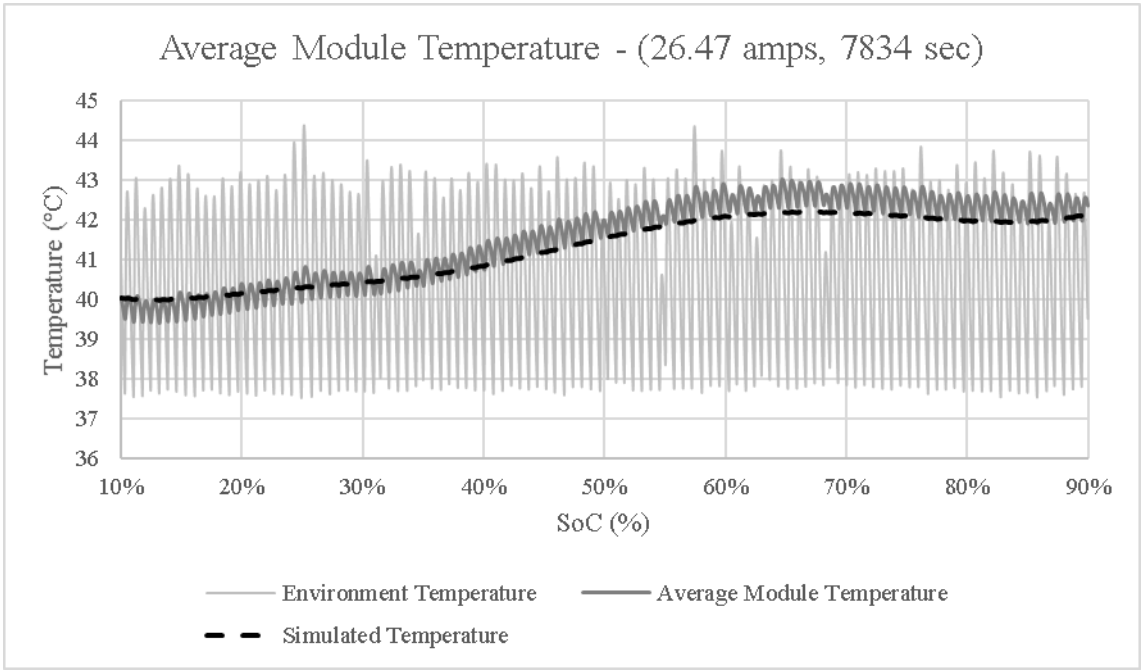

Figure 9-32: Simulated temperature and Experimental temperature obtained during charging at 40°C.

9.8 Flat – 25°C

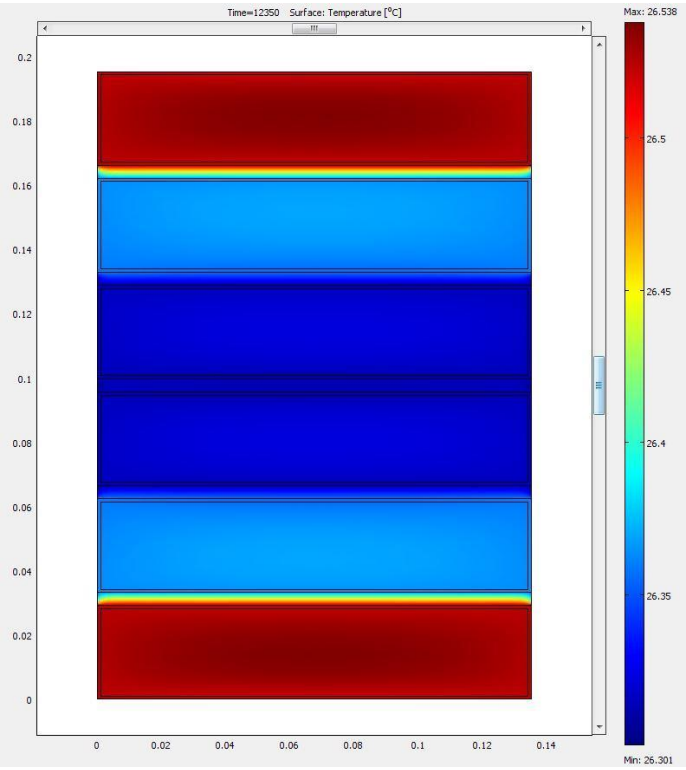

Figure 9-33: Final visual simulation of a temperature gradient along the external battery surface for 16.8A discharging. Total running time of 206 minutes.

Figure 9-34: Thermal picture from the battery at 206 minutes for 16.8A discharging, 25°C ambient.

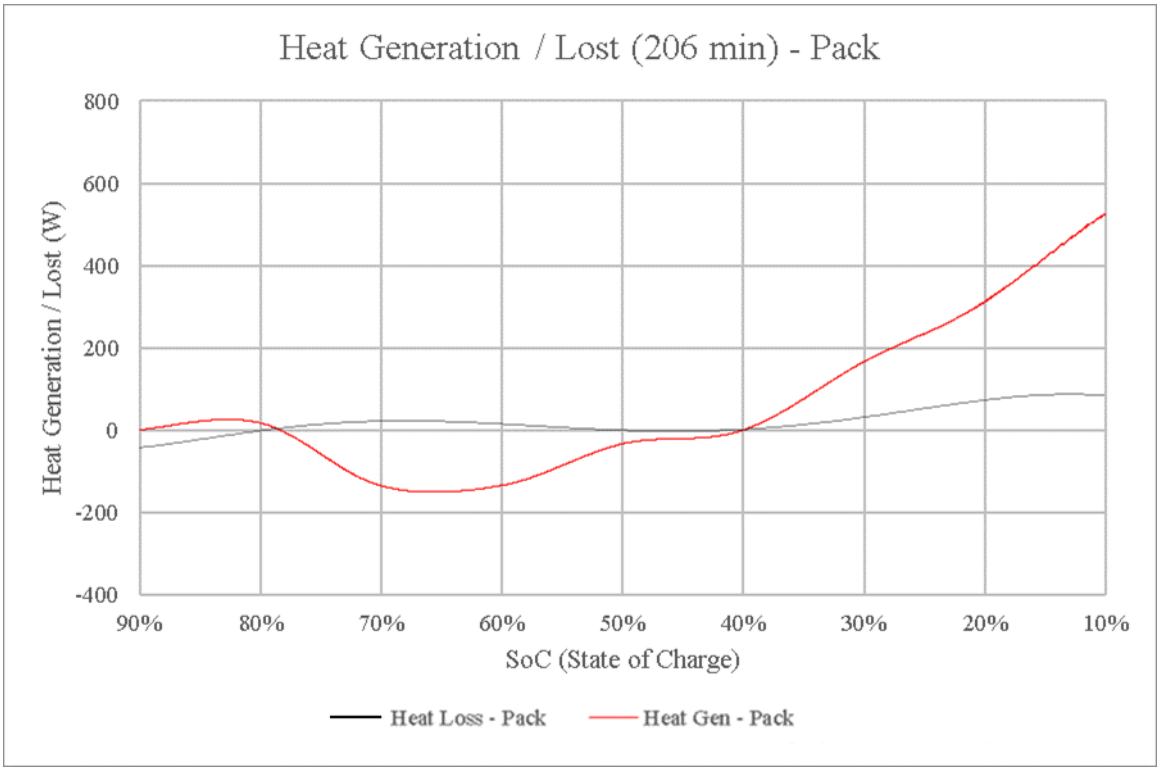

Figure 9-35: Experimental Generated heat and Lost during battery discharge for the flat condition.

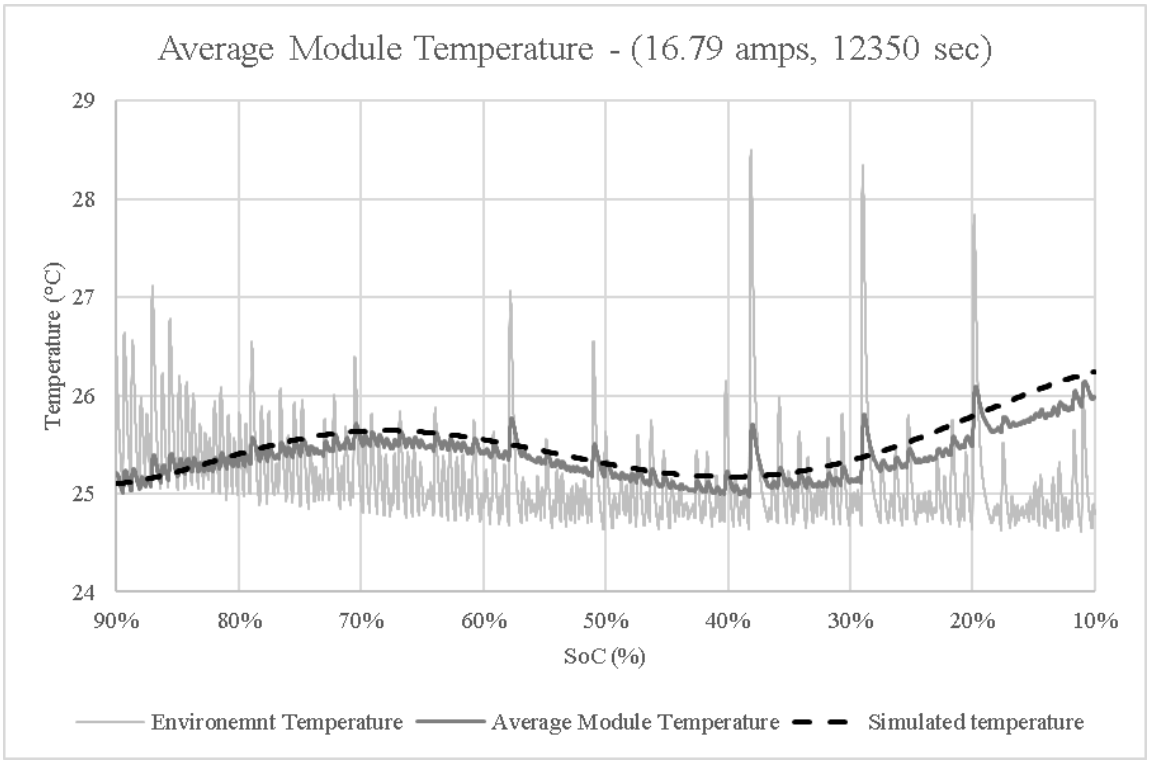

Figure 9-36: Simulated temperature and Experimental temperature obtained during discharging at 25°C.

9.9 Flat – 30°C

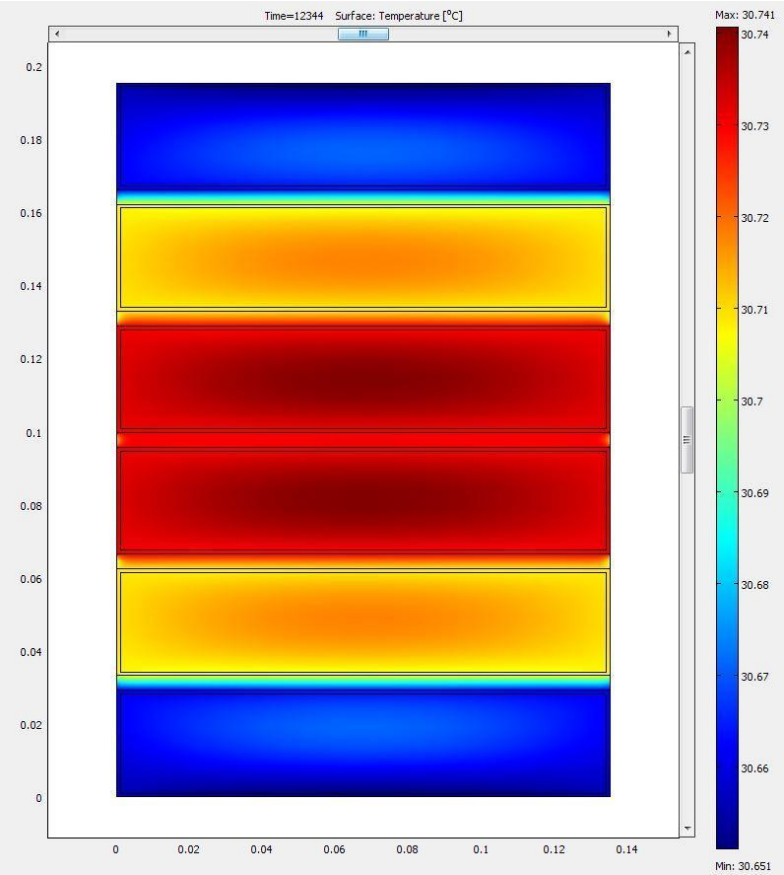

Figure 9-37: Final visual simulation of a temperature gradient along the external battery surface for 16.8A discharging. Total running time of 206 minutes.

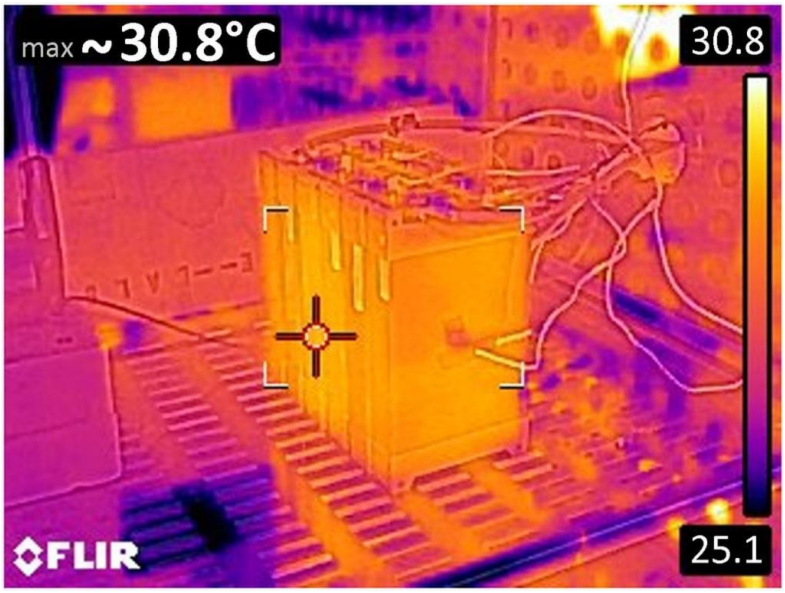

Figure 9-38: Thermal picture from the battery at 206 minutes for 16.8A discharging, 30°C ambient.

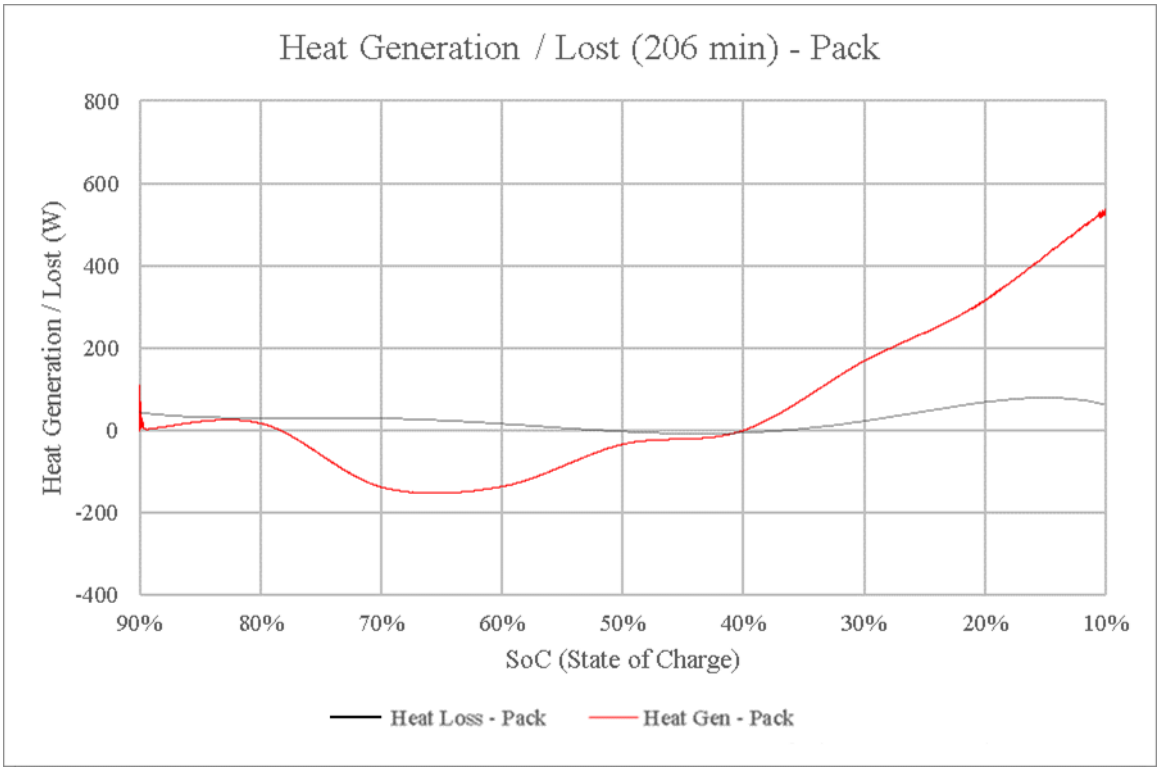

Figure 9-39: Experimental Generated heat and Lost during battery discharge for the flat condition.

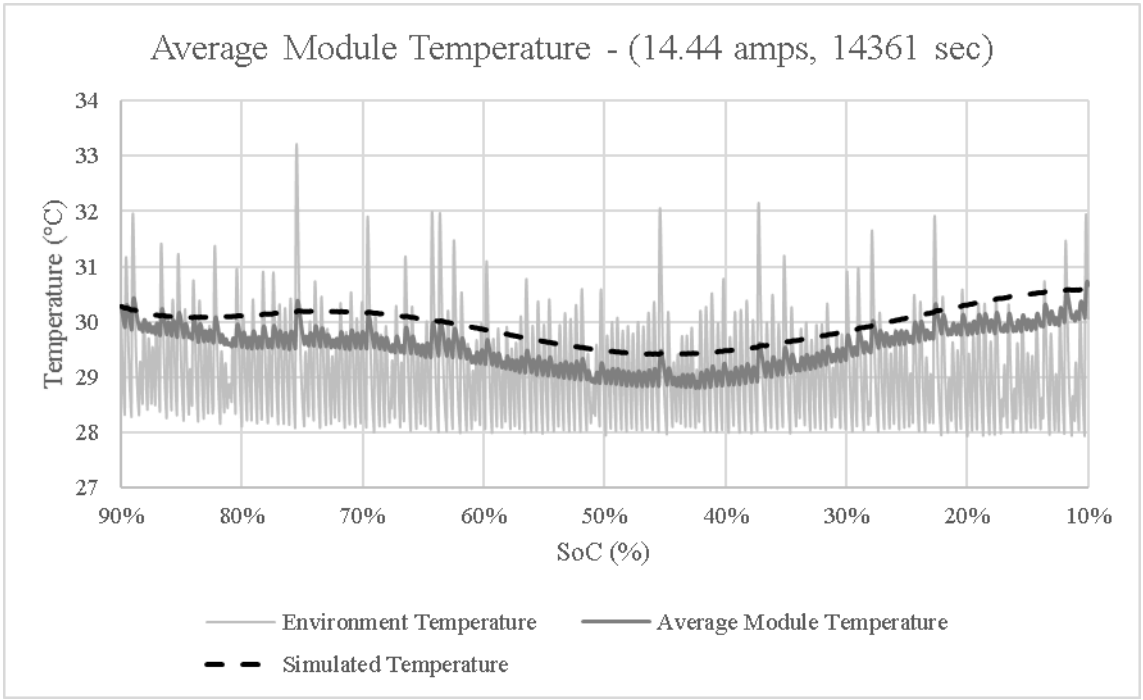

Figure 9-40: Simulated temperature and Experimental temperature obtained during discharging at 30°C.

9.10 Flat – 35°C

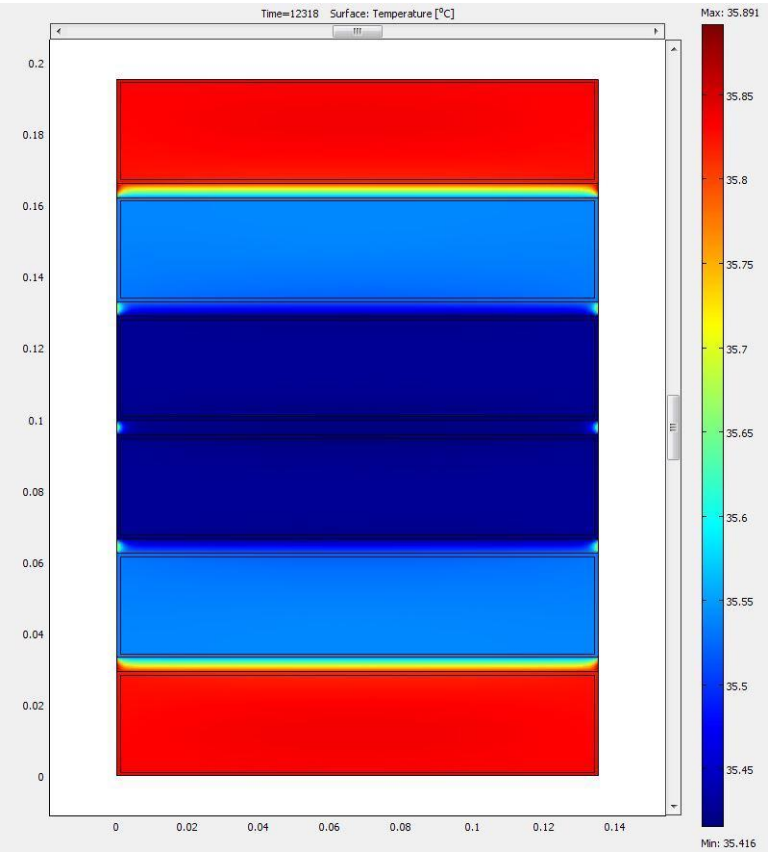

Figure 9-41: Final visual simulation of a temperature gradient along the external battery surface for 16.8A discharging. Total running time of 205 minutes.

Figure 9-42: Thermal picture from the battery at 205 minutes for 16.8A discharging, 35°C ambient.

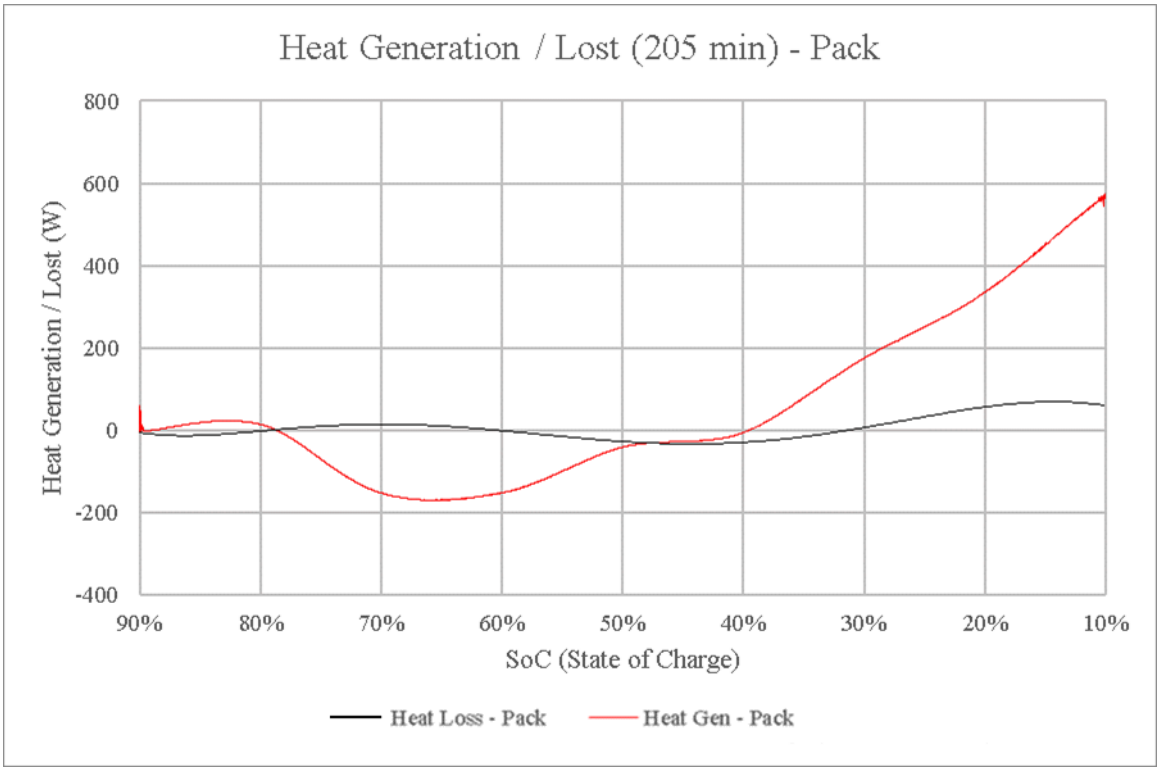

Figure 9-43: Experimental Generated heat and Lost during battery discharge for the flat condition.

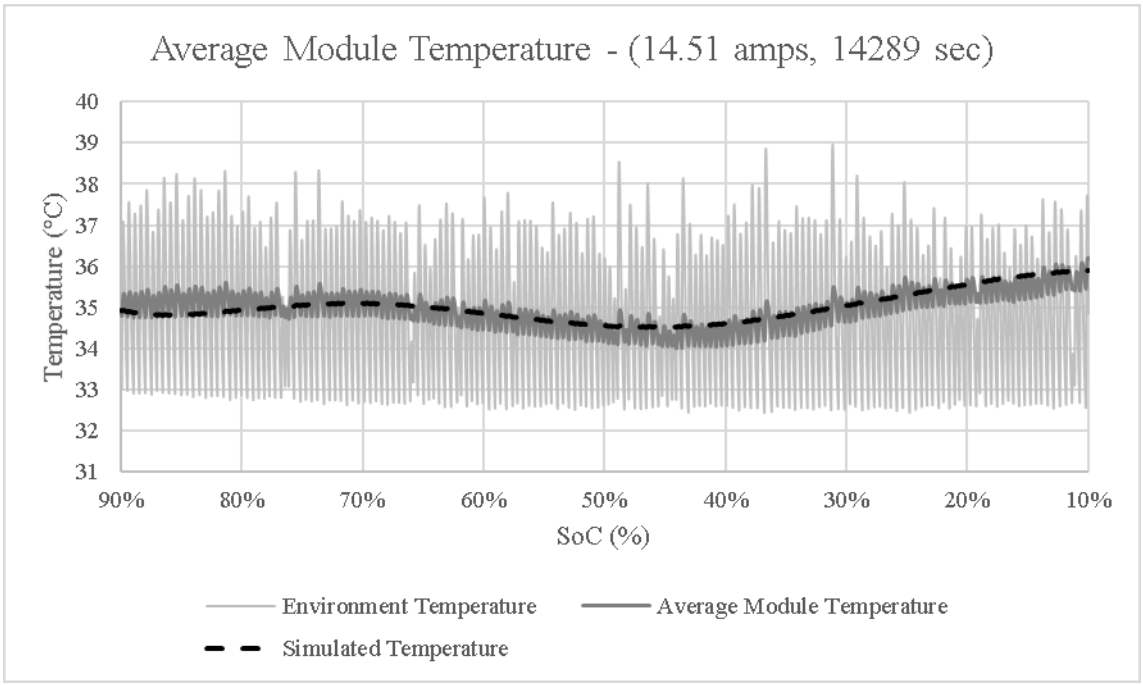

Figure 9-44: Simulated temperature and Experimental temperature obtained during discharging at 35°C.

9.11 Flat – 40°C

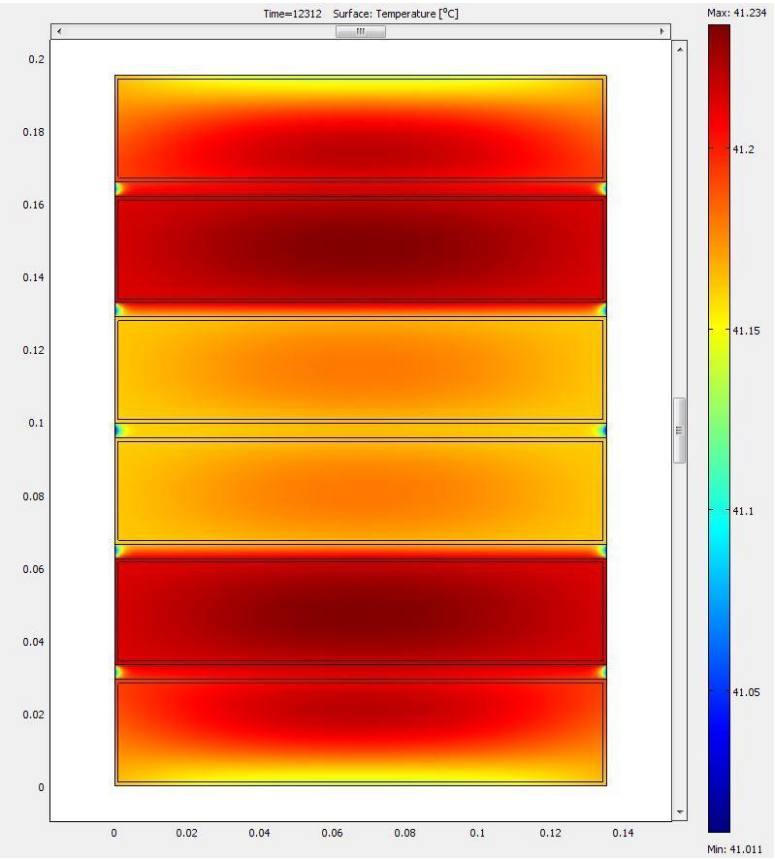

Figure 9-45: Final visual simulation of a temperature gradient along the external battery surface for 16.2A discharging. Total running time of 206 minutes.

Figure 9-46: Thermal picture from the battery at 206 minutes for 16.2A discharging, 40°C ambient.

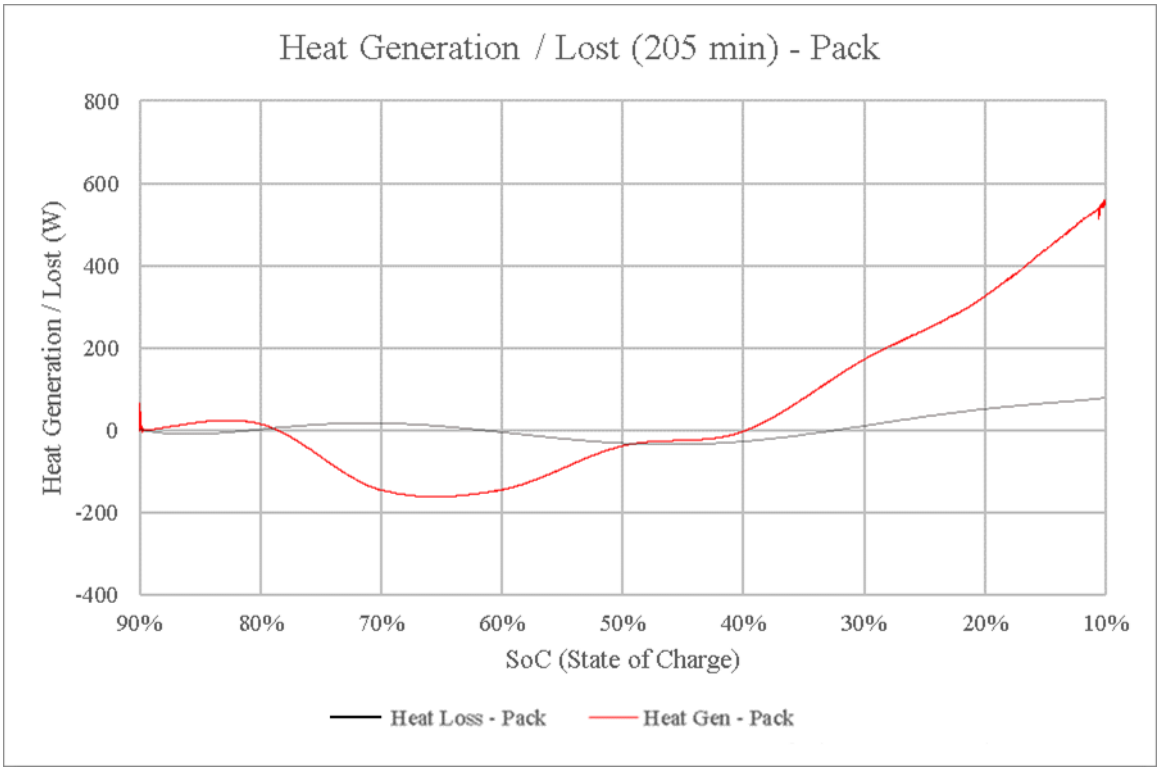

Figure 9-47: Experimental Generated heat and Lost during battery discharge for the flat condition.

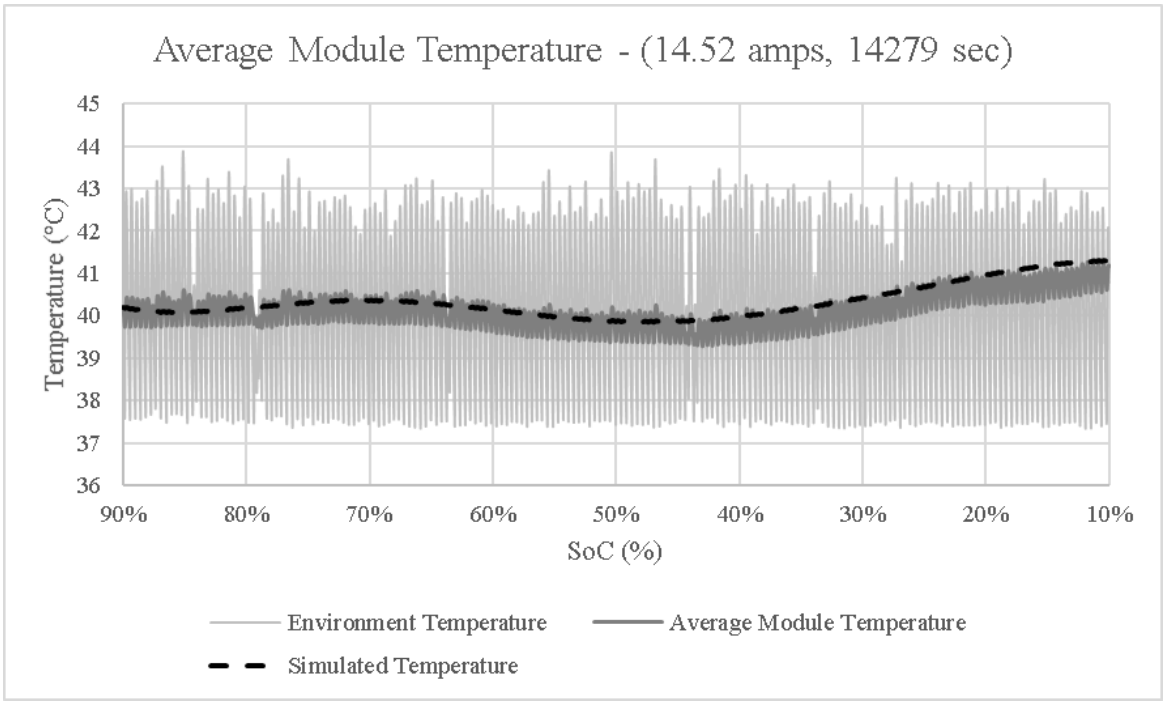

Figure 9-48: Simulated temperature and Experimental temperature obtained during discharging at 40°C.

9.12 Uphill – 25°C

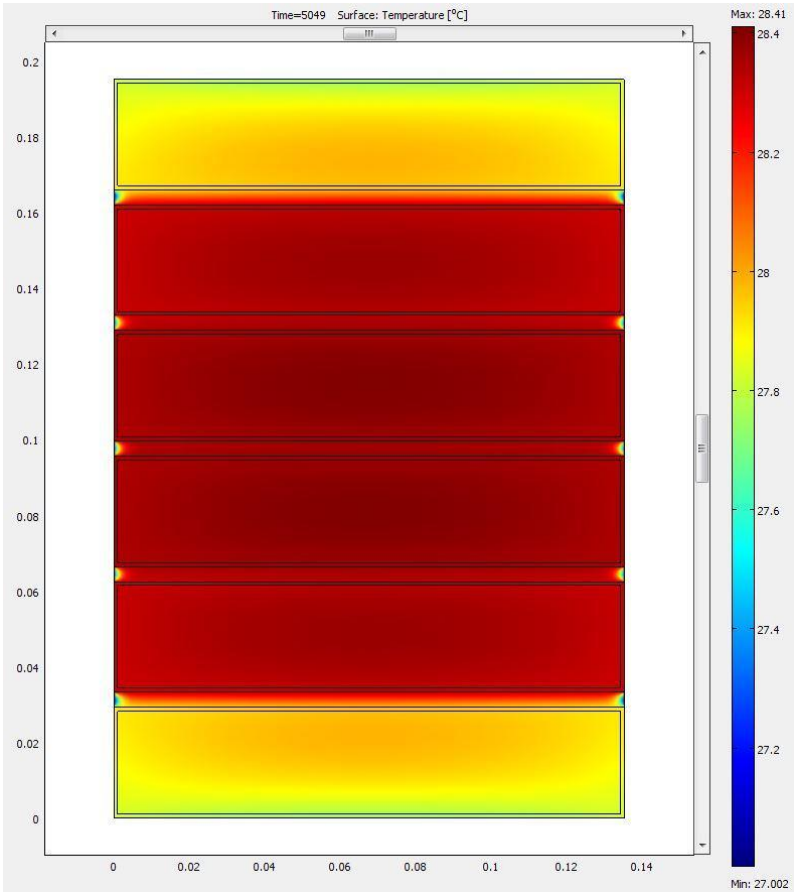

Figure 9-49: Final visual simulation of a temperature gradient along the external battery surface for 41.1A discharging. Total running time of 84 minutes.

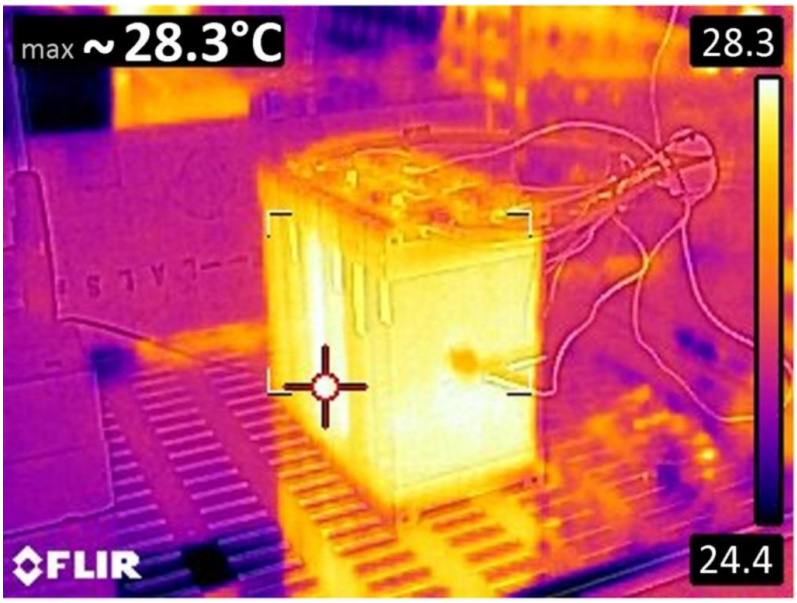

Figure 9-50: Thermal picture from the battery at 84 minutes for 41.1A discharging, 25°C ambient.

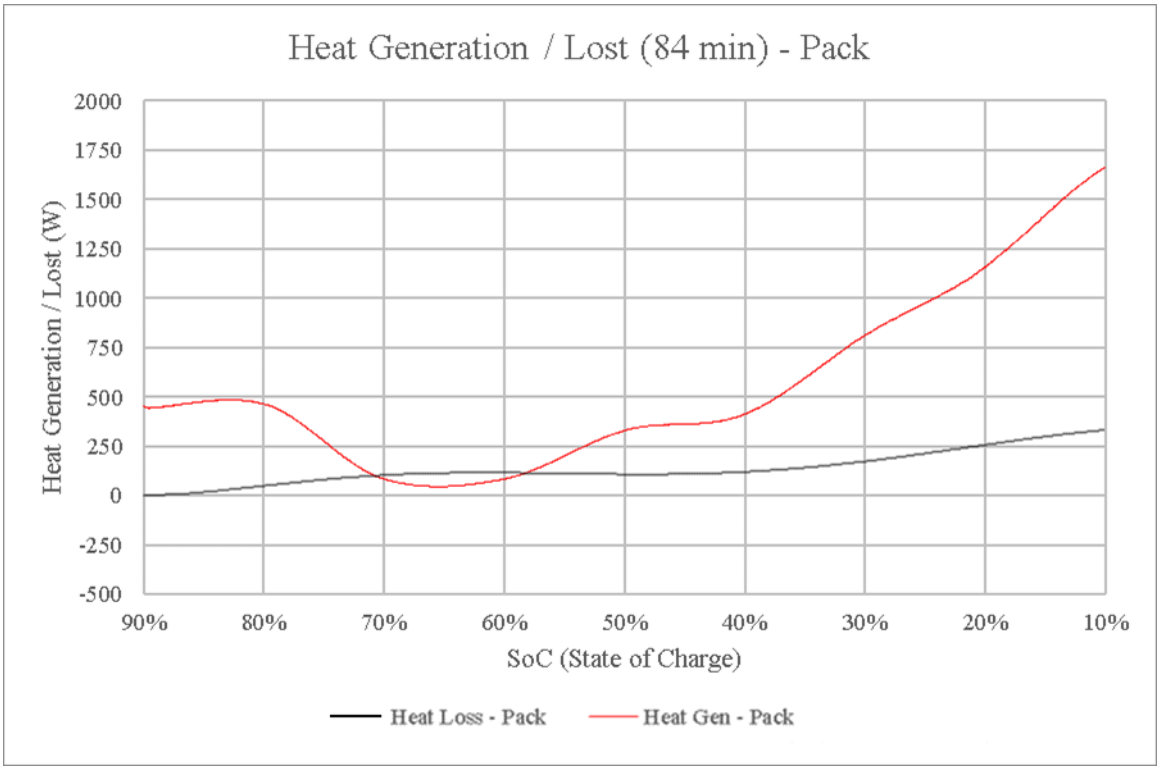

Figure 9-51: Experimental Generated heat and Lost during battery discharge for the Uphill condition.

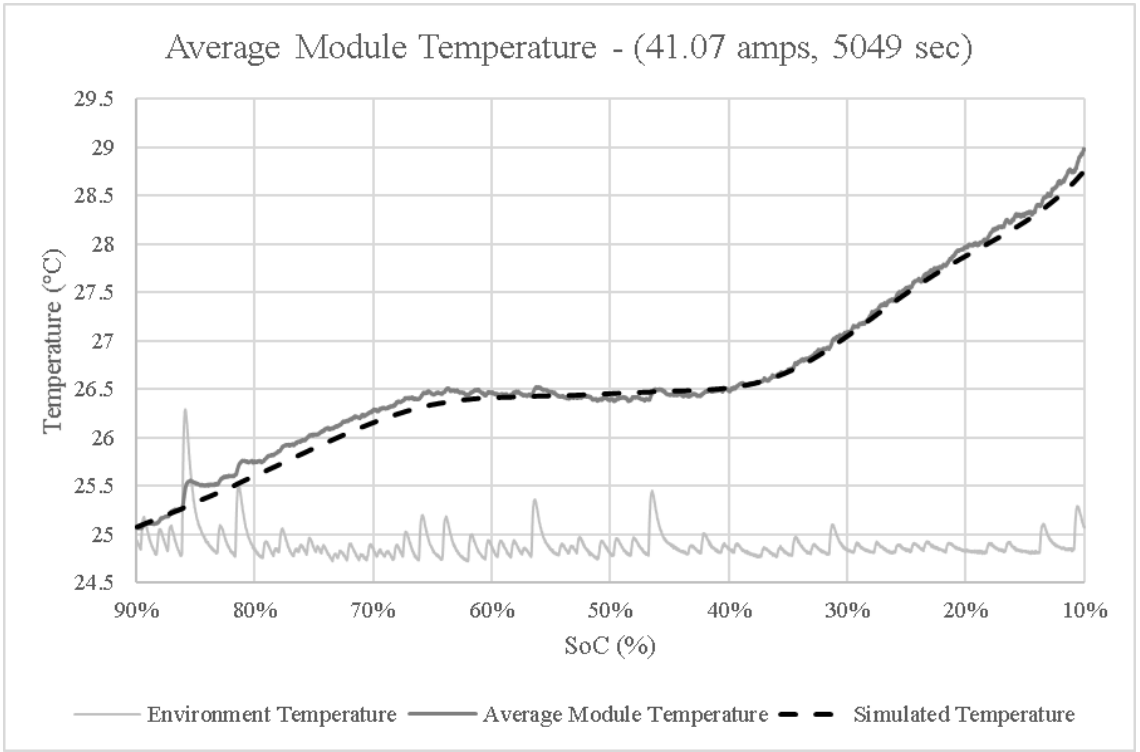

Figure 9-52: Simulated temperature and Experimental temperature obtained during discharging at 25°C.

9.13 Uphill – 30°C

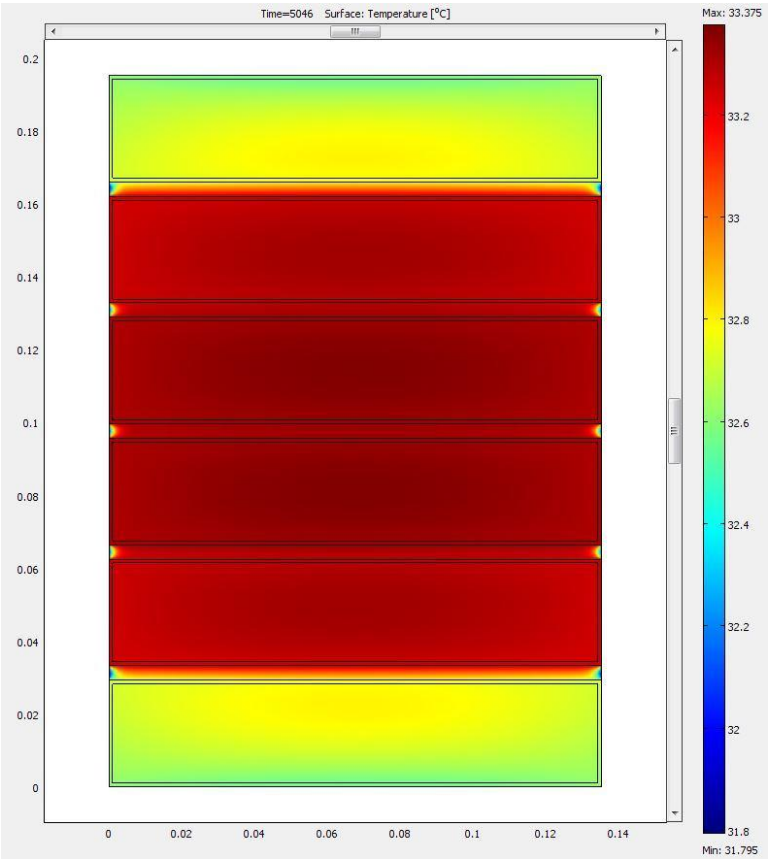

Figure 9-53: Final visual simulation of a temperature gradient along the external battery surface for 41.1A discharging. Total running time of 84 minutes.

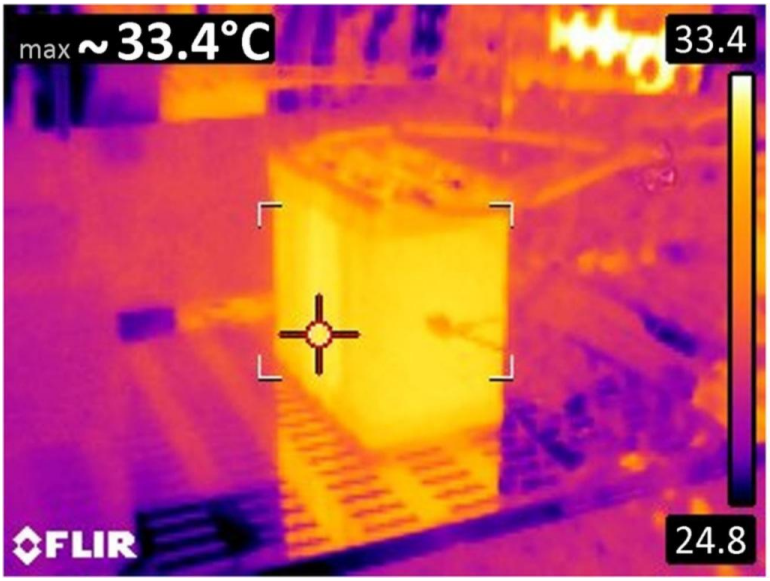

Figure 9-54: Thermal picture from the battery at 84 minutes for 41.1A discharging, 30°C ambient.

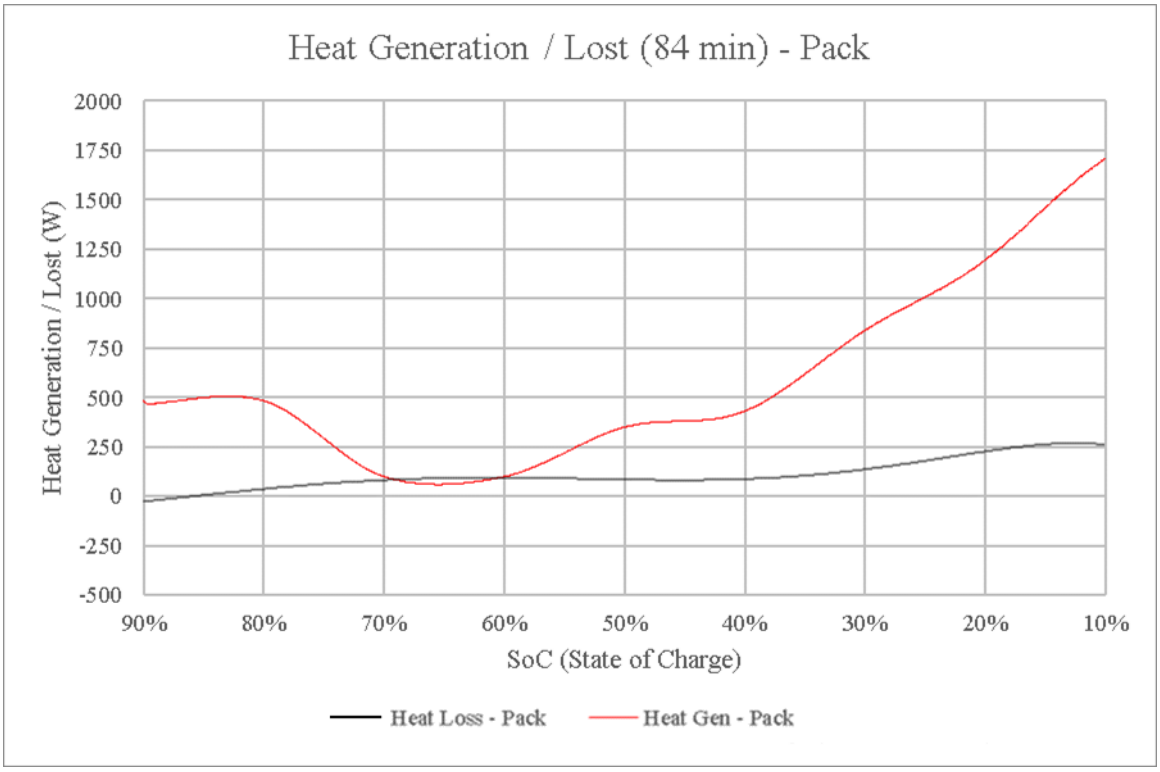

Figure 9-55: Experimental Generated heat and Lost during battery discharge for the Uphill condition.

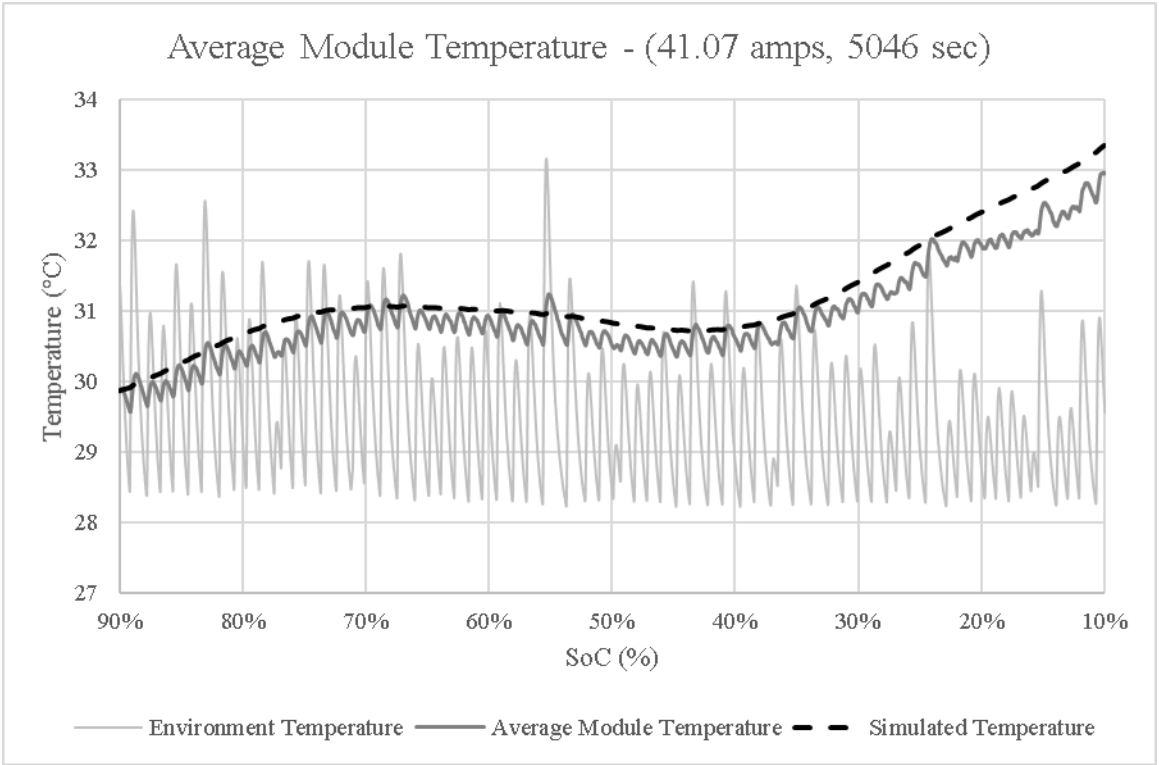

Figure 9-56: Simulated temperature and Experimental temperature obtained during discharging at 30°C.

9.14 Uphill – 35°C

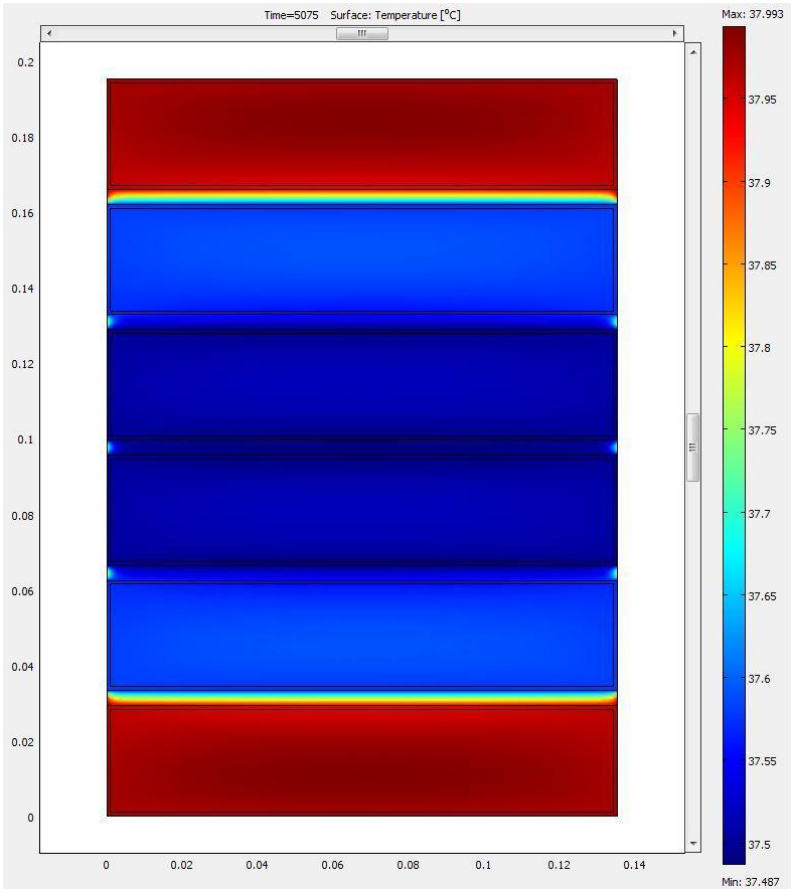

Figure 9-57: Final visual simulation of a temperature gradient along the external battery surface for 40.9A discharging. Total running time of 85 minutes.

Figure 9-58: Thermal picture from the battery at 85 minutes for 40.9A discharging, 35°C ambient.

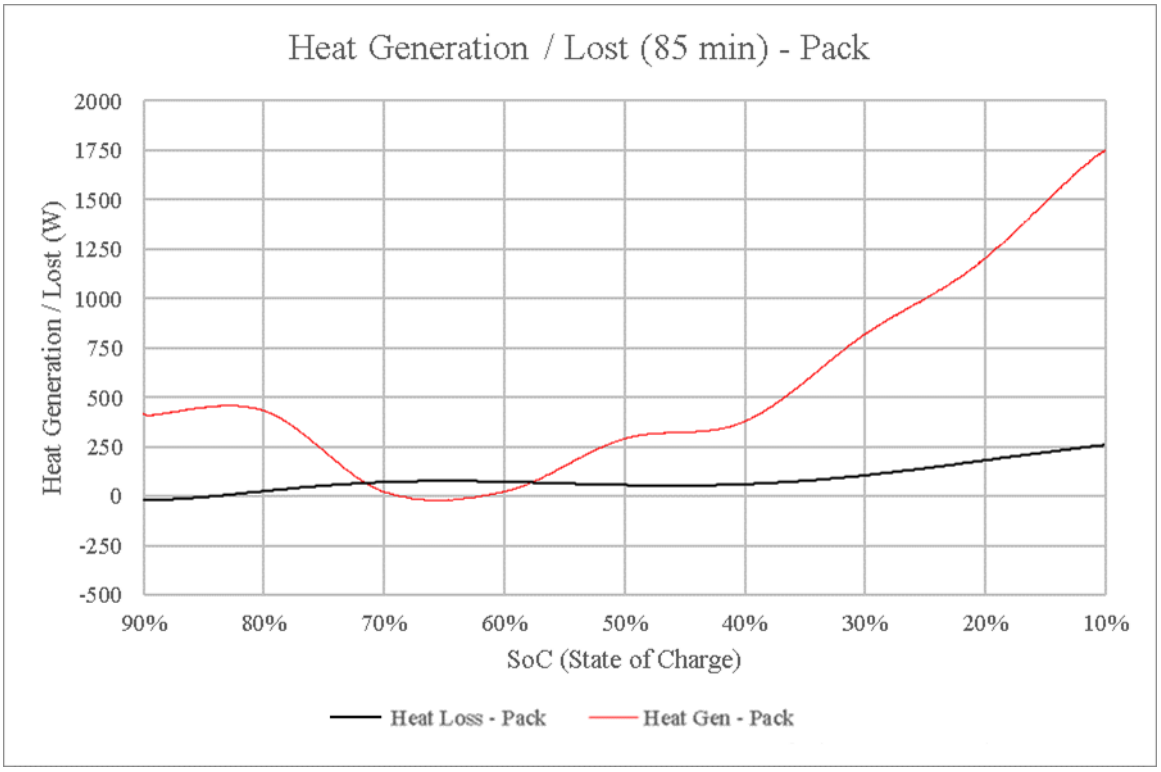

Figure 9-59: Experimental Generated heat and Lost during battery discharge for the Uphill condition.

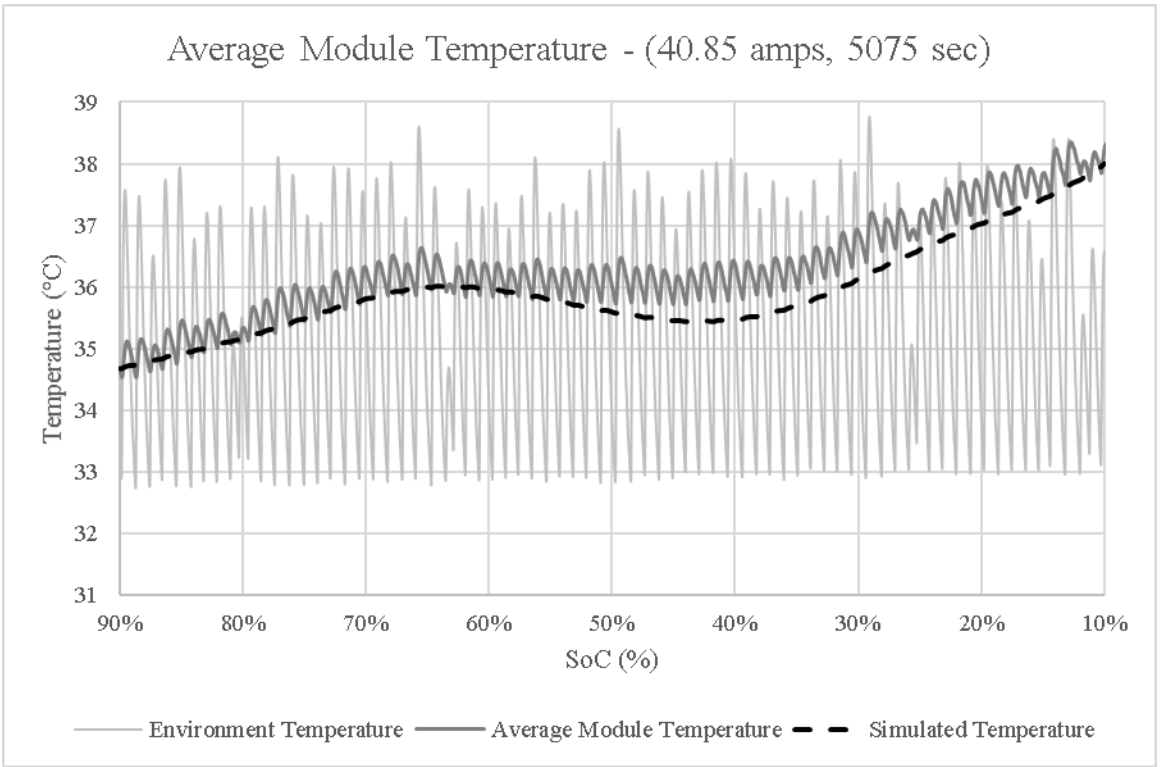

Figure 9-60: Simulated temperature and Experimental temperature obtained during discharging at 35°C.

9.15 Uphill – 40°C

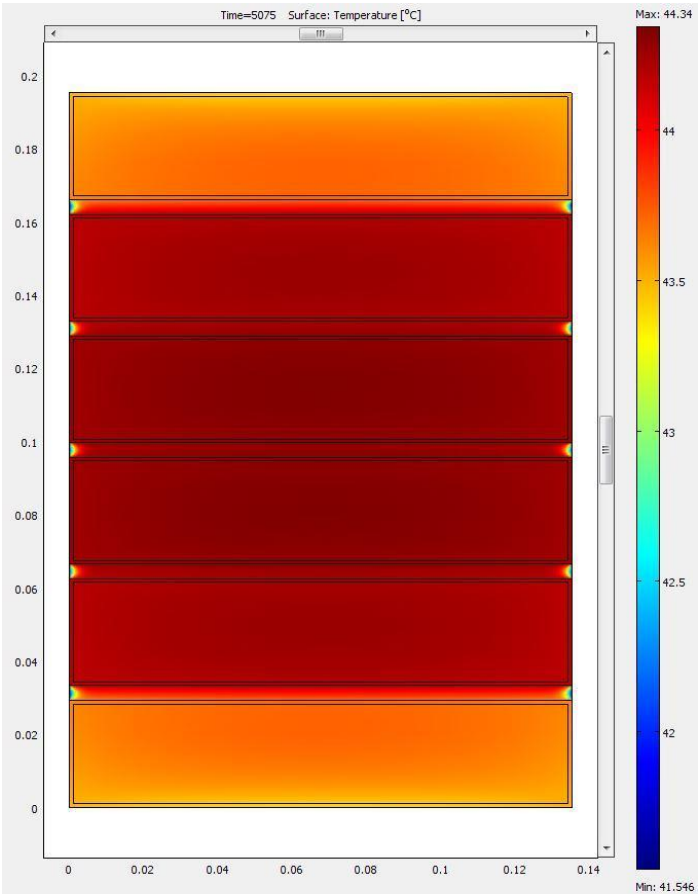

Figure 9-61: Final visual simulation of a temperature gradient along the external battery surface for 40.9A discharging. Total running time of 85 minutes.

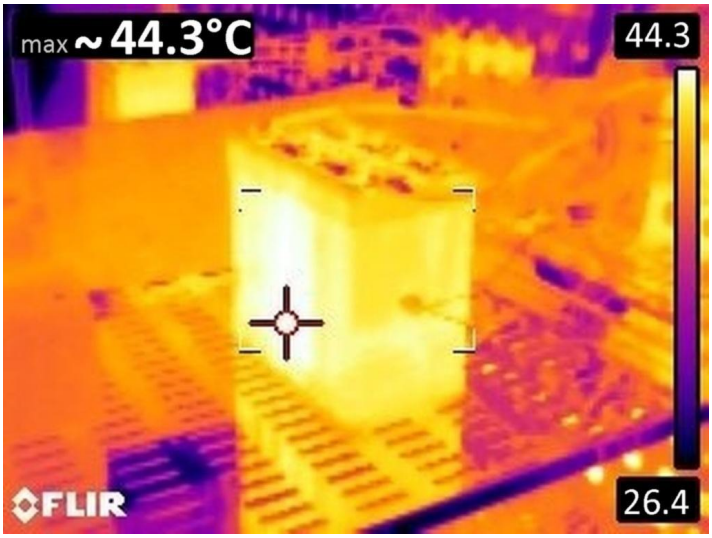

Figure 9-62: Thermal picture from the battery at 85 minutes for 40.9A discharging, 40°C ambient.

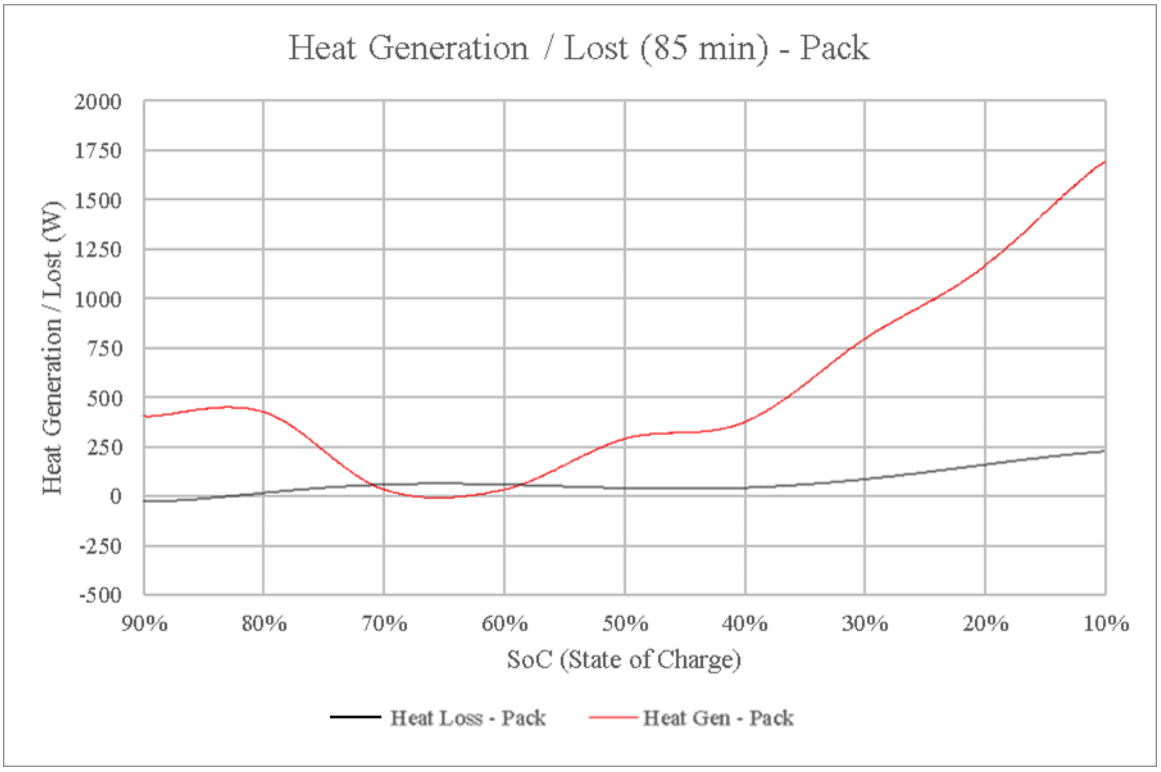

Figure 9-63: Experimental Generated heat and Lost during battery discharge for the Uphill condition.

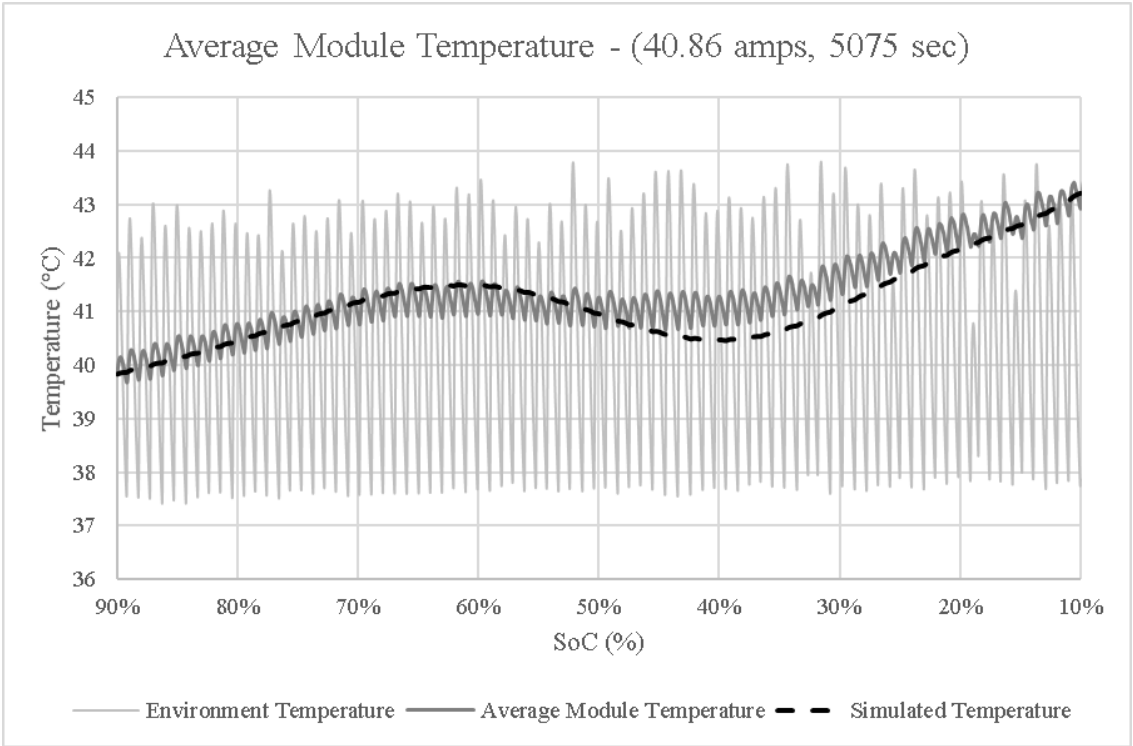

Figure 9-64: Simulated temperature and Experimental temperature obtained during discharging at 40°C.